transactions of the ASME

Published Quarterly by
The American Society of
Mechanical Engineers
Volume 94 • Series C • Number 3
AUGUST 1972

journal of heat transfer

EDITED and PUBLISHED quarterly at the offices of The American Society of Mechanical Engineers, United Engineering Center, 345 E. 47th St., New York, N. Y. 10017. Cable address, "Mechaneer," New York. Second-class postage paid at New York, N. Y., and at additional mailing offices.

CHANGES OF ADDRESS must be received at Society headquarters seven weeks before they are to be effective. Please send old label and new address.

PRICES: To members, $15.00, annually; to nonmembers, $30.00. Single copies, $10.00 each. Add $1.50 for postage to countries outside the United States and Canada.

INDEXED by the Engineering Index, Inc.

R. R. ADT, JR.
Assistant Professor,
Department of Mechanical Engineering,
University of Miami,
Coral Gables, Fla.
Assoc. Mem. ASME

G. N. HATSOPOULOS
President.

W. J. BORNHORST
Thermo Electron Engineering Corp.,
Waltham, Mass.

A Study of the Liquid–Vapor Phase Change of Mercury Based on Irreversible Thermodynamics

The object of this work is to determine the transport coefficients which appear in linear irreversible-thermodynamic rate equations of a phase change. An experiment which involves the steady-state evaporation of mercury was performed to measure the principal transport coefficient appearing in the mass-rate equation and the coupling transport coefficient appearing in both the mass-rate equation and the energy-rate equation. The principal transport coefficient σ, usually termed the "condensation" or "evaporation" coefficient, is found to be approximately 0.9, which is higher than that measured previously in condensation-of-mercury experiments. The experimental value of the coupling coefficient K does not agree with the value predicted from Schrage's kinetic analysis of the phase change. A modified kinetic analysis in which the Onsager reciprocal law and the conservation laws are invoked is presented which removes this discrepancy but which shows that the use of Schrage's equation for predicting mass rates of phase change is a good approximation.

1 Introduction

Bornhorst and Hatsopoulos [1][1] have presented an analysis of the liquid–vapor phase-change process based on the concepts of linear irreversible thermodynamics. The mass-rate equation from their analysis is

$$J_i = \frac{2\sigma}{2-\sigma} J_s \left[\frac{2h_{fg}}{RT} \left(\frac{K}{K+1} \right) \frac{\delta T}{2T} - \frac{\delta P}{P} \right] \qquad (1)$$

where J_i is the mass flux or rate of phase change, δT is the difference between the temperature at the vapor side of the interface T_{gi} and the temperature at the liquid side T_{fi}, δP is the difference between the actual pressure at the interface P and the saturation pressure P_s corresponding to the temperature T_{fi}, R is the gas constant, $h_{fg} = h_{gi} - h_{fi}$ is the difference between the enthalpy of the vapor h_{gi} and that of the liquid h_{fi} at the interface, σ is the principal mass-rate transport coefficient, and K is the coupling transport coefficient. The linear irreversible-thermodynamic energy-rate equation is

$$J_u = \left[h_{gi} - \frac{K}{K+1} h_{fg} \right] J_i - \frac{L_k}{T} \frac{\delta T}{T} \qquad (2)$$

where J_u is the energy flux and L_k is the principal energy-rate transport coefficient. The nomenclature is illustrated in Fig. 1 for condensation on a vertical wall. The transport coefficients σ, L_k, and K are thermodynamic properties which must be determined from experiment.

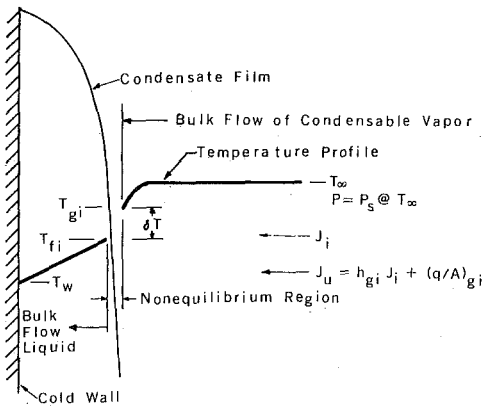

Fig. 1 Condensation on a vertical wall

2 Present Investigation

The purpose of this investigation is to measure transport coefficients. Since it is difficult to measure all three coefficients [2], L_k, σ, and K, we assume the kinetic-theory prediction of L_k and perform the experiment described in Sections 3 and 4 to obtain K and σ. The validity of the kinetic-theory assumption

[1] Numbers in brackets designate References at end of paper.

Contributed by the Heat Transfer Division for publication (without presentation) in the Journal of Heat Transfer. Manuscript received by the Heat Transfer Division August 10, 1970. Paper No. 72-HT-A.

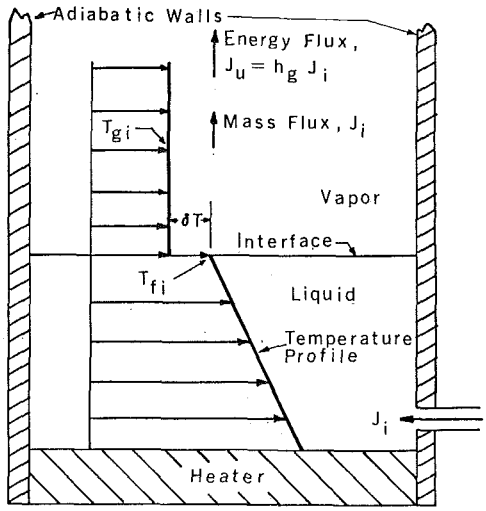

Fig. 2 Steady-state evaporation

is discussed in [2]. In the light of the experimental results obtained, a kinetic model of the phase change is developed which is consistent with the conservation laws, Onsager's reciprocal law, and experiment.

No measurements of the coupling transport coefficient K have been reported for any fluid in the past. Moreover, most values of σ reported in the literature have been measured for condensation processes, whereas in the present work σ is measured for an evaporation process.

3 Steady-State Evaporation Experiment

In general, phase-change processes result in a nonuniform temperature distribution in the vapor phase which is difficult to measure. For this reason an experiment termed the steady-state (*ss*) evaporation experiment has been devised in which the vapor temperature is uniform.

A *ss* evaporation experiment, shown schematically in Fig. 2, is one in which liquid changes to the vapor phase at a constant rate by evaporation at the liquid–vapor interface with the absence of boiling, and in which the heat transfer necessary for evaporation is supplied solely from the liquid side of the interface. There is no heat transfer to the vapor. For such a situation the vapor temperature far from the interface will eventually reach some uniform value. It can be shown [1] from first-law considerations that the vapor temperature will be uniform up to the interface. It follows that for *ss* evaporation equation (2) reduces to

$$\frac{K}{K+1}\frac{2h_{fg}}{RT} = -\frac{\gamma+1}{\gamma+1}\left[\frac{2}{\pi R}\right]^{1/2}\frac{P}{T^{3/2}}\left[\frac{\delta T}{J_i}\right]_{ss} \qquad (3)$$

where γ is the specific heat ratio and L_k is replaced by its kinetic-theory value. Equation (1), except for the subscript *ss* on J_i, δT, and δP, remains the same. The quantities needed from the experiment to evaluate K and σ are thus $(J_i)_{ss}$, T_{fi}, T_{gi}, and P.

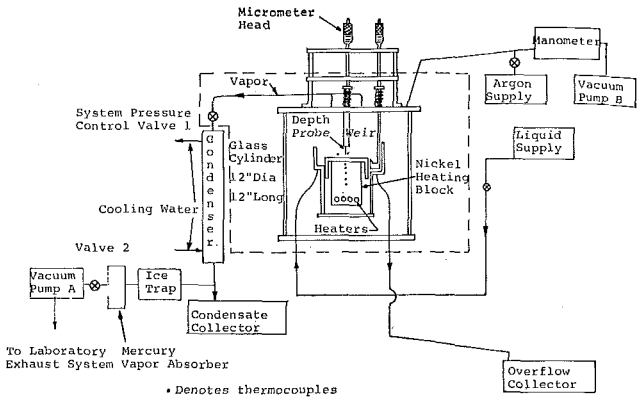

Fig. 3 Flow diagram of experiment

Experimental Apparatus

A flow diagram of the *ss* evaporation experimental apparatus is sketched in Fig. 3. Fig. 4 contains a drawing of the test section. Evaporation takes place at the surface of a thin layer of liquid mercury on the nickel block, the necessary heat being supplied by electrical heaters placed in the nickel. To obtain the liquid interface temperature T_{fi}, a least-squares straight line is fitted through the temperature measurements made in the nickel heating block where the temperature profile is approximately a straight line. This line is then linearly extrapolated through the liquid, taking into account the differences in thermal conductivity. To extrapolate it is necessary to know the depth of the liquid layer. The liquid depth is determined by measuring the displacement of a needle-like probe when it is moved from the solid nickel surface to the liquid surface by means of micrometer heads.

Nickel was chosen as the material for the heating block because mercury wets nickel. It is necessary to have a wettable surface if a thin film of liquid is to be realized; also the wetting minimizes any contact resistance which may exist at the solid–liquid interface.

It is desirable to have a thin layer of liquid so that any error in the extrapolation which may result from a nonlinear temperature profile in the liquid will be minimized. Also, a thin layer minimizes the possibility of convection. Finally, a thin layer of liquid will minimize the possibility of having active nucleation sites for boiling by reducing the superheat at the nickel surface.

It should be noted that there is a means of having a liquid flow rate into the test section which is greater than that evaporated. This excess flow rate is termed the overflow. The reason for incorporating the overflow is to provide some means of keeping the liquid surface clean.

The temperature in the vapor T_g is measured by thermocouples at various locations and orientations, as is shown in Fig. 4.

The thermocouples are copper–constantan enclosed in stainless steel sheaths. They were calibrated against a standard platinum resistance thermometer.

The rate of evaporation J_i is determined from the heat transfer to the liquid (which is given by the temperature gradient and conductivity in the nickel) divided by the latent heat h_{fg}. A means of checking this is by taking the difference between the supply and overflow rate of liquid mercury.

Nomenclature

h = specific enthalpy
$h_{fg} = h_{gi} - h_{fi}$
J_i = mass flux
J_u = energy flux
$J_s = P/(2\pi RT)^{1/2}$
K = coupling transport coefficient
L_k = principal energy-rate transport coefficient
P = pressure
R = gas constant
T = temperature
U = related to K, see equation (4)
$\delta P = P - P_s(T_{fi})$
$\delta T = T_{gi} - T_{fi}$
γ = specific heat ratio
σ = principal mass-rate transport coefficient or condensation (or evaporation) coefficient

Subscripts

f = liquid
g = vapor
i = liquid–vapor interface
s = saturation condition
ss = steady state

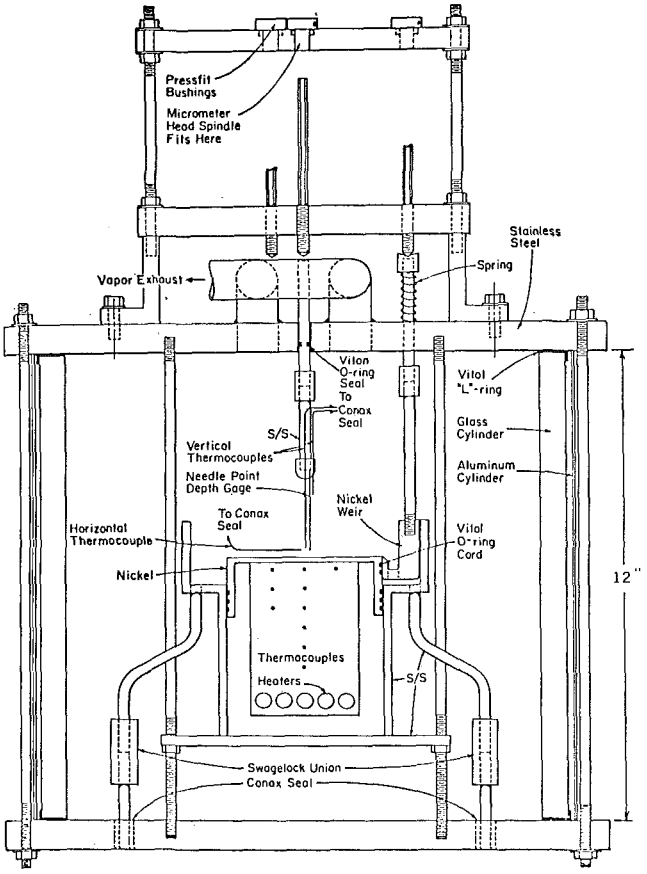

Fig. 4 Drawing of test section

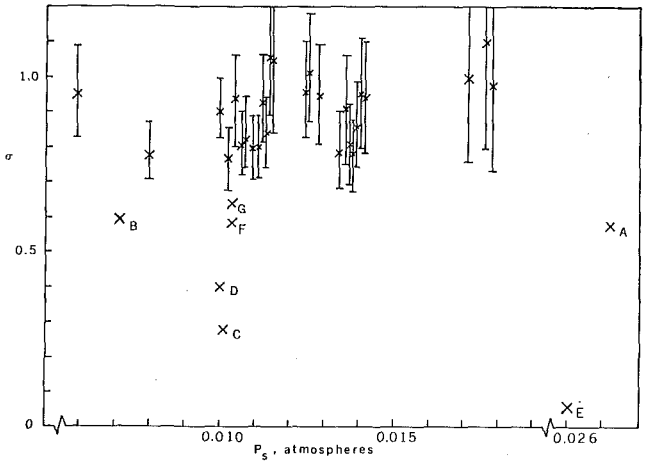

Fig. 5 Principal mass-rate transport coefficient σ versus pressure P_s for steady-state evaporation experiment

The pressure in the test section P_g is measured by a manometer. One leg of the manometer is connected to a vacuum reference.

The saturation pressure data for mercury were taken from [4], the other properties of mercury from [5], and the thermal conductivity of nickel from [6].

The details of the experimental operating procedure are given in [2] along with a discussion of the errors due to measurement and errors inherent in assuming the above relationships between the measurements and the desired physical quantities.

5 Experimental Results

Fig. 5 shows the values of σ obtained from the steady-state evaporation experiment. Included are the error bands resulting from the experimental uncertainties discussed in [2]. It should

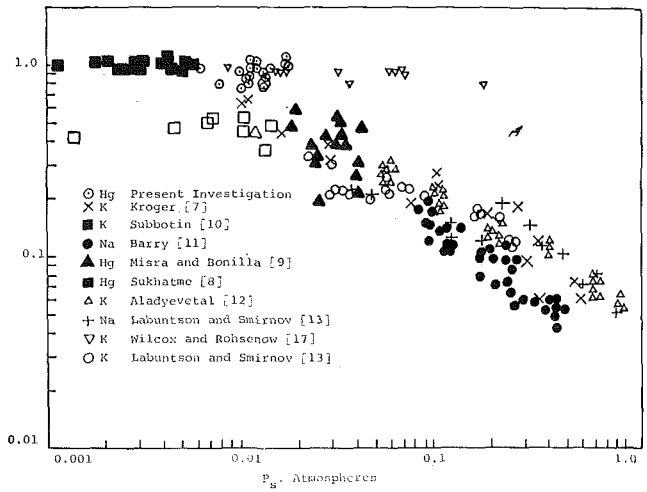

Fig. 6 Principal mass-rate transport coefficient versus pressure P_s for various liquid metals

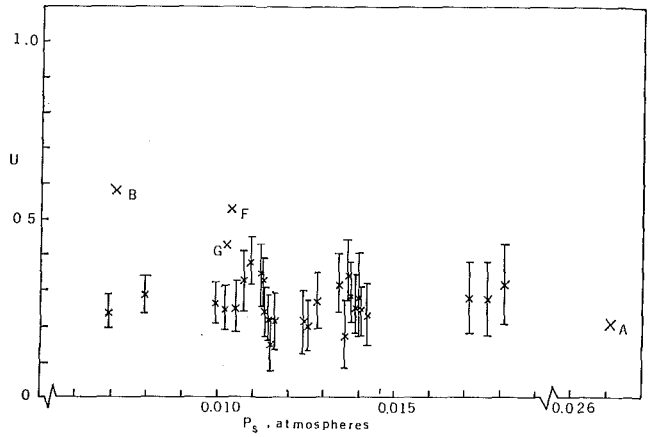

Fig. 7 Coupling transport coefficient U versus pressure P_s

be observed that none of the lower limits of the error bands are above unity. There are three points C, D, and E having values of σ which are less than 0.4. At the time these points were taken, a film of impurities was observed on the liquid surface. This film would result whenever the overflow region of the nickel heating block did not wet properly. Instead of having the entire surface freely flowing, there would be regions of stagnant surface fluid. In these stagnant regions, a film would develop with time. The film acts as a resistance to the evaporation thereby requiring a large driving force δP which results in low values of σ. These three points clearly show the strong influence of the condition of the surface on the coefficient σ. There are four data points having values of $\sigma \approx 0.6$. The impurity film was not observed for these points; however, points F and G were taken during a time in which much difficulty was encountered in preventing the buildup of the film. The remaining points are found to be scattered within their error bands around σ of about 0.9. From this we conclude that the scatter outside of the experimental uncertainties is due to the absence of a sufficiently free-flowing surface.

The values of σ, excluding those from the present investigation affected by contamination, are shown in Fig. 6 along with the condensation results of previous investigations for various liquid metals. In Fig. 7 K is presented in terms of U where

$$U = \frac{K}{K+1}\frac{2h_{fg}}{RT} \tag{4}$$

6 Discussion of Experimental Results

In the present study σ was found to decrease when contamination in the form of an impurity film was present. Knudsen [15]

observed this same effect when he measured σ for evaporation of a mercury droplet into a vacuum. To eliminate contamination, he renewed the droplet every fourth second and the resulting values of σ were unity. Volmer and Esterman [16] also obtained σ equal to unity for the evaporation of mercury into a vacuum by taking precautions to avoid surface contamination.

The condensation coefficient σ determined from the steady-state evaporation-of-mercury experiment does not appear to follow the downward trend with increasing pressure as found during condensation of the other liquid metals (Fig. 6). This could be attributed to a basic difference between condensation and evaporation; however, in the light of the thermodynamic analysis which makes no distinction between the direction of phase change, we are inclined to reject this premise. Besides, Wilcox and Rohsenow [17] conclude from their data and error analysis that the condensation coefficient is equal to unity and that the pressure-dependence reported by others is due to experimental error.

The experimental value of U is found to be less than unity. As discussed in the next section, an extension of Schrage's kinetic method of analyzing the phase-change process is not in accord as it requires that U be unity. A more general kinetic model of the phase-change process, however, which is also discussed in the next section, shows that U is not necessarily equal to unity.

7 Analytical Considerations

In his kinetic model of the phase-change process Schrage considers the liquid and vapor phases to be uniform and to be separated by a mathematical plane, called the liquid–vapor interface. He considers a control surface α placed a distance less than a mean free path away from the interface in the vapor. (Consider the vapor to be to the right of the interface.) He then assumes that the velocity distribution of the incident molecules crossing α to the left is half-Maxwellian[2] with a superimposed bulk velocity V and characterized by the temperature T_g and the pressure P_g. This distribution is the same as that of the vapor molecules far from the interface which have a velocity toward the interface. The persistence of such a distribution up to the interface would require a collisionless region on the vapor side of the interface. The molecules crossing α to the right are considered to be composed of two parts, the first of which consists of molecules emitted from the liquid. The emission process is assumed to depend only on the temperature of the liquid surface. The expression for the rate of emission is obtained by considering an equilibrium situation where the incident distribution is half-Maxwellian at the temperature of the liquid surface T_{fi} and the corresponding saturation pressure $P_s(T_{fi})$. The second part crossing α to the right consists of those incident molecules which are reflected from the interface. This second part is related to the incident flux by way of the condensation coefficient σ which is defined as the fraction of incident molecules which condense. On integrating the assumed velocity distributions, using the definition of σ and assuming small driving forces δP and δT, Schrage's result may be written in the following form [1, 2]:

$$J_i = \frac{2\sigma}{2 - \sigma} J_s \left(\frac{\delta T}{2T} - \frac{\delta P}{P} \right) \tag{5}$$

where σ is the evaporation or condensation coefficient. From equations (1) and (5) we see that the transport coefficient σ can be interpreted as the evaporation or condensation coefficient as defined above. If we consider equations (1), (4), and (5) when $J_i = 0$ we see that the kinetic analysis predicts a value of unity for U which is not in accord with the measurements. It can also be shown [2] that Schrage's selection of P_g to characterize the incident distribution violates the conservation-of-momentum requirement. In addition it can be shown [2] that even if the conservation of momentum and energy are invoked, the kinetics of the vapor at the liquid–vapor interface cannot be modeled with half-Maxwellian velocity distributions if agreement with the data is required.

An improved method of modeling the interface kinetics is to account for the error in the velocity distribution by superimposing fluxes of mass, momentum, and energy on those obtained by integrating the distributions. This method is best illustrated by considering the familiar situation of a temperature gradient dT/dx in a semiperfect monatomic gas moving at a low Mach number. At a control surface in the gas, we consider the molecules to be described by a Maxwellian distribution with a superimposed bulk flow velocity. Integration of this distribution yields the enthalpy flux $h_g J_i$. The net energy flux is greater than this, however, by the amount $-k(dT/dx)$, where k is the thermal conductivity of the gas. This method is still an approximation as we are still ignorant of the actual kinetics at the interface. To obtain a better understanding of the vapor-side kinetics the Boltzmann equation should be employed. By using this method of describing the vapor kinetics at the interface and requiring that the conservation laws and Onsager's reciprocal law be satisfied, it can be shown that [2]

$$J_i = J_s C_\sigma \left[\frac{1}{1 + \dfrac{C_\sigma U(1 - U)}{16}} \right] \left[U \frac{\delta T}{2T} - \frac{\delta P}{P} \right] \tag{6}$$

where

$$C_\sigma = \frac{2\sigma}{2 - \sigma} \tag{7}$$

It should be pointed out that the value of the coefficient σ determined from equation (5) and the experimental results is approximately the same as that found using the improved analysis. Therefore, even though Schrage's model is not consistent with the momentum equation and does not yield the correct value of U, it does result in an equation containing a coefficient σ the value of which, as determined from experiment, is a good approximation of the condensation coefficient.

8 Conclusions

In the present investigation it was found that the evaporation or condensation coefficient σ, measured during the steady-state evaporation-of-mercury experiment, is higher than that obtained previously in condensation-of-mercury experiments. It was also found that contamination of the liquid surface results in low values of σ.

From the measured values of the coupling transport coefficient K (or U) and the analysis discussed in Section 7, we conclude that the events taking place at the liquid–vapor interface during the phase change cannot be represented by half-Maxwellian velocity distributions.

From the results of the analysis discussed in Section 7, where we allowed for non-Maxwellian velocity distributions, we conclude that even though Schrage's equation is not exact, it is a good approximation to use this equation in conjunction with experimental measurements to arrive at the condensation coefficient.

Acknowledgments

The authors wish to thank Professors Peter Griffith, Warren M. Rohsenow, and S. William Gouse, Jr., for many valuable discussions. Also Dr. Detlev G. Kroger and Professor E. J. LeFevre. This work was supported by the National Aeronautics and Space Administration under contract number NAS8-20013

[2] By a half-Maxwellian distribution, it is meant that the velocity distribution is Maxwellian and that the limits on the velocity u are $-\infty \leq u \leq 0$ for the incident distribution and $0 \leq u \leq \infty$ for the emitted distribution while v and w are allowed to vary from $+\infty$ to $-\infty$. The velocity u is in a direction perpendicular to the interface and to the right. The velocities v and w are perpendicular to each other and to u.

and was done in part at the Computation Center at the Massachusetts Institute of Technology, Cambridge, Mass.

References

1 Bornhorst, W. J., and Hatsopoulos, G. N., "Analysis of a Liquid Vapor Phase Change by the Methods of Irreversible Thermodynamics," *Journal of Applied Mechanics*, Vol. 34, TRANS. ASME, Series E, Vol. 89, No. 4, Dec. 1967, pp. 840–846.

2 Adt, R. R., Jr., "A Study of the Liquid-Vapor Phase Change of Mercury Based on Irreversible Thermodynamics," ScD thesis, M.I.T., Cambridge, Mass., June 1967.

3 Hatsopoulos, G. N., and Keenan, J. H., *Principles of General Thermodynamics*, John Wiley & Sons, New York, N. Y., 1965.

4 Ditchburn, R. W., and Gilmour, J. C., "The Vapor Pressures of Monatomic Vapors," *Rev. Mod. Phys.*, Vol. 13, Oct. 1941.

5 Weatherford, W. D., Jr., Tyler, J. C., and Ku, P. M., "Properties of Inorganic Energy-Conversion and Heat-Transfer Fluids for Space Applications," WADD Technical Report 61-96, Nov. 1961.

6 Technical Bulletin T-15, The International Nickel Co.

7 Kroger, D. G., "Heat Transfer During Film Condensation of Potassium Vapor," ScD thesis, M.I.T., Cambridge, Mass., Sept. 1966.

8 Sukhatme, S., and Rohsenow, W., "Heat Transfer During Film Condensation of a Liquid Metal Vapor," Report No. 9167-27, Dept. of Mech. Engr., M.I.T., Cambridge, Mass., Apr. 1964.

9 Misra's data are presented by: Wilhelm, D. J., "Condensation of Metal Vapors: Mercury and the Kinetic Theory of Condensation," ANL-6948, 1964.

10 Subbotin, V. I., Ivanovsky, M. N., Sorokin, V. P., and Chulkov, V. A., *Teplofizika Vysokikh Temperatur*, No. 4, 1964.

11 Barry, R. E., PhD thesis, University of Michigan, 1965.

12 Aladyev, I. T., et al., "Thermal Resistance of Phase Transition with Condensation of Potassium Vapor," *Proceedings of the Third International Heat Transfer Conference*, 1966.

13 Labuntsov, P. A., and Smirnov, S. I., "Heat Transfer in Condensation of Liquid Metal Vapors," *Proceedings of the Third International Heat Transfer Conference*, 1966.

14 Schrage, R. W., *A Theoretical Study of Interphase Mass Transfer*, Columbia University Press, New York, N. Y., 1953.

15 Knudsen, M., *The Kinetic Theory of Gases*, Methuen and Co. and John Wiley & Sons, New York, N. Y., 1950.

16 Volmer and Esterman's results are discussed in reference [15].

17 Wilcox, S. J., and Rohsenow, W. M., "Film Condensation of Metals—Precision of Measurement," Report No. DSR 71475-62, Engineering Projects Laboratory, M.I.T., Cambridge, Mass., 1969.

H. EHYA
Research Assistant.

F. M. FAUBERT
Research Assistant.

G. S. SPRINGER
Professor.
Mem. ASME

Fluid Dynamics Laboratory,
Department of Mechanical Engineering,
University of Michigan,
Ann Arbor, Mich.

Thermal-Conductivity Measurements of Propane and N-Butane in the Range 300 to 1000 deg K

Using a thermal-conductivity column the thermal conductivity of propane and normal butane were measured at 760 mm Hg in the range 300–1000 deg K. The thermal-conductivity values obtained were compared with existing data and with the Misic–Thodos formula.

Introduction

Although the need for thermal-conductivity values of hydrocarbons at high temperatures is evident, there are few data available at temperatures above 500 deg K. In this paper thermal-conductivity data are reported for normal butane and propane at atmospheric pressure in the range 300–1000 deg K. A thermal-conductivity column was used in the experiments. This type of apparatus offers the possibility of good accuracy and precision as has been demonstrated recently by its use in measuring thermal conductivities of gases up to 2400 deg K [1, 2].[1]

Experimental Apparatus and Procedure

The experimental apparatus has been described in detail in references [2, 3] and therefore only the major features of the apparatus and procedure are presented here. The apparatus consisted of a conductivity column, the electrical system, and the vacuum system.

A schematic of the column is shown in Fig. 1. A 0.0101-cm-dia and 50-cm-long tungsten filament was mounted coaxially in a 56-cm-long vertical precision-bore Pyrex tube (0.635 cm ID). The filament was resistance-welded to 0.0760-cm-dia tungsten "rods," which were attached to precision-machined lava spacers placed at each end of the column. The top spacer was firmly mounted while the bottom one was allowed to slide in the tube to compensate for the expansion of the filament at higher temperatures. The filament was accurately centered in the tube by viewing the filament–tube assembly through a shadowgraph and adjusting the support rods as needed. Approximately 10 cm from each end of the filament a 0.00761-cm-dia wire (potential lead) was spot-welded to the filament. The potential leads were wound in a loose coil and were also attached to the lava spacers by 0.0760-cm-dia tungsten rods. The filament was kept at a constant tension by an 8-gram weight attached to the bottom lava spacer.

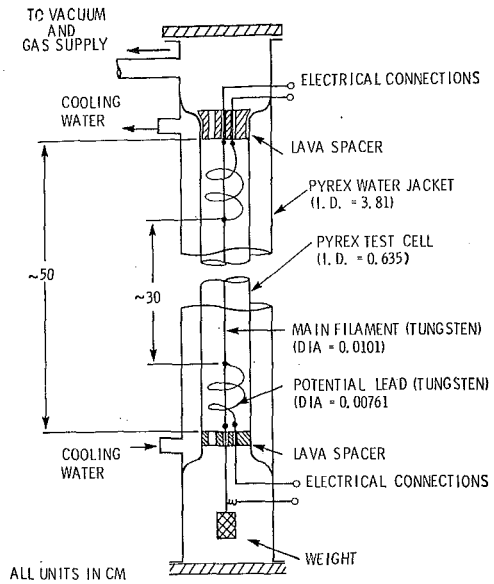

Fig. 1 Schematic of conductivity column

The column was surrounded by a Pyrex jacket through which water was circulated constantly at a rate of about 10 liter/min. The water temperatures at the inlet and outlet ports were monitored with thermocouples and were kept within 0.1 deg C at 25 deg C.

The electrical leads were attached to the top and bottom tungsten rods above and below the respective lava spacers.

[1] Numbers in brackets designate References at end of paper.

Contributed by the Heat Transfer Division for publication (without presentation) in the Journal of Heat Transfer. Manuscript received by the Heat Transfer Division April 15, 1971. Paper No. 72-HT-B.

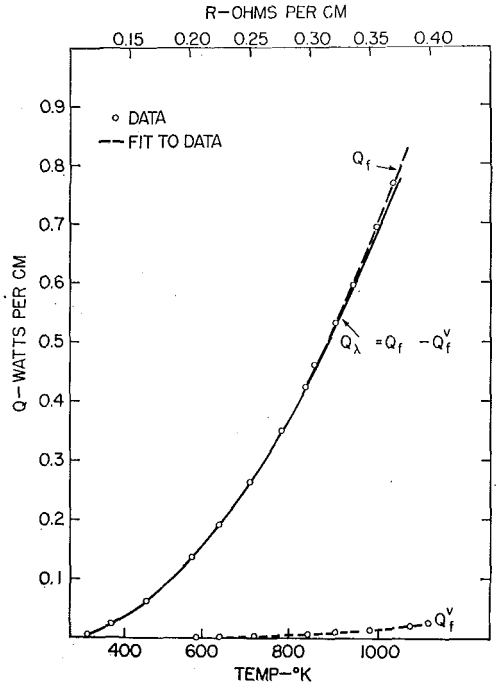

Fig. 2 Experimental results for normal butane

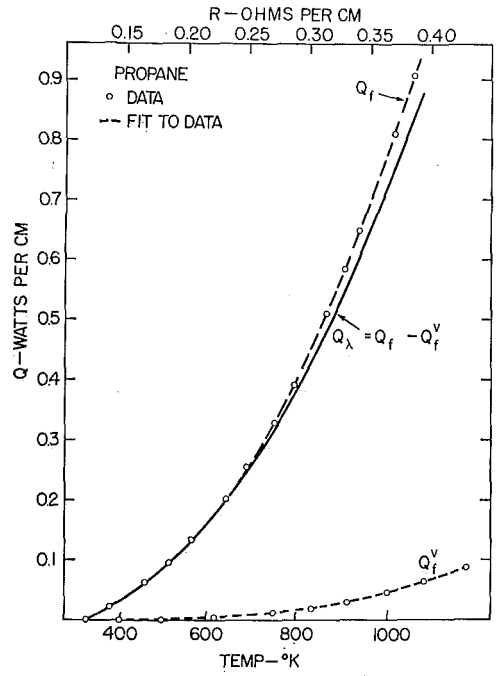

Fig. 3 Experimental results for propane

Power to the filament was provided by a highly regulated d-c power supply. The current through the filament was determined by measuring the potential drop across a high-precision standard resistor (0.0999996 ohm) placed in series with the filament and kept in a constant-temperature oil bath. The potential drop across the filament between the potential leads was also measured, and thus the power dissipated could readily be calculated. The electrical measurements were made with EDC models MV 100N and VS-1000/007 high-precision d-c voltage standards.

The column was connected to the vacuum pumps and gas-supply bottles through a Pyrex vacuum system. The lowest attainable pressure in the system was $\sim 5 \times 10^{-7}$ mm Hg as indicated by an ionization gauge. With the test gas in the system the pressure was measured by a U-tube mercury manometer and was maintained constant at 760 mm Hg. The test gases were "research grade" supplied by the Phillips Petroleum Co. Each gas was admitted into the column through a dry-ice-acetone cold trap and, prior to taking data, the system was purged several times with the gas.

Before taking data the filament was heated in vacuum to 2400 deg K for 24 hr to stabilize its electrical properties. Then the resistance versus temperature characteristic of the filament was determined. Above 1100 deg K the temperature of the filament was measured with an optical pyrometer [2, 3]. At 300 deg K the resistance of the filament was determined according to the procedure described by Thomas and Brown [4]. It was found that at both 300 deg K and above 1100 deg K the relationship between the filament temperature and resistance agreed closely with that given by Smithells [5]. Therefore, between 300–1100 deg K the filament temperature was determined from the measured average resistance per unit length together with the resistivity tables of Smithells.

Upon completion of the calibration the filament temperature was set at the required value and the heat loss from the center section of the filament (i.e., the section between the potential leads) was measured both in vacuum and in the presence of the gas. The length of the filament between the potential leads, L, was also measured throughout the experiment with a cathetometer.

Treatment of the Data

Due to the large temperature differences between the filament and the outer cylinder the gas moves upward near the filament and downward in the outer portion of the column. In addition to this "primary" motion, multicellular secondary motion may also occur in the column. Both of these motions may result in significant heat convection from the filament. However, if only the primary motion is present, then at some distance from each end of the column the axial temperature gradients diminish and the heat convected from the filament, Q_c, becomes negligible compared to the conductive and radiative heat transfer [6, 7–12]. The distance from the ends of the column where this condition is met can be approximated by [9]

$$Z_p = D \frac{\mathrm{Ra}}{7670} \qquad (\mathrm{Ra} \geq 7670) \tag{1}$$

where D is the inner diameter of the outer cylinder and Ra is the Rayleigh number defined as

$$\mathrm{Ra} = \left[\frac{g\rho^2 \Delta T D^3}{\eta^2 T} \frac{C_p \eta}{\lambda} \right]_{T=\bar{T}} \tag{2}$$

In equation (2) g is the gravitational acceleration, ρ the density, η the dynamic viscosity, C_p the constant-pressure specific heat, and λ the thermal conductivity of the gas. ΔT is the temperature difference between the filament and the outer cylinder, and $\bar{T}$ is the average temperature of the gas. In the present experiments the maximum Rayleigh number was $\sim 8 \times 10^4$ and for this Rayleigh number equation (2) gives a Z_p value of ~ 6.6 cm. In the apparatus the potential leads were attached at 10 cm from the ends, and therefore at the center section of the filament Q_c should be negligible.

Multicellular secondary motion arises in the column when a critical value of the Rayleigh number is exceeded [10–12]. For the present experimental conditions the expression recommended by Thomas and deVahl-Davis [10] gives the critical Rayleigh number as 1×10^{12}. In the experiments the Rayleigh numbers were considerably below this value (see above) and consequently multicellular secondary motion was not expected to occur in the column.

The foregoing results imply that convective effects were negligible in the experiments. The validity of this conclusion was

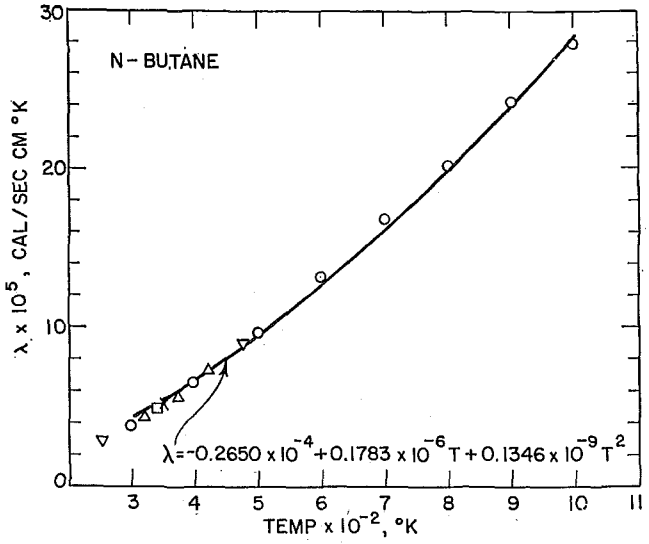

Fig. 4 Thermal conductivity of normal butane; — present result, equation (7a); ▽ Mann and Dickens [16]; × Senftleben and Gladisch [17]; □ Lambert et al. [19]; △ Smith et al. [21]; ○ Misic–Thodos formula [23]

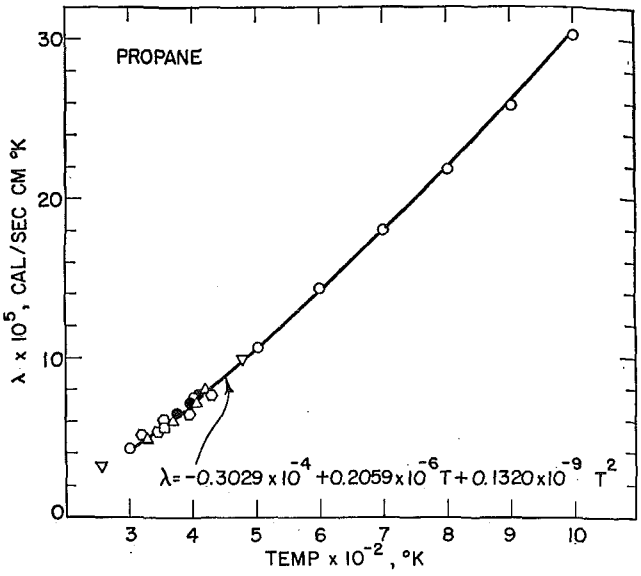

Fig. 5 Thermal conductivity of propane; — present result, equation (7b); ▽ Mann and Dickens [16]; × Senftleben and Gladisch [17]; ● Vines and Bennett [18]; □ Lambert et al. [19]; hexagon, Leng and Comings [20]; △ Smith et al. [21]; ○ Misic–Thodos formula [23]

borne out by measurements of thermal conductivities of argon, helium, krypton, and nitrogen made in two columns of different diameters [2, 3].

Neglecting convection effects, the heat conducted from unit length of the filament can be written as

$$Q_\lambda = Q_f - (Q_r + Q_p) \tag{3}$$

where, on a unit-length basis, Q_f is the power input to the filament, Q_r is the heat loss from the filament due to radiation, and Q_p is the heat loss through the potential leads. In vacuum ($Q_\lambda{}^v \cong 0$) the energy balance for the filament gives

$$Q_f{}^v = Q_r{}^v + Q_p{}^v \tag{4}$$

The experimentally determined values of Q_f and $Q_f{}^v$ were plotted versus filament temperature and a smoothed least-squares-fit curve was drawn through the data points. Q_λ was then evaluated by taking differences of the smoothed values at equal temperature intervals ($Q_\lambda = Q_f - Q_f{}^v$). These plots are shown in Figs. 2 and 3. This procedure is based on the assumption that the radiation and potential-lead losses in vacuum and in gas are the same. This assumption was evaluated experimentally for the present apparatus using argon, helium, krypton, and nitrogen, and the error introduced by this assumption was found to be negligible [2, 3].

The thermal conductivity of the gas at the filament temperature T_f was calculated from the expression

$$\lambda(T_f) = \left(\frac{dQ_\lambda}{dT}\right)_{T_f} \frac{\ln(D/d)}{2\pi}(1 + \lambda') \tag{5}$$

where λ' is a correction due to the temperature drop across the Pyrex outer cylinder

$$\lambda' \cong \frac{\lambda_b}{\lambda_g} \frac{\ln\left(1 + \frac{2w}{D}\right)}{\ln(D/d)} \tag{6}$$

λ_b is the thermal conductivity of the gas at the water-bath temperature, λ_g is the thermal conductivity of the Pyrex, d is the filament diameter, and w is the wall thickness of the Pyrex envelope ($w = 0.158$ cm). In the present experiments λ' was found to be less than 0.0015. $(dQ_\lambda/dT)_{T_f}$ was determined by numerical differentiation based on Stirling's interpolation formula [13] using five points at 10 deg C temperature intervals for each derivative.

Equation (5) is applicable only if temperature-jump effects are negligible, which is the case when the Knudsen number (Kn = mean free path/filament diameter) is less than ~0.003 [14, 15]. In the experiments the Knudsen numbers were well below this value and therefore it was unnecessary to correct for the temperature jump.

Results and Discussion

Thermal conductivities of normal butane and propane were determined at 760 mm Hg in the range 300–1000 deg K. A detailed analysis was made of the experimental errors and the most probable random error was estimated to be about 2 percent. Systematic errors were estimated to cause at most an additional uncertainty of 1 percent. The experimental thermal-conductivity values could be correlated within an average absolute deviation of ~0.3 percent by the following polynomials:

n-butane

$$\lambda = -0.2650 \times 10^{-4} + 0.1783 \times 10^{-6}\, T + 0.1346 \times 10^{-9}\, T^2 \tag{7a}$$

propane

$$\lambda = -0.3029 \times 10^{-4} + 0.2059 \times 10^{-6}\, T + 0.1320 \times 10^{-9}\, T^2 \tag{7b}$$

In Figs. 4 and 5 the results, as given by equations (7a) and (7b), are compared to previous data. The latter extend only up to 500 deg K. There is excellent agreement between the present and previous data, lending confidence to the results.

There have been several expressions proposed in the past for calculating thermal conductivities of hydrocarbons and a comprehensive summary of these expressions is given in reference [22]. Most of the existing correlations express the thermal conductivity in terms of the viscosity, which itself is not known accurately, particularly at higher temperatures. One notable exception is the formula recommended by Misic and Thodos [23] which is

$$\lambda(T) = \frac{C_p \times 10^{-6}[14.52(T/T_c) - 5.14]^{2/3}(P_c)^{2/3}}{M^{1/2}(T_c)^{1/6}} \tag{8}$$

where C_p is the heat capacity (cal/sec-cm-deg K), M the molecular weight, and T_c and P_c the critical temperature (deg K) and pressure (atm), respectively. Thermal-conductivity values

given by equation (8) are compared to the data in Figs. 4 and 5. As can be seen, up to ~1000 deg K the Misic–Thodos formula approximates very closely the measured thermal conductivity.

Above ~800 deg K the pressure increased in the system[2] and around 1000 deg K vapor condensation became visible on the inside of the outer cylinder. These phenomena, caused by pyrolysis of the test gas, may have occurred to a lesser extent at lower temperatures [24]. It is noteworthy, however, that in spite of the pyrolysis the measured thermal conductivity agrees well with the prediction of Misic and Thodos.

Acknowledgment

This work was supported by the National Science Foundation under grant number GK-14006.

References

1 Ziebland, H., "Experimental Determinations of the Thermal Conductivity of Fluids," in: *Thermal Conductivity*, Vol. 2, R. P. Tye, ed., Academic Press, New York, N. Y., 1969, pp. 66–148.

2 Faubert, F. M., and Springer, G. S., "Measurement of the Thermal Conductivity of Argon, Krypton and Nitrogen in the Range 800–2000°K," *J. Chem. Phys.*, in press.

3 Faubert, F. M., "The Thermal Conductivity of Gases at High Temperatures," PhD thesis, University of Michigan, Ann Arbor, Mich., 1971.

4 Thomas, L. B., and Brown, R. E., "The Accommodation Coefficient of Gases on Platinum as a Function of Pressure," *J. Chem. Phys.*, Vol. 18, 1950, pp. 1367–1372.

5 Smithells, C. J., *Tungsten*, 3rd ed., Chapman and Hall, London, England, 1952, p. 177.

6 Blais, N. C., and Mann, J. B., "Thermal Conductivity of Helium and Hydrogen at High Temperatures," *J. Chem. Phys.*, Vol. 32, 1960, pp. 1459–1465.

7 Batchelor, G. K., "Heat Transfer by Free Convection across a Closed Cavity between Vertical Boundaries at Different Temperatures," *Q. Appl. Math.*, Vol. 12, 1954, pp. 209–233.

8 Eckert, E. R. G., and Carlson, W. O., "Natural Convection in an Air Layer Enclosed between Two Vertical Plates with Different Temperatures," *International Journal of Heat and Mass Transfer*, Vol. 2, 1961, pp. 106–120.

9 Lipkea, W. H., and Springer, G. S., "Heat Transfer through Gases Contained between Two Vertical Cylinders at Different Temperatures," *International Journal of Heat and Mass Transfer*, Vol. 11, 1968, pp. 1341–1350.

10 Thomas, R. W., and deVahl-Davis, G., "Natural Convection in Annular and Rectangular Cavities, A Numerical Study," *Fourth International Heat Transfer Conference*, Paris-Versailles, France, 1970, Vol. 4, NC2.4.

11 Elder, J. W., "Numerical Experiments with Free Convection in a Vertical Slot," *Journal of Fluid Mechanics*, Vol. 24, 1966, pp. 823–843.

12 Vest, C. M., "Stability of Natural Convection in a Vertical Slot," *Journal of Fluid Mechanics*, Vol. 36, 1969, pp. 1–15.

13 Scarborough, J. B., *Numerical Mathematical Analysis*, Johns Hopkins Press, Baltimore, Md., 1955.

14 Springer, G. S., "Heat Transfer in Rarefied Gases," in: *Advances in Heat Transfer*, Vol. 7, T. F. Irvine, Jr., and J. P. Hartnett, eds., Academic Press, New York, N. Y., 1971, pp. 163–218.

15 Sheldon, D. B., and Springer, G. S., "Experimental Study of Rarefied Argon Contained between Concentric Cylinders," *Physics of Fluids*, Vol. 11, 1968, pp. 1312–1320.

16 Mann, W. B., and Dickens, B. G., "The Thermal Conductivities of the Saturated Hydrocarbons in the Gaseous State," *Proceedings of the Royal Society*, London, Series A, Vol. 134, 1932, pp. 77–96.

17 Senftleben, H., and Gladisch, H., "Eine Methode zur Bestimmung der spezifischen Warme der inneren Reibung und des Warmeleitvermogens von Gasen," *Z. Physik*, Vol. 125, 1949, pp. 653–658.

18 Vines, R. G., and Bennett, L. A., "The Thermal Conductivity of Organic Vapours: The Relationship between Thermal Conductivity and Viscosity, and the Significance of the Eucken Factor," *J. Chem. Phys.*, Vol. 22, 1954, pp. 360–366.

19 Lambert, J. D., Cotton, K. J., Pailthorpe, M. W., Robinson, A. M., Scrivens, J., Vale, W. R. F., and Young, R. M., "Transport Properties of Gaseous Hydrocarbons," *Proceedings of the Royal Society*, London, Series A, Vol. 231, 1955, pp. 280–290.

20 Leng, D. E., and Comings, E. W., "Thermal Conductivity of Propane," *Ind. Eng. Chem.*, Vol. 49, 1957, pp. 2042–2045.

21 Smith, W. J. S., Durbin, L. D., Kobayashi, R., "Thermal Conductivity of Light Hydrocarbons and Methane–Propane Mixtures at Low Pressures," *J. Chem. Eng. Data*, Vol. 5, 1960, pp. 316–321.

22 "Documentation of the Basis for Selection of the Contents of Chapter 12, Thermal Conductivity, in Technical Data Book, Petroleum Refining," Documentation Report No. 12-66, American Petroleum Institute, 1966

23 Misic, D., and Thodos, G., "The Thermal Conductivity of Hydrocarbon Gases at Normal Pressures," *AIChE Journal*, Vol. 7, 1961, pp. 264–267.

24 Zdonik, S. B., Green, E. J., and Hallee, L. P., *Manufacturing Ethylene*, Petroleum Publishing Co., Tulsa, Okla., 1970, pp. 25–30.

[2] The pressure was maintained at 760 mm Hg by pumping out the gas from the test cell.

N. KONOPLIV
Mem. ASME

E. M. SPARROW
Professor.
Mem. ASME

Department of Mechanical Engineering,
University of Minnesota,
Minneapolis, Minn.

Unsteady Heat Transfer and Temperature for Stokesian Flow about a Sphere

An analysis is made of the unsteady thermal processes which result when a moving sphere encounters a fluid environment whose initial temperature is different from that of the sphere. The fluid velocity field is steady and Stokesian, and the temperature field is of the boundary-layer type. Two related physical situations are analyzed. In one of these, the sphere is a solid of high thermal conductance such that its temperature is spatially uniform, but varies with time as a result of heat transfer with the fluid. In the other, the sphere heat capacity and conductance are both large so that its surface temperature is spatially and temporally uniform for a finite period of time. A number of solution methods is employed, including numerical inversion of integral transforms, series, and asymptotic expansions. Results are presented both in graphical and algebraic form for the local and overall heat-transfer rates, for the temperature history, and and for the time required to reach thermal equilibrium.

Introduction

THIS PAPER is concerned with transient forced-convection heat-transfer problems involving a sphere which translates relative to its fluid surroundings, the velocity field being steady and Stokesian. The thermal transient is initiated when the sphere, possessing a uniform temperature corresponding to its previous history, encounters a fluid environment of a different temperature. One of the cases to be analyzed is that in which the sphere is a solid of high thermal conductance such that its temperature is spatially uniform at any instant of time. The temperature of the sphere changes with time as a result of heat exchange with the fluid environment. The other case which will be studied is characterized by the condition that the sphere surface temperature is spatially uniform and unchanging with time. In practice, such behavior can be approximately realized during a substantial portion of the transient period provided that the sphere has sufficiently high heat capacity and conductance. While this case is of technical interest in its own right, it has a special relevance here in that its solution also serves as a stepping-stone to the solution of the first case described in this paragraph.

In the presentation which follows, the case of constant sphere surface temperature is treated first, and this is followed by the analysis of the case of time-varying sphere temperature. The solutions that are obtained make use of a variety of techniques, including series, asymptotic expansions, and numerical inversion of integral transforms. From the solutions, results are deduced for both heat transfer and temperature distributions during the transient period. The solutions and results pertain to sufficiently high Prandtl numbers such that there exists a thermal boundary layer which is very thin compared with the extent of the velocity field.

The present paper complements other available analytical studies, but there is little in the published literature that bears directly on the work reported here. Mention may be made of the elegant contributions by Chao [1][1] and by Chao and Chen [2] for the transient temperature response of a fluid sphere. The only prior study known to the authors of the thermal transient for a solid sphere in Stokesian flow is that of Bentwich, Szwarcbaum, and Sideman [3], who used a finite-difference technique for the case in which the sphere surface temperature is spatially uniform and unchanging with time. The paper does not present transient heat-transfer results. The steady-state solution for the isothermal sphere in Stokesian flow was found analytically by Acrivos and Taylor [4]. In an earlier paper [5], the present authors examined the transient heat-transfer problem for a sphere when the Peclet number is small compared to unity.

The coordinates and other dimensional nomenclature are pictured in Fig. 1. The spherical coordinates r, ϕ are fixed with respect to the translating sphere. In such a frame, the sphere is stationary and the fluid approaches it with a far-field velocity U. The velocity field about the sphere itself is that of Stokes and is steady. Owing to flow symmetry, the velocity and temperature fields do not depend on the azimuthal angle, and furthermore the only velocity components participating in the convection of heat are u_r and u_ϕ.

Contributed by the Heat Transfer Division for publication (without presentation) in the JOURNAL OF HEAT TRANSFER. Manuscript received by the Heat Transfer Division December 2, 1970. Paper No. 72-HT-C.

[1] Numbers in brackets designate References at end of paper.

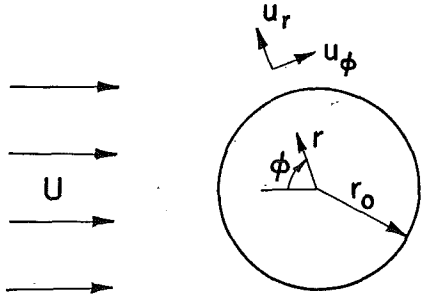

Fig. 1 Coordinates and other dimensional nomenclature

Constant Surface Temperature

Formulation of the Problem. Consider a solid spherical body having an initially uniform temperature T_i which, at time = 0, encounters a fluid whose initial temperature is uniform and equal to T_∞. The fluid free-stream temperature for all subsequent times is also T_∞. The sphere surface temperature for $t > 0$ is assumed to be unchanging and equal to T_i. As discussed in the Introduction, this condition can be approximately fulfilled for some finite period of time (whose extent is examined later) following the initiation of the transient.

The transient thermal processes for the problem just described are governed by the energy equation for the fluid

$$\frac{\partial T_f^*}{\partial t} + u_r \frac{\partial T_f^*}{\partial r} + \frac{u_\phi}{r} \frac{\partial T_f^*}{\partial \phi} = \alpha_f \left[\frac{1}{r^2} \frac{\partial}{\partial r} \left(r^2 \frac{\partial T_f^*}{\partial r} \right) + \frac{1}{r^2 \sin \phi} \frac{\partial}{\partial \phi} \left(\sin \phi \frac{\partial T_f^*}{\partial \phi} \right) \right] \quad (1)$$

where $T_f^*(t, r, \phi)$ denotes the fluid temperature. The asterisk is used to distinguish the case of constant surface temperature from the more general case in which the sphere temperature is time-dependent.

The flow field that is to be considered here is steady and of the Stokes type. As is well known, a Stokesian flow is not a velocity boundary-layer flow. Rather, the influence of the sphere extends far out into the flow, to distances which are on the order of 100 sphere radii. The velocity components u_r and u_ϕ for Stokesian flow about a sphere are

$$\frac{u_r}{U} = -\left(1 - \frac{3}{2}\frac{r_0}{r} + \frac{1}{2}\frac{r_0^3}{r^3}\right) \cos \phi, \qquad \frac{u_\phi}{U} = \left(1 - \frac{3}{4}\frac{r_0}{r} - \frac{1}{4}\frac{r_0^3}{r^3}\right) \sin \phi \quad (2)$$

The analysis of the temperature field is carried out for sufficiently high Prandtl numbers that the temperature field is confined to a boundary layer which is very thin compared with the velocity field. Correspondingly, the ϕ heat-conduction term may be deleted from the right side of the energy equation (1). Furthermore, it is only necessary that the velocity field be accurately represented within the thermal boundary layer, so that equations (2) can be replaced by

$$\frac{u_r}{U} \cong -\frac{3}{2}\left(\frac{r - r_0}{r_0}\right)^2 \cos \phi, \qquad \frac{u_\phi}{U} \cong \frac{3}{2}\left(\frac{r - r_0}{r_0}\right) \sin \phi \quad (3)$$

Comparable simplifications were used by Chao [1] in studying the fluid sphere.

A discussion of the conditions for which the aforementioned thermal boundary-layer model yields accurate results will be given later. For the present, it may be noted that the heat-transfer results are unaffected by the thermal boundary-layer assumptions during a substantial portion of the transient period. Their role becomes more prominent as steady-state conditions are approached, such that the accuracy of the results depends on the Prandtl number being sufficiently large. For near-steady-state conditions, the present results may be regarded as being asymptotic for high Prandtl numbers. Such asymptotic solutions are widely used in steady-state convective heat-transfer problems, for instance, Acrivos and Taylor [4], Acrivos and Goddard [9], Morgan and Warner [10], and many others.

Upon introducing dimensionless variables and parameters

$$\theta^* = \frac{T_f^* - T_\infty}{T_i - T_\infty}, \qquad \zeta = \left(\frac{3}{4}\,\mathrm{Pe}\right)^{1/3} \frac{r - r_0}{r_0}, \qquad \tau = \left(\frac{3}{4}\,\mathrm{Pe}\right)^{2/3} \frac{\alpha_f t}{r_0^2}, \qquad \mathrm{Pe} = \frac{2r_0 U}{\alpha_f} \quad (4)$$

the energy equation (1) becomes

$$\frac{\partial \theta^*}{\partial \tau} - \zeta^2 \cos \phi \frac{\partial \theta^*}{\partial \zeta} + \zeta \sin \phi \frac{\partial \theta^*}{\partial \phi} = \frac{\partial^2 \theta^*}{\partial \zeta^2} \quad (5)$$

The boundary conditions ($T_f^* = T_i$ at the sphere surface and $T_f^* = T_\infty$ in the free stream), along with the initial condition ($T_f^* = T_\infty$ for $r > r_0$), transform into conditions on $\theta^*(\tau, \zeta, \phi)$ as follows:

$$\theta^*(\tau, 0, \phi) = 1, \quad \theta^*(\tau, \infty, \phi) = 0, \quad \theta^*(0, \zeta, \phi) = 0 \quad (6)$$

Since the forward stagnation region is of special interest in heat-transfer research, it is treated first. The solution of equations (5) and (6) for arbitrary ϕ will be obtained later.

Stagnation Region. The application of equation (5) to $\phi = 0$, and letting $\theta^*(\tau, \zeta, 0) = \theta_0^*(\tau, \zeta)$, gives

$$\frac{\partial \theta_0^*}{\partial \tau} - \zeta^2 \frac{\partial \theta_0^*}{\partial \zeta} = \frac{\partial^2 \theta_0^*}{\partial \zeta^2} \quad (7)$$

Nomenclature

a, b, c = numerical-inversion constants, equation (11)
c = specific heat
k = thermal conductivity
Nu* = Nusselt number for constant surface temperature, equation (31)
Pe = Peclet number, $2r_0U/\alpha_f$
Q = time-integrated overall heat transfer, equation (43)
q = local instantaneous heat flux
Res = residue corresponding to S_p
r = radial coordinate
r_0 = radius of sphere
s = Laplace-transform variable
S_p = largest real singularity of equation (38)
T_f = fluid temperature
T_i = initial temperature of sphere
T_s = temperature of sphere
T_∞ = fluid temperature at $t = 0$ or at $r = \infty$
t = time
U = free-stream fluid velocity
u_r = radial velocity component
u_ϕ = tangential velocity component
α = thermal diffusivity
γ = dimensionless parameter $(\rho_s c_s/\rho_f c_f)\mathrm{Pe}^{1/3}$
ζ = dimensionless radial coordinate, equation (4)
$\theta, \theta_s, \theta^*$ = dimensionless temperatures, equations (33) and (4)
ν = dimensionless property grouping $(2\rho_s c_s/3\rho_f c_f)(3\mathrm{Pe}/4)^{2/3}$
ρ = density
τ = dimensionless time, equation (4)
ϕ = cone angle

Subscripts and superscripts

av = average over sphere surface
f = fluid
0 = forward stagnation region
s = sphere
ss = steady state
* corresponds to constant sphere surface temperature
¯ denotes Laplace transform

The boundary and initial conditions are similar to those stated by equations (6).

Two methods are employed to obtain solutions of equation (7) subject to its boundary and initial conditions. One method involves numerical inversion of an integral transform, while the second is based on an asymptotic expansion in the Laplace-transform s plane. To facilitate the application of either method, one begins by taking the Laplace transformation of (6) and (7) with respect to the time variable τ, giving

$$s\bar{\theta}_0^* - \zeta^2 \frac{d\bar{\theta}_0^*}{d\zeta} = \frac{d^2\bar{\theta}_0^*}{d\zeta^2}, \quad \bar{\theta}_0^*(s, 0) = \frac{1}{s}, \quad \bar{\theta}_0^*(s, \infty) = 0 \quad (8)$$

where $\bar{\theta}_0^*$ is the Laplace-transformed temperature.

The implementation of the numerical-inversion method requires that solutions of equations (8) be available for a number of discrete values of s. Such solutions are readily obtained via the Runge–Kutta numerical-integration procedure, with s playing the role of a prescribed parameter. Once $\bar{\theta}_0^*(\zeta)$ and $(d\bar{\theta}_0^*/d\zeta)_{\zeta=0}$ are found, then the numerical-inversion method can be employed to determine the time variation of the temperature at any position ζ, or of the surface heat flux. For the sake of generality, let either of the aforementioned quantities be represented by the prototype variable $\bar{\chi}$, that is,

$$\bar{\chi} = -\left(\frac{d\bar{\theta}_0^*}{d\zeta}\right)_{\zeta=0} - \frac{1}{\sqrt{s}} \quad \text{or} \quad \bar{\chi} = \bar{\theta}_0^*(\zeta) \quad (9)$$

where the subtractive factor $1/\sqrt{s}$ is employed to insure accurate results for small values of τ. Indeed, $\bar{\chi}$ may represent any known function of s (for a fixed ζ).

To recover $\chi(\tau)$ from the known $\bar{\chi}(s)$, one begins with the defining equation for the Laplace transform

$$\bar{\chi}(s) = \int_0^\infty \exp(-s\tau)\chi(\tau)d\tau \quad (10)$$

which is in essence an integral equation for $\chi(\tau)$, the solution of which will be obtained by numerical means. Although there are some papers in the mathematical literature that deal with numerical inversion of Laplace transforms, e.g., [6, 7], little has been done in this area by applied researchers. The approach outlined below has been found to be highly serviceable by the present authors in a number of problems and to yield results of good accuracy ([5], Fig. 2).

To begin, the integration range in equation (10) is reduced to the unit interval and a more convenient variable $\hat{\chi}$ is introduced via the definitions

$$\tau = -(a \ln \Lambda)/b, \quad \chi(\tau) = b\hat{\chi}(b\tau)\exp(c\tau) \quad (11)$$

so that (10) becomes

$$\bar{\chi}(sb + c) = a\int_0^1 \Lambda^{as-1}\hat{\chi}(-a \ln \Lambda)d\Lambda \quad (12)$$

where a, b, and c are prescribable real constants.

The solution of the integral equation (12) for $\hat{\chi}$ is accomplished via the aid of the Gaussian-quadrature integration formula. For a pre-selected number of points N in the interval $0 \leq \Lambda \leq 1$, the integral is approximated by N terms, each term containing a known weight w_i and a known abscissa Λ_i. The approximating procedure introduces N unknowns $\hat{\chi}(-a \ln \Lambda_i)$, $1 \leq i \leq N$. Since one is at liberty to assign N real values of s, say s_j, $1 \leq j \leq N$, the unknowns $\hat{\chi}$ are found by solving the following set of linear algebraic equations:

$$\bar{\chi}(s_j b + c) = a\sum_{i=1}^{N} w_i \Lambda_i^{as_j - 1}\hat{\chi}(-a \ln \Lambda_i), \quad j = 1, 2, \ldots, N \quad (13)$$

Once $\hat{\chi}(-a \ln \Lambda) = \hat{\chi}(b\tau)$ has been found, the $\chi(\tau)$ is calculated by employing equations (11).

It remains to specify the number of points N, the values of s_j, and the constants a, b, and c. The experience of the authors, accumulated from a number of different problems, suggests that $N = 10$ and $s_j = j$ ($j = 0, 1, \ldots, 9$) lead to results of good accuracy. The constant a was taken as one, while b was chosen to provide the desired range for τ in accordance with the first of equations (11) (note that the Λ values in the range $0 \leq \Lambda \leq 1$ are fixed by the rules of the Gaussian quadrature). The remaining constant c was selected by trial and error, in such a way that agreement is attained between results corresponding to different values of b.

Results obtained by application of the numerical-inversion method are presented later.

It may be relevant at this point to summarize some of the strengths of the numerical-inversion method. In general, relatively little preparatory analysis is needed prior to the numerical computations. Furthermore, the computations themselves are performed with a very small expenditure of computer time. Other candidate solution methods, such as that of [2], presumably also possess specific strengths. For instance, the method of [2] naturally leads to the small-time solution by manipulation of the general solution. On the other hand, that method requires substantial analytical work prior to the computational stage of the problem.

The series solution at the stagnation point is alternative to that provided by numerical inversion, but is more restricted in the range of the independent variables. The solution begins with equations (8), which are recast in a form suitable to the series expansion by employing the transformation

$$\bar{H}(s, \hat{\zeta}) = s\bar{\theta}_0^*(s, \zeta), \quad \hat{\zeta} = \sqrt{s}\zeta \quad (14)$$

which gives

$$\frac{d^2\bar{H}}{d\hat{\zeta}^2} = \bar{H} - \left(\frac{1}{s^{3/2}}\right)\hat{\zeta}^2\frac{d\bar{H}}{d\hat{\zeta}}, \quad \bar{H}(s, 0) = 1, \quad \bar{H}(s, \infty) = 0 \quad (15)$$

The series solution of equation (15) is expressed in powers of $1/s^{3/2}$ (that is, the expansion is for large s). Differential equations for the unknown functions of $\hat{\zeta}$ that appear in the series are deduced by equating terms having like powers of s and are subsequently solved in closed form. Then, the thus-determined series for $\bar{H}(s, \hat{\zeta})$ is inverse-transformed, yielding the following representations for the transient temperature and for the temperature gradient at the stagnation point (i.e., the surface heat transfer):

$$\theta_0^*(\tau, \zeta) = \operatorname{erfc}\left(\frac{\zeta}{2\sqrt{\tau}}\right) + \frac{\zeta}{2\sqrt{\pi}}\sum_{n=1}^{\infty}\sum_{k=1}^{3n}\frac{a_{k,n}\zeta^k}{\Gamma\left(\frac{3n+2-k}{2}\right)} \times \int_0^\tau (\tau - \Lambda)^{\frac{3n-k}{2}}\exp\left(-\frac{\zeta^2}{4\Lambda}\right)\frac{d\Lambda}{\Lambda^{3/2}} \quad (16)$$

$$\left(\frac{\partial\theta_0^*}{\partial\zeta}\right)_{\zeta=0} = -\frac{1}{\sqrt{\pi\tau}} + \sum_{n=1}^{\infty} a_{1,n}\tau^{\frac{3n-1}{2}}\Big/\Gamma\left(\frac{3n+1}{2}\right) \quad (17)$$

It remains to specify the constants $a_{k,n}$ that appear in the foregoing. For $n = 1$, the relevant constants are $a_{1,1} = -1/4$, $a_{2,1} = -1/4$, and $a_{3,1} = -1/6$. The $a_{k,n}$ for $n \geq 2$ are calculated from a recurrence relationship

$$a_{k,n} = -\frac{1}{2k}[-a_{(k-3),(n-1)} + (k - n - 1)a_{(k-2),(n-1)} - k(k+1)a_{(k+1),n}] \quad (18)$$

where $a_{k,n} = 0$ when either k or $n \leq 0$ or when $k > 3n$. It should be noted that the series (16) and (17) are of asymptotic type, and, as will be shown in the presentation of results, are most accurate when τ and ζ are not too large.

Solution for Arbitrary ϕ. From Laplace transformation of equations (5) and (6), and with a subsequent change of variable defined by

$$\bar{\theta}^*(s, \zeta, \phi) = \bar{G}(s, \zeta, \phi) \exp(-\tfrac{1}{6}\zeta^3 \cos\phi)/s \qquad (19)$$

one obtains

$$\frac{\partial^2 \bar{G}}{\partial \zeta^2} - [s + g(\zeta, \phi)]\bar{G} - \zeta \sin\phi \frac{\partial \bar{G}}{\partial \phi},$$

$$\bar{G}(s, 0, \phi) = 1, \quad \bar{G}(s, \infty, \phi) = 0 \qquad (20)$$

where

$$g(\zeta, \phi) = \zeta \cos\phi + \tfrac{1}{6}\zeta^4 + \tfrac{1}{12}\zeta^4 \cos^2\phi \qquad (21)$$

The differential equation (20) resembles, in form, one that was investigated by Liouville and discussed by Erdelyi [8]. Correspondingly, a series solution for $\bar{G}$ is constructed as

$$\bar{G}(s, \zeta, \phi) = \exp(-s^{1/2}\zeta) \sum_{i=0}^{\infty} y_i(\zeta, \phi) s^{-i/2} \qquad (22)$$

This is an asymptotic expansion for large s (large s corresponds to small τ). Equation (22), taken together with the boundary conditions in (20), requires that

$$y_0(0, \phi) = 1, \qquad y_i(0, \phi) = 0 \quad \text{for} \quad i \geq 1 \qquad (23)$$

The substitution of (22) into the differential equation (20) and subsequent grouping of terms according to powers of s yields for y_0

$$y_0(\zeta, \phi) = 1 \qquad (24)$$

which satisfies the boundary condition (23). The other y_i, $i \geq 1$, are governed by the differential equation

$$\frac{\partial y_i}{\partial \zeta} = \frac{1}{2}\frac{\partial^2 y_{i-1}}{\partial \zeta^2} - \frac{1}{2} g(\zeta, \phi) y_{i-1} - \frac{\zeta}{2} \sin\phi \frac{\partial y_{i-1}}{\partial \phi} \qquad (25)$$

subject to the boundary conditions (23). Since the surface heat transfer is of greater practical importance than the fluid temperature, attention is given here to evaluation of $(\partial y_i/\partial\zeta)_{\zeta=0}$, expressions for which are as follows:

$$(\partial y_2/\partial\zeta)_{\zeta=0} = -\tfrac{1}{4}\cos\phi, \qquad (\partial y_5/\partial\zeta)_{\zeta=0} = -\tfrac{9}{32} + \tfrac{1}{4}\cos^2\phi,$$

$$(\partial y_8/\partial\zeta)_{\zeta=0} = \tfrac{95}{64}\cos\phi - \tfrac{25}{32}\cos^3\phi,$$

$$(\partial y_{11}/\partial\zeta)_{\zeta=0} = \tfrac{14121}{2048} - \tfrac{2803}{256}\cos^2\phi + \tfrac{1083}{256}\cos^4\phi \qquad (26)$$

Evidently, non-vanishing $(\partial y_i/\partial\zeta)_{\zeta=0}$ are those which correspond to values of i given by $i = 2 + 3j$, $j = 0, 1, 2, \ldots$. For the subsequent determination of the surface heat transfer, the quantity $(\partial\theta^*/\partial\zeta)_{\zeta=0}$ is required. Equations (19) and (22), taken together with (26), yield $(\partial\bar{\theta}^*/\partial\zeta)_{\zeta=0}$, and upon inverse transformation one obtains

$$\left(\frac{\partial\theta^*}{\partial\zeta}\right)_{\zeta=0} = -\frac{1}{\sqrt{\pi\tau}} + \left(\frac{\partial y_2}{\partial\zeta}\right)_{\zeta=0}\tau + \frac{8}{3\sqrt{\pi}}\left(\frac{\partial y_5}{\partial\zeta}\right)_{\zeta=0}\tau^{5/2}$$

$$+ \frac{1}{4!}\left(\frac{\partial y_8}{\partial\zeta}\right)_{\zeta=0}\tau^4 + \frac{64}{10395\sqrt{\pi}}\left(\frac{\partial y_{11}}{\partial\zeta}\right)_{\zeta=0}\tau^{11/2} + \ldots \qquad (27)$$

Results and Discussion. The instantaneous heat flux q at any surface location may be deduced by applying Fourier's law $q = -k_f(\partial T/\partial r)_{r_0}$ which, when expressed in terms of the variables of the analysis, takes the form

$$\frac{2r_0 q^*}{(T_i - T_\infty)k_f}\left(\frac{3}{4}\,\mathrm{Pe}\right)^{-1/3} = -2(\partial\theta^*/\partial\zeta)_{\zeta=0} \qquad (28)$$

where, as before, the asterisk distinguishes the case of constant surface temperature.

For the stagnation region, the numerical-inversion solution provides values of $-(\partial\theta_0^*/\partial\zeta)_{\zeta=0} - 1/\sqrt{\pi\tau}$ as a function of τ, and, with these, the instantaneous heat flux follows directly from equation (28). An alternative set of results for the stagnation-point heat flux is obtained by introducing the series representation (17) into the right-hand side of equation (28), with six terms being retained for the computations.

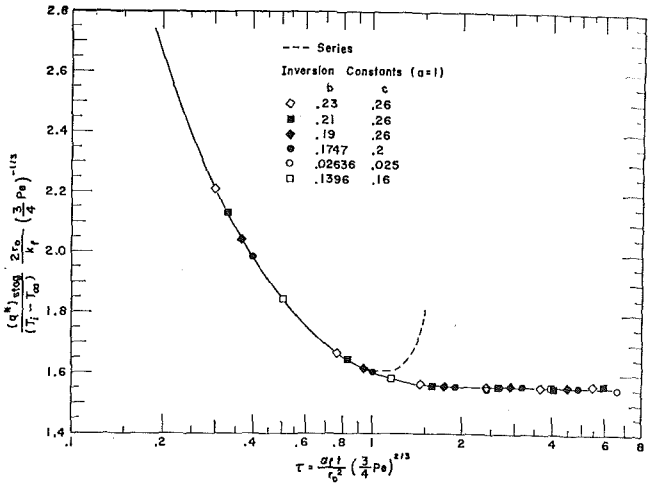

Fig. 2 Stagnation-point heat transfer vs. time (case of constant surface temperature)

The timewise variation of the stagnation-point heat transfer is shown in Fig. 2 as a solid line. The heat-transfer rates are very large at small times and decrease monotonically as time increases, eventually approaching the steady-state value of 1.553. At $\tau \approx 1$, the instantaneous heat flux is 3 percent larger than that for the steady state. The series and numerical-inversion solutions are virtually congruent for τ values up to 0.9, whereupon the former begins to diverge. Numerical values of the constants a, b, and c for the numerical-inversion solution are also listed in the figure.

An expression for the instantaneous heat flux q^* at any surface location ϕ is obtained by combining equations (27) and (28), and numerical results can be evaluated by introducing the values of ϕ and τ that are of interest. The equation for q^* is employed here to deduce an expression for the surface-averaged heat flux $(q^*)_{av}$ defined by

$$(q^*)_{av} = (1/4\pi r_0^2)\int_0^{\pi} q^* 2\pi r_0^2 \sin\phi d\phi \qquad (29)$$

with the result that

$$\left(\frac{3}{4}\,\mathrm{Pe}\right)^{-1/3}\mathrm{Nu}^* = \frac{2}{\sqrt{\pi\tau}} + \frac{19}{48}\frac{\tau}{\Gamma(7/2)} - \frac{125687}{15380}\frac{\tau^{11/2}}{\Gamma(13/2)} + \ldots \qquad (30)$$

where

$$\mathrm{Nu}^* = (q^*)_{av} 2r_0/[(T_i - T_\infty)k_f] \qquad (31)$$

It can be verified that the first term on the right side of (30) is due to conduction, while the other terms are associated with convection. Clearly, conduction is the dominant mode at small times.

The time dependence of $\mathrm{Nu}^*/\mathrm{Pe}^{1/3}$, evaluated from equation (30), is depicted in Fig. 3. The three solid lines appearing in the figure correspond, respectively, to one-, two-, or three-term representations. In addition, there is a dashed line, expressed by

$$\mathrm{Nu}^*/\mathrm{Pe}^{1/3} = 1.54\exp(-2.6\tau) + 0.991 \qquad (32)$$

which serves as a reasonable bridge between the results of equation (30) and the fully developed value of 0.991 [4]. The recommended range of applicability of equation (30) extends from $\tau = 0$ to $\tau = 0.8$, whereafter equation (32) is to be used.

The trend of the surface-averaged heat transfer, as expressed

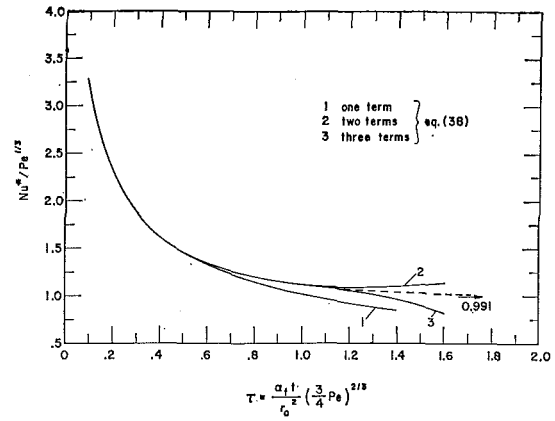

Fig. 3 Nusselt number vs. time (case of constant surface temperature)

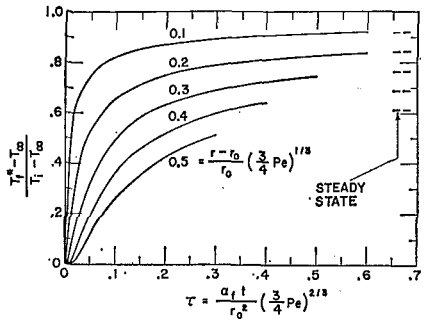

Fig. 4 Time history of fluid temperature in stagnation region (case of constant surface temperature)

by Nu*, is the same as that for the stagnation-point heat transfer (Fig. 2). However, somewhat longer times are required for the former to approach its steady-state value. Thus, for instance, a 3 percent approach to steady state is achieved at $\tau = 1.5$ for the surface-averaged heat flux and at $\tau = 1$ for the stagnation-point heat flux. This behavior is altogether physically reasonable, since the thinnest and more responsive thermal boundary layer is at the forward stagnation point.

It is also interesting to note that in the conduction regime ($\tau \leq 0.5$), Nu* does not depend explicitly on the Peclet number (i.e., $\mathrm{Nu}^* = 2/\sqrt{\pi\alpha_f t/r_0^2}$). On the other hand, for steady-state conditions, $\mathrm{Nu}^* \sim \mathrm{Pe}^{1/3}$.

At this point, it is appropriate to discuss the relationship of the results to the simplifications that were introduced in connection with the thermal boundary-layer model. During the conduction regime ($0 \leq \tau \leq 0.5$), the Nusselt-number results are unaffected by the thermal boundary-layer assumptions. Since the thickness of the thermal boundary layer increases with time, the boundary-layer assumptions come into play most prominently for the steady-state results. For the steady state, Acrivos and Goddard [9] have derived a Nusselt-number result by using a velocity-field representation which is a closer approximation to the Stokes velocities, equation (2), than is equation (3). In the present notation, Acrivos and Goddard's steady-state result is $\mathrm{Nu}_{ss}^*/\mathrm{Pe}^{1/3} = 0.991 + 0.922/\mathrm{Pe}^{1/3} +$ higher-order terms. On the other hand, for the velocity field of equation (3), the steady-state result is $\mathrm{Nu}_{ss}^*/\mathrm{Pe}^{1/3} = 0.991$. The fractional deviation between these results is equal to $0.93/\mathrm{Pe}^{1/3}$, which can be taken to be the relative error associated with the use of equation (3) for the velocity field. Therefore, for sufficiently high Peclet numbers, the error is tolerably small. During the transient period, the Peclet-number limitation is less stringent than for the steady state, and in particular there is no Peclet-number limitation for $\tau < 0.5$.

Representative results for the transient temperature history in the fluid are presented in Fig. 4. This figure pertains to the stagnation region ($\phi = 0$), and the curves were evaluated from equation (16) for parametric values of the dimensionless radial coordinate. It is seen from the figure that the most rapid transient response is at locations nearest the surface. Seven terms (i.e., $n = 1, 2, \ldots, 7$) were employed in the evaluation of equation (16), the curves being terminated when satisfactory convergence was no longer achieved.

Time-Dependent Sphere Temperature

Attention is now turned to the situation wherein the sphere has a sufficiently high thermal conductance that its temperature is spatially uniform at any instant of time. Timewise variations of the sphere temperature are controlled by the balance between the surface heat transfer and the change of the internal energy of the solid. Initially, at time $t = 0$, the solid and fluid are at different uniform temperatures, T_i and T_∞, respectively.

In the analysis, the sphere temperature is denoted by $T_s(t)$, while $T_f(t, r, \phi)$ represents the temperature field in the fluid. The dimensionless counterparts of these temperature variables are

$$\theta_s = (T_s - T_\infty)/(T_i - T_\infty), \qquad \theta = (T_f - T_\infty)/(T_i - T_\infty) \quad (33)$$

Continuity of temperature at the surface of the sphere requires that $\theta_s(t) = \theta(t, r_0, \phi)$ for $t > 0$ and for all ϕ.

The first step in the analysis is to obtain the solution of the energy equation for the fluid. This is most expeditiously accomplished via Duhamel's theorem, which makes use of the already determined function $\theta^*(\tau, \zeta, \phi)$, representing the fluid-temperature solution for the case of constant sphere temperature. Upon integrating the standard form of Duhamel's theorem by parts and using the conditions $\theta^*(0, \zeta, \phi) = 0$ and $\theta_s(0) = 1$, one obtains

$$\theta(\tau, \zeta, \phi) = \theta^*(\tau, \zeta, \phi) + \int_0^\tau \theta^*(\tau - \lambda, \zeta, \phi)\frac{d\theta_s}{d\lambda}\,d\lambda \quad (34)$$

Equation (34) constitutes one link between the fluid- and sphere-temperature variables θ and θ_s.

A second link is provided by the balance between the surface heat transfer and the change of internal energy of the solid, that is

$$\rho_s c_s\left(\frac{4}{3}\pi r_0^3\right)\frac{dT_s}{dt} = \int_0^\pi k_f\left(\frac{\partial T_f}{\partial r}\right)_{r_0} 2\pi r_0^2 \sin\phi\, d\phi \quad (35)$$

the dimensionless form of which is

$$\frac{2}{3}\frac{\rho_s c_s}{\rho_f c_f}\left(\frac{3}{4}\mathrm{Pe}\right)^{1/3}\frac{d\theta_s}{d\tau} = \int_0^\pi \left(\frac{\partial\theta}{\partial\zeta}\right)_{\zeta=0}\sin\phi\, d\phi \quad (36)$$

The elimination of θ between equations (34) and (36) leads to

$$\nu\frac{d\theta_s}{d\tau} = -\mathrm{Nu}^*(\tau) - \int_0^\tau \mathrm{Nu}^*(\tau - \lambda)\frac{d\theta_s}{d\lambda}\,d\lambda \quad (37)$$

where ν is a property grouping defined in the Nomenclature. $\mathrm{Nu}^*(\tau)$, the surface-averaged Nusselt number for the case of constant sphere surface temperature, is expressed by equation (31). The solution of equation (37), which will yield $\theta_s(\tau)$, is to be performed here by employing a method based on integral transforms.

The basic equation for the solution method is deduced by taking the Laplace transform of equation (37) with respect to τ, which gives

$$\bar{\theta}_s(s) = \frac{1}{s[1 + \overline{\mathrm{Nu}}^*(s)/\nu]} \quad (38)$$

where $\bar{\theta}_s(s)$ and $\overline{\mathrm{Nu}}^*(s)$ are transformed counterparts of $\theta_s(\tau)$ and $\mathrm{Nu}^*(\tau)$. The Nusselt number $\mathrm{Nu}^*(\tau)$ is known from the analysis that was described earlier in the paper, and its Laplace transform $\overline{\mathrm{Nu}}^*(s)$ can also be found. With $\overline{\mathrm{Nu}}^*(s)$ as input, $\bar{\theta}_s(s)$ is determined from equation (38). It then remains to carry out the inverse transformation, thereby solving for $\theta_s(\tau)$.

Four solutions for $\theta_s(\tau)$ will be described here. The first, based on numerical inversion of equation (38), is a general solution valid for all times τ. The other three solutions are: (*a*) small-time, (*b*) large-time, and (*c*) quasi-steady. Depending on the values of the governing parameters, each of the three aforementioned approximate solutions may have a substantial time span of high accuracy, especially the large-time solution.

General Solution via Numerical Inversion. The $\overline{\mathrm{Nu}}^*(s)$ needed as input to equation (38) is deduced by direct application of the definition of the Laplace transform to $\mathrm{Nu}^*(\tau)$ as expressed by equation (30) for $\tau < 0.8$ and by equation (32) for $\tau \geq 0.8$

$$\left(\frac{3}{4}\,\mathrm{Pe}\right)^{-1/3}\overline{\mathrm{Nu}}^*(s) = \frac{2}{\sqrt{s}}\,\mathrm{erf}\,(\sqrt{\tau_1 s}) + \frac{19}{48\Gamma(7/2)} \times \int_0^{\tau_1} \tau^{5/2}\exp(-s\tau)d\tau - \frac{125687}{15380\Gamma(13/2)}\int_0^{\tau_1}\tau^{11/2}\exp(-s\tau)d\tau + 1.69\exp[-(2.6+s)\tau_1]/(2.6+s) + 0.991(4/3)^{1/3}\exp(-s\tau_1)/s \quad (39)$$

where $\tau_1 = 0.8$. The integrals appearing in the foregoing are easily carried out in closed form. In view of equations (39) and (38), $\bar{\theta}_s$ is a known algebraic function of s.

Now let $\bar{\theta}_s(s)$ be associated with the function $\bar{\chi}(s)$ of equation (10). Then the numerical inversion described in the paragraphs subsequent to equation (10) applies without modification, yielding $\theta_s(\tau)$. Results obtained in this way will be presented later.

Small-Time Solution. As was noted earlier, heat conduction provides the dominant contribution to $\mathrm{Nu}^*(\tau)$ at sufficiently small values of time. Therefore, to generate a small-time solution for $\theta_s(\tau)$, only the first term of the series (30) for $\mathrm{Nu}^*(\tau)$ is used in the determination of $\overline{\mathrm{Nu}}^*(s)$. Upon employing this $\overline{\mathrm{Nu}}^*(s)$ as input to equation (38) and carrying out the inverse transformation for large s (small τ), one finds

$$\theta_s(\tau) \cong 1 - \frac{6}{(3/4)^{1/3}\sqrt{\pi}}\frac{\tau^{1/2}}{\gamma}, \qquad \gamma = \frac{\rho_s c_s}{\rho_f c_f}\,\mathrm{Pe}^{1/3} \quad (40)$$

The range of applicability of this solution will be explored when the results are presented.

Large-Time Solution. From the asymptotic theory of Laplace-transformed functions as applied to equation (38), it follows that

$$\theta_s(\tau) \cong (\mathrm{Res})\exp(S_p\tau) \quad (41)$$

The quantity S_p is a real negative number determined by studying the singularities of the function appearing on the right side of equation (38). Specifically, S_p is the largest real part among the singularities of the function. Res is the residue corresponding to S_p.

In the determination of the numerical values of S_p and Res, two models were used for the function $\overline{\mathrm{Nu}}^*(s)$ that appears in equation (38). For the first model, $\overline{\mathrm{Nu}}^*(s)$ is expressed by equation (39), which corresponds to $\mathrm{Nu}^*(\tau)$ from equations (30) and (32). For the second model, $\overline{\mathrm{Nu}}^*(s)$ is based on equation (30) for the range $0 \leq \tau < 1.32$ and on $\mathrm{Nu}^*(\tau) = 0.991\,\mathrm{Pe}^{1/3}$ for $\tau \geq 1.32$. Referring to Fig. 3, the second model is seen to consist of curve 3 up to $\tau = 1.32$ and of a horizontal line thereafter. The motivation for using two different models is to demonstrate that the accuracy of the $\theta_s(\tau)$ from equation (41) is not prejudiced by the tail that is fitted to the series solution (30).

A comparison of the values of S_p and Res showed only small differences between models 1 and 2. An even more decisive comparison of θ_s results is made in the forthcoming presentation of results.

Quasi-steady Solution. If the transient were to consist of a sequence of instantaneous steady states, then $\mathrm{Nu}^*(\tau) = \mathrm{Nu}_{ss}^*$ and $\overline{\mathrm{Nu}}^*(s) = \mathrm{Nu}_{ss}^*/s$. With this, and with the subsequent inversion of equation (38), there is obtained

$$\theta_s(\tau) \cong \exp(-1.8\tau/\gamma) \quad (42)$$

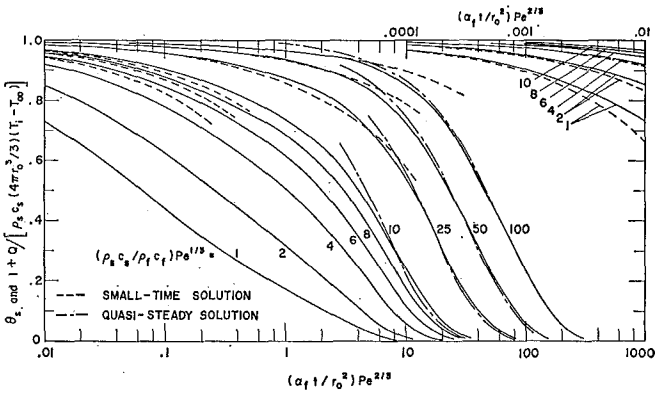

Fig. 5(*a*) Time history of sphere temperature and of time-integrated overall heat transfer

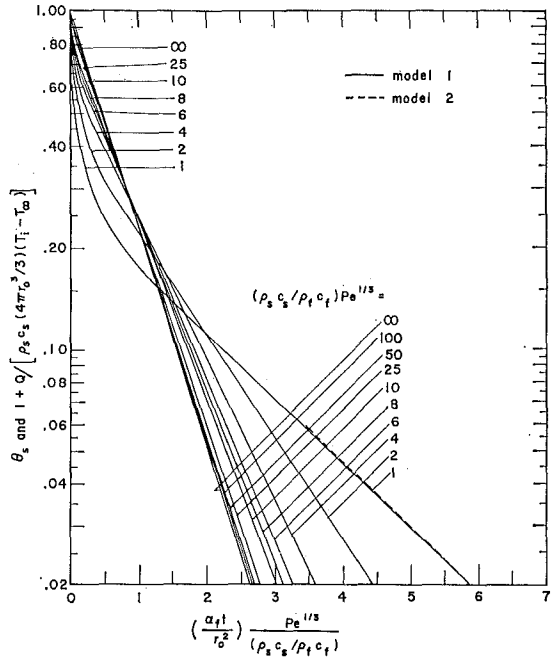

Fig. 5(*b*) Time history of sphere temperature and of time-integrated overall heat transfer

Results and Discussion. Among the results, perhaps of greatest interest is the time variation of the sphere temperature $\theta_s = (T_s - T_\infty)/(T_i - T_\infty)$ and the time-integrated overall heat transfer Q defined as

$$Q = \int_0^t \left[\int_A q\,dA\right]dt \quad (43)$$

These quantities are connected by the relation

$$1 + Q/[\rho_s c_s(4\pi r_0^3/3)(T_i - T_\infty)] = \theta_s \quad (44)$$

Numerical results for the time variations of θ_s and Q are presented in Figs. 5(*a*) and 5(*b*).

In Fig. 5(*a*), the aforementioned quantities are plotted as a function of $(\alpha_f t/r_0^2)\mathrm{Pe}^{2/3}$ with $(\rho_s c_s/\rho_f c_f)\mathrm{Pe}^{1/3}$ as curve parameter. The inset at the upper right provides results for small values of the abscissa variable. The solid lines appearing in the figure correspond to the general solution obtained by numerical inversion, while the dashed and dot–dashed lines respectively represent the small-time and quasi-steady solutions. Fig. 5(*a*) verifies the expected physical trend that θ_s decreases monotonically with time, approaching the equilibrium condition $\theta_s = 0$, that is, $T_s = T_\infty$.

Further inspection shows that the rate at which θ_s decays increases markedly as $\rho_s c_s/\rho_f c_f$ increases (at fixed Pe), that is, when the heat capacity of the sphere increases relative to that of the fluid. For sufficiently large values of $(\rho_s c_s/\rho_f c_f)\mathrm{Pe}^{1/3}$, there is a long period during which θ_s is nearly one. Furthermore, for any $(\rho_s c_s/\rho_f c_f)\mathrm{Pe}^{1/3}$, one can use Fig. 5(*a*) to find the range of $(\alpha_f t/r_0^2)\mathrm{Pe}^{2/3}$ for which the condition $\theta_s \cong 1$ is satisfied. Therefore, the range of applicability of the analysis for constant sphere surface temperature can be ascertained.

Fig. 5(*a*) also provides insights into the ranges of applicability of the small-time and quasi-steady solutions. The former is reasonably accurate within the range $0.9 \leq \theta_s \leq 1$. On the other hand, the quasi-steady solution is most accurate for large values of $(\rho_s c_s/\rho_f c_f)\mathrm{Pe}^{1/3}$, and then only at large $(\alpha_f t/r_0^2)\mathrm{Pe}^{2/3}$.

It remains to explore the behavior of the results at large times, and Fig. 5(*b*) has been prepared for this purpose. The coordinates of Fig. 5(*b*) were selected so that, for a given value of $(\rho_s c_s/\rho_f c_f)\mathrm{Pe}^{1/3}$, the large-time solution would be a straight line when plotted thereon, as per equation (41). The solid curves of Fig. 5(*b*) correspond to the numerical-inversion solution. These curves show straight-line portions of considerable length which coincide with the large-time solution, equation (41). In particular, for the larger values of $(\rho_s c_s/\rho_f c_f)\mathrm{Pe}^{1/3}$, almost the entirety of the curves are straight lines, and furthermore these lines are packed so closely together as to be hardly distinguishable from one another. Thus, for systems characterized by large values of the aforementioned parameter (say, ≥ 50, e.g., a metal sphere in oil), one may regard the results for sphere temperature and heat transfer as independent of the curve parameter. For this range, the results are represented by the quasi-steady solution, equation (42).

Within the scale of Fig. 5(*b*), the results computed using models 1 and 2 for $\overline{\mathrm{Nu}}^*(s)$ are indistinguishable for all values of $(\rho_s c_s/\rho_f c_f)\mathrm{Pe}^{1/3}$ except unity, where a dashed line has been used for model 2.

Another result of interest is the duration of the transient, which may be defined as the time required for θ_s to reach some small preassigned value, typically 0.05 or smaller. Since the large-time solution holds for this range, the steady-state times t_{ss} may be deduced from equation (41), so that

$$\frac{\alpha_f t_{ss}}{r_0^2} = \frac{\ln(\theta_s/\mathrm{Res})}{S_p(3/4)^{2/3}}\,\mathrm{Pe}^{-2/3} \tag{45}$$

Steady-state times, evaluated from equation (45) in conjunction with the values of S_p and Res from model 1, are shown in Fig. 6 for $\theta_s = 0.05$, 0.03, and 0.01. One can readily verify that for a fixed Pe, the Fourier number $\alpha_f t_{ss}/r_0^2$ increases with increasing $\rho_s c_s/\rho_f c_f$. The curves become essentially horizontal for abscissa values greater than 100.

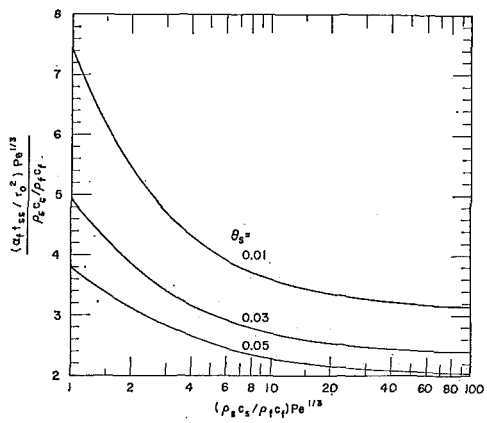

Fig. 6 Dimensionless steady-state times

Acknowledgment

Fellowship support accorded to N. Konopliv by the Whirlpool Corp. is gratefully acknowledged.

References

1 Chao, B. T., "Transient Heat and Mass Transfer to a Translating Droplet," JOURNAL OF HEAT TRANSFER, TRANS. ASME, Series C, Vol. 91, No. 2, May 1969, pp. 273–281.

2 Chao, B. T., and Chen, J., "Series Solution of Unsteady Heat and Mass Transfer to a Translating Fluid Sphere," *International Journal of Heat and Mass Transfer*, Vol. 13, 1970, pp. 359–367.

3 Bentwich, M., Szwarcbaum, G., and Sideman, S., "Time Dependent Temperature Distribution in Flow Past a Sphere," ASME Paper 65-HT-38.

4 Acrivos, A., and Taylor, T. D., "Heat and Mass Transfer from Single Spheres in Stokes Flow," *Physics of Fluids*, Vol. 5, 1962, pp. 387–394.

5 Konopliv, N., and Sparrow, E. M., "Temperature and Heat Transfer History of a Solid Body in a Forced Convection Flow," *Quarterly of Applied Mathematics*, Vol. 29, 1971, pp. 225–235.

6 Spinelli, R. A., "Numerical Inversion of a Laplace Transform," *SIAM Journal on Numerical Analysis*, Vol. 4, 1966, pp. 636–649.

7 Miller, M. K., and Guy, W. T., Jr., "Numerical Inversion of the Laplace Transform by Use of Jakobi Polynomials," *SIAM Journal on Numerical Analysis*, Vol. 4, 1966, pp. 624–635.

8 Erdelyi, A., *Asymptotic Expansions*, Dover Publications, New York, N. Y., 1956.

9 Acrivos, A., and Goddard, J. D., "Asymptotic Expansions for Laminar Forced-Convection Heat and Mass Transfer. Part 1. Low Speed Flows," *Journal of Fluid Mechanics*, Vol. 23, 1965, pp. 273–291.

10 Morgan, G. W., and Warner, W. H., "On Heat Transfer in Laminar Boundary Layers at High Prandtl Number," *Journal of the Aeronautical Sciences*, Vol. 23, 1956, pp. 937–948.

R. P. FORSLUND
Associate Professor,
Department of Mechanical Engineering,
Pontifícia Universidade Católica,
Rio de Janeiro, Brazil.
Assoc. Mem. ASME

An Experimental Technique for Determining the Diffusion Effect of Braze Material on the Thermal Conductance of Thin Copper Fins

The purpose of this communication is to report on a successful technique for the measurement of thermal conductance in thin radiating fins. This work was required in the development of a lightweight radiator-condenser for the mercury Rankine cycle of the SNAP II program at Atomics International.

The thermal conductance of thin radiating fins can be determined employing thermal radiation itself as the calorimeter. When the emissivity of the surface is well known and thermocouples are properly installed, very accurate results can be obtained. Thermal equilibrium is attained rapidly since no guard heaters are required. The cost for specimen preparation can be significantly lower than that for the standard type of conductivity test when the fin material or construction is of a special nature.

Problem

A cross-sectional view of a concept for the lightweight radiator-condenser is shown in Fig. 1. It consists of a conical array of stainless steel condenser tubes sandwiched between two thin face sheets of stainless steel with stainless steel honeycomb filling the space between the tubes. Very thin tapered copper fins are brazed to the outside face sheet to provide a high-conductivity path for transferring the condenser heat to the surface of the radiator where it is rejected to space. During the brazing operation the braze alloy diffuses into the copper fin and degrades the thermal conductance of the fin. Two questions existed: (1) Was the diffusion homogeneous throughout the thickness of the fin or was it confined to a thin layer and (2) if it were homogeneous, what would be the percentage reduction in thermal conductivity of the copper, or if it were confined to a thin layer, what would be the defect in conductance in terms of an equivalent thickness of a layer of copper?

In the first case the degradation of conductivity would be isotropic and uniform. In the second case the average conductivity would be anisotropic, the average lateral conductivity for heat flow along the fin being different than an averaged conductivity for flow of heat normal to the fin. This study, however, is only concerned with lateral conductance since it is the important term in the design of thin fins.

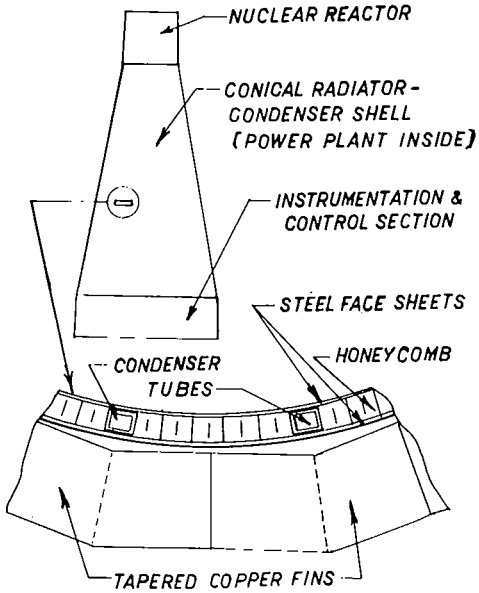

Fig. 1 Perspective view of cut-out from the SNAP II radiator-condenser

Modeling

In the design procedure for the radiator portion of the radiator-condenser, a two-dimensional conduction-radiation equation is solved with the appropriate boundary conditions for a given fin geometry to ascertain whether the entire radiator will perform as desired. The following one-dimensional equation is basically of the same form as the two-dimensional equation;

Contributed by the Heat Transfer Division for publication (without presentation) in the Journal of Heat Transfer. Manuscript received by the Heat Transfer Division June 7, 1971. Paper No. 72-HT-F.

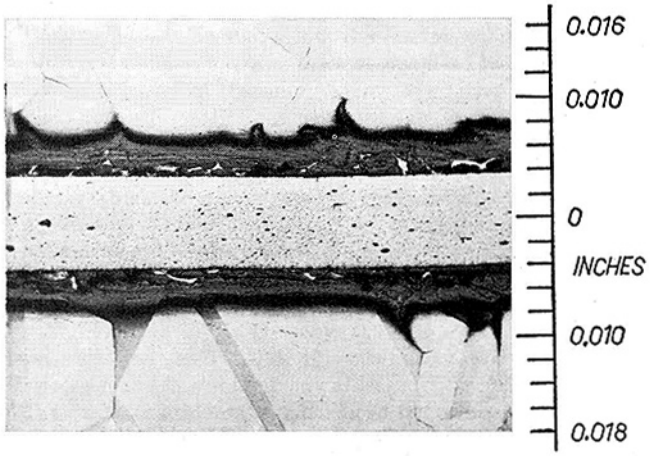

Fig. 2(a) Microphotograph of back-to-back fin specimen prepared with 0.002 in. of Cu–Mn braze; central portion of photo is 0.008 in. of Ph15–7Mo stainless steel; outer portions of photo are pure copper

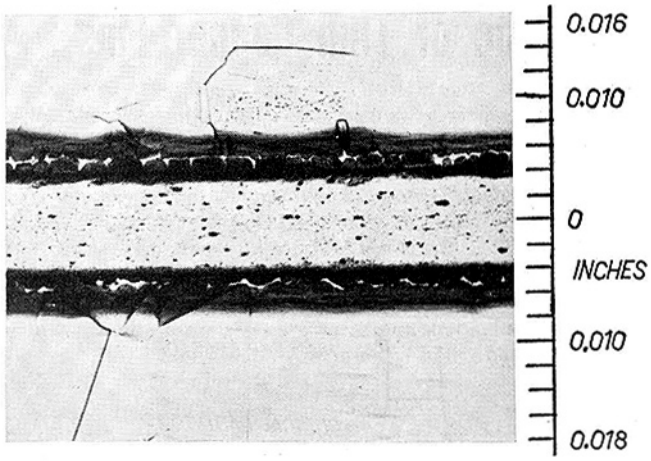

Fig. 2(b) Microphotograph of back-to-back fin specimen prepared with 0.0015 in. of Cu–Ag–Li braze

it contains the same term for the lateral thermal conductance K that is required:

$$d(K\,dT/dx)/dx = \sigma\epsilon(T^4 - T_s^4) \qquad (1)$$

Here $K = k_s t_s + k_b t_b + k_d t_d + k_c(t_c - t_d) = K_1 + k_c t_c$ for the case where diffusion of the braze into the copper is limited to a uniform layer along the fin. Attention will be limited to this case since it was determined that diffusion is indeed limited, as indicated by microphotographs shown in Fig. 2 and by the results of the test shown in Fig. 4. K_1 is a constant which can be negative if the conductivity in the diffusion zone k_d is very poor or if the diffusion zone t_d is very thick. Negative values of K_1 indicate that an increased thickness of copper is required in the final design to compensate for the degradation, the thickness being equal to K_1/k_c.

Experimental Technique

The value of K as a function of t_c was determined by conducting heat-transfer experiments on one-dimensional rectangular fins of various thicknesses of copper. The fins, 8 in. long by 1 in. wide, were constructed by brazing a layer of copper to both

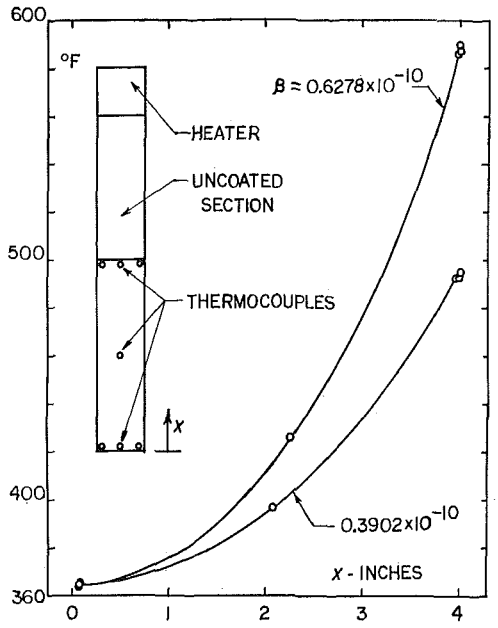

Fig. 3 Comparison of computed temperature profiles with measured temperatures for two different fins at same tip temperature; heater and thermocouple arrangements shown in inset

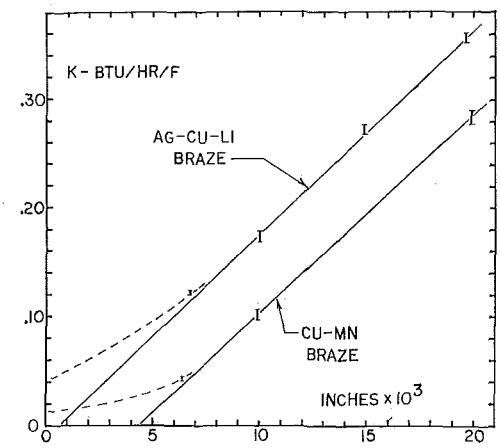

Fig. 4 Measured thermal conductance of fins versus copper thickness

sides of an 8-mil sheet of Ph15–7Mo stainless steel, resulting in a "back-to-back" type of specimen. The lower 4 in. of the specimen was coated with a well-known high-emissivity (ϵ = 0.91 ± 2 percent) ceramic coating that was developed for the radiator–condenser.[1] This portion of the fin specimen represented the test section where the heat-transfer rate from the fin surface would be a well-known function of the local temperature. Thermocouples were installed at both ends and in the middle of the coated region of the fin as shown in Fig. 3. Five-mil-dia iron–constantan wires were swaged into No. 80 holes drilled through the fin. The low thermal conductivity of iron and constantan minimized conduction losses in the leads and the leads were well separated at the surface of the fin so that the junction remained below the surface. Blockage of thermal

[1] Crosby, J. R., and Perlow, H. A., "SNAP 10 A Thermal Control Coatings," in: *Progress in Astronautics and Aeronautics*, Vol. 18, Academic Press, New York, N. Y., 1966.

Nomenclature

K = conductance
k = conductivity
t = thickness
T = temperature
χ = distance from fin tip
σ = Stefan–Boltzmann constant
ϵ = emissivity
$\beta = \sigma\epsilon/K$

Subscripts

s = steel
b = braze
d = diffusion
c = copper

radiation by the thermocouples was minimized by leading the very thin bare thermocouple wires directly away from the view of the surface. An electrical heater was installed at the top of the uncoated portion of the fin. The uncoated portion was polished to produce a low-emissivity (low-heat-loss) section for conducting the heat from the heater to the coated test section. A can-shaped water-cooled heat sink 6 in. in diameter and 11 in. long closed at both ends was used to provide a well-known thermal environment for the test section. The fin specimen was suspended through a slit in the top of the can, the coated portion as well as a good part of the uncoated portion being inside the tank while the heater remained outside. The entire assembly was placed inside a vacuum tank. Thermal tests were conducted at various temperature levels in the range of design. A total of seven specimens, four with a silver–copper–lithium braze and three with a copper–manganese braze, were tested.

Since the conductivities of the various layers within the composite fin do not vary significantly with temperature, the value for K is independent of x; thus equation (1) can be simply expressed for the conditions of the experiment as

$$d^2T/dx^2 = \beta(T^4 - T_s^4) \tag{2}$$

where $\beta = \sigma\epsilon/K$. The boundary condition $dT/dx = 0$ applies at the tip of the specimen. The tip is essentially adiabatic, being a well-polished metal of low emissivity and of small cross-sectional area.

Results

The value for β, hence K, for each test was determined by matching temperature profiles generated by computer to the temperatures measured in the experiment. The profiles were obtained by numerical integration of equation (2) starting with the experimental tip temperature and using selected values for β. The experimental tip temperature is the measured tip temperature corrected for thermocouple displacement from the tip. Two typical temperature profiles are shown in Fig. 3 for two different fins whose tip temperatures were the same. Note the excellent agreement of the profiles with the data at the midpoint. The values for K are plotted in Fig. 4 as a function of the original thickness of copper. The data behave linearly in the region where the copper thickness is greater than the diffusion thickness. In this region the slope of the curve is equal to the conductivity of pure copper, since additional copper is unaffected by the diffusion layer. At small thicknesses of copper the curves might be expected to behave as indicated by the dashed lines. The measured lateral thermal conductance will always have some finite value even at zero copper thickness, since the conductivities of the braze material and steel are positive, although small. It is expected that the Ag–Cu–Li braze has a higher conductivity than the Cu–Mn braze. Since design requirements preclude fin designs using less than approximately 7 mil of copper, the straight-line model (solid lines) satisfies design needs.

The intercepts of the straight lines with the abscissa represent the defect in conductance in terms of the additional thickness of copper that would be required for the design. In other words, if a tapered fin were designed based on copper alone, that is assuming no contribution in conductance from the steel or braze and no degradation due to the braze, the eventual design thickness of copper must be increased by that constant amount. In the cases of the Ag–Cu–Li and the Cu–Mn brazes these amounts are 0.6 and 4.5 mil respectively. The greater amount of degradation with the copper–manganese braze is attributed to the intergranular type of diffusion that penetrates deeper into the copper and surrounds the grains of copper with an insulating coating. Diffusion of the silver–copper–lithium braze is intragranular and does not proceed as deeply into the copper. This is indicated in the microphotographs of Fig. 2.

Conclusions

Lateral thermal conductance of thin radiating fins can be determined quite accurately by using thermal radiation itself as the calorimeter. There is no need to either measure electrical power to heaters and account for losses or to measure heat flow by other calorimetric techniques. The only major requirements of this type of thermal test are that a well-known emissivity coating be used (the accuracy to which the conductance is known is equal to that of the emissivity) and that care be taken in the installation of thermocouples so that they measure the temperature inside the fin (spot-welding or brazing thermocouples to the surface is a questionable method). The great advantage of using this type of test in the radiator–condenser development program was the significantly lower cost of manufacturing fin-type specimens compared to that of the bar-type specimens used in the standard type of conductivity test. Bar-type specimens require as much as 10 times the materials in their construction, so savings were made in this case where experimental braze melts and laminate preparation was expensive. Preparation of bar-type specimens from the laminates is a difficult and expensive procedure, also. Another advantage is that there is no need to guard against heat losses at the high design temperatures used, as would be the case in the standard type of conductivity test, and the time required to achieve steady state is considerably less because of this.

Acknowledgments

The author would like to acknowledge the various contributions of the Atomics International personnel involved in the study, principally R. T. Lancet for help in coordination and J. D. Stearns and his technical group for their patient experimental work.

T. R. THOMAS
Mechanical Engineering Department,
Teesside Polytechnic,
Middlesborough, Teesside, U. K.

S. D. PROBERT
Lecturer,
Mechanical Engineering Department,
University College,
Swansea, United Kingdom

Correlations for Thermal Contact Conductance In Vacuo

A correlation developed by Holm for thermal contact conductance measurements made in vacuo is discussed and its physical basis is deduced with the help of dimensional analysis. On modifying Holm's treatment by including surface roughness and neglecting nominal contact area, the analysis yields a dimensionless conductance $C^* = C/\sigma k$ and a dimensionless load $W^* = W/\sigma^2 M$. When 350 data points from the literature for aluminum and stainless steel contacts in vacuo are plotted in this form C^* is found to be proportional to about $W^{*0.73}$ with correlation coefficients of better than 0.9. The correlations for the two materials do not coincide, however, and this and other discrepancies are discussed.

Introduction

With the continuing trend toward higher efficiencies for industrial processes and machinery which use or generate heat the economic importance of thermal contact resistance has become increasingly recognized, and the literature on the subject now amounts to several hundred papers [1][1] mostly dating from the last 20 years. Several comprehensive reviews [2–4] are available. The theoretical base of the subject is fairly well established, but the simplified models used have proved difficult to apply directly to the types of interfaces of practical interest to engineers and designers. A situation almost unique in heat transfer exists where the very large body of published experimental data is for various reasons quite inaccessible for comparison. This paper is an attempt to collate a portion of the available results in a form more convenient for the design engineer and for research workers in the field.

Previous Work

A number of attempts to correlate thermal contact conductance data have been made [5–9], generally with only partial success. Several of these are usefully criticized by Minges [3]. Exact solutions have been developed for one special case, the plastic contact in vacuo between flat and isotropically rough surfaces whose heights are distributed normally about a mean plane. Tien [9] has shown from dimensional considerations that for such a case a relationship exists between dimensionless conductance $C\sigma/\psi Ak$ and dimensionless load W/AM, where σ is the rms surface roughness and ψ is the mean absolute surface slope. This has been confirmed analytically by Cooper et al. [10] and Thomas and Probert [11], who showed independently that over a wide range of loads the dimensionless conductance is proportional to the 0.99 power [10] or 0.92 power [11] of the dimensionless load. These theories are in fair agreement with experiment (Fig. 1).

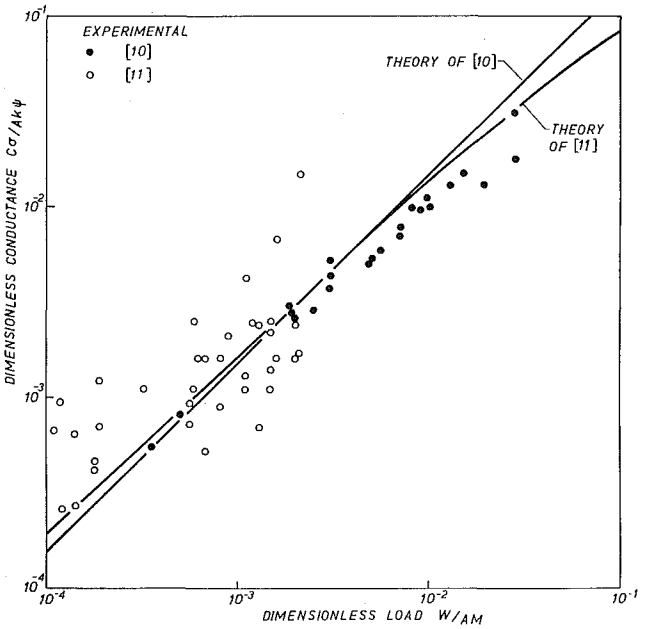

Fig. 1 Variation of dimensionless conductance with dimensionless load for plastic contacts between flat isotropically rough surfaces

However, the majority of published measurements have been made with the wavy anisotropic surfaces of everyday engineering practice. Contacts between such surfaces are less susceptible to

[1] Numbers in brackets designate References at end of paper.

Contributed by the Heat Transfer Division for publication (without presentation) in the JOURNAL OF HEAT TRANSFER. Manuscript received by the Heat Transfer Division January 5, 1971. Paper No. 71-HT-AA.

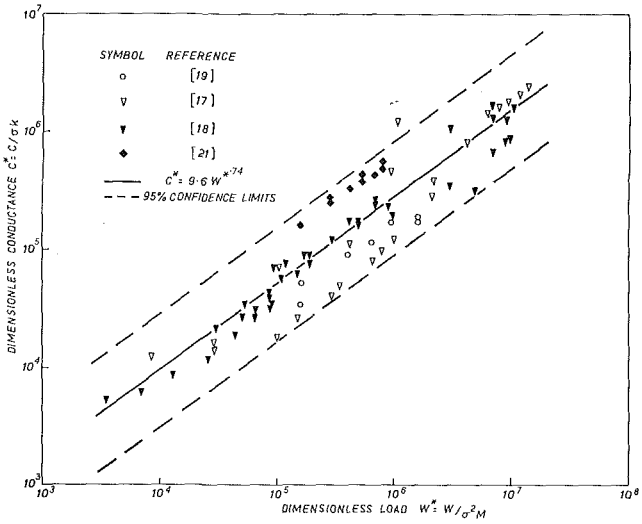

Fig. 2 Variation of dimensionless conductance with dimensionless load for stainless steel contacts in vacuo (see Table 1)

mathematical analysis than the case discussed above, but Holm [12] has attempted a correlation aimed specifically at engineering surfaces in vacuo. He suggested that the thermal resistance R of machined joints in vacuo is independent of the roughness of the contacting surfaces, and can be written as

$$R = \phi f(W)$$

where ϕ is a dimensionless function of the contact materials proportional to $\sqrt{M}/k$ and $f(W)$ is a resistance depending on the applied load W. The function $f(W)$ was obtained empirically from values of R/ϕ and W taken from the work of eight investigators, together with some electrical results of his own. In this way Holm obtained a relation of the approximate form

$$Rk/\sqrt{M} \propto W^{-0.7} \tag{1}$$

Because of the fractional index of W, equation (1) cannot be transformed into a relation between resistance (or conductance) per unit area and nominal pressure by dividing both sides by A. This is clearly a result of some importance, but in Holm's paper it is based on only 23 experimental points. A survey of the literature was therefore undertaken in an attempt to confirm his conclusions. A preliminary investigation gave a result similar to Holm's, but as more results came to hand, the correlation became progressively worse. It was decided to reexamine the problem using a dimensional approach.

Dimensional Analysis

It was assumed initially that the only parameters affecting the contact conductance besides the load are the surface hardness, thermal conductivity, and nominal contact area. These can together be described in terms of the five dimensions of mass, length, time, temperature, and quantity of heat. There are by inspection three independent equations in the coefficients of the variables, and by the Pi theorem these can be grouped into $5 - 3 = 2$ dimensionless numbers, say $C/k\sqrt{A}$ and W/AM.

When a selection of data from the literature was plotted in this form correlation was little better than for the extended version of Holm, but the slope of the logarithmic plot was again about 0.7, i.e.

$$C/k\sqrt{A} \propto (W/AM)^{0.7}$$

or

$$C\sqrt{M}/k \propto (AM)^{0.2}W^{0.7}$$

If the term in AM, which is virtually constant, is neglected the relation reduces to equation (1) and provides a physical basis for Holm's correlation.

At this juncture the evidence was that the nominal contact area did not play a significant role in the variation of contact conductance and it was decided to replace it in the analysis. Despite Holm's conclusion it seemed reasonable that the surface topography would exert some influence on the contact conductance. The dimensional analysis was therefore repeated with σ, which is the topography parameter most widely quoted by experimenters, in place of A, and again yielded two dimensionless numbers, chosen as dimensionless conductance $C^* = C/\sigma k$ and dimensionless load $W^* = W/\sigma^2 M$.

The experimental results of ten authors [11, 13–21] for stainless steel and aluminum alloy contacts were plotted in this form. These materials were chosen because of their widespread practical use, and also because between them they comprise the majority of published conductance data. The stainless steel data (Fig. 2) are all for contact between similar specimens, but the data for aluminum (Fig. 3) include results for contacts between aluminum and harder metals. In the latter the hardness of the softer material and the harmonic mean thermal conductivity have been used in the calculations. The value adopted for the surface roughness is the sum of the rms roughnesses of the individual surfaces. Where authors have not quoted physical properties of their specimens these have been taken from tables; where the hardness was not stated a value of three times the yield strength was assumed. For measurements made over a range of temperatures, appropriate mean values of hardness and thermal conductivity have been interpolated (Tables 1 and 2).

Only data for joints where at least one surface was machined have been used. Contacts where both surfaces are described as lapped or polished are not anisotropic and data for such surfaces have been excluded. Two other sets of measurements have been deliberately omitted: those of Clausing [22] were made on convex contacts, while the very high surface roughness values quoted by Shlykov and Ganin [23] suggest a misprint or mistranslation of units. Measurements were made on bar specimens except where otherwise indicated in the tables.

Discussion

Least-squares fits were made to 102 stainless steel data points and 240 aluminum data points. Not all of these are displayed in the figures because of overlapping. The best straight line through the stainless steel data is

$$\ln C^* = (0.743 \pm 0.067) \ln W^* + 2.26 \pm 0.88$$

while the best line through the aluminum results is given by

$$\ln C^* = (0.720 \pm 0.044) \ln W^* + 0.66 \pm 0.62$$

The errors shown are probable errors. The correlation coefficients for the two sets of data are respectively 0.915 and 0.913.

Bearing in mind the number of data sources and the wide range

Nomenclature

A = nominal contact area (m^2)
C = thermal conductance (w/deg K)
C^* = dimensionless conductance $C/\sigma k$
k = thermal conductivity (w/m-deg K)
M = surface hardness (N/m^2)
R = thermal resistance (deg K/w)
W = load (N)
W^* = dimensionless load $W/\sigma^2 M$
σ = rms surface roughness (m)
ϕ = dimensionless contact parameter
ψ = mean absolute surface slope (radians)

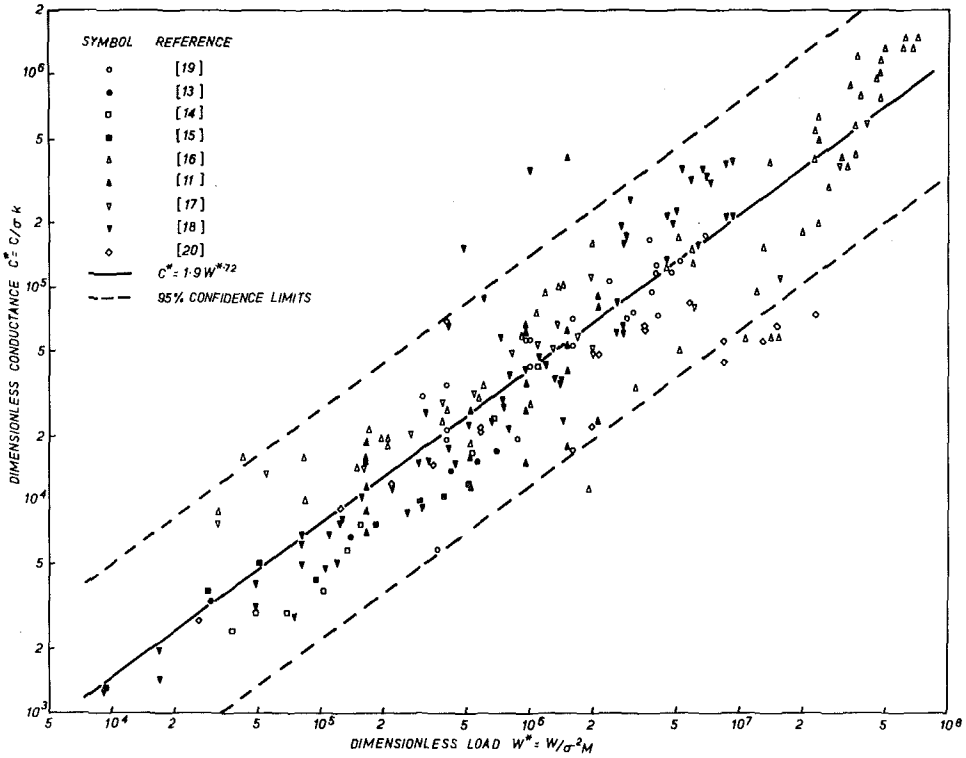

Fig. 3 Variation of dimensionless conductance with dimensionless load for contacts in vacuo where one or both surfaces are aluminum (see Table 2)

Table 1 Stainless steel contacts

Reference	Material	Finish	A (10^{-4} m²)	σ (10^{-6} m)	M (10^{8} N/m²)	k (w/m-deg K)	Number of data points
21*	18-8	rolled	2.84	0.74	31	15	21
19†	302	rolled	0.58	0.77	8.5	16.2	7
18	17-4 PH	ground	20.2	0.86	44.4	11.7	15
				1.78	44.4	11.7	12
				3.7	44.4	11.7	11
				5.7	44.4	11.7	14
17	304	ground	20.3	2.4	27	15	11
				0.63	27	15	11

Table 2 Contacts where one or both surfaces are aluminum

Reference	Material	Finish	A (10^{-4} m²)	σ (10^{-6} m)	M (10^{8} N/m²)	k (w/m-deg K)	Number of data points
13	6061-T6	flycutter	10.14	3.0	10	200	7
14	6061-T6	turned	19	3.65	10.5	170	9
15	6061-T4	milled	5.1	0.762	10.5	190	5
		turned	5.1	2.44	10.5	190	3
11	Al / stainless steel	lapped / ground	1.86	0.6	18	35.5	26
20†	2024-T3	rolled	156	0.36	13	190	6
		flycutter	156	0.71	13	190	7
		shaper	156	2.9	13	190	4
19†	6061-T6	rolled	58	0.48	8.8	172	25
18	7075-T6	ground	20.2	0.81	20.2	93	13
				2.3	20.2	93	15
				3.1	20.2	93	18
				6.6	20.2	93	13
18	7075-T6 / stainless steel 17-4 PH	ground / ground	20.2	0.81	20.2	20.7	12
17	6061-T6	turned	20.3	0.60	10.5	190	9
				2.8	10.5	190	9
16	2024-T4	turned	20.2	2.3	15	120	20
				0.4	15	120	32
16	2024-T4 / stainless steel 304	turned / ground	20.2	0.5	15	26.7	7

* 0.05-mm disks; † 3.2-mm plates.

of experimental parameters, the degree of correlation is encouraging. In particular the decision to neglect the nominal contact area appears justified; variations of up to 40 times in this parameter have not had any appreciable effect on the correlation.

It is interesting to note that the correlations include measurements made on specimens of sheet or plate form. To treat a specimen as semi-infinite it is necessary that its dimensions in the direction of heat flow should be greater than the limits of the regions of disturbance caused by individual macroscopic constrictions. These limits are smaller than might be thought. It has recently been shown [24] that over 90 percent of the resistance of a circular constriction occurs within five constriction diameters of the surface. If the diameter of a macroscopic constriction, i.e., the envelope of a cluster of microscopic constrictions, is assumed to be of the order of the separation of machining ridges, say 0.5 mm on a typical turned surface, then any body of thickness greater than 2.5 mm can be treated as semi-infinite. For sheet material where the striations are closer together the limit might be rather less.

The hysteresis effect of loading might be a factor in explaining the degree of scatter within each correlation. Experimenters rarely mention the loading history of their specimens, though as Mikic [25] has shown conductances can differ by a factor of four or more according to whether they were measured under increasing or decreasing load. In certain cases the directional effect [11] could also cause variations.

A more serious problem is the discrepancy between the correlations for stainless steel and aluminum. It is clear from an inspection of the 95 percent confidence limits (Figs. 2 and 3) that the two sets of data do not belong to the same statistical population. Clearly the dimensional analysis is incomplete. The fact that the data for two different materials falls into two well-defined groups indicates that the missing parameter or parameters must represent the intrinsic properties of the material. The good agreement of the slopes of the correlations is evidence that the other variable involved is dimensionless.

A possibility is that other surface parameters are involved. It has been suggested [26] that an isotropic surface may be completely specified by two parameters, the rms roughness and the correlation length (the distance in which the autocorrelation function of the surface profile decreases to a tenth of its initial value). Preliminary studies in this department (to be published elsewhere), however, indicate that correlation lengths of stainless steel and aluminum surfaces with similar finishes do not differ significantly. Clearly the correlation length of an anisotropic surface will depend on the direction of measurement relative to the lay. Such a surface will therefore need at least one additional parameter to describe its contact properties, and it is possible that this parameter may be specific to a particular material. Further work on this problem is needed.

Conclusions

If the thermal conductance of an interface in vacuo is assumed to be independent of the nominal area of contact, the application of dimensional analysis has been shown to yield two dimensionless numbers, a load number $W^* = W/\sigma^2 M$ and a conductance number $C^* = C/\sigma k$. The high degree of correlation of data from the literature plotted in this form has confirmed the assumptions of the analysis. The correlations hold over a range of more than three orders of magnitude in dimensionless load; in the case of aluminum the correlation applies to joints between dissimilar materials where there are differences of more than an order of magnitude in the thermal conductivities of the contacting materials.

From the point of view of the designer it is convenient that only three parameters besides the load need to be known to predict the conductance. One of these, the thermal conductivity, may easily be found from tables, while the other two, surface hardness and rms roughness, can usually be measured in-house. It is also useful that the correlations can be applied to interfaces between materials in sheet or plate form, as many practical contacts are likely to be of this type.

In the present correlations only measurements made in vacuo have been used. It has been suggested, however [27, 28], that when heat flows between two solid bodies in the presence of a conducting fluid the contribution of the fluid to the total conductance is in most practical cases independent of the conductance through the contact spots and invariant with load. Evidence in support of this hypothesis was provided by Thomas and Probert [29], who took a large number of conductance measurements made in air and other fluids from the literature and extrapolated the best line through each set of data to zero load. When this intercept, which was interpreted as the constant fluid conductance term, was subtracted from the total conductances to give the contact-spot conductances, almost all the sets of data were best represented by linear relations between conductance and fractional powers of the load. It would be interesting to repeat the present correlations with the inclusion of data obtained in the above way from the large published body of measurements on gas- or liquid-filled contacts.

Acknowledgments

This work was supported by the Science Research Council. One of us (T.R.T.) would also like to acknowledge the financial help of the British Steel Corporation.

References

1 Hsieh, C. K., and Davis, F. E., "Bibliography on Thermal Contact Conductance," USAF Report AFML-TR-69-24, 1969.

2 Thomas, T. R., and Probert, S. D., "Thermal Contact of Solids," *Chemical and Process Engineering*, Vol. 47, 1966, pp. 51–60.

3 Minges, M. L., "Thermal Contact Resistance," USAF Report AFML-TR-65-375, 1966.

4 Wong, H. Y., "A Survey of the Thermal Conductance of Metallic Contacts," Aeronautical Research Council Report C.P. 973, HMSO, London, 1968.

5 Wheeler, R. G., "Thermal Conductance of Fuel Element Materials," USAEC Report HW 60343, 1959.

6 Graff, W. J., "Thermal Conductance across Metal Joints," *Machine Design*, Vol. 32, 1960, pp. 166–172.

7 Rapier, A. C., Jones, T. M., and McIntosh, J. E., "The Thermal Conductance of Uranium Dioxide/Stainless Steel Interfaces," *International Journal of Heat and Mass Transfer*, Vol. 6, 1963, pp. 397–416.

8 Veziroglu, T. N., "Correlation of Thermal Contact Conductance Experimental Results," University of Miami Mechanical Engineering Department Report on NASA Grant NGR 10-007-010-Sub 11, 1967.

9 Tien, C. L., "A Correlation for Thermal Contact Conductance of Nominally Flat Surfaces in a Vacuum," *Proceedings 7th Thermal Conductivity Conference*, U. S. Bureau of Standards, 1968, pp. 755–759.

10 Cooper, M. G., Mikic, B. B., and Yovanovich, M. M., "Thermal Contact Conductance," *International Journal of Heat and Mass Transfer*, Vol. 12, 1969, pp. 279–300.

11 Thomas, T. R., and Probert, S. D., "Thermal Contact Resistance: The Directional Effect and Other Problems," *International Journal of Heat and Mass Transfer*, Vol. 13, 1970, pp. 789–807.

12 Holm, R., "Thermal Conduction through Nominally Flat Metallic Contacts in Vacuum Environment," Stackpole Carbon Co. Report, 1965.

13 Kaspareck, W., and Dailey, R., "Measurement of Thermal Contact Conductance Between Dissimilar Metals in a Vacuum," ASME Paper No. 64-HT-38.

14 Petri, F. J., "An Experimental Investigation of Thermal Contact Resistance in a Vacuum," ASME Paper No. 63-WA-156.

15 Cunnington, G. R., "Thermal Conductance of Filled Aluminum and Magnesium Joints in a Vacuum Environment," ASME Paper No. 64-WA/HT-40.

16 Fried, E., "Study of Interface Thermal Contact Conductance," General Electric Co. Report 65 SD4395, 1965.

17 Fried, E., "Metallic Interface Thermal Conductance," paper presented at NPL Thermal Conductivity Conference, London, 1964.

18 Bloom, M. F., "Thermal Contact Conductance in a Vacuum Environment," Douglas Aircraft Co. Report SM 47700, 1964.

19 Stubstad, W. R., "Thermal Contact Resistance between Thin plates in a Vacuum," Collins Radio Co. Report 52-0756961-00181M, 1964.

20 Fried, E., and Costello, F. A., "Interface Thermal Contact

Resistance Problem in Space Vehicles," *Journal of the American Rocket Society*, Vol. 32, 1962, pp. 237–243.

21 Thomas, T. R., and Probert, S. D., "Thermal Resistances of Some Multilayer Contacts under Static Loads," *International Journal of Heat and Mass Transfer*, Vol. 9, 1966, pp. 739–754.

22 Clausing, A. M., and Chao, B. T., "Thermal Contact Resistance in a Vacuum Environment," JOURNAL OF HEAT TRANSFER, TRANS. ASME, Series C, Vol. 87, No. 2, May 1965, pp. 243–251.

23 Shlykov, Yu. P., and Ganin, Ye. A., "Thermal Resistance of Metallic Contacts," *International Journal of Heat and Mass Transfer*, Vol. 7, 1964, pp. 921–929.

24 Yovanovich, M., Cordier, H., and Coutanceau, J., "Sur la résistance thermique due à un contact unique de section circulaire," *C. R. Acad. Sci.*, Paris, Vol. 268, 1969, pp. 1–4.

25 Mikic, B. B., "Effect of Previous Loading on Thermal Contact Conductance," Massachusetts nstitute of Technology, 1969.

26 Whitehouse, D. J., and Archard, J. F., "The Properties of Random Surfaces of Significance in their Contact," *Proceedings of the Royal Society*, Series A, Vol. 316, 1970, pp. 97–121.

27 Ross, A. M., and Stoute, R. L., "Heat Transfer Coefficient between Uranium Dioxide and Zircaloy-2," Atomic Energy of Canada Ltd., Report AECL-1552, 1962.

28 Von Kiss, M., "Der Wärmeübergang zwischen sich berührenden metallischen Oberflächen," *Neue Technik*, Vol. 5, 1963, pp. 714–724.

29 Thomas, T. R., and Probert, S. D., "Thermal Resistance of Pressed Contacts," UKAEA Report 1013 (R/X), HMSO, London, 1965.

Resistance Problem in Space Vehicles," *Journal of the American Rocket Society*, Vol. 32, 1962, pp. 237–243.
21 Thomas, T. R., and Probert, S. D., "Thermal Resistances of Some Multilayer Contacts under Static Loads," *International Journal of Heat and Mass Transfer*, Vol. 9, 1966, pp. 739–754.
22 Clausing, A. M., and Chao, B. T., "Thermal Contact Resistance in a Vacuum Environment," JOURNAL OF HEAT TRANSFER, TRANS. ASME, Series C, Vol. 87, No. 2, May 1965, pp. 243–251.
23 Shlykov, Yu. P., and Ganin, Ye. A., "Thermal Resistance of Metallic Contacts," *International Journal of Heat and Mass Transfer*, Vol. 7, 1964, pp. 921–929.
24 Yovanovich, M., Cordier, H., and Coutanceau, J., "Sur la résistance thermique due à un contact unique de section circulaire," *C. R. Acad. Sci.*, Paris, Vol. 268, 196?, pp. 1–4.
25 Mikic, B. B., "Effect of Previous Loading on Thermal Contact Conductance," Massachusetts nstitute of Technology, 1969.
26 Whitehouse, D. J., and Archard, J. F., "The Properties of Random Surfaces of Significance in their Contact," *Proceedings of the Royal Society*, Series A, Vol. 316, 1970, pp. 97–121.
27 Ross, A. M., and Stoute, R. L., "Heat Transfer Coefficient between Uranium Dioxide and Zircaloy-2," Atomic Energy of Canada Ltd., Report AECL-1552, 1962.
28 Von Kiss, M., "Der Wärmeübergang zwischen sich berührenden metallischen Oberflächen," *Neue Technik*, Vol. 5, 1963, pp. 714–724.
29 Thomas, T. R., and Probert, S. D., "Thermal Resistance of Pressed Contacts," UKAEA Report 1013 (R/X), HMSO, London, 1965.

DISCUSSION

L. S. Fletcher[2]

The authors have utilized dimensional analysis in the formulation of correlation parameters for the estimation of thermal contact conductance in a vacuum. Such an approach has been used before, but the results usually have not met with as much success as the correlation parameters of the present work. An analysis of this type, however, should indicate the limitations of the correlation parameters so that they will not be generalized beyond their limits of application.

Although the paper discusses some of the previous work on the correlation of thermal contact conductance, several of the more extensive correlation investigations have been omitted. In particular, the work of Laming [30], Hsieh and Touloukian [31], Fletcher [32, 33], and Malkov [34] should be considered in a discussion of the correlation of thermal contact conductance. In addition, Fried [35] has recently critically reviewed correlation and prediction techniques for thermal contact conductance, and established some guidelines for the correlation and prediction of the contact conductance of a joint. It would have been instructive had the authors compared their correlation expressions and techniques to those of other investigators.

One of the recently developed correlation expressions [33] complements the present work but includes an additional parameter for compensation of the variation of mean junction temperature. The correlation parameters were dimensionless conductance $C\delta/Ak$ and dimensionless contact load $(W/AE)\beta T_m$. The surface parameter δ represented flatness deviation and roughness deviation of both surfaces, and the apparent contact pressure was made dimensionless with the modulus of elasticity E. The mean junction temperature T_m was made dimensionless with the coefficient of thermal expansion β for the material. These parameters were found to correlate both high- and low-mean-junction-temperature aluminum, stainless steel, brass, and magnesium experimental conductance data [32] on one dimensionless curve.

An analysis of some selected data (both ground and sanded surfaces [18, 32]) in terms of the present correlation parameters indicated the probable importance of mean junction temperature to the correlation of thermal-contact-conductance data. Although these data demonstrated reasonable agreement, lower-temperature data for the same surface contacts and apparent contact pressure were further removed from the correlation curves. It would appear, then, that the inclusion of the effect of mean junction temperature would lead to even more successful correlation parameters.

[2] Associate Professor, Mechanical and Aerospace Engineering Department, Rutgers University, New Brunswick, N. J. Mem. ASME.

Additional References

30 Laming, L. C., "Thermal Conductance of Machined Contacts," *International Developments in Heat Transfer*, ASME, New York, N. Y., 1963, pp. 65–76.
31 Hsieh, C. K., and Touloukian, Y. S., "Correlation and Prediction of Thermal Contact Conductance for Nominally Flat Surfaces," *Thermal Conductivity*, Plenum Press, New York, N. Y., 1969.
32 Fletcher, L. S., "Thermal Contact Resistance of Metallic Interfaces: An Analytical and Experimental Study," PhD dissertation, Arizona State University, Tempe, Ariz., June 1969.
33 Fletcher, L. S., and Gyorog, D. A., "Prediction of Thermal Contact Conductance between Similar Metal Surfaces," *Progress in Aeronautics and Astronautics*, Vol. 24, *Heat Transfer and Spacecraft Thermal Control*, M.I.T. Press, Cambridge, Mass., 1971, pp. 273–288.
34 Malkov, V. A., "Thermal Contact Resistance of Machined Metal Surfaces in a Vacuum Environment," *Heat Transfer–Soviet Research*, Vol. 2, No. 4, July 1970, p. 24.
35 Fried, E., "A Joint Heat Transfer Data Critical Study and Design Guideline," GE Document No. 71SD4241, NASA CR-119933, June 1971.

W. M. Rohsenow[3] and B. B. Mikic[4]

Dimensional analysis can lead to deceiving results. The problem in this paper is that the quantities $C\ (= q/\Delta T)$ and W are used as significant variables instead of $h = C/A = (q/A)/\Delta T$ and pressure $p = W/A$. The difference is the A in each denominator. Surely q/A and p are more appropriate quantities for this work than q and W.

Using the quantities h, σ, k, p, and M, dimensional analysis leads to the groups

$$\frac{h\sigma}{k} \quad \text{and} \quad \frac{p}{M}$$

equally valid from dimensional analysis, but much better physical quantities. The mean slope ψ is dimensionless, so dimensional analysis cannot tell us where it belongs; however, the theory as developed in the authors' reference [10] leads to

$$\frac{h\sigma}{k\psi} \quad \text{and} \quad \frac{p}{M}$$

which are the coordinates of Fig. 1

Using q and W in Fig. 2 instead of q/A and W/A spreads data for various test-sample sizes along the line, even though pressure is the same. Note five-decade scales in Fig. 2 vs. three-decade scales in Fig. 1.

Note also that the effect of doing the dimensional analysis with q and W is not only to remove A from each denominator, but also to put σ in the denominator of $C/\sigma k$ instead of the numerator $h\sigma/k\psi$ where the analysis of reference [10] suggests it should properly be.

We suggest the appropriate way to interpret contact-conductance data is with the parameters of Fig. 1 and not those of Fig. 2.

[3] Professor, Department of Mechanical Engineering, Massachusetts Institute of Technology, Cambridge, Mass. Fellow ASME.

[4] Associate Professor, Department of Mechanical Engineering, Massachusetts Institute of Technology, Cambridge, Mass. Mem. ASME.

E. Fried[5]

The authors of this paper are to be commended for having undertaken the tedious task of evaluating, reducing, and presenting data of many investigators for the purpose of developing a general correlation for thermal contacts in a vacuum. Having attempted a number of such empirical correlations, this discusser is aware of the difficulty inherent in such a task, especially if the objective of such work is to provide results in a form convenient for design engineers.

While Holm's original work on electric contacts [36] has provided the basis of a significant portion of the existing thermal-contact literature, the reason for use of reference [12] in preference to Tien [9] or Cooper et al. [10] to obtain the authors' dimensionless conductance C^* and load W^* would be of interest to many workers in this field. Holm's objection to the use of nominal areas could readily be accommodated by converting the experimental data to conductance C and load W by multiplying the appropriate terms by the nominal area before attempting the correlation. This was, in fact, done when this discusser supplied Holm with experimental data, when Holm prepared reference [12]. Having attempted to use it, this discusser agrees with the present authors that Holm's correlation [12] is inconclusive and not suitable for design applications.

This leads to the question of whether a suitable general correlation of thermal-contact conductance exists or can be developed. The present authors have been able to correlate data for aluminum joints and data for stainless steel joints, where the slopes of the correlation are in good agreement but do not coincide. Correlations similar to these, but using Holm's [36] a-spots ($\bar{a}$ = radius of contact spots) as the characteristic dimension in the dimensionless conductance number, have been presented by Hsieh and Touloukian [31] and Malkov [34]. Hsieh in particular has utilized many of the experimental results cited in the present work and in [1] and categorized them according to ferrous and non-ferrous materials, wavy and nominally flat surfaces, and constant $\bar{a}$ or variable $\bar{a}$. Hsieh's correlations also show significant scatter, which indicates that there may be a missing parameter. Another general nondimensional correlation which deserves citation is that by Fletcher [37], who utilized the initial gap dimension as a characteristic dimension, in addition to a nondimensional temperature. This correlation had remarkably limited scatter and was the only correlation to consider interface temperature explicitly.

At this point, it is of interest to consider the common features of the present and all cited dimensionless correlations. They are, with the exception of Fletcher [37], of the form (Conductance Number) = Constant (Load Number)^n but differ in the value of the constant and in the value of the exponent n. Table 3 shows typical forms of the nondimensional correlation terms used. From this, it can be seen that the terms other than the load W serve to "normalize" the conductance C for different materials, surface parameters, and physical properties. It is also evident, as the authors state in their discussion, that present correlations are either inadequate or that parts of the experimental data obtained and used for these correlations are inadequately defined.

[5] Consulting Engineer, General Electric Co., Schenectady, N. Y. Mem. ASME.

Table 3

Reference	Conductance term	Load term	Load-term exponent (approx.)
Authors	$C/\sigma k$	$W/\sigma^2 M$	0.73
Tien [9]	$C\sigma/\psi Ak$	W/AM	0.85
Cooper et al. [10]	$C\sigma/\psi Ak$	W/AM	0.99
Hsieh et al. [31]	$C\bar{a}/Ak$	W/AM	1.0
Malkov [34]	$C\bar{a}/Ak$	W/AM	0.66

Assumption: 3 × yield strength = M.

Additional References

36 Holm, R., *Electric Contacts Handbook*, Springer-Verlag, Berlin, 1958.

37 Fletcher, L. S., Smuda, P., and Gyorog, D. A., "Thermal Contact Resistance of Selected Low-Conductance Interstitial Materials," *AIAA Journal*, Vol. 7, No. 7, July 1969, pp. 1302–1309.

Authors' Closure

We regret that we were unable to discuss references [33] and [35] as they did not appear until after our manuscript had been submitted. We agree with Fletcher and Fried that inclusion of the mean interface temperature is likely to lead to a significant improvement in correlation, though it is a parameter which is not always readily available from published data. Fletcher's use of the elastic modulus in preference to the surface hardness is interesting. We are now ourselves of the opinion that surface contact in most engineering situations is elastic rather than plastic, and of course the elastic modulus is a much more well-defined parameter. We hope to repeat our present correlation with an appropriate modification.

The dimensionless groups suggested by Rohsenow and Mikic may well be more physically significant than ours, particularly for isotropic surfaces. However, the point of our paper was really to provide a useful, if limited, correlation using published experimental data. Values of surface slopes have not hitherto been quoted in the heat transfer literature as the necessary measuring techniques have only recently become available and there are difficulties associated with their interpretation. It is not therefore very convenient at present to use $h\sigma/k\psi$ as a dimensionless conductance. A more fundamental objection to the suggestion is the difficulty of defining a unique value of ψ for an anisotropic surface.

G. A. CARLSON
Lawrence Radiation Laboratory,
University of California,
Livermore, Calif.
Assoc. Mem. ASME

M. A. HOFFMAN
Professor,
Department of Mechanical and
Aerospace Engineering,
University of California,
Davis, Calif.

Heat Pipes in the Magnetic-Field Environment of a Fusion Reactor[1]

Heat pipes have been proposed for use in environments where there are strong magnetic fields such as in controlled fusion reactors. The presence of a magnetic field can influence the performance of a heat pipe significantly, depending on the heat-pipe geometry, its orientation in the magnetic field, the heat-pipe materials and fluid properties, as well as the magnetic-field strength. A liquid-metal heat pipe, specifically designed to operate in a magnetic field, will employ a compound wick structure with the optimum liquid-flow passage size larger and the vapor flow passage proportionately smaller than for the no-magnetic-field design. The basic conclusion is that the presence of a magnetic field always results in a lower maximum heat-flux capability, but the detrimental effects of the magnetic field can be greatly reduced by using a heat-pipe geometry optimized for operation in the specific magnetic-field environment.

Introduction

Heat pipes have received a great deal of attention in recent years for application in a variety of thermal devices including advanced power systems. This particular study of heat pipes in magnetic fields was motivated by an imaginative application of heat pipes in a conceptual design of a controlled thermonuclear fusion power system [1].[2]

In a fusion power system, the hot fusion plasma would be in a vacuum vessel but would be kept away from the walls by strong magnetic fields (Fig. 1). As presently visualized, a substantial fraction of the energy release of the fusion reactions would appear in the form of high-energy neutrons. The kinetic energy of these neutrons would be converted into thermal energy in a moderator "blanket" of liquid lithium which would surround the plasma just outside of the vacuum vessel. The neutrons would be slowed down by collisions with the lithium nuclei, thereby transferring the neutron energy to the lithium. The lithium would be carried in pipes to a steam boiler where it would act as a heat-transfer medium to generate high-temperature steam for a steam power plant.

Unfortunately, the neutrons deposit their energy very nonuniformly in the lithium blanket. In fact, the energy deposition falls off approximately exponentially with radial distance. In order to "smooth out" this unfavorable power-density profile,

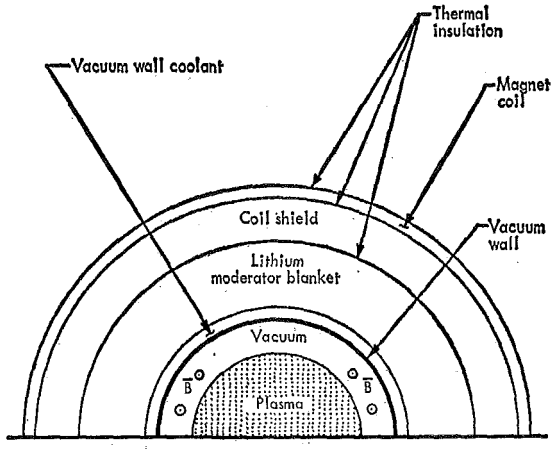

Fig. 1 Section through a fusion reactor looking along axis of reactor (from Homeyer [2])

Werner proposed using heat pipes integrated into a specially designed vacuum vessel [1]. A simplified schematic diagram of this concept is shown in Fig. 2.

The superconducting magnet coils used to generate the high-strength magnetic fields must be outside the heavy neutron-flux regions. As a result, they would have to be outside the lithium blanket. This in turn means that the heat pipes would be inside the magnetic-field region. Since it is well known from studies of magnetohydrodynamic (MHD) flowmeters and MHD generators that there are pressure losses associated with the motion of conducting fluids in magnetic fields, a study was undertaken to ascertain the importance of the magnetic effects on heat pipes.

In the following sections, the important effects of the magnetic field on the liquid-phase flow in the wick structure are discussed

---

[1] This work performed under the auspices of the U. S. Atomic Energy Commission.

[2] Numbers in brackets designate References at end of paper.

Based on a paper contributed by the Heat Transfer Division and presented at the Space Technology and Heat Transfer Conference, Los Angeles, Calif., June 21–24, 1970, of The American Society of Mechanical Engineers as Paper No. 70-HT/SpT-10. Manuscript received by the Heat Transfer Division March 26, 1970; revised manuscript received December 2, 1970.

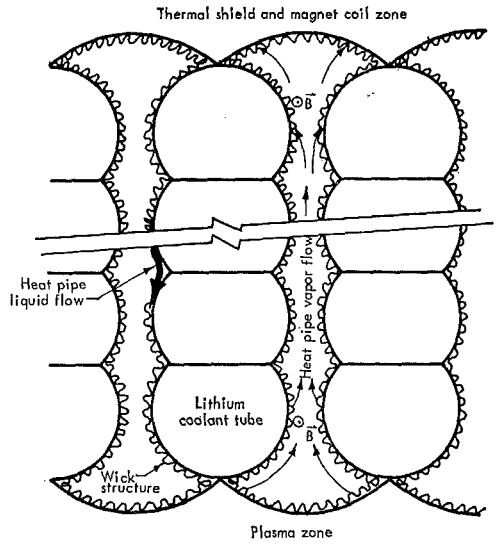

Fig. 2 Schematic of heat-pipe moderator blanket looking along axis of reactor (from Werner [1])

first. It is shown that a magnetic field affects the performance of a heat pipe most strongly when a component of the field is perpendicular to the heat-pipe axis and an electrically conducting fluid is used along with a metallic wick structure. For this situation there are three main effects of the magnetic field, each of which increases the pressure drop in the liquid-phase flow:

(*a*) Electrical eddy currents flow in the liquid in a plane perpendicular to the fluid velocity, causing thinning of the side-wall boundary layers.

(*b*) The electrical currents of effect (*a*) are increased if the wick walls are electrically conducting, resulting in a magnetic body force in the liquid which opposes its motion.

(*c*) Electrical eddy currents flow in "end regions" in a plane perpendicular to the magnetic field where the liquid enters or leaves the magnetic field or where there are gradients of magnetic-field strength.

Each of these important magnetic effects is examined in turn and generalized results for the various contributions to the pressure drop are derived wherever possible. These results are then combined with the vapor-pressure-drop equations to determine the optimum heat-pipe geometry for a specific example. The optimized design is compared to a conventional heat pipe operating in the magnetic field to show the enormous improvement in performance possible with careful design.

In this paper, a *conventional heat pipe* means one with a simple wick structure characterized by a single capillary pore size r_c, and will be referred to simply as a Type I heat pipe.

A more advanced heat-pipe design is one with a compound wick structure such as a channel or groove covered on the inside by a fine mesh or screen. The channel is of large hydraulic diameter to reduce the liquid pressure drop while the screen has as small a pore size as practical for efficient capillary pumping. Such a *compound-wick heat pipe* will be referred to as a Type II heat pipe.

Liquid-Flow Pressure Drop in Uniform Magnetic Field

The pressure gradient of an electrically conducting fluid flowing transversely to a uniform magnetic field is a function of the duct geometry, the ratio of wall to fluid conductance C, and the Hartmann number H. These two important nondimensional parameters are defined as follows:

$$C \equiv \frac{\sigma_w t_w}{\sigma_L w_\parallel}$$

and

$$\mathrm{H} \equiv w_\parallel B \sqrt{\frac{\sigma_L}{\eta_L}}$$

where σ_L and σ_w are the electrical conductivities of the liquid and channel wall (including any contact-resistance effects) respectively, $w_\parallel$ is the half-width of the liquid-flow passage in the direction parallel to the magnetic field, t_w is the effective channel-wall thickness, η_L is the liquid viscosity, and B is the magnetic-field strength. The parameter C is a measure of the ease with which magnetically induced currents can leak through the channel walls; the wall current leakage is zero when $C = 0$ and increases to a maximum as $C \to \infty$.

The Hartmann number H is essentially the ratio of magnetic to viscous forces in the fluid. It is a measure of the strength of magnetically induced current loops in the fluid. When H = 0, we have the ordinary viscous incompressible boundary-layer pressure drop; as H increases, the pressure drop increases as a function of both H and C, as will be discussed in the following paragraphs.

For flow between *parallel plates*, there is a simple analytical relation for pressure gradient valid for all values of C and H. Exact infinite-series solutions exist for other geometries (in particular circular and rectangular ducts), but these are cumbersome to use. Fortunately, the pressure drop in these ducts may be closely approximated by a simple empirical formula based on the parallel-plate solution.

The pressure gradient of incompressible fully developed laminar flow between parallel plates with a uniform transverse magnetic field is derived in [3] and may be written

$$P_u \equiv \frac{w_\parallel^2}{\eta_L \bar{u}} \left(-\frac{dp}{dz} \right) = \frac{\mathrm{H}^2 \tanh \mathrm{H}}{\mathrm{H} - \tanh \mathrm{H}} + \frac{\mathrm{H}^2 C}{1 + C} \qquad (1)$$

Nomenclature

a = heat-pipe dimension, see Fig. 7
A = area
b = heat-pipe dimension, see Fig. 7
B = magnetic-flux density
C = wall-to-fluid electrical-conductance ratio
d = heat-pipe dimension, see Fig. 7
D_h = hydraulic diameter
g = acceleration of gravity
H = Hartmann number
j = electrical current density
l = channel length
L = heat of vaporization
p = pressure
P = dimensionless pressure gradient
$q_{\max}$ = maximum axial heat-flux density in heat pipe
r_c = capillary pore radius
Re = Reynolds number
t = wall thickness
u = velocity in flow direction
v = velocity perpendicular to flow direction
w = channel half-width
z = flow-direction coordinate
γ = surface tension
Δp = pressure rise or drop
ϵ = void fraction
η = fluid viscosity
θ = wetting angle
ρ = fluid density
σ = electrical conductivity

Subscripts

c = heat-pipe condenser
cap = capillary
e = heat-pipe evaporator
L = liquid
tot = total
u = uniform magnetic field
v = vapor
w = wall
$\parallel$ = parallel to magnetic field
$\perp$ = perpendicular to magnetic field

where $\bar{u}$ is the average fluid-flow velocity. The first term is just the classical Hartmann boundary layer between insulated parallel plates. The second term is the pressure drop due to the $\bar{j} \times \bar{B}$ body force on the fluid.

The pressure gradient for incompressible fully developed laminar flow in a *rectangular duct* with a uniform transverse magnetic field has been derived for the two cases $C = 0$ and $C = \infty$ [4, 5]. The solution in each case is an infinite series.

A good approximation for the pressure gradient in rectangular ducts is [6]

$$P_{u(\text{approx})}\left(\text{H}, \frac{w_\perp}{w_\parallel}\right) = \frac{\text{H}^2 \tanh \text{H}}{\text{H} - \tanh \text{H}} - 3 + P_u\left(\text{H} = 0, \frac{w_\perp}{w_\parallel}\right) + \frac{\text{H}^2 C}{1 + C} \quad (2)$$

where P_u (H = 0, $w_\perp/w_\parallel$) is the ordinary laminar-flow pressure drop. For example, P_u(H = 0) is 7.11 for square channels and 3.0 for infinite parallel plates ($w_\perp/w_\parallel = \infty$). This approximation is based on the idea that the two basic magnetic effects are almost uncoupled and hence additive for rectangular channels as they were for infinite parallel plates. For the parallel-plate case, the first term of equation (2) yields the correct laminar incompressible boundary-layer pressure drop of $P_u = 3.0$ as H → 0.

In order to obtain reasonably accurate results for the rectangular channels as H → 0, we have forced equation (2) to yield the exact results at H = 0 by adding the second and third terms, $-3 + P_u$ (H = 0, $w_\perp/w_\parallel$). This empirical equation is also exact for very large H and results in only modest errors for intermediate H. For example, for $C = 0$, the errors for aspect ratios greater than 0.1 never exceed about 11 percent. For $C = \infty$, the errors are almost an order of magnitude smaller. Exact results for intermediate values of C reported by Chu [7] are also well approximated by equation (2).

Equation (2) is also a good approximation for the pressure gradient in a *circular duct* (for which P_u (H = 0) = 8.0). An exact solution based on an infinite series of Bessel functions has been derived by Ihara [8]. His results have not been recomputed, but based on numbers taken from his graphical presentation of the results the maximum error of our approximate formula appears to be less than 10 percent.

There are several effects which equation (2) does not include, such as wall roughness and mass addition and removal. In a heat pipe, the liquid-flow channels are usually not smooth-walled closed ducts. In a Type I heat pipe, the capillary pores may have interconnections; in a Type II heat pipe, the flow channels are covered with a layer of fine screen or mesh on one side. The effect of wall roughness would result primarily in a modification of the P_u(H = 0, $w_\perp/w_\parallel$) term in equation (2).

The effects of mass addition to or removal from the liquid flow should be small if

$$\text{Re}_{L(\text{radial})} \equiv \frac{\rho_L \bar{v}_{L(\text{rad})} D_h}{\eta_L} \ll 1$$

In a Type I heat pipe, this condition is almost always satisfied because of the extremely small hydraulic diameter of the capillary liquid-flow channels. In a Type II heat pipe specifically designed to operate in a high transverse magnetic field, the hydraulic diameter of the liquid-flow passage and hence the radial Reynolds number tend to be much larger. Consequently, the viscous and momentum effects will both be important near the channel wall which is porous. Further analytical work remains to be done to evaluate the magnitude of the momentum effect, and certainly experiments will be required to substantiate the results.

In addition to the above requirement for viscous-dominated flow, it is also necessary to insure that the axial Reynolds number everywhere be much greater than the radial Reynolds number. This condition is easily met in the typical heat pipe everywhere except at the extreme ends of the pipe where the axial velocity goes to zero.

In summary, we propose that equation (2) is an excellent analytical approximation for the pressure drop in electrically conducting fluids flowing in closed channels with conducting walls in the presence of a transverse uniform magnetic field. The only restriction is that the flow be fully developed laminar and incompressible. This condition is almost always satisfied in the liquid flow of a Type I heat pipe because the axial Reynolds numbers are less than the laminar–turbulent transition value of 2300, and the very large length-to-diameter ratio insures that the flow-development effects are negligible. In a Type II heat pipe the hydraulic diameter of the liquid-flow passage is increased such that the condition may not be satisfied, at least for the no-magnetic-field case. However, a strong transverse magnetic field both increases the transitional Reynolds number [9] and shortens the development length [10], so the fully developed laminar assumption may still be valid. We shall assume equation (2) to apply for both types of heat pipes, with or without magnetic fields.

Liquid Pressure Drop due to Magnetic-Field Gradients

The pressure drop of a conducting liquid at entry into and exit from a transverse magnetic field is caused by $\bar{j} \times \bar{B}$ body forces due to eddy currents which flow in the end regions in planes perpendicular to the magnetic field [11, 12]. The eddy currents, in turn, are driven by the electromotive forces in the end region due to the finite $\nabla \times (\bar{u} \times \bar{B})$ where the magnetic-field strength varies.

For the case of the fusion reactor to be considered shortly, the heat pipes are envisioned as being completely within the uniform magnetic field. The conventional end loss does not arise for this case. However, there is a small loss associated with the addition (or removal) of liquid due to condensation (or evaporation). Because of the variable mass flow, the liquid velocity will change along the length of the heat pipe, assuming constant flow area. This causes a finite $\nabla \times (\bar{u} \times \bar{B})$ even when the magnetic-field strength B is uniform. This nonuniform $\bar{u} \times \bar{B}$ can drive eddy currents analogous to those in the end regions. However, these eddy currents should be very weak since the velocity and hence $\bar{u} \times \bar{B}$ decay slowly to zero over the entire length of the condenser or evaporator section.

Vapor-Flow Pressure Drop

The vapor flow in a heat pipe is characterized by mass addition in the evaporator region and mass removal in the condenser region. The axial pressure drop in the vapor is the result of three effects: the magnetic effects, the viscous effects, and the momentum effects due to mass addition or removal.

For the usual operating temperatures and pressures of heat pipes using metallic working fluids, the magnetic effects on the vapor-flow pressure drop are negligible. The two remaining effects due to viscosity and momentum changes are strongly coupled in that the mass addition to or removal from the vapor changes the velocity profile and hence the viscous shear at the wall. The flow regime of primary interest for the application to fusion reactors is the high-heat-flux regime. This implies that the axial Reynolds number is above the turbulent-flow transition value of about 2300 for most of the heat-pipe length and that the radial Reynolds number is much larger than unity. In this flow regime momentum effects dominate viscous effects.

There are some excellent experimental results in this flow regime by Olson and Eckert [13] for turbulent flows in porous circular pipes with uniform injection. Tests were run with both fully developed turbulent entrance flows and flows with zero entrance velocity at the upstream end (much like a heat-pipe evaporator section). The pertinent results are summarized in Fig. 6, which shows the nondimensionalized pressure gradient as

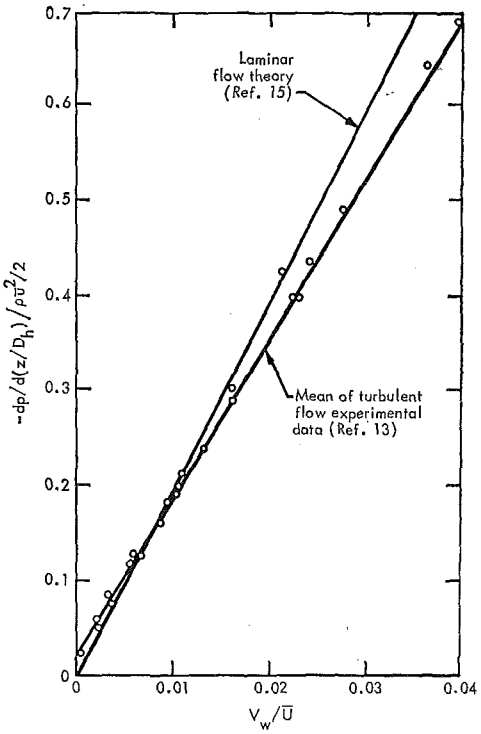

Fig. 3 Local dimensionless axial pressure gradient in porous tube with injection as a function of local injection rate; data include flow with zero entrance velocity

a function of the ratio of the local injection velocity at the wall v_w to the average local axial velocity $\bar{u}$. For ratios of $v_w/\bar{u}$ greater than about 0.005, the pressure gradient is accurately represented by

$$\frac{dp}{dz} = -C_p\left(\frac{\rho_v\bar{u}^2}{2}\right)\left(\frac{1}{D_h}\right)\left(\frac{v_w}{\bar{u}}\right) \tag{3}$$

where C_p is between 17.5 and 18.3, $\bar{u}(z)$ is the local average axial (z direction) flow velocity, and v_w is the uniform injection velocity at the wall. Additional experimental data by Wageman and Guevara [14] in closed-end porous tubes are available. Their experiments were also run in the turbulent-flow regimes with high radial Reynolds numbers and yielded a $C_p \approx 19.8$ for uniform injection.

Wageman and Guevara also ran a series of experiments in the turbulent-flow regime with uniform suction, which simulates the heat-pipe condenser region. They found a $C_p \approx 7.8$ for this case.

An exact solution of the Navier–Stokes equations for the laminar-flow case is given by Knight and McInteer [15]. In the limit when the momentum effects dominate the viscous effects, they find the following expressions for the axial pressure gradient between semi-infinite parallel porous plates with uniform injection or suction:

injection:

$$\frac{dp}{dz} = -2\pi^2\left(\frac{\rho_v\bar{u}^2}{2}\right)\left(\frac{1}{D_h}\right)\frac{v_w}{\bar{u}} \tag{4a}$$

suction:

$$\frac{dp}{dz} = -8\left(\frac{\rho_v\bar{u}^2}{2}\right)\frac{1}{D_h}\frac{v_w}{\bar{u}} \tag{4b}$$

It is interesting to note that these theoretical solutions for laminar flow yield results very close to the turbulent-flow experiments (see Fig. 3). This tends to support the idea that at high radial Reynolds numbers where momentum effects dominate, neither the flow regime nor the channel shape are important in determining the axial pressure drop. In order for momentum effects to dominate, we require that $\mathrm{Re}_{v(\mathrm{rad})} \equiv (\rho_v v_w D_h/\eta_v) \gg 1$.

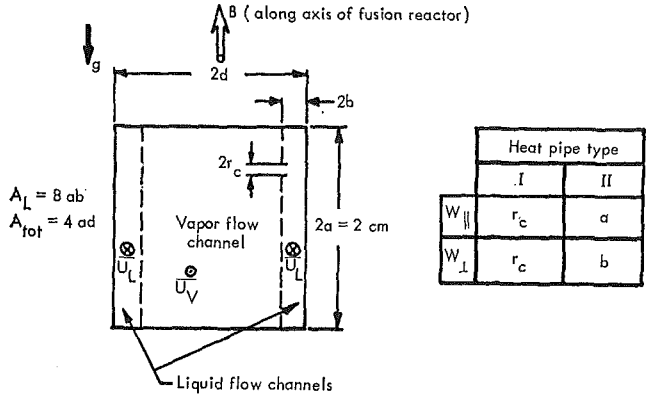

Fig. 4 Heat-pipe cross section looking radially inward toward center of reactor

In the following numerical examples we will use the results of the turbulent-flow experiments to calculate the vapor-flow pressure drop. The following pressure-drop relations are found by integrating equation (3):

evaporator:

$$\Delta p_v = -\frac{C_{PE}}{16}\frac{{q_{\max}}^2}{\rho_v\left(1-\frac{A_L}{A_{\mathrm{tot}}}\right)^2 L^2} \qquad \text{(pressure drop)} \tag{5}$$

condenser:

$$\Delta p_v = +\frac{C_{PC}}{16}\frac{{q_{\max}}^2}{\rho_v\left(1-\frac{A_L}{A_{\mathrm{tot}}}\right)^2 L^2} \qquad \text{(pressure rise)} \tag{6}$$

where $q_{\max}$ is the maximum axial heat flux divided by the total heat-pipe cross-sectional area, A_{tot}, and A_L is the liquid-flow-passage cross-sectional area. We will take $C_{PE} \cong 20$ and $C_{PC} \cong 8$.

Heat-Pipe Application in Magnetic-Field Environment

Figure 4 shows the cross section of a heat pipe which might be used in the blanket of a controlled fusion reactor (the reactor axis is envisioned to be oriented in the vertical direction). The purpose of the heat pipe would be to transfer heat radially outward (out of the paper) from the inner zones of the blanket and thus average the power density [1]. The applied magnetic field is vertically upward as shown in the figure. The heat-pipe axial-vapor-flow direction is out of the paper; the axial liquid flow is into the paper. The dimension a is held constant at 1 cm. Liquid and total cross-sectional areas are computed as indicated in the figure.

The maximum fluid circulation in the heat pipe and hence the maximum heat-transfer capability are calculated by requiring that

$$|\Delta P_L| + |\Delta P_v| = \Delta P_{\mathrm{cap}} \tag{7}$$

where ΔP_{cap} is the pressure rise due to capillary pumping and ΔP_L and ΔP_v are the pressure drops in the liquid and vapor, respectively. The capillary pumping term may be written

$$\Delta P_{\mathrm{cap}} = \frac{2\gamma\cos\theta}{r_c} \tag{8}$$

where γ is the surface tension of the liquid, θ is the wetting angle (taken to be zero on the basis of experiments on high-performance heat pipes [16]), and r_c is the capillary pore radius. The liquid-pressure-drop term ΔP_L is found by integrating equation (2)

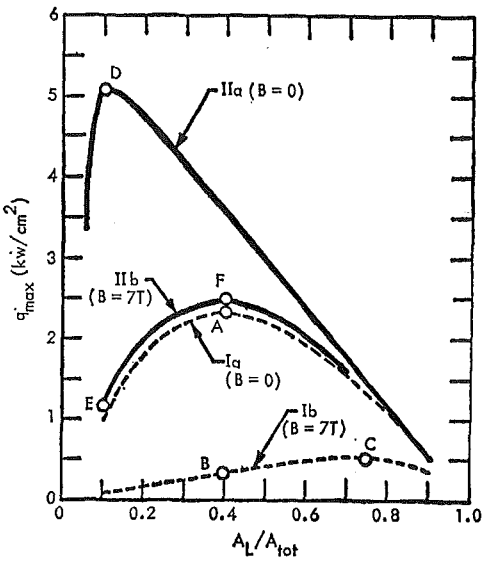

Fig. 5 Performance of Type I and Type II heat pipes with and without an applied magnetic field; C = 0.001

over the length of the pipe. For uniform heat addition and removal (mass flow varies linearly with distance) this gives

$$|\Delta P_L| = \frac{\eta_L l q_{max}}{2w_{\parallel}^2 \rho_L L \epsilon A_L/A_{tot}} \times \left[\frac{H^2 \tanh H}{H - \tanh H} - 3 + P\left(H = 0, \frac{w_\perp}{w_{\parallel}}\right) + \frac{H^2 C}{1 + C}\right] \quad (9)$$

where ϵ is the void fraction of the liquid-flow area (approaches unity for a Type II heat pipe; less than unity for a Type I heat pipe because of the capillary pore structure). The vapor-pressure-drop term ΔP_v is given by the sum of equations (5) and (6). These relations are substituted into equation (7) and the resulting equation is solved for q_{max}.

It is assumed in this solution that vapor and liquid pressure equality exists at the condenser end of the heat pipe. Thus, equation (7) is written for the total length of the heat pipe. In some cases this model can result in a calculated value of $p_v/p_L < 1$ at the evaporator–condenser interface. This implies a meniscus profile bulging into the vapor region. It is argued in [17] that this result is unrealistic and that for these cases vapor and liquid pressure equality should be assumed to exist at the evaporator–condenser interface. Then equation (7) is written for only the evaporator portion of the heat pipe. Calculations were made for this alternative model for the cases where it was appropriate, but the effects on optimum A_L/A_{tot} and maximum q_{max} were found to be small.

Numerical Example

Equation (7) has been solved for a series of heat-pipe designs. These designs will be described and compared in the following paragraphs. All the designs have the following characteristics in common. They are assumed to employ sodium at 1000 deg K as the heat-pipe working fluid. All the sodium properties (listed in Table 1) were taken from [18], except for ρ_v and γ which were taken from [19, 20] respectively. All heat pipes are assumed to have a total length $l = 1$ m and a height in the B field direction $2a = 2$ cm, see Fig. 4.

For the Type I heat-pipe designs, the simple wick structure has a single average capillary pore radius $r_c = 0.01$ cm. This wick structure is assumed to have a void fraction $\epsilon = 0.8$, but tortuosity is neglected giving the flow passages an effective length of 1 m. The average aspect ratio of these liquid-flow passages is taken to be unity, so the ordinary laminar-pressure-drop parameter $P_u(H = 0) \approx 7.11$, assuming roughly square flow passages.

Table 1 Properties of sodium at 1000 deg K

Property	Symbol	Value
liquid density	ρ_L	780.0 kg/m^3
vapor density	ρ_v	0.0611 kg/m^3
liquid viscosity	η_L	1.8×10^{-4} newton-sec/m^2
heat of vaporization	L	4.07×10^6 joule/kg
electrical conductivity of liquid	σ	2.5×10^6 mho/m
surface tension	γ	0.13 newton/m

For this fixed aspect ratio, the solution of equation (7) for q_{max} is dependent only on the area ratio A_L/A_{tot}, and not on the areas themselves. The wick fills the area $A_L = 8ab$, shown as the liquid-flow channels in Fig. 4.

In general, an optimum pore size exists for a Type I heat pipe. For zero magnetic field it can be shown that for the present case

$$r_{c(opt)} = 0.00876 \left(\frac{1 - A_L/A_{tot}}{A_L/A_{tot}}\right)^{2/3} \text{cm}$$

which varies from 0.038 cm at $A_L/A_{tot} = 0.1$ to 0.0020 cm at $A_L/A_{tot} = 0.9$. The latter value is rather small for a practical high-porosity capillary structure. For this reason and also to simplify comparison with Type II heat pipes, r_c was held constant at the intermediate value of 0.01 cm. For the case of large magnetic field the mathematical optimum r_c is extremely small and q_{max} is very insensitive to off-optimum variations, so again r_c was held constant at 0.01 cm.

The performance of heat pipe Type Ia was calculated assuming H = 0 (i.e., $B = 0$). As can be seen from the appropriate dashed curve of Fig. 5, there is an entire family of designs for different ratios A_L/A_{tot}. The optimum design, labeled point A, occurs at an area ratio of 0.40 and yields a maximum axial heat flux of 2.35 kw/cm^2.

The performance of a second family of heat pipes, Type Ib, was calculated including the magnetic pressure drop for $B = 7$ tesla and a typical wall conductance ratio $C = 0.001$. If the heat pipe of point A is operated in this magnetic field it will have the performance shown by point B on the second dashed curve in Fig. 5. That is, for $A_L/A_{tot} = 0.40$, the q_{max} attainable drops from 2.35 to 0.33 kw/cm^2 due to the magnetic pressure drops. If the new optimum heat pipe with the larger area ratio of 0.75 is used, a disappointingly small increase in q_{max} to 0.54 kw/cm^2 is achievable (point C). The conclusion from this example is that Type I heat pipes suffer extremely large performance penalties when operated in strong magnetic fields, even when optimized for these field conditions.

Type II heat pipes with compound wicks can reduce the effect of the magnetic pressure losses significantly. For these heat pipes, there are two liquid-flow channels with dimensions $2a \times 2b$ as shown in Fig. 4. The two liquid-flow channels are assumed to be separated from the vapor-flow channel by screens with the same effective pore size as the simple wicks of the Type I heat pipes, namely $r_c = 0.01$ cm. (There is no optimum pore size for a Type II heat pipe—the smaller the better. The value chosen is a reasonable lower limit for practical high-porosity screens.)

The first family of designs, Type IIa, is for $B = 0$. For this case, the aspect ratio of the liquid-flow passages is

$$\frac{w_\perp}{w_{\parallel}} = \frac{b}{a} = \frac{A_{tot}}{8a^2}\frac{A_L}{A_{tot}}$$

The performance capability of the Type IIa heat pipes for $A_{tot} = 3$ cm^2 is shown as the appropriate solid curve in Fig. 5. The best $B = 0$ performance occurs at point D for the design with the rather small $A_L/A_{tot} = 0.10$ and yields a $q_{max} = 5.05$ kw/cm^2. This is more than double the q_{max} for the best Type Ia heat pipe (point A), and demonstrates that compound wick structures are better than simple wicks even with no magnetic-field effects.

A second family of compound-wick heat-pipe designs was calculated for $B = 7$ tesla and $C = 0.001$. (These are labeled

Type IIb in Fig. 5.) If a heat pipe with the optimum $A_L/A_{tot} = 0.10$ for the Type IIa heat pipes is operated under these B field conditions, it yields the performance shown at point E, that is, the q_{max} is now only 1.15 kw/cm², down by more than a factor of four from the $B = 0$ performance of 5.05 kw/cm².

The optimum Type IIb design for operation in the magnetic field (point F) has the larger area ratio of 0.40 and a $q_{max} = 2.50$ kw/cm², which is over twice that obtainable from the original Type IIa design for $A_L/A_{tot} = 0.10$ operating in the same magnetic field (point E). We conclude that it is definitely worthwhile optimizing a compound-wick heat pipe for operation in strong transverse magnetic fields.

For $B = 7$ tesla, the spread between the q_{max} for the best Type Ib heat pipe and the best Type IIb heat pipe is from 0.54 (point C) to 2.50 kw/cm² (point F), or almost a factor of five difference in performance capability. On the other hand, for $B = 0$, the best Type IIa heat pipe (point D) is only twice as good as the best Type Ia heat pipe (point A). It is clear from these calculations that it is even more important to use compound-wick heat pipes in the presence of strong magnetic fields than for applications with no magnetic fields.

It should be noted that the liquid Hartmann number for the Type II heat pipe with $B = 7$ tesla is 8250, so the contributions of the first and last terms of equation (9) to the liquid pressure drop far outweigh the contribution of the ordinary viscous effect which depends on the aspect ratio. Therefore, the Type II solutions for $B = 7$ are essentially functions of only A_L/A_{tot} and not the areas themselves.

However, there is a constraint on A_{tot} due to the requirement for self-priming of the wick if the heat pipe is oriented with respect to the gravity vector as shown in Fig. 4. The requirement that the total height of the wick, $2a$, be wetted in a 1-g gravity field may be stated

$$\frac{\gamma \cos \theta}{b} \geq \rho_L g 2a$$

or, for this example,

$$A_{tot}\ (\text{cm}^2) \leq \frac{0.68}{A_L/A_{tot}}$$

A large part of the magnetic pressure loss in the above examples is due to the currents which return through the conducting wick walls. As a result it would be highly desirable to use a nonconducting wick structure if at all possible. The gains to be made if C can be made to approach zero are illustrated in Fig. 6.

A new family of compound-wick heat pipes, Type IIc, has been designed for $C = 0$ and $B = 7$ tesla. The new optimum is at $A_L/A_{tot} = 0.15$ (point G), which is much smaller than the optimum area ratio for $C = 0.001$ (point F) because the magnetic pressure losses are less severe. The improved q_{max} for $C = 0$ is 4.37 kw/cm², almost twice as large as the best $C = 0.001$ value of 2.50 kw/cm². We conclude that electrically insulating wick structures can be very beneficial in strong magnetic fields.

It should be noted that if it were possible to utilize an electrically nonconducting working fluid, the best performance of the Type II heat pipes would be 5.05 kw/cm² if the other fluid properties remained the same (point D in Fig. 5). That is, a nonconducting working fluid suffers no magnetic pressure losses even if the wick is electrically conducting. However, a nonconducting wick structure can yield a $q_{max} = 4.37$ kw/cm² (point G) even with our electrically conducting working fluid (sodium). Consequently, if we are forced to use metallic working fluids, the effort should be toward developing insulating compound wick structures which permit almost as high a q_{max} capability in high magnetic fields as is obtainable in zero magnetic fields.

As a final example of the detrimental effects of electrically conducting wicks, the additional case of $C = 0.01$ (Type IId heat pipes) has been plotted in Fig. 6 to show the trends. If the wick is this highly conducting, the best possible performance occurs at point H for $A_L/A_{tot} = 0.70$, and only yields a $q_{max} = 0.77$ kw/cm². Once again it is clear that small electrical conductivity of the wick structure (i.e., small C) is an extremely important goal for heat pipes using metallic working fluids and designed to operate in strong magnetic fields.

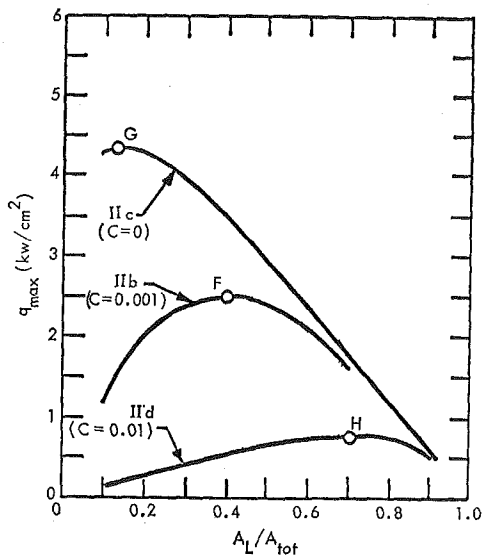

Fig. 6 Performance of Type II heat pipes with a strong applied magnetic field ($B = 7$ tesla) for various wall conductance ratios

Conclusions

The presence of a magnetic field can have a profound effect on both the optimum design and the ultimate performance capability of heat pipes. The following four points must be considered in the design of heat pipes for operation in environments where there are strong magnetic fields:

(*a*) If at all possible, the heat-pipe axis should be aligned with the magnetic field, or an electrically nonconducting heat-pipe working fluid should be used. Either of these solutions will completely eliminate the magnetic pressure drop in the heat-pipe liquid flow.

(*b*) If neither of these ideal solutions is possible, then the magnetic losses may be minimized by using a wick structure with as small a wall electrical conductance as possible. Example calculations show that a factor of five increase in heat-transfer capacity can be realized by decreasing the ratio of wall to liquid conductance C from 0.01 to zero.

(*c*) In all cases (including no magnetic field) the heat-transfer capacity may be increased by using a compound wick structure with large liquid-flow passages to decrease liquid pressure drop. However, the advantage of the compound wick becomes greater with increasing magnetic-field strength. Example calculations show that a compound-wick heat pipe can have five times the heat-transfer capacity of a simple-wick heat pipe for $B = 7$ tesla.

(*d*) In all cases substantial gains in performance may be realized by optimizing the liquid–vapor area apportionment in the heat pipe for the particular magnetic field to be encountered.

In summary, the optimum design for a heat pipe using an electrically conducting working fluid and operating in a strong transverse magnetic field will employ a compound wick structure of as low an electrical conductance as possible. Calculations show that heat pipes with $C = 0.001$ can have maximum axial fluxes in excess of 2 kw/cm² even in the presence of transverse magnetic fields as strong as 7 tesla.

References

1 Werner, R. W., "The Module Approach to Blanket Design—A Vacuum Wall Free Blanket using Heat Pipes," *Proceedings of the International Conference on Nuclear Fusion Reactors*, Culham, England, 1969.

2 Homeyer, W. G., "Thermal and Chemical Aspects of the Thermonuclear Blanket Problem," Technical Report No. 435, Massachusetts Institute of Technology, Cambridge, Mass., June 1965.

3 Sutton, G. W., and Sherman, A., *Engineering Magnetohydrodynamics*, McGraw-Hill, New York, N. Y., 1965.

4 Hughes, W. F., and Young, F. J., *The Electromagnetodynamics of Fluids*, John Wiley & Sons, New York, N. Y., 1966.

5 Chang, C. C., and Lundgen, Th. S., "Duct Flow in Magnetohydrodynamics," *Z.A.M.P.*, Vol. 12, 1961, p. 100.

6 Carlson, G. A., and Hoffman, M. A., "Effect of Magnetic Fields on Heat Pipes," Lawrence Radiation Laboratory Report UCRL-72060, Dec. 1969; ASME Paper No. 70-HT/SpT-10.

7 Chu, W. H., "On MHD Flow in a Rectangular Duct of Arbitrary Conductivity for Arbitrary Hartmann Number," *Journal of Applied Mechanics*, Vol. 36, TRANS. ASME, Series E, Vol. 91, No. 4, Dec. 1969, pp. 702–710.

8 Ihara, S., Tajima, K., and Matsushima, A., "The Flow of Conducting Fluids in Circular Pipes With Finite Conductivity Under Uniform Transverse Magnetic Fields," *Journal of Applied Mechanics*, Vol. 34, TRANS. ASME, Series E, Vol. 89, No. 1, Mar. 1967, pp. 29–36.

9 Loeffler, A. L., Maciulaitis, A., and Hoff, M., "MHD Round Pipe Flow Experiments," USAF Office of Aerospace Research Report ARL 67-0236, 1967.

10 Shercliff, J. A., "Entry of Conducting and Non-Conducting Fluids in Pipes," *Proceedings of the Cambridge Philosophical Society*, Vol. 52, Part 3, 1956, p. 573.

11 Shercliff, J. A., "Edge Effects of Electromagnetic Flowmeters," *Journal of Nuclear Energy*, Vol. 3, 1956, p. 305.

12 Shercliff, J. A., *The Theory of Electromagnetic Flow-Measurement*, Cambridge University Press, 1962.

13 Olson, R. M., and Eckert, E. R. G., "Experimental Studies of Turbulent Flow in a Porous Circular Tube With Uniform Fluid Injection Through the Tube Wall," *Journal of Applied Mechanics*, Vol. 33, TRANS. ASME, Series E, Vol. 88, No. 1, Mar. 1966, pp. 7–17.

14 Wageman, W. E., and Guevara, F. A., "Fluid Flow through a Porous Channel," *Physics of Fluids*, Vol. 3, No. 6, 1960, p. 878.

15 Knight, B. K., and McInteer, B. B., "Laminar Incompressible Flow in Channels with Porous Walls," Los Alamos Scientific Laboratory Report LADC-5309.

16 Kemme, J. E., "Heat Pipe Capability Experiments," Los Alamos Scientific Laboratory Report LA-3585-MS, 1966.

17 Irvine, T. F., Jr., and Hartnett, J. P., eds., *Advances in Heat Transfer*, Vol. 7, Academic Press, New York, N. Y., 1971.

18 Achener, P. Y., Mackewicz, W. V., Fisher, D. L., and Camp, D. C., "Thermophysical and Heat Transfer Properties of Alkali Metals," Nuclear Division, Aerojet-General Corp. Report AGN-8195, Vol. I.

19 Ewing, C. T., Stone, J. P., Spann, J. R., Steinkuller, E. W., Williams, D. D., and Miller, R. R., "High Temperature Properties of Sodium," U. S. Naval Research Laboratory Report NRL-6241, 1965.

20 Taylor, J. W., "Wetting by Liquid Metals," *Progress in Nuclear Energy Series V*, Vol. 2, 1959, pp. 398–416.

R. P. CAREN
Director,
Engineering Sciences,
Lockheed Missiles and Space Co.,
Palo Alto, Calif.

Radiation Energy Density and Radiation Heat Flux in Small Rectangular Cavities

The present paper investigates the impact of one or more small cavity dimensions on the radiation energy density and radiation heat flux in rectangular metallic cavities. The emphasis of the present analysis is the exact treatment of the modal structure of the electromagnetic field in a small cavity in determining the properties of the thermal radiation field in the cavity. The excitation spectrum of the modes is assumed to be given by the Planck distribution function. The Poynting theorem is invoked in order to determine the radiative heat flux absorbed by the walls from the radiation in the cavity. Variation of the dimensions of the rectangular cavity allows the effects of cavity size and shape on the radiant energy density and radiant heat transfer to be assessed, particularly in several interesting limiting cases. It is found that significant deviations from the classical theory occur whenever any of the cavity dimensions satisfy the inequality $lT \leq 1$ cm-deg K. It is further found that, when two or more of the cavity dimensions satisfy the above inequality, the radiant energy density and radiant heat transfer are significantly reduced in comparison to the results of classical theory. However, when only one dimension is limited, as in the case of a closely spaced parallel-surface geometry, the radiant energy density and radiant heat transfer are significantly increased compared to the classical theory.

Introduction

THE CLASSICAL analysis of the radiation density and radiation flux in cavities proceeds from the determination of the discrete spectrum of the normal modes of the electromagnetic field in a cavity with perfectly conducting walls and thence the direct passage to the continuum limit to define the density of normal modes on a spectral basis. The excitation spectrum of the normal modes at a given cavity temperature is determined by the Planck distribution function. The spectral energy density in the cavity is given by the product of the spectral modal density and the Planck distribution function. Using this expression for the spectral modal density, the total energy density, spectral radiation flux and total radiation flux in the cavity, and the spectral and total radiation fluxes absorbed by lossy cavity walls are determined. These classical expressions for the radiation density and radiation transport properties are valid providing that the necessary conditions for the passage to the continuum limit are satisfied. If the spectral properties of the thermal radiation are required, the conditions that must be satisfied for passage to the continuum limit are that the spectral interval of concern satisfy the inequality

$$\frac{\Delta\lambda}{\lambda} \ll 1$$

and that the cavity dimensions satisfy the inequality

$$\frac{\lambda}{l} \ll 1$$

For the total radiation properties the condition that must be satisfied for a valid transition to the continuum limit is that

$$\frac{\lambda}{l} \ll 1$$

where λ refers to the principal wavelength having a significant contribution to the energy density, i.e., those wavelengths for which the Planck distribution function has any significant contribution. Recently several papers have appeared analyzing small spacing effects on radiative heat transfer between metal surfaces at low temperature [1–3].[1] In all cases the continuum limit for the density of normal modes was utilized even though the conditions for its application were violated. These previous analyses are further suspect since they assumed as a point of departure a radiant intensity in the metal based on the Fragstein model [4]. Rytov [5] has shown that the Fragstein model is incorrect and has further placed the theory of the thermal radiation characteristics of metals on a rigorous foundation. The present analysis is the first in a series of three papers intended to place the theory of radiation heat transfer in small cavities on a solid theoretical foundation. Here the effect of the cavity size on the energy density and the radiation heat flux to the cavity walls due to traveling waves will be analyzed for an isothermal cavity.

Contributed by the Heat Transfer Division and presented at the ASME-AIChE Heat Transfer Conference, Tulsa, Okla., August 15–18, 1971. Manuscript received by the Heat Transfer Division April 20, 1971; revised manuscript received September 28, 1971. Paper No. 71-HT-16.

[1] Numbers in brackets designate References at end of paper.

The Hagen–Rubens approximation is used to describe the absorbing characteristics of the cavity walls simply to illustrate that the effect of cavity size on the heat transfer to the walls is determined primarily by cavity-size-effect-induced changes in the radiation energy density in the cavity. The second paper [6] will consider close spacing effects on the heat transfer between metal surfaces at low temperature due to traveling waves. Here the anomalous skin-effect theory will be used to describe the absorption characteristics of the surfaces. A comparison of the results of this analysis to analogous results in the present paper will show that the ratio of the heat flux to the walls in a large cavity to that in a small cavity in the same wall material is almost independent of the model used to describe the absorption characteristics of the walls. This result justifies the use of the Hagen–Rubens approximation (in the present paper) to describe the wall absorptance in order to describe cavity size effects on the heat-transfer characteristics in a nondimensional framework. The final paper [7] in this series will consider the contribution of near surface waves as well as traveling waves to the heat transfer in metal cavities at low temperatures and is based on the rigorous description of the thermally induced electrodynamics of metals developed by Rytov. This latter analysis provides results for the traveling-wave contribution which are identical with the present theory.

In the present paper the impact on radiative heat-transfer effects due to the limited number of normal modes of the radiation field in rectangular metallic cavities is investigated. Case and Chiu have already shown that for a small cubical cavity the radiation density departs substantially from its classical value [8]. In the present analysis, the cavities are assumed to have walls of high conductivity so that the modal structure is not compromised by the presence of strongly absorbing walls. The excitation spectrum of the modes is assumed to be given by the Planck distribution function. The Poynting theorem is invoked in order to determine the energy absorbed by the walls from the radiative field in the cavity. Variation of the dimensions of the rectangular cavity allows the effects of cavity size on the radiant energy density and radiant heat transfer to be assessed, particularly in several interesting limiting cases. These limiting cases include the cubical cavity of small dimensions, a rectangular cavity of two small dimensions, and the cavity of one small dimension. This latter case passes in the limit to an infinite-parallel-surface geometry. Generally, it is found that significant deviations from the classical expressions for radiant energy density and radiant heat transfer occur whenever any of the cavity dimensions satisfies the inequality $lT \lesssim 1$ cm-deg K, where T is the cavity temperature. This means that due to the graininess in the modal structure, the heat transfer departs substantially from the classical value for $l \lesssim 3\lambda_m$. In the present analysis, it is found that when two or more of the cavity dimensions satisfy the above inequality, i.e., $lT \lesssim 1$ cm-deg K, the radiant energy density and radiant heat transfer are sharply reduced in comparison with the results of classical theory. However, where only one dimension is limited, as for example in the case of a closely spaced parallel-surface geometry, the radiant energy density and radiant heat transfer are sharply increased as compared to the classical theory.

Normal Modes of the Radiation Field

Consider the eigenvalues and eigenfrequencies of the electromagnetic field in a vacuum region totally enclosed by rectangular conducting walls [9, 10]. The field equations in the cavity are given by

$$(\nabla^2 + k^2)\begin{Bmatrix}\bar{E}\\ \bar{H}\end{Bmatrix} = 0 \tag{1}$$

where $k^2 = \omega^2/c^2$. If l_1, l_2, and l_3 are the dimensions of the cavity, then it can be readily verified that the electric-field components are

$$\begin{aligned} E_1 &= E_{10} \cos k_1 \sin k_2 y \sin k_3 z e^{-j\omega t} \\ E_2 &= E_{20} \sin k_1 \cos k_2 y \sin k_3 z e^{-j\omega t} \\ E_3 &= E_{30} \sin k_1 \sin k_2 y \cos k_3 z e^{-j\omega t} \end{aligned} \tag{2}$$

where the eigenvalues of the separation parameters needed to satisfy the boundary conditions are

$$k_1 = \frac{n_1\pi}{l_1} \qquad k_2 = \frac{n_2\pi}{l_2} \qquad k_3 = \frac{n_3\pi}{l_3}$$

where n_1, n_2, and n_3 are integers. The allowed eigenfrequencies are given by

$$\frac{\omega^2}{c^2} = k^2 = \pi^2\left[\left(\frac{n_1}{l_1}\right)^2 + \left(\frac{n_2}{l_2}\right)^2 + \left(\frac{n_3}{l_3}\right)^2\right] \tag{3}$$

It is clear from equations (2) that at least two of the integers n_1, n_2, and n_3 must be nonzero in order to have nonvanishing fields. The magnetic fields obtained by use of the Maxwell equation $\nabla \times \bar{E} = j\omega\bar{B}$ automatically satisfy the proper boundary conditions, and are seen to be in time quadrature with the electric fields. This allows the sum of electric- and magnetic-field energies in the cavity to remain constant although the two terms fluctuate separately.

There are, in general, two linearly independent electric-field

Nomenclature

$a = \dfrac{KTl}{\pi\hbar c} = 0.404\,\dfrac{l}{\lambda_m}$, nondimensional length
c = velocity of light, cm/sec
$\bar{E}$ = electric-field vector
$\bar{E}_p$ = electric-field vector polarized in plane of incidence
$\bar{E}_s$ = electric-field vector polarized normal to plane of incidence
$\hbar$ = Planck's constant/2π, J-sec
$\bar{H}$ = magnetic-field vector
$\hat{\imath}_x, \hat{\imath}_y, \hat{\imath}_z$ = unit vectors defining coordinate axes
$\bar{k} = \dfrac{\bar{k}}{|\bar{k}|}\cdot\dfrac{2\pi}{\lambda}$ = electromagnetic-field propagation vector, cm^{-1}
K = Boltzmann constant, J/deg K
l = length of cavity wall, cm
$p(\omega)$ = occupation probability given by Planck distribution function
$\bar{P}(\omega)$ = Poynting flux per mode, w/cm^2
$\bar{P}$ = total Poynting flux, w/cm^2
$\bar{P}_\infty$ = total Poynting flux to wall in infinite cavity, w/cm^2
T = temperature, deg K
$\bar{U}(\omega)$ = energy density per mode, J/cm^3
$\bar{U}$ = total energy density, J/cm^3
$\bar{U}_\infty$ = energy density in an infinite cavity, J/cm^3
V = cavity volume, cm^3
$\alpha(\omega) = 2\sqrt{\dfrac{2\epsilon\omega}{\sigma'}}$ = spectral absorptance of cavity wall
ϵ = electric permittivity of free space, farad/cm
λ = wavelength of electromagnetic wave, cm
λ_m = wavelength of maximum spectral radiant intensity as given by Wien displacement law = $2.898 \times 10^{-1}/T$, cm
μ = magnetic permittivity of free space, henry/cm
φ = azimuth
ρ = electric resistivity of wall, ohm-cm
$\sigma = \dfrac{8\pi^5K^4}{15c^3h^3}$ = Stefan–Boltzmann constant with respect to radiant energy density, J/cm^3 deg K^4
σ' = electric conductivity of wall, mho/cm
θ = colatitude
ω = angular frequency of electromagnetic field, sec^{-1}

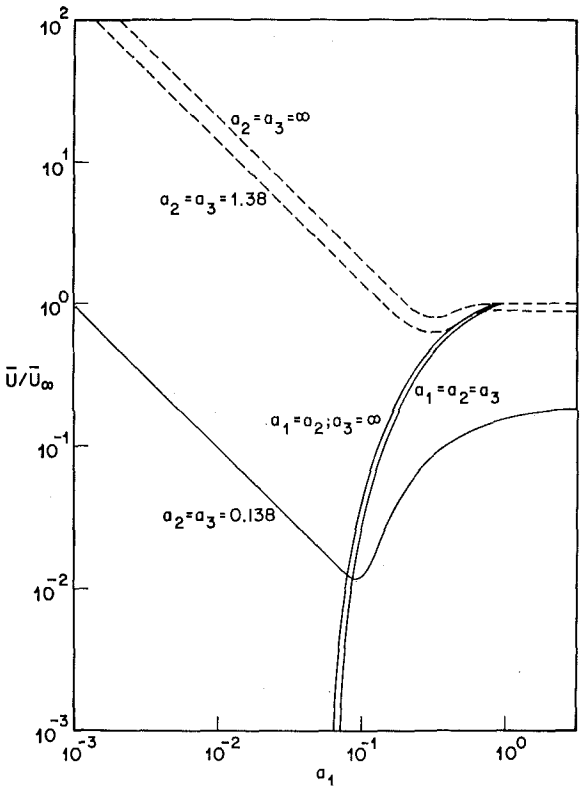

Fig. 1 Energy density in a cavity as a function of cavity size and temperature

vectors for each frequency eigenvalue corresponding to two allowed polarization states. For each of these polarization states the magnitude of the various electric-field components appearing in equations (2) are not independent but satisfy the divergence conditions $\nabla \cdot \bar{E} = 0$, which can be rewritten as

$$k_1 E_1 + k_2 E_2 + k_3 E_3 = 0 \tag{4}$$

The total field in the cavity is a sum over all possible modes of vibration, with intensity factors that depend on the method of excitation. For the thermal radiation field in a cavity the intensity factor is determined by the occupation probability given by the Planck distribution function [11].

$$p(\omega) = \frac{1}{\exp(\hbar\omega/KT) - 1} \tag{5}$$

Energy Density in a Cavity. The total energy density in a cavity is given by a sum of the average energy per normal mode $\hbar\omega p(\omega)$ over all the allowed normal modes of the cavity; $p(\omega)$ is the Planck distribution factor defined in equation (5). Thus, the energy density can be written nondimensionally as

$$\frac{\bar{U}}{\bar{U}_\infty} = \frac{15}{4\pi^5}\frac{1}{a_1 a_2 a_3} \times \sum_{n_1, n_2, n_3=\infty}^{\infty}{}' \frac{(n_1^2/a_1^2 + n_2^2/a_2^2 + n_3^2/a_3^2)^{1/2}}{\exp(n_1^2/a_1^2 + n_2^2/a_2^2 + n_3^2/a_3^2)^{1/2} - 1} \tag{6}$$

with

$$a_i = \frac{KTl_i}{\pi\hbar c}$$

where $\bar{U}_\infty$ is the energy density in a cavity of infinite volume. The prime on the summation occurring in equation (6) and subsequent summations indicates that no more than one of the summation indices is simultaneously zero.

The effects of cavity size on the radiant energy density based on equation (6) are depicted in Fig. 1. It should be noted that size effects are not important until any one of the a values is less than unity. Since $a = 0.404l/\lambda_m$, and from the Wien displacement law $\lambda_m T = 0.2898$ cm-deg K, we have that a value of $a = 1$ corresponds to a wall-dimension–temperature (lT) product of 0.725 cm-deg K. Thus the numerical value of a approximately defines the corresponding value of the lT product expressed in units of cm-deg K. For a cubical box, as the a parameter is lowered, either through reduction of the size or wall temperature of the box, the energy density in the cavity tends to vanish as a becomes smaller than 10^{-1}. The same conclusion also holds for a cavity of two small dimensions and one large dimension. If the a parameters associated with the two small dimensions drop below approximately 10^{-1} while the other a parameter remains large, i.e., $a \gg 1$, the radiant energy density in the cavity still vanishes in a fashion similar to that of a cubical box, albeit in a slower fashion. On the other hand, if two of the dimensions remain finite as the other dimensions are reduced, as in a parallel-plate geometry, the energy density rises drastically as the small dimension tends toward zero. In Fig. 1 this latter effect is shown particularly for a square cavity with one small dimension. As the large dimensions of the box tend toward infinity, the energy density approaches the asymptote given by $\bar{U}/\bar{U}_\infty = 0.184/a_1$ as a function of the small dimension of the box; this is shown in Fig. 1. For the square box with one small dimension, say a_1, then the only significant contribution to the radiant energy density according to equation (6) is for $n_1 = 0$. Hence, in this limit, equation (6) reduces to

$$\frac{\bar{U}}{\bar{U}_\infty} = \frac{15}{4\pi^5}\frac{1}{a_1 a_2^3} \sum_{\substack{n_2, n_3=\infty \\ n_2, n_3 \neq 0}}^{\infty} \frac{(n_2^2 + n_3^2)^{1/2}}{\exp[(n_2^2 + n_3^2)^{1/2}/a_2] - 1} \tag{7}$$

Evaluation of the sum in the above equation using the Poisson summation formula [12] yields in the first order for small values of a_1 the following relationship:

$$\frac{\bar{U}}{\bar{U}_\infty} \approx \frac{1.84 \times 10^{-1}}{a_1} - \frac{7.9 \times 10^2}{a_1 a_2} \tag{8}$$

From equation (8) it follows that for infinite parallel metal surfaces, i.e., $a_2 = a_3 \to \infty$, the radiant energy density at small spacing distances, i.e., $a_1 \ll 1$, departs from the classical value as $U/U_\infty \to 1.84 \times 10^{-1}/a_1$. This asymptote is shown in Fig. 1. This means that in the case of closely spaced metal surfaces of infinite extent, the modal density corresponding to long wavelengths exceeds the classical expression for the density of normal modes in the continuum limit for the electromagnetic radiation field. The physics underlying this behavior will be discussed in the last section of this paper. Where the other dimensions are finite, i.e., a_2 and $a_3 \neq 0$, then the expression for the energy density departs from this asymptotic limit. In particular, when $a_2 = a_3$, equation (8) indicates to the first order the departure for finite surface dimensions of the expression for the energy density from that for infinite parallel surfaces. Equation (8) is consistent with the degree of departure for the data for $a_2 = a_3 = 1.38$ shown in Fig. 1 for small values of a_1 from the asymptotic limit of infinite surfaces. However, equation (8) does not extend as far as the case $a_2 = a_3 = 0.138$, data for which are also shown in Fig. 1. For the case of the cubical cavity, equation (6) reduces to

$$\frac{\bar{U}}{\bar{U}_\infty} \approx \frac{1.2 \times 10^{-2}}{a^4} \sum_{n_1, n_2, n_3=-\infty}^{\infty}{}' \frac{(n_1^2 + n_2^2 + n_3^2)^{1/2}}{\exp[(n_1^2 + n_2^2 + n_3^2)^{1/2}/a] - 1} \tag{9}$$

For $a_1 \lesssim 10^{-1}$, this above expression reduces to

$$\frac{\bar{U}}{\bar{U}_\infty} \approx \frac{5.1 \times 10^{-2}}{a^4} e^{-1.41/a} \tag{10}$$

This expression closely fits the more exact numerical results developed in Fig. 1 for the case of the cubical cavity for small values of a. Returning to equation (6) for the cavity of one large

dimension, we let a_1 and a_2 tend toward zero with $a_1 = a_2$, while keeping a_3 finite, i.e., $a_3 \gg 1$; then for the limiting case we choose terms from equation (6) for which $n_3 \neq 0$. Further, the principal contribution for these latter parameters will be limited to $n_1 = \pm 1$ or $n_2 = \pm 1$. Thus equation (6) reduces to

$$\frac{\bar{U}}{\bar{U}_\infty} \approx \frac{15}{\pi^5 a_1^2 a_3} e^{-1/a_1} \sum_{\substack{n_3=-\infty \\ n_3 \neq 0}}^{\infty} \left(\frac{1}{a_1^2} + \frac{n_3^2}{a_3^2}\right)^{1/2} e^{-|n_3|/a_3} \quad (11)$$

Since a_3 is of "reasonable" size, in order to assess the value of this latter sum it is necessary to carry out the summation in a complete fashion. Utilizing the Poisson summation formula for evaluation of this sum, the following asymptotic expression results:

$$\frac{\bar{U}}{\bar{U}_\infty} \approx \frac{9.66 \times 10^{-2}}{a_1^3} e^{-1/a_1} \quad (12)$$

Heat Flux Absorbed by a Cavity Wall

Now that we have established the magnitude and the behavioral characteristics of the radiation energy density in small cavities as a function of cavity size and shape, we turn to the question of the radiation flux absorbed (or equivalently, emitted) by the cavity walls. In order that the presence of absorbing walls does not modify the structure of the normal modes appreciably, we assume that the spectral-absorption coefficient $\alpha(\omega)$ of the walls is low, i.e., the walls have a high conductivity. We will, in fact, utilize the Hagen–Rubens approximation to describe the spectral absorption of the walls, i.e.,

$$\alpha(\omega) = 2\sqrt{\frac{2\epsilon\omega}{\sigma'}} \quad (13)$$

To find the power loss from each mode to a cavity wall, we must compute the time average of the Poynting flux corresponding to this mode over the area of the wall. The Poynting flux is given by [13]

$$P = \frac{1}{2}\sqrt{\frac{\mu\omega}{2\sigma'}} H^2_{\tan} \quad (14)$$

where $H_{\tan}$ is the crest value of the tangential component of the magnetic field at the surface. The magnetic-field vector is related to the electric-field vectors [see equations (2)] through the Maxwell equation $\bar{H} = \frac{1}{j\omega\mu} \nabla \times \bar{E}$. If we take the cavity wall on which the power loss is to be evaluated to be the y–z plane at $x = 0$, then the tangential components of $\bar{H}$ are given by

$$\bar{H}_{\tan} = \frac{1}{j\omega\mu}\left\{\hat{\imath}_y\left(\frac{\partial E_1}{\partial z} - \frac{\partial E_3}{\partial x}\right) + \hat{\imath}_z\left(\frac{\partial E_2}{\partial x} - \frac{\partial E_1}{\partial y}\right)\right\} \quad (15)$$

and utilizing equations (2) in equation (15), it follows that

$$\bar{H}_{\tan}\cdot\bar{H}^*_{\tan} = \frac{1}{\omega^2\mu^2}[(k_3E_{10} - k_1E_{30})^2 \sin^2 k_2 y \cos^2 k_3 z + (k_1E_{20} - k_2E_{10})^2 \cos^2 k_2 y \sin^2 k_3 z] \quad (16)$$

The average value of the Poynting flux into the wall is therefore given by

$$\bar{P}(\omega) = \frac{1}{2}\sqrt{\frac{\mu\omega}{2\sigma'}}\frac{1}{l_2 l_3}\int_0^{l_3}\int_0^{l_2} \bar{H}_{\tan}\cdot\bar{H}^*_{\tan}\, dydz = \frac{1}{8\omega^2\mu^2}\sqrt{\frac{\mu\omega}{2\sigma'}}[(k_3E_{10} - k_1E_{30})^2 + (k_1E_{20} - k_2E_{10})^2] \quad (17)$$

This gives the average energy flow into the wall at $x = 0$ per unit area per unit time for a normal mode having the electric-field components E_{10}, E_{20}, E_{30} [see equations (2)] and a propagation vector having components k_1, k_2, k_3. Consider the coordinate system in which polarization states are referred to the plane defined by the propagation vector $\bar{k}$ and the x axis. The electric-field vector for one polarization state, $\bar{E}_s$, is defined to be normal to this plane, whereas the electric-field vector for the second polarization state, $\bar{E}_p$, is contained within this plane. Substituting the components of the electric-field vectors and propagation vector as defined by this coordinate system into equation (19), the average Poynting flux for the two polarization states is given by

$$\bar{P}(\omega)_s = \frac{1}{2}\sqrt{\frac{\mu\omega}{2\sigma'}}\cdot\frac{1}{4\omega^2\mu^2}|\bar{E}_{0s}|^2 k_1^2$$
$$\bar{P}(\omega)_p = \frac{1}{2}\sqrt{\frac{\mu\omega}{2\sigma'}}\cdot\frac{1}{4\omega^2\mu^2}|\bar{E}_{0p}|^2|\bar{k}|^2 \quad (18)$$

The spectral energy density associated with a given normal mode is simply

$$U(\omega) = \frac{1}{V}\frac{\epsilon}{2}\int_0^{l_3}\int_0^{l_2}\int_0^{l_1}\{|\bar{E}_s|^2 + |\bar{E}_p|^2\}dxdydz = \frac{1}{16}\epsilon\{|\bar{E}_{0s}|^2 + |\bar{E}_{0p}|^2\} \quad (19)$$

where equations (2) have been used to evaluate the integral. Further, the spectral energy densities associated with each polarization state in the mode are equal; thus, we may write

$$U(\omega) = \frac{1}{8}\epsilon|\bar{E}_{0s}|^2 = \frac{1}{8}\epsilon|\bar{E}_{0p}|^2 \quad (20)$$

Now if we denote the average Poynting flux associated with a given mode into the wall at $x = 0$ by $P(\omega)$, then $\bar{P}(\omega) = \bar{P}(\omega)_s + \bar{P}(\omega)_p$, and utilizing equation (13), equation (18), and equation (20), we may write

$$\bar{P}(\omega) = \frac{1}{4}(1 + k_1^2/|\bar{k}|^2)\alpha(\omega)cU(\omega) \quad (21)$$

The total Poynting flux is simply the sum of the spectral Poynting fluxes over the normal modes; using equations (6), (14), and (21) this total Poynting flux is therefore given by

$$\bar{P} = \sum_\omega \bar{P}(\omega) = \frac{15}{8\pi^5}\sqrt{\frac{2\epsilon}{\sigma'}}\frac{c}{a_1a_2a_3} \times \left[\sum_{n_1,\,n_2,\,n_3=-\infty}^{\infty}{}' \frac{(n_1^2/a_1^2 + n_2^2/a_2^2 + n_3^2/a_3^2)^{3/4}}{\exp(n_1^2/a_1^2 + n_2^2/a_2^2 + n_3^2/a_3^2)^{1/2} - 1} + \sum_{n_1,\,n_2,\,n_3=-\infty}^{\infty}{}' \frac{(n_1^2/a_1^2)(n_1^2/a_1^2 + n_2^2/a_2^2 + n_3^2/a_3^2)^{-1/4}}{\exp(n_1^2/a_1^2 + n_2^2/a_2^2 + n_3^2/a_3^2)^{1/2} - 1}\right] \quad (22)$$

Equation (22) may be written in complete nondimensional form in terms of the parameter $\bar{P}/\bar{P}_\infty$, where $\bar{P}_\infty$ is the radiant heat flux absorbed by a wall in a cavity of large dimensions, i.e., $\bar{P}_\infty = 0.766\sqrt{\frac{T}{\sigma'}}\cdot\frac{c\sigma T^4}{4}$; thus we have

$$\frac{\bar{P}}{\bar{P}_\infty} = \frac{0.482}{a_1a_2a_3} \times \left[\sum_{n_1,\,n_2,\,n_3=-\infty}^{\infty}{}' \frac{(n_1^2/a_1^2 + n_2^2/a_2^2 + n_3^2/a_3^2)^{3/4}}{\exp(n_1^2/a_1^2 + n_2^2/a_2^2 + n_3^2/a_3^2)^{1/2} - 1} + \sum_{n_1,\,n_2,\,n_3=-\infty}^{\infty}{}' \frac{(n_1^2/a_1^2)(n_1^2/a_1^2 + n_2^2/a_2^2 + n_3^2/a_3^2)^{-1/4}}{\exp(n_1^2/a_1^2 + n_2^2/a_2^2 + n_3^2/a_3^2)^{1/2} - 1}\right] \quad (23)$$

The effects of cavity size on the radiant heat flux absorbed by the wall are shown in Fig. 2. The data are presented in terms of

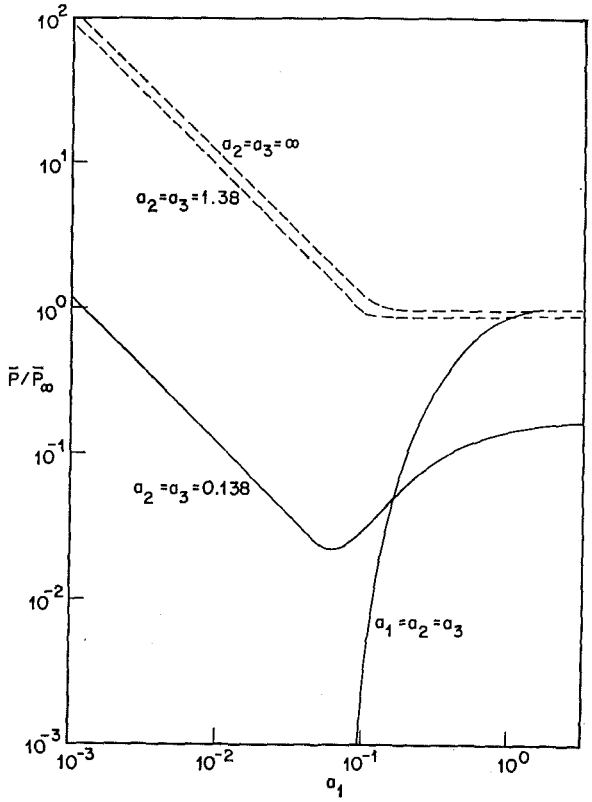

Fig. 2 Radiant heat flux to a cavity wall as a function of cavity size and temperature

the nondimensional heat flux absorbed by the cavity walls $\bar{P}/\bar{P}_\infty$ as a function of the nondimensional cavity size. For the square cavity with one small dimension, say a_1, then the only significant contribution to equation (23) is for $n_1 = 0$. Hence, in this limit, equation (23) reduces to

$$\frac{\bar{P}}{\bar{P}_\infty} \approx \frac{4.87 \times 10^{-3}}{a_1 a_2 a_3} \left\{ \sum_{n_2,\, n_3 = -\infty}^{\infty} \frac{(n_2^2/a_2^2 + n_3^2/a_3^2)^{3/4}}{\exp\,(n_2^2/a_2^2 + n_3^2/a_3^2)^{1/2} - 1} - 2 \sum_{n_2 = -\infty}^{\infty} \frac{|n_2|^{3/2}/a_2^{3/2}}{\exp\,[|n_2|/a_2] - 1} \right\} \quad (24)$$

where $a_2 = a_3$ are the a values corresponding to large dimensions of the cavity. Utilizing the Poisson summation formula, equation (24) reduces in the first order to

$$\frac{\bar{P}}{\bar{P}_\infty} \approx \frac{0.115}{a_1} - \frac{0.0338}{a_1 a_2} \quad (25)$$

For parallel metal surfaces of infinite extent, i.e., $a_2 \gg a_1$, this provides the asymptotic limit for the radiant heat transfer for small values of a_1, i.e., $a_1 \ll 0.1$ as $\bar{P}/\bar{P}_\infty \approx 0.11/a_1$. This limit is depicted in Fig. 2 as the dotted line. For finite values of the parameters a_2 and a_3 associated with the major dimensions of the cavity, equation (25) provides to first order a description of the nature of the deviation of the heat transfer from that associated with parallel surfaces of infinite extent.

Consider next a cavity of one large dimension. This dimension can either lie along the surface to which the heat flux is being computed, i.e., l_2 or l_3, or may correspond to the dimension normal to this surface, i.e., l_1. We shall consider both these cases. First, consider a_1, i.e., l_1, to be finite while a_2 and a_3, with $a_2 = a_3$, are allowed to tend toward zero. From equation (23) we note the principal contributions come from terms for which $n_1 \neq 0$; also, we should limit ourselves to terms for which either $n_2 \neq 0$ or $n_3 \neq 0$, and here the principal contribution will be for $n_2 = \pm 1$ and $n_3 = \pm 1$. Utilizing these assumptions and the Poisson summation formula, to first order equation (23) becomes

$$\frac{\bar{P}}{\bar{P}_\infty} \approx \left(\frac{3.86 \times 10^{-2}}{a_2^{3.5}} - \frac{1.93 \times 10^{-2}}{a_2^{3.5} a_1} + \frac{9.26 \times 10^{-2}}{a_2^{1.5} a_1^2} \right) e^{-1/a_2} \quad (26)$$

Consider now the case in which a_2 is finite (i.e., l_2 is finite), a_1 and a_3 are small, and $a_1 = a_3$. The principal contribution to the radiant heat transfer will come from terms for which $n_2 \neq 0$ and for which either $n_1 \neq 0$ or $n_2 \neq 0$; again the principal contributions for these latter factors can be limited to $n_1 = \pm 1$ and $n_3 = \pm 1$. Utilizing these assumptions and the Poisson summation formula, to first order equation (23) becomes

$$\frac{\bar{P}}{\bar{P}_\infty} \approx \left(\frac{5.784 \times 10^{-2}}{a_1^{3.5}} - \frac{2.892 \times 10^{-2}}{a_2 a_1^{3.5}} \right) e^{-1/a_1} \quad (27)$$

Note that in equation (26) $a_2 = a_3$ are the small dimensions of the cavity, whereas in equation (27) $a_1 = a_3$ are the small dimensions of the cavity. Then it is clear to the first order (ignoring a factor of 1.5) that for a cavity of two small dimensions, whether both small dimensions form the wall to which the heat flux is computed or whether only one small dimension is along this wall, the heat flux is almost identical in both cases.

Where all the cavity dimensions are small, i.e., $a_1 = a_2 = a_3$ and $a_1 \to 0$, the principal terms in equation (23) are for $n_1 = \pm 1$, $n_2 = \pm 1$, or $n_1 = \pm 1$, $n_3 = \pm 1$, or $n_2 = \pm 1$, $n_3 = \pm 1$. Under these conditions, equation (23) reduces to

$$\frac{\bar{P}}{\bar{P}_\infty} \approx \frac{9.8 \times 10^{-2}}{a_1^{4.5}} e^{-1.41/a_1} \quad (28)$$

Discussion

We have considered the energy density and flux of thermal radiation to the walls of small metallic rectangular cavities. The assumption of a cavity with metal walls of high conductivity was made to insure that well-defined normal modes of the electromagnetic field constituting the thermal radiation field in the cavity should be present. The principal point of departure in these analyses from the classical blackbody radiation theory is the exact treatment of the discrete spectrum of normal modes occurring in the cavity rather than passing to the continuum limit for the density of normal modes as is done in classical theory. These departures from the results of classical theory take place whenever any one of the cavity dimensions satisfies the inequality $lT \leq 1$ cm-deg K. This criterion can also be written in terms of the wavelength of maximum spectral emission for classical blackbody radiation as given by the Wien displacement law. Then the above inequality becomes $l \leq 3\lambda_m$.

The total radiation energy density in a cavity is determined by a sum of the average energy per normal mode $\hbar\omega p(\omega)$ over the normal modes of the cavity. The resulting expression for the radiation energy density in a rectangular cavity is investigated in several cases as one or more of the cavity dimensions tends toward zero: the cubical cavity, the cavity of two small and one large dimension, and the cavity of one small and two large dimensions. The latter case is also considered where the two large dimensions tend to infinity; in this limit, it constitutes a two-dimensional infinite-parallel-surface geometry.

From equation (3), we have that the wavelength corresponding to a particular normal mode is given by

$$\lambda_{n_1, n_2, n_3} = \frac{2}{\sqrt{n_1^2/l_1^2 + n_2^2/l_2^2 + n_3^2/l_3^2}} \quad (29)$$

and, further, the eigenfunctions for the electromagnetic field in the cavity are restricted such that two or more of the integers n_1, n_2, and n_3 must be nonzero. This means that for a cubical cavity where $l = l_1 = l_2 = l_3$ the maximum or cutoff wavelength for the cavity is given by $\lambda_{max} = \sqrt{2}\, l$. Thus, to a first approximation, the radiation energy density in the cavity may be computed assuming a continuum density of normal modes given by the Jeans'

number with a cutoff wavelength of $\sqrt{2}\,l$; hence,

$$\bar{U} \approx 16\pi^2\hbar c \int_0^{\sqrt{2}\,l} \frac{d\lambda}{\lambda^5[\exp 2\pi\hbar c/\lambda KT - 1]}$$

$$\approx 1.5 \times 10^{-2}\bar{U}_\infty \int_{\sqrt{2/a}}^{0} \frac{\xi^4 d\xi}{[\exp \xi - 1]} \quad (30)$$

In the asymptotic limit where $a \ll 1$, an integration by parts of the integral in equation (30) results in the following expression:

$$U/U_\infty \approx \frac{1.5 \times 10^{-2}}{a^4}\, e^{-1.41/a} \quad (31)$$

This expression is in substantive agreement with the more exact expression developed in equation (10). Again, for the cavity of two very small dimensions ($l = l_1 = l_2$) and one large dimension, the cavity cutoff wavelength predicted by equation (29) is $2l$. Thus, one would anticipate an expression very similar to the above for the variation in the energy density with respect to the classical expression for the energy density, with the principal difference being that because of the difference in cutoff wavelength, the argument for the exponential factor would be $-1/a$ instead of $-1.41/a$. The validity of these arguments is demonstrated in the expression for the asymptotic limit for the energy density in a rectangular cavity of two small dimensions given by equation (12).

Now consider the radiant energy density in a rectangular cavity having two large dimensions, l_2 and l_3, and one small dimension, l_1. Assume further that the temperature of the cavity is such that $\lambda_m \gg l_1$. Under these conditions, it follows from equation (29) that all modes for which $n_1 \neq 0$ essentially do not contribute to the thermal energy density since $\lambda_{n_1,n_2,n_3} \ll \lambda_m$. Thus the modes that do contribute to the thermal energy density under these conditions are those for which $n_1 = 0$. There are a large number of such modes, since for large values of l_2 and l_3 there will be a large number of combinations of integers for which $\lambda_{0,n_2,n_3} \approx \lambda_m$. Under these conditions, as the small dimension l_1 of the box tends toward zero, the number and therefore the total energy associated with these modes remains fixed, yet the volume containing this total radiant energy decreases as l_1 and thus the corresponding energy density increases as $1/l_1$. Since the breakpoint for the departure from the classical expression for the energy density should occur where $l_1 \approx \lambda_m$, we should expect for small values of l_1 or a_1 that

$$\bar{U} \approx \bar{U}_\infty \frac{\lambda_m}{l_1} \quad \text{or} \quad \approx \frac{0.4}{a_1}\,\bar{U}_\infty \quad (32)$$

where we have utilized the Wien displacement law to arrive at the final expression in equation (34). This latter estimate is in good agreement with the exact expression given by equation (8) for the asymptotic limit of the energy density between closely spaced infinite metal surfaces.

To compute the net heat transfer to the cavity walls, the Hagen–Rubens approximation has been utilized to illustrate cavity size effects on the heat flux absorbed by the walls. The power absorbed by the wall for each normal mode is computed utilizing the Poynting theorem to compute the fraction of the modal power flow to the wall that is absorbed by the wall. This consideration none too surprisingly shows that the power absorbed by the cavity wall for each normal mode is related in a simple fashion to the modal energy density. This relationship is provided by equation (21). A sum of the power absorbed by the wall for each normal mode over all normal modes results in an exact expression for the total radiant heat flux absorbed by a cavity wall and is given by equation (23). Since equation (21) shows that the modal power flow into a cavity wall is related directly to the modal radiant energy density in the cavity, it is clear that the total radiant heat flux to a cavity wall should roughly reflect the cavity size effects on the total radiant energy density. This is evident from a comparison of the results for the cavity radiant energy density and the radiant heat flux to the walls illustrated respectively in Figs. 1 and 2.

References

1 Caren, R. P., "The Theory of Electromagnetic Tunneling of Thermal Radiation Between Highly Absorbing Media," *Proceedings of the Fourth Symposium on Thermophysical Properties*, ASME, New York, N. Y., 1968, p. 243.

2 Caren, R. P., and Liu, C. K., "Emission, Total Internal Reflection, and Tunneling of Thermal Radiation in Metals," *Progress in Astronautics and Aeronautics*, Vol. 21, Bevans, ed., Academic Press, New York, N. Y., 1969, p. 509.

3 Boehm, R. F., and Tien, C. L., "Small Spacing Analysis of Radiative Transfer Between Parallel Metallic Surfaces," JOURNAL OF HEAT TRANSFER, TRANS. ASME, Series C, Vol. 92, No. 3, Aug. 1970, pp. 405–411.

4 Fragstein, C. v., "Energy Transfer at the Interface between Two Absorbing Media with an Emphasis on the Heat Radiation in Absorbing Bodies," *Ann. Physik*, Vol. 7, 1950, pp. 63–72.

5 Rytov, S. M., *Theory of Electrical Fluctuations and Thermal Radiation*, translated by H. Erkuu, Academy of Sciences Press, Moscow, 1953, AFCRC-TR-59-162, 1959, p. 27.

6 Caren, R. P., "Radiation Heat Transfer between Closely Spaced Metal Surfaces at Low Temperature: The Impact of Discrete Modes of the Radiation Field," JOURNAL OF HEAT TRANSFER, TRANS. ASME, Series C, Vol. 94, No. 3, Aug. 1972, pp. 295–299.

7 Caren, R. P., "Thermal Radiation between Closely Spaced Metal Surfaces at Low Temperature Due to Traveling and Quasi-stationary Components of the Radiation Field," to be published.

8 Case, K. M., and Chiu, S. C., "Electromagnetic Fluctuations in a Cavity," *Phys. Rev. A*, Vol. 1, No. 4, 1970, p. 1170.

9 Condon, E. V., "Principles of Microwave Radio," *Rev. Mod. Phys.*, Vol. 14, 1942, p. 341.

10 Panofsky, W. H. H., and Philips, M., *Classical Electricity and Magnetism*, Addison-Wesley, Cambridge, Mass., 1955, pp. 190–192.

11 Kittel, C., *Elementary Statistical Physics*, John Wiley & Sons, New York, N. Y., 1958, p. 102.

12 Morse, P. M., and Feshbach, H., *Methods of Mathematical Physics*, McGraw-Hill, New York, N. Y., 1953, p. 467.

13 Panofsky and Philips, loc. cit., p. 192.

14 Parker, W. J., and Abbott, G. L., "Theoretical and Experimental Studies of the Total Emittance of Metals," *Symposium on Thermal Radiation of Solids*, S. Katzoff, ed., NASA SP-55, 1965, p. 21.

R. P. CAREN
Director,
Engineering Sciences,
Lockheed Missiles and Space Co.,
Palo Alto, Calif.

Radiation Heat Transfer between Closely Spaced Metal Surfaces at Low Temperature: The Impact of Discrete Modes of the Radiation Field

The present analysis shows that for closely spaced metal surfaces at low temperature, the heat transfer due to traveling waves greatly exceeds the results of classical theory. The origin of this nonclassical behavior is due to the fact that for closely spaced metal surfaces the density of normal modes of the radiation field greatly exceeds Jeans' number. This higher modal density results in a greater than classical energy density in the cavity and thus greater heat transfer. The results of this theory are shown to be consistent with the experiments of Domoto, Boehm, and Tien on heat transfer between closely spaced metal surfaces at low temperatures.

Introduction

THIS PAPER investigates the effect of the discrete modal structure on the propagating portion of the thermal radiation field between closely spaced metal surfaces at low temperature. Limiting the analysis to the propagating portion of the thermal radiation field means that radiation tunneling (evanescent wave) effects [1–3][1] are neglected. The analyses begin with the spectral radiant energy density in a rectangular cavity as developed previously by Case and Chiu [4]. The Poynting theorem is invoked utilizing the approximate expression of Domoto, Boehm, and Tien for the spectral absorptance in the anomalous-skin-effect (ASE) region [5] to compute the flux radiant energy absorbed by a wall in terms of the spectral energy density in the cavity. A summation over all frequencies of this latter expression provides the total radiant flux to a wall. In this expression, two of the dimensions are then allowed to tend toward infinity; the resulting expression represents the heat flux to the wall in an infinite-parallel-surface geometry. From Kirchhoff's law, this latter expression also represents the heat flux emitted by the surfaces. The results show that for close spacing of the two surfaces, i.e., $l_1T \leq 0.1$ cm-deg K, the radiant heat flux emitted by or absorbed by the wall substantially departs from the results of classical theory according to the following prescription:

$$\bar{P}/\bar{P}_\infty = \frac{0.160}{a_1}$$

where numerically

$$a_1 = 1.38 l_1 T$$

if l_1T is expressed in units of cm-deg K.

For metals at low temperature, the ASE theory predicts that the spectral-absorption coefficient for a metal is approximately temperature-independent. As a result of the temperature-independence of the spectral absorptance, a simple relationship can be derived for the net heat transfer between infinite metal surfaces at different temperatures. It predicts heat transfer at small spacing distances that is much greater than the prediction of classical theory, and differs substantially from the results of earlier wave-interference analyses [3] for the freely propagating portion of the thermal radiation field.

The resulting expressions for the net heat transfer agree very well with the measurements of Domoto, Boehm, and Tien [6].

Energy Density

The analysis of Case and Chiu [4] shows that the total spectral energy density associated with both polarization states of a normal mode for thermal radiation in a rectangular cavity with perfectly conducting walls is given by

$$U(\omega) = \frac{1}{4V} \frac{\hbar\omega}{\exp \hbar\omega/KT - 1} \quad (1)$$

where the angular eigenfrequencies are determined by

[1] Numbers in brackets designate References at end of paper.

Contributed by the Heat Transfer Division for publication (without presentation) in the JOURNAL OF HEAT TRANSFER. Manuscript received by the Heat Transfer Division June 7, 1971. Paper No. 72-HT-O.

$$\omega^2 = \frac{(2\pi)^2 c^2}{\lambda^2} \pi^2 c^2 (n_1^2/l_1^2 + n_2^2/l_2^2 + n_3^2/l_3^2) \qquad (2)$$

with n_1, n_2, and n_3 being integers varying from plus to minus infinity, but limited such that two or more of the integers cannot be zero simultaneously. This latter restriction follows from the fact that no normal modes of this cavity exist for which two or more of the integers n_1, n_2, or n_3 are zero [7]. The total energy density of the thermal radiation is given by a sum of the spectral energy density over all the allowed normal modes. The resulting expression for the total energy density is

$$\frac{\bar{U}}{\bar{U}_\infty} = \frac{15}{4\pi^5} \frac{1}{a_1 a_2 a_3}$$

$$\times \sum_{n_1, n_2, n_3 = -\infty}^{\infty}{}' \frac{[n_1^2/a_1^2 + n_2^2/a_2^2 + n_3^2/a_3^2]^{1/2}}{\exp [n_1^2/a_1^2 + n_2^2/a_2^2 + n_3^2/a_3^2]^{1/2} - 1} \qquad (3)$$

with $a_i = KTl_i/\pi\hbar c$, and where $\bar{U}_\infty$ is the energy density in a cavity of infinite volume. The prime on the sum in equation (3) indicates the restriction that two or more of the integers cannot be zero simultaneously. If we let a_2 and a_3 tend toward infinity, then n_2/a_2 and n_3/a_3 form a two-dimensional continuum and the sums over n_2 and n_3 in equation (3) can be replaced by integrals with respect to a two-dimensional Jeans' number, i.e.,

$$\sum_{n_2, n_3 = -\infty}^{\infty} \rightarrow 2\pi a_2 a_3 \int n^* dn^*$$

where

$$n^* = \sqrt{n_2^{*2} + n_3^{*2}}$$

$$n_2^* = n_2/a_2$$

$$n_3^* = n_3/a_3$$

In this limit, equation (3) becomes[2]

$$\lim_{a_2, a_3 \rightarrow \infty} \frac{\bar{U}}{\bar{U}_\infty} = \frac{15}{2\pi^4} \frac{1}{a_1} \sum_{n_1 = -\infty}^{\infty} \int_{|n_1/a_1|}^{\infty} \frac{n^2 dn}{\exp n - 1} = \frac{15}{\pi^4} \frac{1}{a_1}$$

$$\times \left\{ \sum_{n_1=1}^{\infty} \sum_{r=0}^{\infty} \frac{2}{(r+1)^2} \Gamma\left[3, (r+1)\frac{n_1}{a_1}\right] + \zeta(3)\Gamma(3) \right\} \qquad (4)$$

Equation (4) is convergent for values of $a_1 < 1$; as such it covers a range of values of a_1 extending from dramatically unclassical behavior of $\bar{U}/\bar{U}_\infty$, i.e., $\bar{U}/\bar{U} \gg 1$ for $a_1 \ll 0.1$, to where $\bar{U}/\bar{U}_\infty$ enters the classical range, i.e., $\bar{U}/\bar{U}_\infty \approx 1$ for $a_1 \approx 1$. This behavior of $\bar{U}/\bar{U}_\infty$ as a function of a_1 is shown graphically in Fig. 1. For values of $a_1 \ll 1$, the energy density approaches the asymptote

$$\frac{\bar{U}}{\bar{U}_\infty} = \frac{1.84 \times 10^{-1}}{a_1} \qquad (5)$$

This latter result follows in an obvious manner from equation (4). The explanation of this behavior results from the fact that for a cavity of one limited dimension, the modal density of a low frequency exceeds that given by the three-dimensional Jeans' number. This characteristic of the modes in a cavity of one limited dimension has previously been investigated [8].

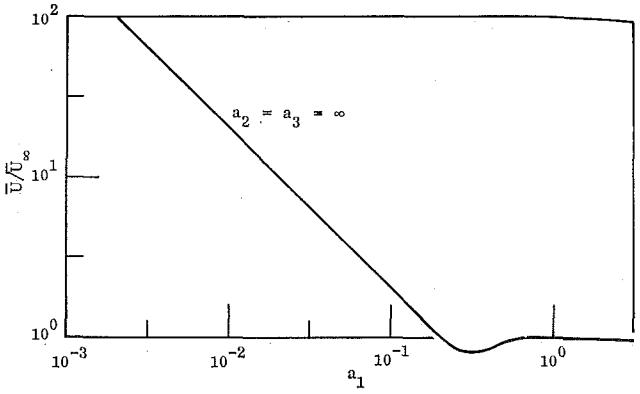

Fig. 1 Energy density in a cavity as a function of cavity size and temperature

To understand this behavior, consider the energy density in a rectangular cavity having two large dimensions, l_2 and l_3, and one small dimension, l_1. Assume further that the temperature of the cavity is such that $\lambda_m \gg l_1$. As previously stated, the eigenfunctions for the electromagnetic field in the cavity are restricted such that two or more of the integers n_1, n_2, and n_3 must be nonzero. Under these conditions, it follows from equation (2) that all modes for which $n_1 \neq 0$ essentially do not contribute to the thermal radiation density since $\lambda_{n_1,n_2,n_3} \ll \lambda_m$. Thus the modes that do contribute to the thermal radiation density are those for which $n_1 = 0$. There are a large number of such modes, since for large values of l_2 and l_3 there will be a large number of combinations of integers n_2 and n_3 for which $\lambda_{0,n_2,n_3} \approx \lambda_m$. Under these conditions, as the small dimension l_1 of the box tends toward zero, the number and therefore the total energy associated with these modes remains fixed, yet the volume containing this total radiant energy decreases as l_1 and thus the corresponding energy density increases as $1/l_1$. Since the breakpoint for the departure from the classical

[2] The sums have been written in terms of incomplete gamma functions since they are available in most computer-tape libraries.

Nomenclature

$a = \frac{KTl}{\pi\hbar c} = 0.404 \frac{l}{\lambda_m}$, nondimensional length
c = velocity of light, cm/sec
e = electronic charge, coulomb
$\bar{E}$ = electric-field vector
$\hbar$ = Planck's constant/2π, J-sec
$\bar{H}$ = magnetic-field vector
$k = \frac{\bar{k}}{|\bar{k}|} \cdot \frac{2\pi}{\lambda}$ = electromagnetic propagation vector, cm^{-1}
K = Boltzmann constant, J/deg K
l = length of cavity wall, cm
m = electron mass, kg
N = electron density, e/cm^3
$\bar{P}(\omega)$ = Poynting flux per mode, w/cm^2
$\bar{P}$ = total Poynting flux, w/cm^2
$\bar{P}_\infty$ = total Poynting flux to wall in infinite cavity, w/cm^2
R_S = metal skin resistance
T = temperature, deg K
$\bar{U}(\omega)$ = energy density per mode, J/cm^3
$\bar{U}$ = total energy density, J/cm^3
$\bar{U}_\infty$ = energy density in infinite cavity, J/cm^3
$\bar{v} = v/c$, nondimensional Fermi velocity
v = Fermi velocity, cm/sec
V = cavity volume, cm^3
$\alpha_n(\omega)$ = normal spectral absorptance of cavity wall
ϵ = electrical-capacitivity free space, F/cm
λ_m = wavelength of maximum spectral radiant intensity as given by Wien displacement law = $2.898 \times 10^{-1}/T$, cm
λ = wavelength of electromagnetic wave, cm
Γ = gamma function
μ = magnetic permeability of free space, H/cm
$\bar{\nu} = \nu \left[\frac{4}{3v}\left(\frac{3m}{Ne^2\mu}\right)^{1/2}\right]$, nondimensional frequency
ν = frequency of electromagnetic wave, sec^{-1}
$\bar{\sigma}' = \sigma'\left[\frac{v}{2}\left(\frac{3m\mu}{Ne^2}\right)^{1/2}\right]$, nondimensional conductivity
σ' = electrical conductivity, ohm-cm
σ = Stefan–Boltzmann constant, w/cm^2-deg K^4
ω = angular frequency, sec^{-1}
ζ = Riemann zeta function

expression for the energy density should occur where $l_1 \approx \lambda_m$, we should expect for small values of l_1 that

$$\bar{U} \approx \bar{U}_\infty \frac{\lambda_m}{l_1}$$

or

$$\bar{U} \approx \bar{U}_\infty \frac{0.4}{a_1} \tag{6}$$

where the Wien displacement law has been used to arrive at the final expression in equation (6). This latter estimate is in good agreement with the exact expression given by equation (5) for the asymptotic limit for small l_1 of the energy density between closely spaced infinite metal surfaces.

Radiant Flux Absorbed by a Cavity Wall

Equations (1) and (2) describe the spectral characteristics of the energy density in a cavity with perfectly conducting walls. The next step is to calculate the spectral radiant flux to the walls where the walls have a finite, but large, conductivity. In this case, as is done in microwave practice, the modal structure in the cavity is assumed, to a first approximation, to be the same as that in the case of a perfectly conducting or lossless cavity. The Poynting flux to the walls is then determined in the following fashion. For perfectly conducting walls, the magnetic component of the electromagnetic field has an antinode at the walls and is responsible for a surface current

$$\hat{n} \times \bar{H} = \bar{K}$$

For a finite, but large, surface conductivity, the magnetic field at the wall will still have, to a high degree of approximation, the same value and the above expression will hold for the surface current. But now, due to the resistance of the walls, there will be an average power loss per unit area to the walls given by

$$P_{\text{av}} = \frac{1}{2S} Re \iint R_S |\bar{K}|^2 dS = \frac{1}{2S} Re \iint R_S |H_{\tan}|^2 dS \tag{7}$$

The surface resistance R_S is related to the spectral absorptance of the walls through the equation

$$R_S = \frac{1}{4}\sqrt{\frac{\mu}{\epsilon}}\,\alpha(\omega) \tag{8}$$

If we take the electric-field vectors for the normal modes in a rectangular cavity, they are given by [7]

$$\begin{aligned} E_1 &= E_{10} \cos k_1 x \sin k_2 y \sin k_3 z e^{-j\omega t} \\ E_2 &= E_{20} \sin k_1 x \cos k_2 y \sin k_3 z e^{-j\omega t} \\ E_3 &= E_{30} \sin k_1 x \sin k_2 y \cos k_3 z e^{-j\omega t} \end{aligned} \tag{9}$$

where the eigenvalues of the separation parameters needed to satisfy the boundary conditions are $k_1 = n_1\pi/l_1$, $k_2 = n_2\pi/l_2$, and $k_3 = n_3\pi/l_3$. The magnetic-field vector is related to the electric-field vector through the Maxwell equation $\bar{H} = (1/j\omega\mu)\nabla \times \bar{E}$. If we take the cavity wall in which the power loss is to be evaluated to be the y–z plane where $x = 0$, then the tangential component of $\bar{H}$ is given by

$$\bar{H}_{\tan} = \frac{1}{j\omega\mu}\left\{\hat{i}_y\left(\frac{\partial E_1}{\partial z} - \frac{\partial E_3}{\partial x}\right) + \hat{i}_z\left(\frac{\partial E_2}{\partial x} - \frac{\partial E_1}{\partial y}\right)\right\} \tag{10}$$

Previous analyses [8] using this starting point have shown that the spectral Poynting flux into the walls is related to the modal energy density through the equation

$$\bar{P}(\omega) = \frac{1}{4}(1 + k_1^2/|\bar{k}|^2)\alpha(\omega)cU(\omega) \tag{11}$$

where k_1 is the component of the propagation vector normal to the wall in question. Domoto, Boehm, and Tien have shown that in the ASE regime the absorptance of a metal surface is given by [5]

$$\alpha_n(\tilde{\nu}, T) = \tilde{\nu}\left(\frac{3}{4} + \frac{\sqrt{3}}{\tilde{\sigma}'}\right)\left\{1 - \exp\left[-\frac{3}{2}(\tilde{\nu})^{2/3}\right]\right\} \tag{12}$$

At low temperature for most metals of interest $\sqrt{3}/\tilde{\sigma} \ll 3/4$. Further, taking Pippard's "standard metal" ($N = 6 \times 10^{22}$ e/cm^3, $v = 1.40 \times 10^8$ cm/sec)[3] [9], we have at low temperature

$$\alpha_n(\omega, T) \approx 3.5 \times 10^{-3}\{1 - \exp\left[-9.47 \times 10^{-10}\omega^{2/3}\right]\} \tag{13}$$

Utilizing equations (1), (11), and (13) we have for the total Poynting flux into the wall

$$\bar{P} = \sum_\omega \bar{P}(\omega) = 3.5 \times 10^{-3}\,\frac{15}{4\pi^5}\cdot\frac{\sigma T^4}{a_1 a_2 a_3}\sum_{n_1,\,n_2,\,n_3=-\infty}^{\infty}{}' \{1 - \exp\left[-2.44 \times 10^{-2} T^{2/3}(n_1^2/a_1^2 + n_2^2/a_2^2 + n_3^2/a_3^2)^{1/3}\right]\}$$
$$\times \left\{\frac{(n_1^2/a_1^2 + n_2^2/a_2^2 + n_3^2/a_3^2)^{1/2} + (n_1^2/a_1^2)(n_1^2/a_1^2 + n_2^2/a_2^2 + n_3^2/a_3^2)^{-1/2}}{\exp\,(n_1^2/a_1^2 + n_2^2/a_2^2 + n_3^2/a_3^2)^{1/2} - 1}\right\} \tag{14}$$

where the prime on the summation indicates that no terms are involved where two or more of the integers n_1, n_2, n_3 are zero. Since the total Poynting flux into the wall is simply the sum of the spectral Poynting fluxes and since the spectral Poynting flux strongly reflects the spectral or modal energy density, it follows that the total Poynting flux should reflect the total energy density in the cavity. As it has already been stated, for an infinite-parallel-plate geometry at small spacing distances, i.e., $l_1 T \ll 1$ cm-deg K, the energy density exceeds the classical value as $\bar{U} = 1.84 \times 10^{-1}\,\bar{U}_\infty/a_1$; we would anticipate a similar behavior for the Poynting flux to the wall at small values of a_1. If we let a_2 and a_3 tend toward infinity, then n_2/a_2 and n_3/a_3 form a two-dimensional continuum and the sums over n_2 and n_3 in equation (14) can be replaced by integrals with respect to a two-dimensional Jeans' number. Proceeding in this manner, equation (14) becomes

$$\lim_{a_2,a_3\to\infty} \bar{P} = 3.5 \times 10^{-3}\cdot\frac{15}{2\pi^4}\cdot\frac{\sigma T^4}{a_1}$$
$$\cdot \sum_{n_1=-\infty}^{\infty}\int_{\left|\frac{n_1}{a_1}\right|}^{\infty}\{1 - \exp\left[-2.44 \times 10^{-2} T^{2/3} n'^{2/3}\right]\}$$
$$\times \left\{\frac{n' + n_1^2/a_1^2 n'}{\exp n' - 1}\right\} n'\,dn' \tag{15}$$

Finally, expanding the first term in the integrand of equation (15) in a power series, this equation may be integrated to yield

$$\lim_{a_2,\,a_3\to\infty} \bar{P} = 3.5 \times 10^{-3}\cdot\frac{15}{2\pi^4}$$
$$\cdot\frac{\sigma T^4}{a_1}\sum_{n_1=1}^{\infty}\sum_{s=1}^{\infty}\sum_{r=0}^{\infty}\left[(-1)^{s+1}\frac{(2.44 \times 10^{-2} T^{2/3})^s}{s!}\right]$$

[3] These particular values for the electron density and Fermi velocity closely approximate those for the noble metals. The Fermi velocity for the "standard" metal is within 15 percent of the value for copper and aluminum. The electron density of the standard metal is equal to that of aluminum but deviates from that of copper by 40 percent. However, in the expression for $\alpha_n(\omega, T)$ the dependence on N goes as $N^{1/3}$ so we are not sensitive to reasonable percentage deviations in N. Also, as will become obvious later in the analysis, we are more interested in certain ratios involving $\alpha_n(\omega, T)$, so that we will be even less sensitive to deviations of $\alpha_n(\omega, T)$ for the real materials of interest as compared to the "standard" metal.

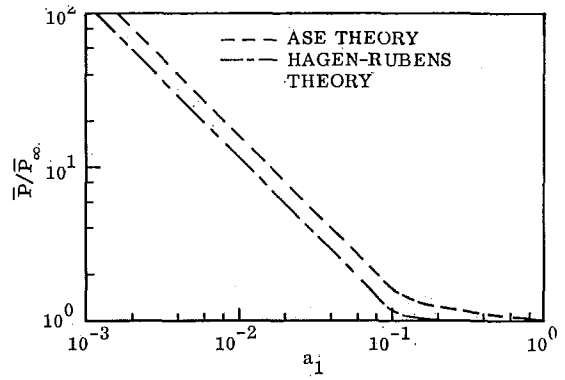

Fig. 2 Heat flux to the wall for a two-dimensionally infinite cavity

$$\times \left[2 \left(\frac{1}{r+1} \right)^{\frac{9+2s}{3}} \Gamma \left(\frac{9+2s}{3}, (r+1)\frac{n_1}{a_1} \right) + 2\frac{n_1^2}{a_1^2} \left(\frac{1}{r+1} \right)^{\frac{3+2s}{3}} \Gamma \left(\frac{3+2s}{3}, (r+1)\frac{n_1}{a_1} \right) + \left(\frac{1}{r+1} \right)^{\frac{9+2s}{3}} \Gamma \left(\frac{9+2s}{3} \right) \right] \quad (16)$$

We may also integrate equation (14) in the continuum limit for a_1, a_2, and a_3, tending toward infinity to derive an expression for the heat flux absorbed or emitted by the cavity walls in the classical limit; the resulting expression is

$$\bar{P}_\infty = 3.5 \times 10^{-3} \cdot \frac{20}{\pi^4} \cdot \sigma T^4 \cdot \sum_{s=1}^{\infty} (-1)^{s+1} \times \frac{(2.44 \times 10^{-2} T^{2/3})^s}{s!} \Gamma \left(\frac{12+2s}{3} \right) \zeta \left(\frac{12+2s}{3} \right) \quad (17)$$

Figure 2 shows the ratio of the total Poynting flux absorbed or emitted by either of the two dimensionally infinite cavity walls in the ASE region as a function of a_1 as given by equation (16) to the corresponding flux for large spacing distances given by equation (17). The curve representing these data in Fig. 2 was computed using equation (16) for wall temperatures of 5, 10, and 15 deg K; in all cases, the resulting data fell within 1 percent of the curve. It is reasonable then to suggest that the ASE data represented by the corresponding curve in Fig. 1 should hold to good accuracy over a much larger temperature range. The data show that the heat flux departs from its classical value for $a_1 \leq 0.1$, and for small values of a_1 satisfies the equation[4]

$$\bar{P}/\bar{P}_\infty = \frac{0.160}{a_1} \quad (18)$$

These data may be translated into absolute heat fluxes using the results in Table 1 for $\bar{P}_\infty$ at 5, 10, and 15 deg K for ASE theory. Figure 2 also shows the ratio of the total Poynting flux absorbed or emitted by the cavity walls, assuming that the Hagen–Rubens approximation holds to these low temperatures.[5]

Figure 1 indicates that whether the Hagen–Rubens or ASE theory is used to compute the wall absorptance at low temperature, the results for $\bar{P}/\bar{P}_\infty$ are similar. The absolute heat fluxes may be obtained using the results for $\bar{P}_\infty$ in conjunction with each of these two theories; these data are provided in Table 1. The absolute heat fluxes for the two theories differ by more than an order of magnitude. Nevertheless, the conclusion may be tentatively drawn that the ratio $\bar{P}/\bar{P}_\infty$ is fairly independent of the theory used to describe the wall absorptance as long as the theory used provides a reasonable description of the absorptance of a high-conductivity metal.

Heat Transfer between Infinite Parallel Plates

Equation (16) provides a solution for the heat flux absorbed by either surface from the equilibrium thermal radiation contained between two parallel metal surfaces of infinite extent at temperature T. Under equilibrium conditions, this is also equal to the heat flux emitted by either surface into the cavity. As has been argued by Weinstein [10], this is also equal to the heat flux emitted by either of the surfaces even under nonequilibrium conditions. Equation (12) indicates that at low temperature, spectral absorptance of the metal surface is temperature-independent; further, the magnitude of the absorptance is on the order of 10^{-3}. Thus, the heat flux emitted by a given surface will be almost exactly equally divided between the two surfaces under ASE-effect theory. This would also be the case if the Hagen–Rubens theory held to low temperature, for as can be seen from the footnote in Table 1, the conductivity of a high-conductivity metal is almost temperature-independent at a sufficiently low temperature. Hence, we have for the net heat flux between two parallel surfaces of infinite extent at temperatures T_1 and T_2

$$\bar{q} = \frac{1}{2} [\bar{P}(T_1) - \bar{P}(T_2)] \quad (19)$$

Using the ASE data presented previously in Fig. 2 and Table 1 in equation (19), and comparing these results with the data of Domoto, Boehm, and Tien, one finds a disagreement of approximately one order of magnitude. This is none too surprising as these authors have reported that the equivalent emittance of their copper surfaces for large spacing distances was approximately one order of magnitude greater than the value given by ASE theory. However, considering the results of the previous section, one can consider the present theory as also describing relative effects, i.e., it predicts the ratio of $\bar{P}/\bar{P}_\infty$. The radiation energy density in a cavity under equilibrium conditions is independent of the absorption characteristics of the wall material as long as it has low enough absorptivity that the normal modes of the radiation field in the cavity are well defined. Then, $\bar{P}_\infty$ measures the degree to which the cavity walls are coupled to the radiation field in the cavity through the absorption characteristics of the walls. Variation of the cavity dimensions alters the radiant energy density of the cavity through a purely geometric effect, i.e., only those normal modes are allowed that have wavelengths such that antinodes occur at the walls.

If the walls were gray, then variation of $\bar{P}/\bar{P}_\infty$ with cavity size would be exactly proportional to $\bar{U}/\bar{U}_\infty$. Metal surfaces are not spectrally gray; however, the absorption characteristics are in general sufficiently spectrally well-behaved that the ratio of $\bar{P}/\bar{P}_\infty$ should be, to the first order of approximation, independent of the spectral absorption characteristics of the wall. This is

Table 1 Heat fluxes to wall for infinite cavity

T	$\bar{P}_\infty$ (ASE)	$\bar{P}_\infty$ (Hagen–Rubens)*
5	1.76×10^{-12}	7.87×10^{-14}
10	4.30×10^{-11}	1.77×10^{-12}
15	2.77×10^{-10}	1.04×10^{-11}

* The resistivity is taken to be that of copper $\rho = 1.47 \times 10^{-10}$ ohm-cm at 15 deg K, $\rho = 1.64 \times 10^{-10}$ ohm-cm at 10 deg K, $\rho = 1.67 \times 10^{-10}$ ohm-cm at 5 deg K.

[4] This expression for the heat flux for small spacing distances should hold down to the point where the spacing distance becomes on the order of the electromagnetic skin depth which is given by $\delta = \sqrt{2/\omega\mu\sigma'}$. For the frequencies characterizing the thermal radiation field at low temperature and for high-conductivity metal walls at low temperature, $\delta \lesssim 10^{-6}$ cm.

[5] These analyses were carried out by the present author using the same methodology as contained herein. The basic point of departure is that in this case the normal spectral absorptance $\alpha_n(\omega, T)$ becomes $\alpha_n(\omega, T) = 2\sqrt{2\epsilon\omega/\sigma'}$. These results have been previously reported [8].

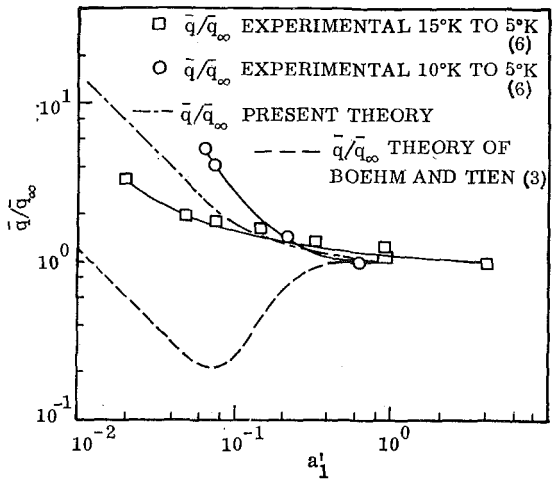

Fig. 3 Heat flux between closely spaced metal surfaces—comparison of theory and experiment

illustrated by the results shown in Fig. 3, where the ratios of $\bar{P}/\bar{P}_\infty$, assuming ASE theory and Hagen–Rubens theory, are shown to be almost identical. Figure 3 shows a comparison of the prediction of the present theory for $\bar{q}/\bar{q}_\infty$ with the experimental results of Domoto, Boehm, and Tien. It is assumed that for the latter experimental results, the net heat-transfer measurements at the greatest spacing distances used in the experiments represented $\bar{q}_\infty$. The nondimensional parameter in Fig. 3 is associated with the temperature of the hotter surface. Neglecting a maximum deviation of 2 percent, the theoretical curve is valid for the higher-temperature surface being either 10 or 15 deg K and the lower-temperature surface at 5 deg K. As can be seen, the present theory duplicates the form of the experimental results, but does not reflect the temperature-dependence shown experimentally. However, although Domoto, Boehm, and Tien are confident of their displacement measurements in a relative sense, they feel that there was some question of the displacements in an absolute sense [11]. It should be noted in this regard that a shift of the curve through the data for $T = 15$ deg K of $\Delta a_1 = 0.03$, i.e., $\Delta l = -0.00145$ cm, provides an almost exact agreement between experiment and theory for $a_1 \leq 0.1$, whereas for the curve through the data for $T = 10$ deg K a shift in the curve for the data of $\Delta a = +0.04$, i.e., $\Delta l = -0.0029$ cm, provides good agreement between theory and experiment for $a_1 \leq 0.1$ cm.

Figure 3 also shows the results of the previous wave-interference analysis of Boehm and Tien [3]. The previous wave-interference analyses of Boehm and Tien were based on a model due to Fragstein [12] for the radiation intensity in a metal. The heat transfer between metals due to traveling waves was calculated by Boehm and Tien based on the radiation-intensity model of Fragstein and the application of simple electromagnetic boundary-value theory to calculate the total radiant interchange between metal surfaces resulting from this radiation source. Rytov [13] has criticized this type of analysis on the basis that there is no well-defined radiation field within a highly absorbing medium, and therefore any theory based on this assumption is incorrect. The present theory would seem to be better founded theoretically, and perhaps not too surprisingly, therefore, is in much better agreement with the limited experimental measurements.

It should be noted, however, that because the present analysis is based on the coupling between the walls of a cavity and the normal modes of the cavity, it is limited to the contribution to the heat transfer due to traveling waves. Previous analyses [1–3] have also identified an important contribution to the heat transfer due to radiation tunneling, i.e., near surface waves. These analyses were based on the model of Fragstein for the radiant intensity in a metal and the application of simple electromagnetic boundary theory to determine the heat transfer due to damped (near surface) waves. The damped waves in these analyses are the near surface waves produced in the vacuum region surrounding a metal surface by the internally reflected portion of the radiation field in the metal. The internal reflection is frustrated by the near presence of a second metal surface leading to heat transfer via the so-called radiation tunneling mechanism [14].

The results of these analyses indicated that radiation tunneling does not provide a significant contribution to the heat transfer between metal surfaces except when $a_1 < 10^{-2}$ deg K. However, the criticism of Rytov is also applicable to these results and they are also therefore subject to doubt. A forthcoming analysis [15] by the present author will place the theory of heat-transfer contributions due to near surface waves on a solid theoretical foundation and will show that the contribution to the heat transfer due to near surface waves alters the present results in the range of nondimensional spacing distances below 10^{-1}. Further, at nondimensional spacing distances less than 5×10^{-2}, near surface waves are the dominant heat-transfer mechanism.

References

1 Caren, R. P., "The Theory of Electromagnetic Tunneling of Thermal Radiation Between Highly Absorbing Media," *Proceedings of the Fourth Symposium on Thermophysical Properties*, ASME, New York, N. Y., 1968, p. 243.

2 Caren, R. P., and Liu, C. K., "Emission, Total Internal Reflection, and Tunneling of Thermal Radiation in Metals," *Progress in Astronautics and Aeronautics*, Vol. 21, Bevans, ed., Academic Press, New York, N. Y., 1969, p. 509.

3 Boehm, R. F., and Tien, C. L., "Small Spacing Analysis of Radiative Transfer Between Parallel Metallic Surfaces," JOURNAL OF HEAT TRANSFER, TRANS. ASME, Series C, Vol. 92, No. 3, Aug. 1970, pp. 405–411.

4 Case, K. M., and Chiu, S. C., "Electromagnetic Fluctuations in a Cavity," *Phys. Rev. A*, Vol. 1, No. 4, 1970, p. 1170.

5 Domoto, G. A., Boehm, R. F., and Tien, C. L., "Prediction of the Total Emissivity of Metals at Cryogenic Temperatures," *Advances in Cryogenic Engineering*, Vol. 14, 1969, pp. 230–239.

6 Domoto, G. A., Boehm, R. F., and Tien, C. L., "Experimental Investigation of Radiative Transfer Between Metallic Surfaces at Cryogenic Temperatures," JOURNAL OF HEAT TRANSFER, TRANS. ASME, Series C, Vol. 92, No. 3, Aug. 1970, pp. 412–417.

7 Panofsky, W. H. H., and Philips, M., *Classical Electricity and Magnetism*, Addison-Wesley, Cambridge, Mass., 1955, p. 191.

8 Caren, R. P., "Radiation Energy Density and Radiation Heat Flux in Small Rectangular Cavities," JOURNAL OF HEAT TRANSFER, TRANS. ASME, Series C, Vol. 94, No. 3, Aug. 1972, pp. 289–294.

9 Olsen, J. L., *Electron Transport in Metals*, Interscience, New York, N. Y., 1962, p. 108.

10 Weinstein, M. A., "On the Validity of Kirchhoff's Law for a Freely Radiating Body," *Am. J. Phys.*, Vol. 28, 1960, p. 123.

11 Private communication from C. L. Tien.

12 Fragstein, C. v., "Energy Transfer at the Interface between Two Absorbing Media with an Emphasis on the Heat Radiation in Absorbing Bodies," *Ann. Physik*, Vol. 7, 1950, pp. 63–72.

13 Rytov, S. M., *Theory of Electrical Fluctuations and Thermal Radiation*, translated by H. Erkuu, Academy of Sciences Press, Moscow, 1953, AFCRC-TR-59-162, 1959, p. 27.

14 Cravalho, E. G., Tien, C. L., and Caren, R. P., "Effect of Small Spacings on Radiative Transfer Between Two Dielectrics," JOURNAL OF HEAT TRANSFER, TRANS. ASME, Series C, Vol. 89, No. 4, Nov. 1967, pp. 351–358.

15 Caren, R. P., "Thermal Radiation between Closely Spaced Metal Surfaces at Low Temperature Due to Traveling and Quasi-stationary Components of the Radiation Field," to be published.

RALPH M. SINGER
Associate Chemical Engineer.
Mem. ASME

ROBERT E. HOLTZ
Associate Mechanical Engineer.

Reactor Analysis and Safety Div.,
Argonne National Laboratory,
Argonne, Ill.

The Vaporization of Superheated Sodium in a Vertical Channel

Measurements of the vapor growth patterns and rates following the nucleation of superheated sodium in a vertical rectangular channel are presented and discussed. The vapor was found to grow as a single bubble for incipient bulk-liquid superheats greater than about 10 deg C, and this single bubble tended to completely fill the channel cross section (except for a thin liquid film on the walls) and to grow as a vapor slug for incipient bulk-liquid superheats greater than about 50 deg C. The temperature gradients in the liquid both normal and parallel to the channel axis prior to nucleation were found to have an important effect upon the dynamics of the vapor slug. Experimental data on the vapor growth and collapse rates and the associated pressure transients are presented for boiling pressures up to 1 atm and incipient superheats up to about 180 deg C.

Introduction

An understanding of the vaporization dynamics of superheated sodium is of considerable importance in developing safety analyses of sodium-cooled fast breeder reactors (LMFBRs). In this situation, where boiling is generally undesirable, the calculation of the safe operating limits of a reactor or the extent of damage resulting from postulated accidents is partially dependent upon knowledge of the mechanism and rate at which sodium may vaporize.

It is well known that under normal circumstances liquids will boil when their temperatures slightly exceed the saturation level, with the resultant generation of a large number of relatively small vapor bubbles. However, under certain circumstances (e.g., a heating surface highly wetted by the liquid, a lack of nucleation sites, or rapid heating or depressurization transients), liquids can become superheated substantially above their normal boiling temperatures. When nucleation occurs under these conditions, the first bubble that forms grows quite rapidly and increases the liquid pressure in its vicinity; this can result in a suppression of nucleation at other possible sites. This phenomenon has been observed in liquid alkali metals [1–4][1] as well as in nonmetallic fluids [5–7]. Furthermore, if the liquid is in a channel (as opposed to a "pool") the initially spherical vapor bubble will deform and grow primarily in the direction of the channel axis.

In these earlier experiments, either uniform heating [1–3] or depressurization [5–7] of a liquid in a circular tube was used to cause superheated boiling; these techniques resulted in either radially symmetric or radially uniform profiles of liquid temperature. As a result, the bubble that was formed was also radially symmetric and filled the entire tube cross section except for a thin liquid film remaining on the walls. Based on these results, several theoretical models of vapor-slug growth in sodium were developed, incorporating the observed symmetries [8, 9]. However, the possibility of an asymmetric liquid-temperature profile causing the bubble to grow asymmetrically was not examined. In the work reported herein, the rectangular-cross-section channel was heated on one face only, resulting in an asymmetric liquid-temperature profile at nucleation, so that possible deviations from symmetric vapor growth could be investigated.

Experimental Apparatus and Procedures

The detailed design of the apparatus used for the tests reported in this paper is available in reference [10]; thus, only the salient features will be outlined here. The sodium was contained in a vertical tube, made of type 304 stainless steel, the lower section having a rectangular cross section of 9.5 × 25.4 mm and a length of 500 mm; the upper section was a circular tube with an internal diameter of 17.5 mm. The internal cross-sectional area of the rectangular section was 2.413 cm² and that of the tube was 2.405 cm². The total length of the tube was 4.3 m.

Low-power-density heaters along the length of the tube were used to establish and maintain a specified vertical temperature distribution, while an electron-bombardment heater was used to supply a large uniform heat flux to a 50- to 90-mm section of one side of the lower rectangular portion of the tube (the back side of this portion of the rectangular tube was unheated). This type of heating arrangement was employed to assure that nucleation would occur in an essentially predetermined region.

Temperatures were measured using 1.6-mm-dia Inconel-sheathed C/A thermocouples immersed in the sodium and similar 0.5-mm-dia thermocouples embedded in the tube wall. The pressure of the upper argon gas blanket was measured by a precision Bourdon-type pressure gauge, while the liquid pressure in the high-heat-flux region was measured by a fast-response (~4 kHz) strain-gauge transducer mounted in a stand-off for temperature

[1] Numbers in brackets designate References at end of paper.

Based on a paper contributed by the Heat Transfer Division and presented at the Winter Annual Meeting, New York, N. Y., November 29-December 3, 1970, of The American Society of Mechanical Engineers as Paper No. 70-HT-23. Manuscript received by the Heat Transfer Division February 27, 1970; revised manuscript received January 11, 1971.

protection. The position of the liquid–vapor (bubble) interface was detected by passing a constant low-power direct electrical current through the tube wall and sodium and measuring the electrical potential at various locations along the length of tube. The displacement of the top of the liquid column (liquid–gas interface) above the growing vapor slug was measured by the use of eddy-current-type coils which could detect the change in electrical conductivity resulting as this interface passed through the field of the coils. The coils were located at intervals of 76 mm along the upper length of the expulsion tube.

A typical experiment was conducted in the following manner: (*a*) the gas-blanket pressure was set at some level, (*b*) the low-power-density heaters were then used to establish a prescribed vertical temperature distribution, (*c*) the electron-bombardment heater was then turned on and maintained at a constant heat flux throughout the entire transient period of heating, nucleation, vapor growth, and collapse, including the final steady boiling condition if it occurred, and (*d*) the heaters were turned off to allow the system to cool prior to the start of a new run. All data were continuously recorded on either oscillographs or strip-chart instruments.

It is of some interest to note that considerable difficulty was encountered in attempting to superheat the sodium following the initial filling of the apparatus. Approximately 6 to 8 weeks of repeated boiling and cooling transients were required before an incipient-boiling wall superheat greater than about 5 to 10 deg C was observed. After this time, the required incipient superheat increased to the range from 50 to 200 deg C. An explanation for this behavior may be found in an examination of the construction of the test section. This rectangular tube was constructed of two separate U-shaped channels that were butt-welded together with something less than 90 percent weld penetration. Apparently these two joints on either side (i.e., the narrow unheated faces) provided excellent nucleation sites which became wetted by the sodium and partially deactivated only following an extensive and lengthy period of thermal cycling. Experimenters should be aware of such a problem in order to avoid the possible misinterpretation of nucleation measurements when such welds are near their heating surfaces.

Experimental Results

Patterns of Vapor Growth. Since direct visual observations of the boiling liquid could not be made, the patterns of vapor growth were inferred from indirect measurements. The two measurements that were primarily used for this purpose were (*a*) the total displacement of the liquid column and (*b*) the axial motion of the liquid–vapor (bubble) interface. The measurements of the electrical potential along the length of the tube during vapor growth indicated that the flow regime was that of a single vapor bubble expanding against the liquid column for incipient-boiling bulk-liquid superheats greater than about 10 deg C. At lower superheats, the presence of many vapor bubbles was apparent.

The average void fraction could be calculated by noting that the total volume of vapor formed equals the product of the column displacement and the channel cross-sectional area. Thus, the void fraction averaged over the length of the bubble, α, is the column displacement divided by the bubble length. Measurements of the sodium-column displacement and the corresponding vapor-slug length indicated that the slug length exceeded the column displacement immediately after nucleation, indicating that the vapor slug does not completely fill the channel cross section, i.e., $\alpha < 1$. There was some difficulty in determining the precise instant of nucleation, which resulted in an error in relating the transient bubble length and column displacement to the same time scale. The criterion chosen in this work for the inception of vapor growth (i.e., nucleation) was the instant at which the liquid pressure started to increase. At large incipient superheats (i.e., $\Delta T_W \gtrsim 100$ deg C), the pressure rise was relatively abrupt at nucleation, resulting in an error in the determination of zero time of ± 1 to ± 2 msec. However, at smaller superheats (i.e., $\Delta T_W \lesssim 50$ deg C), the initial pressure rise was more gradual, resulting in an error in the zero-time location of ± 5 to ± 8 msec.

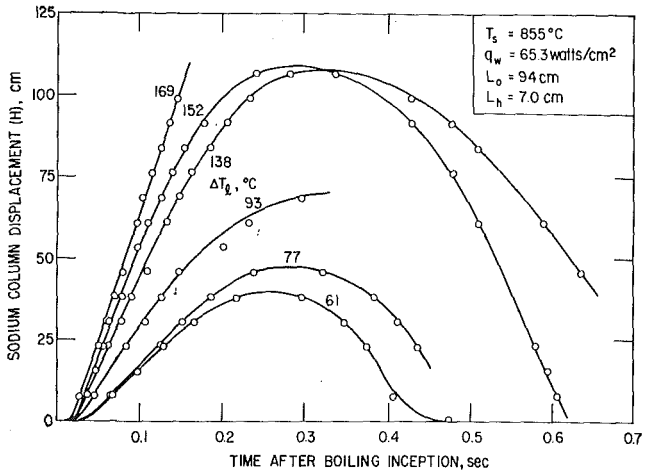

Fig. 1 Sodium-column displacement caused by vaporization at T_s = 855 deg C and at large incipient superheats

The calculation of the average void fraction from the bubble-length and column-displacement data is extremely sensitive to these errors in time. As a result of this sensitivity, the average void fraction as calculated from the displacement data can only be determined within ± 80 percent at low superheats (i.e., 0 to 50 deg C) and within ± 20 percent at higher superheats (i.e., greater than 100 deg C). Because of this uncertainty in these calculations, it is difficult to draw any hard and fast conclusions as to whether or not the bubble initially filled the channel under these particular conditions. However, it is clear that as the bubble grows larger, the void fraction decreases, indicating that the bubble does not continually fill the channel as it grows axially. This, of course, is due in part to a diminished vapor growth rate (and ultimately condensation) as the bubble grows out of the high-heat-flux zone into cooler surroundings.

Under the conditions of an initially asymmetric liquid-temperature gradient (normal to the heated surface) of 4 deg C/mm and using the mean values of the void fraction, α, from each run, it was found that the incipient wall superheat had to be greater than about 100 deg C for α to be greater than 0.9. However, if the upper limits of α are used, a superheat of only 40 deg C was necessary in order to reach $\alpha = 0.9$. In general, it was observed

Nomenclature

A = channel cross-sectional area
C = channel circumference
C_p = specific heat
g = gravitational acceleration
H = liquid-column displacement
h_{fg} = latent heat of vaporization
Ja = Jakob number, $\rho C_{pl}\Delta T/\rho_v h_{fg}$
L_0 = length of liquid column above vapor slug
L_h = length of high-heat-flux zone
P = pressure
q = heat flux
t = time
t_* = time defined in equation (4)
T = temperature
ΔT = superheat, $T - T_s$
α = average void fraction
δ = equivalent liquid-film thickness
κ = integration constant defined in equation (5)
ρ = liquid density

Subscripts

g = gas blanket
l = bulk liquid
s, sat = saturation conditions at top of heat-flux zone
v, V = vapor

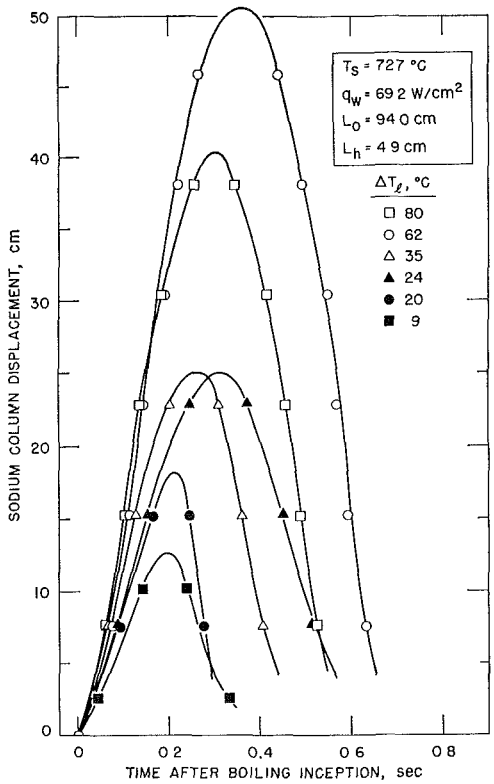

Fig. 2 Sodium-column displacement caused by vaporization at T_s = 851 deg C and at small incipient superheats

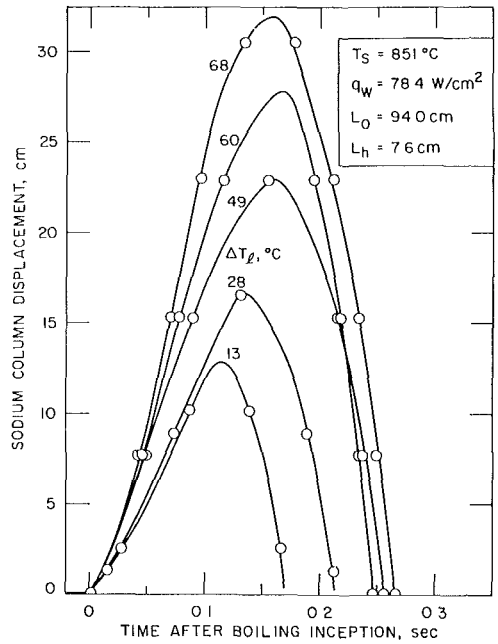

Fig. 3 Sodium-column displacement caused by vaporization at T_s = 727 deg C

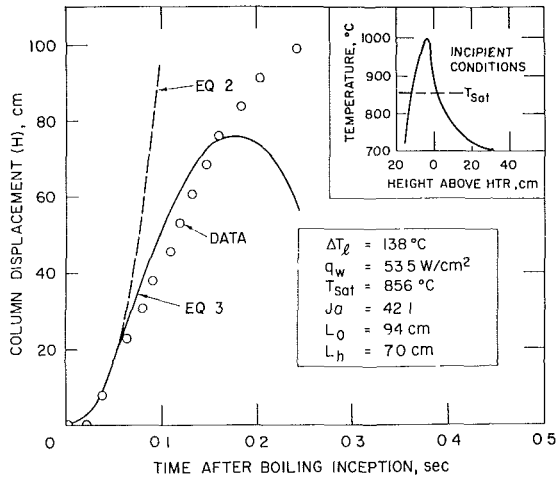

Fig. 4 Comparison of the predicted column displacement with the experimental data at an incipient superheat of 138 deg C

that the mean void fraction became smaller as the incipient superheat was reduced, indicating that the vapor bubble filled less of the channel cross section. This conclusion is reinforced by the observation that for incipient wall superheats less than about 10 deg C with wall heat fluxes from 55 to 290 W/cm² no vapor slug was formed and the sodium went directly into stable nucleate boiling. In the higher ranges of heat flux (greater than about 200 W/cm²) subcooled boiling was occasionally observed.

The implication of this interpretation of the data is that the symmetric vapor-slug models of references [8, 9] may not apply at low incipient superheats (i.e., less than about 20–50 deg C) when an asymmetric temperature profile is present due to the asymmetric thermal conditions existing around the circumference of the vapor slug. If the temperature profile is sufficiently asymmetric (i.e., the temperature gradient sufficiently large) vaporization and condensation can occur at opposite faces of a vapor bubble and its net growth rate will be affected. This phenomenon is most vividly apparent in subcooled boiling, which was observed at the larger heat fluxes (i.e., at larger temperature gradients).

Vaporization Dynamics. As described in the previous section, the vapor growth pattern was most likely that of a single bubble that filled 40 percent to essentially 100 percent of the channel cross section, depending upon the incipient-boiling superheat and the temperature gradient in the liquid. In this section the vaporization dynamics of the vapor slug will be discussed and its dependence upon the superheat and saturation conditions delineated.

In the tests reported herein, the temperature of the liquid sodium far from the high-heat-flux zone was always maintained at approximately 550 deg C, resulting in a large axial temperature gradient at incipient boiling. Only the liquid in and near the high-heat-flux region was superheated; the liquid above and below was subcooled. The result of this temperature gradient was to cause an ultimate collapse (condensation) of the vapor slug as it grew into the cooler regions of the channel.

Measurements of the transient liquid-column displacement caused by the vapor-slug growth and collapse for several saturation temperatures and a variety of incipient-boiling bulk-liquid superheats are shown in Figs. 1, 2, and 3, where the solid curves represent the "best" lines drawn through the data points. These data clearly illustrate the importance of the incipient superheat in determining both the rate and extent of vapor growth. Although it is not shown in these figures, it was observed that the vapor growth rates were relatively insensitive to the value of the wall heat flux in the range of $q_W \cong 60$ to 140 W/cm². Apparently, because of the very short heated lengths used in these tests (about 50 to 90 mm), the effect of the heat flux is minimized; however, if much larger heated lengths are used, the effect of the heat flux would be expected to be more important.

In the tests conducted in the present apparatus, reentry of the liquid column always occurred following the initial vaporization. The behavior of the liquid after it reentered the heated zone was quite erratic and its subsequent vaporization showed no particular dependence upon the value of any of the known parameters. It should be pointed out that if a longer high-heat-flux zone were used along with a smaller-diameter channel, this liquid reentry might not occur, due to the increased maintenance of the vapor pressure in the vapor slug because of the larger surface area of liquid film attached to the heated wall and a smaller slug volume per unit slug length.

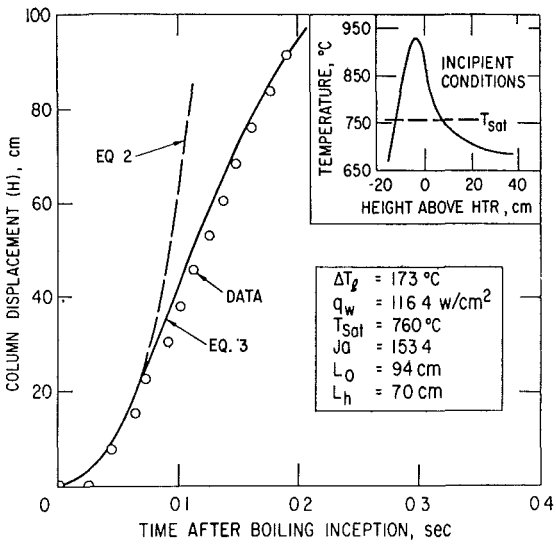

Fig. 5 Comparison of the predicted column displacement with the experimental data at an incipient superheat of 173 deg C

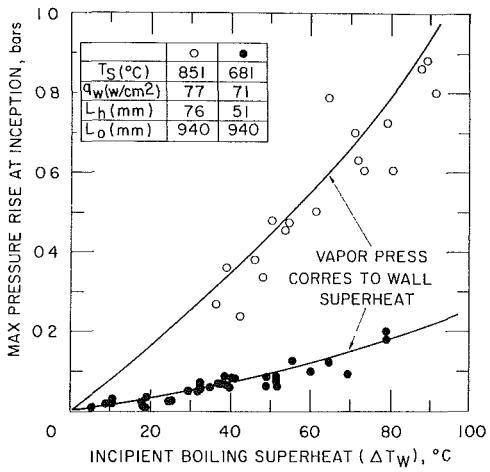

Fig. 6 The variation of the initial pressure rise at vaporization with the incipient superheat

At large incipient-boiling superheats, the vapor slug essentially filled the channel cross section; thus, a simple model of vapor growth driven by the initial superheat pressure against the inertia of the liquid column with vaporization occurring only in the high-heat-flux region can be expected to reasonably model the initial phases of the vaporization process. As derived in reference [10], this model predicts that the liquid-column displacement for times less than t_*, where

$$t_* = \left[\frac{2\rho L_0 L_h}{P_v(T_l) - P_g - \rho L_0}\right]^{1/2} \tag{1}$$

is

$$H(t) = \left(\frac{t^2}{2}\right)\left[\frac{P_v(T_l) - P_g}{\rho L_0}\right] - g \tag{2}$$

and for $t > t_*$,

$$H(t) = L_h + \int_{t_*}^{t} \left\{\left[\frac{2L_h P_v(T_l)}{\rho L_0}\right] \ln H(t') - 2\left(\frac{P_g}{\rho L_0} + g\right) H(t') + \kappa\right\}^{1/2} dt' \tag{3}$$

where the constant κ is

$$\kappa = t_*^2\left[\frac{P_v(T_l) - P_g}{\rho L_0} - g\right]^2 - \left[\frac{2L_h P_v(T_l)}{\rho L_0}\right] \ln L_h + 2\left(\frac{P_g}{\rho L_0} + g\right) L_h \tag{4}$$

A comparison of the predicted liquid-column displacements, equations (2) and (3), with the experimental data is presented in Figs. 4 and 5. Because of the large thermal conductivity of the liquid sodium, it would be expected that the initial vapor growth rate would be inertially limited for sufficiently large incipient superheats, so that the agreement at small times is not surprising; however, at larger times, the model is seen to predict shorter bubble lengths than were measured. This is due to the restriction in the model that no vaporization can occur outside of the high-heat-flux zone; in reality, some vaporization actually does occur there.

These two figures also include the axial temperature profile existing in the liquid just prior to nucleation; such information is crucial when comparing vapor growth data to more refined future models.

Pressure Transients. The transient liquid pressure measured during the growth and collapse of the vapor slug was qualitatively similar to that observed during the rapid transient boiling of water and other fluids in a vertical channel [11]. The pressure would initially rise to a maximum during the vapor growth and then gradually drop to a level considerably below that of the upper gas-blanket pressure during vapor condensation. When the upper liquid column ultimately impacted with the lower column following collapse of the vapor slug, a very sharp rise in pressure resulted. The rise time of the initial pressure increase was typically 10–40 msec, while that of the impact pressure was about 0.1 to 0.3 msec.

Since the initial pressure rise is caused by the rapid vaporization of the superheated liquid, the maximum value of this pressure would be expected to be limited by the vapor pressure corresponding to the superheat. This was the case in all of the tests summarized in this paper. The maximum measured pressure rise above ambient is compared to that calculated from the superheated-liquid vapor pressure in Fig. 6, and the agreement is mostly within the estimated experimental accuracy of the pressure measurements (±0.1 bar). This finding adds further credence to the assumption in the simple vapor growth model that the length of the vapor bubble for short times is determined by the pressure corresponding to the initial liquid superheat.

Conclusions

A considerable amount of new data on the vaporization dynamics of superheated sodium in a vertical channel have been presented. Analysis of these data indicates that the resultant vapor growth pattern is that of a single bubble if the incipient-boiling bulk-liquid superheat is greater than about 10 deg C. However, it appears that an asymmetric radial temperature profile may result in the vapor bubble filling only a portion of the cross section of the channel (as little as 30 to 50 percent) as opposed to the symmetric case where essentially complete filling was observed [1–3]. As the incipient superheat is increased, this asymmetry effect diminishes. For the symmetric bubble (i.e., the channel completely filled with vapor except for a thin liquid film on the walls) the vapor growth is initially limited by liquid inertia, but the subsequent growth is strongly affected by heat transfer. Reentry of the liquid into the heated test section was found to occur after every initial vaporization, but this phenomenon is thought to be strongly geometry-dependent.

The maximum pressure rise associated with vapor growth is limited by the vapor pressure of the superheated liquid, which provides the initial driving force for vapor growth.

Acknowledgment

This work was performed under the auspices of the United States Atomic Energy Commission.

References

1 Spiller, K. H., et al., "Überhitzung und Einzelblasenejektion bei der Verdampfung von stagnierendem Flüssigmetaller," *Atomkernenergie*, Vol. 12, 1967, p. 111.

2 Spiller, K. H., Perschke, D., and Grass, G., "Überhitzen und Einzelblasenejektion von stagnierendem Natrium," *Atomkernenergie*, Vol. 13, 1968, pp. 245–251.

3 Schlechtendahl, E. G., "Sieden des Kuhlmittels in natriumgekuhlten schnellen Reaktoren," Gesellschaft für Kernforschung (Karlsruhe) Report KFK 1020, 1969; also as EUR-4302d.

4 Singer, R. M., Holtz, R. E., and Niemoth, H. R., "Vaporization and Expulsion Measurements with Superheated Sodium," *Trans. American Nuclear Society*, Vol. 12, No. 2, 1969, p. 911.

5 Kosky, P. G., "Bubble Growth Measurements in Uniformly Superheated Liquids," *Chem. Eng. Sci.*, Vol. 23, 1968, p. 695.

6 Fette, P., "Simulation der Kuhlmittelejektion in natriumgekuhlter Brutreaktoren durch Experimente mit Wasser," Gesellschaft für Kernforschung (Karlsruhe) Report KFK-940, 1969; also as EUR-397d.

7 Grolmes, M. A., Fauske, H. K., and Lambert, G. A., "Superheat Expulsion in Single and Multipin Channels—Simulation of Blocked Subassembly Voiding," *Trans. American Nuclear Society*, Vol. 12, No. 2, 1969, p. 907.

8 Schlechtendahl, E. G., "Die Ejektion von Natrium aus Reaktorkuhlkanalen," *Nukleonik*, Vol. 10, 1967, pp. 270–274.

9 Cronenberg, A. W., et al., "A Single-bubble Model for Sodium Expulsion from a Heated Channel," *Nuclear Engineering Design*, Vol. 16, 1971, p. 285.

10 *Liquid-Metal Heat Transfer and Fluid Dynamics*, J. C. Chen and A. A. Bishop, eds., ASME Special Session Proceedings, ASME, New York, N. Y., 1970, pp. 144–152.

11 Singer, R. M., "Transient Two-phase Flow Following Sudden Vaporization," Symposium on Two-phase Flow Dynamics, Vol. 2, Eindhoven, The Netherlands, Sept. 1967, p. 1683.

T. E. MULLIN
Professor and Acting Chairman,
Mechanical Engineering Department.
Assoc. Mem. ASME

R. B. RENDA
Associate Dean,
Speed Scientific School.
Mem. ASME

University of Louisville,
Louisville, Ky.

Falling-Film Solidification Rates for Water inside a Short Vertical Tube

The purpose of this investigation was twofold: (1) to present the results of an experimental investigation of the solidification rates for water at its fusion temperature in falling-film flow inside a short vertical tube and (2) to compare the experimental results to those predicted from the expression developed by London and Seban [1].[1] *The experimental data were in good agreement with those values predicted by their expression when evaluated on a weight-of-ice-formed basis. However, the liquid–solid interface radius r_s could be determined with reasonable accuracy only for large values of r_s. It was shown that by increasing the temperature difference across the ice field, closer agreement was obtained in both cases. It is believed that erosion of the ice by the liquid falling film is responsible for most of the deviations.*

Introduction

One of the basic types of shell-and-tube exchangers employs the principle of a falling liquid film. The fluid is delivered to the top of a set of vertical tubes and is applied by means of a film distributor to the inside surface of the tubes, from where it falls by means of gravity, adhering to the inside surface of the tubes, to the bottom end and into a receiving tank. This paper is concerned with the rate of solidification of water in falling-film flow inside a short vertical tube.

Many authors have addressed themselves to the solution of the solidification problem. London and Seban [1] presented approximate analytical solutions for the slab, cylinder, and sphere which were based on the assumption that thermal-capacity effects may be neglected. They also presented experimental confirmation of the predicted water freezing rates [2]. Cochran [3] presented a literature review of several solutions on the solidification problem and demonstrated that the one-lumped-parameter approximation is sufficiently accurate for many problems of technical interest. Longwell [4] presented a graphical method for the solution of the solidification problem taking into account the heat capacity. It is noted that all of the above references are concerned with solidification in which the liquid is stationary relative to the heat sink.

Solidification in which the liquid is in motion relative to the heat sink has been studied by Siegel and Savino [8] by applying analytical procedures to the investigation of a frozen layer that forms when warm liquid flows over a cold plate. The plate was cooled below the freezing temperature of the liquid by a coolant flowing along the other side of the plate. Stephan [10] investigated analytically the solidification of fluids flowing along a plane wall and through a pipe, assuming a finite ambient heat transfer and known heat flux to the solid–liquid interface. Özişik and Mulligan [11] gave an analytical presentation of the transient freezing of a liquid flowing inside a circular tube under the assumption of a constant tube-wall temperature, constant properties, a slug-flow velocity profile, and quasi-steady-state heat conduction in the solid phase.

Lock and Nyren [12] made a theoretical analysis of ice formation in a long circular tube cooled by external convection utilizing a regular-perturbation expansion for the temperature and interface location.

Zerkle and Sunderland [13] studied the liquid solidification at the inner surface of a circular tube upon laminar-flow heat transfer and pressure drop. Steady-state conditions and uniform wall temperatures were assumed. Their experimental results showed considerable deviations from the theoretical, which was attributed to free convection by the authors.

The purpose of this investigation was twofold:

1 To present the results of an experimental investigation of the solidification rates for water at its fusion temperature in falling-film flow inside a short vertical tube.

2 To compare the experimental results to those predicted from the expression developed by London and Seban [1].

Experimental Apparatus and Operating Procedure

The experimental apparatus consisted of a thin-wall copper tube mounted vertically in the center of a duct, with 32 deg F water flowing as a film on the inside surface of the tube. Refrigerated air of predetermined temperature and velocity passed through the duct. This cooled the tube and solidified a portion of the water film flowing inside the tube, Figs. 1 and 2.

The purpose of the water-supply system was to insure that 32

[1] Numbers in brackets designate References at end of paper.

Contributed by the Heat Transfer Division for publication (without presentation) in the Journal of Heat Transfer. Manuscript received by the Heat Transfer Division May 18, 1971; revised manuscript received September 29, 1971. Paper No. 72-HT-D.

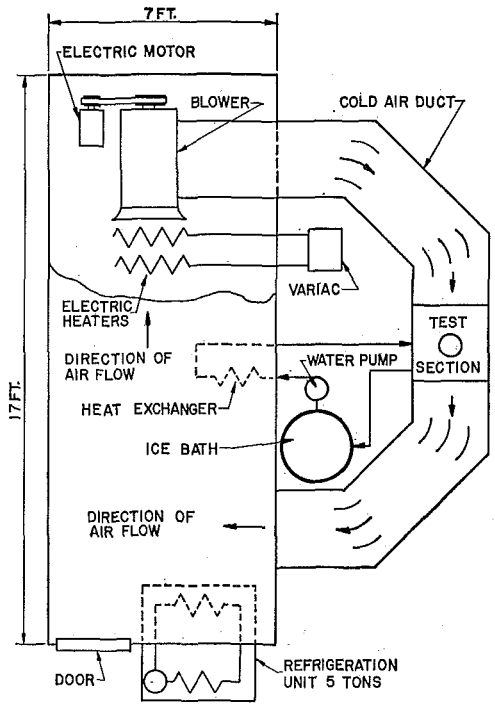

Fig. 1 Experimental apparatus

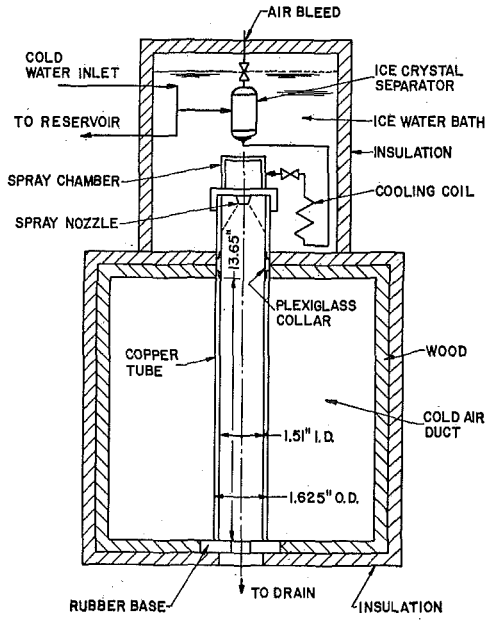

Fig. 2 Test section

deg F water entered the copper tube and to establish a falling-film flow on the inside surface of the tube. The water-supply system was a closed-loop system. From the iced-water reservoir, 32 deg F water was pumped to the air–water heat exchanger. Upon leaving the air–water heat exchanger the water stream separated into two branches. One branch was directed back to the iced-water reservoir while the other was directed to the ice-crystal separator and then through a cooling coil to a spray nozzle. The nozzle directed the 32 deg F water into falling-film flow inside the vertical copper tube. The water leaving the copper tube was then directed back to the iced-water reservoir or to a drain.

The refrigerated-air-supply system was also a closed-loop system. From a room 17 × 7 × 7 ft, refrigerated air was removed by a blower and discharged into the cold-air duct which contained the test section. After leaving the test section the air stream was directed back to the refrigerated room. The temperature of the refrigerated room was maintained by means of a 60,000-Btu/hr refrigeration unit. Two heating units were placed on the suction side of the blower in order to maintain precise temperature control of the cold-air stream. The maximum refrigerated-air-stream velocity to the test section was 33.76 ft/sec. Using sharp-edge orifice plates, air-stream velocities were reduced to 15.4 fps and 5.82 fps.

The outside coefficient of convective heat transfer h_0 for the tube was determined. In order to compute this coefficient it was necessary to measure the heat transferred across the tube wall, the temperature difference between the tube wall and outside air stream, and the outside area of the tube exposed to the air stream. The heat transferred across the tube wall was obtained by creating a situation similar to that for the solidification of the liquid falling film, except that the heat to be removed was provided by an electric heating element having its power input regulated by an autotransformer and measured by a wattmeter. The ends of the heating element as well as those of the tube were insulated in such a way that only radial heat transfer occurred in the region of the tube exposed to the air stream. The measurement of the air-stream temperature was obtained by two different thermocouple readings, and the outside wall temperature was obtained by averaging thermocouple readings at 12 locations. The results of these measurements are shown in Fig. 3.

Nomenclature

C_{ps} = specific heat at constant pressure of the solidified material, Btu/lb_m-deg F
D_o = outside diameter of the cylinder, ft
h_o = outside convective heat-transfer coefficient, Btu/hr-deg F-ft²
h_{sf} = latent heat of fusion, Btu/lb_m
k_f = thermal conductivity of convective fluid, Btu-ft/hr-deg F-ft²
k_s = thermal conductivity of solidified material, Btu-ft/hr-deg F-ft²
k_w = thermal conductivity of material in cylinder wall, Btu-ft/hr-deg F-ft²
L = length of cylinder, ft
ln = logarithms to base e
M = mass of solidified material, lb_m
M_T = mass of solidified material which would completely fill the cylinder = $\rho_s \pi r_i^2 L$, lb_m
$\dot{Q}$ = heat-transfer rate, Btu/hr
r = radial position from center of the tube, ft
r_f = radial distance to inside boundary of film, ft
r_{wi} = radial distance to inside wall of the tube, ft
r_{wo} = radial distance to outside wall of the tube, ft
r_s = radial distance to liquid–solid interface, ft
t = time, hr
T_s = fusion temperature of solidifying liquid, deg F
T_∞ = air-stream temperature, deg F
V_∞ = air-stream velocity, ft/hr
Δt = elapsed time of data run, hr
ρ_s = density of the ice, lb_m/ft^3

Dimensionless Quantities

M^* = dimensionless mass, defined by equation (7)
$\bar{M}^*$ = least-squares curve fit of M^* vs. τ^* data
Nu = Nusselt number = $h_o D_o/k_f$
r^* = dimensionless radius, defined by equation (3)
$\bar{r}^*$ = least-squares curve fit of r^* vs. τ^* data
R^* = dimensionless surface resistance, defined by equation (4)
Re = Reynolds number = $V_\infty D_o/\nu_f$
W^* = dimensionless cylinder-wall resistance, defined by equation (5)
τ^* = dimensionless time, defined by equation (6)
$\tau_{eq}{}^*$ = values computed from equation (2)

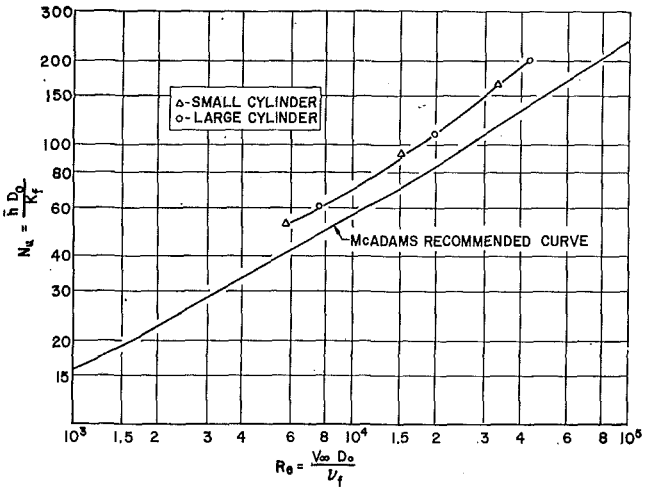

Fig. 3 Nusselt number vs. Reynolds number

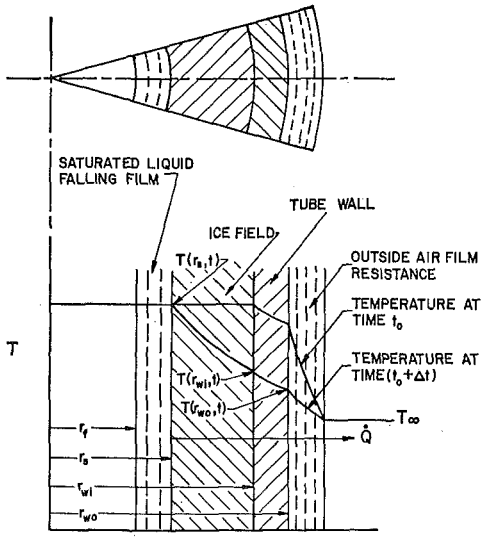

Fig. 4 Temperature profile

At the start of a series of tests, the refrigeration unit was activated and the blower turned on in order to obtain the desired air-stream temperature. At the same time, the water-supply system bypassing the test section was started. During this period an ice bath was provided which surrounded the ice-crystal separator and spray chamber. After steady-state conditions were obtained, the blower was stopped momentarily in order to insert the copper tube into the test section. The supply valve was then opened to allow 32 deg F water to enter the test section. The blower was then restarted. During the period of the test run, the water and air-stream temperatures were monitored to assure steady-state conditions. At the end of the test run, the ice cylinder was removed from the test section and weighed. The inlet flow rate which was held constant through all test runs was 0.773 lb_m/min. The recorded data are contained in Table 1.

Correlation

The expression developed by London and Seban [1] for the rate of ice formation inside a vertical tube in which the saturated liquid is stationary is used to correlate the experimental data for the solidification of a liquid falling film. Their expression is based primarily on the assumptions that the heat capacity is negligible and the properties ρ_s, k_s, and c_{ps} are constant for the ice field, and is given as (see Fig. 4):

$$\frac{1}{2} r^{*2} \ln r^* + \left[\frac{1}{4} + \frac{1}{2R^*} + \frac{1}{2W^*}\right](1 - r^{*2}) = \tau^* \quad (1)$$

or in terms of the mass ratio M^*

$$\frac{1}{2}(1 - M^*) \ln (1 - M^*)^{1/2} + \left[\frac{1}{4} + \frac{1}{2R^*} + \frac{1}{2W^*}\right] M^* = \tau^* \quad (2)$$

where

$$r^* = \frac{r_s}{r_{wi}} = (1 - M^*)^{1/2} \quad (3)$$

$$R^* = \frac{r_{wo} h_o}{k_s} \quad (4)$$

$$W^* = \frac{1}{\frac{k_s}{k_w} \ln \frac{r_{wo}}{r_{wi}}} \quad (5)$$

$$\tau^* = \frac{k_s(T_\infty - T_s)\Delta t}{\rho_s h_{sf} r_{wi}^2} \quad (6)$$

$$M^* = \frac{M}{M_T} = \frac{M}{\rho_s \P r_{wi}^2 L} \quad (7)$$

Observations and Conclusions

The values of M^* vs. τ^* as predicted by equation (2) and the values calculated from experimental data were plotted as shown in Fig. 5. The following observations and conclusions were made:

1 For a given value of τ^* the value of M^* predicted from equation (2) was in all cases greater than the value computed from experimental data. The difference between the predicted and experimental values as a percentage of the predicted value was computed for various experimental runs as shown in Table 2.

Table 1 Experimental data

Run No.	Temp. Difference $T_s - T_\infty$, °F	Weight M, lb	Time t, min
1	12	0.256	30.00
2	12	0.374	45.00
3	12	0.463	60.00
4	12	0.494	61.33
5	12	0.495	60.00
6	12	0.567	75.00
7	12	0.665	90.00
8	12	0.730	110.00
9	12	0.739	105.00
10	12	0.749	110.00
11	12	0.758	110.00
12*	12	0.763	114.50
13	22	0.288	12.00
14	22	0.330	20.00
15	22	0.342	20.00
16	22	0.466	30.08
17	22	0.481	30.00
18	22	0.585	40.00
19	22	0.643	45.00
20	22	0.694	50.00
21	22	0.747	55.10
22	22	0.776	60.00
23	22	0.780	60.00
24*	22	0.821	63.11
25	32	0.208	8.00
26	32	0.310	12.50
27	32	0.406	17.00
28	32	0.488	21.00
29	32	0.557	25.00
30	32	0.612	27.50
31	32	0.633	30.00
32	32	0.647	30.00
33	32	0.667	32.25
34	32	0.707	35.00
35	32	0.747	37.00
36	32	0.767	39.00
37	32	0.794	41.50
38*	32	0.810	44.02

* Tube plugging condition.
Inlet water flow rate M = 350 gm/min = 0.733 lb_m/min.
Outside tube surface = 0.483 sq ft.

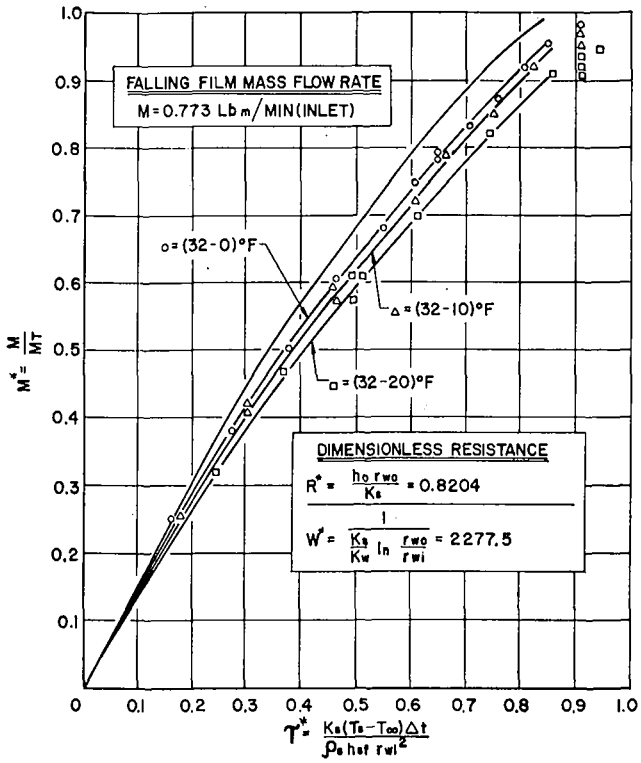

Fig. 5 Dimensionless mass vs. dimensionless time

2 The actual quantity of ice formed M^* was from 85 to 95 percent of the value of M^* predicted from equation (2). As the value of the temperature difference between the liquid falling film and the cold-air stream increased, the predicted and experimental values were in closer agreement. It is believed that part of this difference between the predicted and experimental values was due to the erosion of the ice by the falling liquid film. This erosion effect diminished as the temperature difference increased. It will be remembered that equation (2) does not allow for this possibility.

Also, since the inlet water temperature would be no lower than 32 deg F, but due to experimental error might be slightly higher, the actual quantity of ice formed would always be lower than that predicted by equation (2).

3 The equation used to compute the values of r^* from the experimental data was:

$$r^{*2} = 1 - M^* = 1 - \frac{M}{\rho_s \pi r_{wi}^2 L} \tag{8}$$

which has a derivative of:

$$\frac{dr^*}{dM^*} = -\frac{1}{2r^*} \tag{9}$$

Table 2

Run No.	Temp. Difference	r^*	M^* Difference
1	(32–20)°F	0.2471	15.06%*
2	(32–20)°F	0.3707	13.58%
5	(32–20)°F	0.4943	10.19%
7	(32–20)°F	0.7415	10.78%
14	(32 10)°F	0.3021	8.68%*
16	(32–10)°F	0.4544	9.40%
18	(32–10)°F	0.6042	9.31%
21	(32–10)°F	0.8323	6.37%
26	(32–0)°F	0.2746	6.54%*
28	(32–0)°F	0.4614	6.32%
31	(32–0)°F	0.6591	7.95%
35	(32–0)°F	0.8129	5.20%

* Maximum value computed for a given temperature difference.

An examination of the rate of change or r^* with respect to M^* shows that as $r \rightarrow 0$, a slight increase in the mass of ice would affect the value of r^* greatly. Thus the ability of equation (1) to predict an acceptable value of r^* should not be expected over the range of r^* greater than 0.5. However, for $r^* \leq 0.5$ the value of r^* computed from the experimental data was a maximum of 1.16 times the value predicted by equation (1). As the temperature difference across the ice field increased, the predicted value of r^* and the r^* computed from experimental data were in closer agreement.

Acknowledgments

The authors gratefully acknowledge the assistance of Mr. Robert M. Gregg, a graduate student at the University of Louisville, who built the apparatus and obtained the experimental data, and Dr. Henry Heuser, president of Henry Vogt Machine Company, Louisville, Ky., for financial assistance in obtaining some of the necessary experimental equipment.

References

1 London, A. L., and Seban, R. A., "Rate of Ice Formation," TRANS. ASME, Vol. 65, 1943, pp. 771 778.

2 Seban, R. A., and London, A. L., "Experimental Confirmation of Predicted Water-Freezing Rates," TRANS. ASME, Vol. 67, 1945, pp. 39-44.

3 Cochran, D. L., "An Investigation of Rates of Solidification," *Refrigeration Engineering*, Vol. 63, No. 8, Aug. 1955, pp. 49 56.

Table 3 Dimensionless groups computed from experimental data

Run No.	r^*	M^*	r^*	τ_{eq}^*	$\bar{M}^*$	$\bar{r}^*$
1	0.2471	0.3163	0.8268	0.2069	0.3133	0.8287
2	0.3707	0.4621	0.7334	0.3139	0.4589	0.7356
3	0.4943	0.5720	0.6541	0.4010	0.5936	0.6375
4	0.5053	0.6103	0.6242	0.4330	0.6050	0.6285
5	0.4943	0.6116	0.6232	0.4340	0.5936	0.6375
6	0.6179	0.7005	0.5472	0.5121	0.7144	0.5344
7	0.7415	0.8216	0.4223	0.6296	0.8183	0.4263
8	0.9063	0.9019	0.3131	0.7186	0.9246	0.2745
9	0.8651	0.9131	0.2948	0.7320	0.9018	0.3133
10	0.9063	0.9254	0.2731	0.7473	0.9246	0.2745
11	0.9063	0.9365	0.2519	0.7615	0.9246	0.2745
12	0.9434	0.9427	0.2393	0.7692	0.9428	...
13	0.1812	0.2570	0.8619	0.1658	0.2666	0.8564
14	0.3021	0.4077	0.7695	0.2730	0.4142	0.7654
15	0.3021	0.4225	0.7599	0.2840	0.4142	0.7654
16	0.4544	0.5758	0.6513	0.4041	0.5801	0.6480
17	0.4531	0.5943	0.6369	0.4195	0.5657	0.6590
18	0.6042	0.7228	0.5265	0.5325	0.7285	0.5211
19	0.6797	0.7944	0.4533	0.6018	0.7973	0.4502
20	0.7552	0.8575	0.3775	0.6678	0.8609	0.3729
21	0.8323	0.9229	0.2776	0.7442	0.9179	0.2865
22	0.9063	0.9588	0.2030	0.7915	0.9619	0.1951
23	0.9063	0.9637	0.1905	0.7985	0.9619	0.1951
24	0.9534	...	...	...	...	...
25	0.1757	0.2570	0.8619	0.1658	0.2683	0.8554
26	0.2746	0.3830	0.7854	0.2548	0.3911	0.7803
27	0.3735	0.5016	0.7059	0.3445	0.5022	0.7055
28	0.4614	0.6029	0.6301	0.4267	0.5952	0.6362
29	0.5492	0.6882	0.5584	0.5009	0.6843	0.5619
30	0.6042	0.7561	0.4938	0.5641	0.7383	0.5116
31	0.6591	0.7821	0.4668	0.5894	0.7904	0.4578
32	0.6591	0.7994	0.4479	0.6068	0.7904	0.4578
33	0.7085	0.8364	0.4194	0.6321	0.8352	0.4059
34	0.7690	0.8735	0.3556	0.6857	0.8864	0.3370
35	0.8129	0.9229	0.2776	0.7442	0.9200	0.2829
36	0.8569	0.9476	0.2288	0.7762	0.9493	0.2250
37	0.9118	0.9810	0.1378	0.8247	0.9784	0.1469
38	0.9671	1.0008	...	...	...	...

$R^* = 0.8204$.

The dimensionless groups shown in Table 2 were obtained as follows:

The r^*-column values were computed from equation (6) using experimental data.

The M^*-column values were computed from equation (7) using experimental data.

The r^*-column values were computed from equation (3) using the values in the M^* column.

The τ_{eq}^*-column values were computed from equation (2) using the M^*-column values.

The $\bar{M}^*$-column values were computed from an empirical equation $\bar{M}^* = f(\tau^*)$ which was obtained by the method of least squares.

The $\bar{r}^*$-column values were computed from an empirical equation $\bar{r}^* = f(\tau^*)$ which was obtained by the method of least squares.

Thermal properties of ice:

Density: $\rho_s = 57.3$ lb$_m$/cu ft (avg. 0–32 deg F).

Thermal conductivity: $k_s = 1.34$ Btu-ft/hr-ft^2 deg F (avg. 0–32 deg F).

Latent heat of fusion: $h_{sf} = 143.4$ Btu/lb$_m$ (at 32 deg F).

4 Longwell, P. A., "Graphical Method for Solution of Freezing Problems," *AIChE Journal*, Vol. 4, 1958, pp. 53–57.

5 Carslaw, H. S., and Jaeger, J. C., *Conduction of Heat in Solids*, 2nd ed., Clarendon Press, Oxford, England, 1959, pp. 282–296.

6 Baxter, D. C., "The Fusion Times of Slabs and Cylinders," JOURNAL OF HEAT TRANSFER, TRANS. ASME, Series C, Vol. 84, No. 4, Nov. 1962, pp. 317–326.

7 Poots, G., "The Application of Integral Methods to the Solution of Problems Involving the Solidification of Liquids Initially at the Fusion Temperature," *International Journal of Heat and Mass Transfer*, Vol. 5, 1962, pp. 525–531.

8 Siegel, R., and Savino, J. M., "An Analysis of the Transient Solidification of a Flowing Warm Liquid on a Convectively Cooled Wall," *Proceedings of the 3rd International Heat Transfer Conference*, Vol. 4, 1966, pp. 141–151.

9 Tao, L. C., "Generalized Numerical Solution of Freezing a Saturated Liquid in Cylinders and Spheres," *AIChE Journal*, Vol. 13, 1967, pp. 165–169.

10 Stephan, F., "Influence of Heat Transfer on Melting and Solidification in Force Flow," *International Journal of Heat and Mass Transfer*, Feb. 1969, pp. 199–214.

11 Özişik, M. N., and Mulligan, J. C., "Transient Freezing of Liquids in Forced Flow Inside Circular Tubes," JOURNAL OF HEAT TRANSFER, TRANS. ASME, Series C, Vol. 91, No. 3, Aug. 1969, pp. 385–390.

12 Lock, G. S. H., and Nyren, R. H., "Analysis of Fully Developed Ice Formation in a Convectively Cooled Circular Tube," *International Journal of Heat and Mass Transfer*, June 1971, pp. 825–834.

13 Zerkle, R. D., and Sunderland, J. E., "The Effect of Liquid Solidification in a Tube Upon Laminar-Flow Heat Transfer and Pressure Drop," JOURNAL OF HEAT TRANSFER, TRANS. ASME, Series C, Vol. 90, No. 2, May 1968, pp. 183–190.

J. W. YANG
Associate Professor,
Department of Mechanical Engineering,
State University of New York at Buffalo,
Buffalo, N. Y.
Assoc. Mem. ASME

Periodic Heat Transfer in Straight Fins

The characteristics of heat transfer in straight fins with periodic variation of base temperature have been determined analytically. The heat-transfer process is governed by three dimensionless parameters: the conventional fin parameter N, the frequency parameter B, and the amplitude parameter A. The effects of these parameters on the instantaneous and average heat flow rates, axial and time-wise temperature distributions, and instantaneous and average fin efficiencies are demonstrated by several examples. In general, the time-average fin efficiency is reduced by the periodic variation of the base temperature.

Introduction

HEAT TRANSFER in extended surfaces has been extensively studied under various conditions. Most of the studies were restricted to steady-state heat transfer. In practice, extended surfaces are frequently employed under unsteady conditions. Either the base temperature or the ambient temperature may be time-dependent. Recently, Hung[1] has presented an analysis of the heat transfer in thin fins with stochastic base temperature. The root-mean-square temperature and power spectral density were calculated with pure stochastic and Markoffian base temperature. It appears the case of heat transfer in thin fins with periodic variation of base temperature is not available in literature. Many applications of this type of heat-transfer process can be found in engineering systems. For example, fins attached to electrical or electronic components are frequently subjected to periodic heat transfer in automatic control systems.

This paper presents an analytical method for determining the periodic heat-transfer characteristics in straight convection fins. The physical parameters which govern the transport process are defined. The effects of periodic variation of the base temperature on the flow rate, fin temperature distribution, and fin efficiency are demonstrated through several examples.

Analysis

Consider a thin straight fin with its base temperature varying in a periodic manner as shown in Fig. 1. It is assumed that the base temperature t_b oscillates around a mean temperature t_m which is greater than the ambient temperature t_a. The variation of the base temperature is described by the following equation:

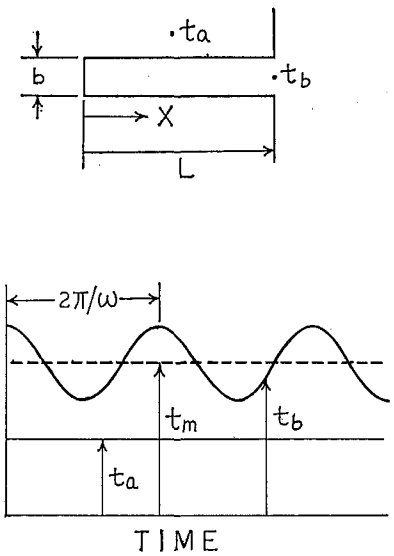

Fig. 1 Fin geometry and base temperature

$$t_b - t_m = (t_m - t_a)A \cos \omega\theta \tag{1}$$

where A is the dimensionless amplitude parameter and $\omega/2\pi$ is the frequency of the oscillation. In practice, A is a positive number less than unity.

The governing differential equation of unit depth, under the usual assumptions for one-dimensional fins, is

$$\frac{\partial^2 t}{\partial x^2} - \frac{2h}{bk}(t - t_a) = \frac{\rho c}{k}\frac{\partial t}{\partial \theta} \tag{2}$$

Equation (1) specifies the boundary condition at $x = L$. At the tip of the fin, it is assumed that

$$\frac{\partial t}{\partial x} = 0 \qquad \text{at} \quad x = 0 \tag{3}$$

[1] Hung, H. M., "Heat Transfer of Thin Fins With Stochastic Root Temperature," JOURNAL OF HEAT TRANSFER, TRANS. ASME, Series C, Vol. 91, No. 1, Feb. 1969, pp. 129–134.

Contributed by the Heat Transfer Division for publication (without presentation) in the JOURNAL OF HEAT TRANSFER. Manuscript received by the Heat Transfer Division June 22, 1971. Paper No. 72-HT-E.

In dimensionless form, equations (1)–(3) become

$$\frac{\partial^2 T}{\partial X^2} - N^2 T = \frac{\partial T}{\partial \tau} \tag{4}$$

$$\frac{\partial T}{\partial X} = 0 \quad \text{at} \quad X = 0 \tag{5}$$

$$T_b = 1 + A \cos(B\tau) \quad \text{at} \quad X = 1 \tag{6}$$

in which

$$N = \left(\frac{2hL^2}{bk}\right)^{1/2} \quad \text{and} \quad B = \frac{\omega L^2}{\alpha} \tag{7}$$

For large time, a solution can be obtained by letting the fin temperature $T(X, \tau)$ be composed of two components: a steady component $T_1(X)$ and an oscillatory component $T_2(X, \tau)$. The two components satisfy the following two sets of equations respectively:

$$\frac{d^2 T_1}{dX^2} - N^2 T_1 = 0 \tag{8}$$

$$\frac{dT_1}{dX} = 0 \quad \text{at} \quad X = 0 \tag{9}$$

$$T_1 = 1 \quad \text{at} \quad X = 1 \tag{10}$$

and

$$\frac{\partial^2 T_2}{\partial X^2} - N^2 T_2 - \frac{\partial T_2}{\partial \tau} = 0 \tag{11}$$

$$\frac{\partial T_2}{\partial X} = 0 \quad \text{at} \quad X = 0 \tag{12}$$

$$T_2 = A \cos(\beta\tau) \quad \text{at} \quad X = 1 \tag{13}$$

The steady component T_1 is obtained immediately through equations (8)–(10)

$$T_1 = \cosh(NX)/\cosh N \tag{14}$$

For the oscillatory component, a complex temperature T_c is defined as

$$T_c = T_2 + iT_3 \tag{15}$$

where T_3 is the auxiliary part of T_2. The auxiliary temperature T_3 satisfies equations (11)–(13) except the periodic boundary-condition function has a shift of $\pi/2$, i.e., sin $(\omega\theta)$ instead of cos $(\omega\theta)$. The complex temperature T_c is the solution of the following equations:

$$\frac{\partial^2 T_c}{\partial X^2} - N^2 T_c - \frac{\partial T_c}{\partial \tau} = 0 \tag{16}$$

$$\frac{\partial T_c}{\partial X} = 0 \quad \text{at} \quad X = 0 \tag{17}$$

$$T_c = Ae^{iB\tau} \quad \text{at} \quad X = 1 \tag{18}$$

Further, it is proposed that the complex temperature is in the form

$$T_c = A\psi(X)e^{iB\tau} \tag{19}$$

Equations (16)–(18) can therefore be reduced to

$$\frac{d^2\psi}{dX^2} - (N^2 + iB)\psi = 0 \tag{20}$$

$$\frac{d\psi}{dX} = 0 \quad \text{at} \quad X = 0 \tag{21}$$

$$\psi = 1 \quad \text{at} \quad X = 1 \tag{22}$$

The solution of the function ψ is

$$\psi = \cosh[(u + iv)X]/\cosh(u + iv) \tag{23}$$

in which

$$u = \left[\frac{N^2 + (N^4 + B^2)^{1/2}}{2}\right]^{1/2}$$
$$v = \left[\frac{-N^2 + (N^4 + B^2)^{1/2}}{2}\right]^{1/2} \tag{24}$$

Now, taking T_2 as the real part of T_c, the complete temperature solution is obtained

$$T(X, \tau) = \cosh(NX)/\cosh N + (A/C)f(X, \tau) \tag{25}$$

where

$$C = (\cosh u \cos v)^2 + (\sinh u \sin v)^2 \tag{26}$$

$$\begin{aligned} f(X, \tau) = {} & \cosh u \cos v\,[\cosh(uX) \cos(vX) \cos(\omega\theta) \\ & - \sinh(uX) \sin(vX) \sin(\omega\theta)] \\ & + \sinh u \sin v\,[\cosh(uX) \cos(vX) \sin(\omega\theta) \\ & + \sinh(uX) \sin(vX) \cos(\omega\theta)] \end{aligned} \tag{27}$$

It is noted that the heat-transfer process is characterized by three parameters: N, B, and A. The parameter N is the standard fin parameter under steady-state conditions; the parameters B and A are the additional ones indicating the oscillatory nature of the problem. Among the three quantities, N and B, which specify the thermal properties of the fin material (α, k) and the geometry of the fin (b, L), are the design parameters upon which the performance of the fin depends.

Discussion of Results

Heat-Transfer Rate. The heat-transfer rate from the fin may now be evaluated in terms of the temperature gradient at the base

$$q = bk\left(\frac{\partial t}{\partial x}\right)_{x=L} \tag{28}$$

In dimensionless form, it becomes

Nomenclature

A = dimensionless amplitude parameter, equation (1)
b = fin thickness
B = dimensionless frequency parameter, equation (7)
c = heat capacity
C = constant, equation (26)
f = temperature function, equation (27)
h = heat-transfer coefficient
k = thermal conductivity
L = fin length
N = dimensionless fin parameter, equation (7)
q = heat flow rate per unit depth
$\bar{q}$ = average heat flow rate per unit depth, equation (30)
Q_c = cumulative heat flow rate, equation (31)
t = fin temperature
t_a = ambient temperature
t_b = fin base temperature
t_m = fin base mean temperature, equation (1)
T = $(t - t_a)/(t_m - t_a)$
T_b = $(t_b - t_a)/(t_m - t_a)$
u = constant, equation (24)
v = constant, equation (24)
x = coordinate
X = x/L
α = thermal diffusivity
η = fin efficiency, equation (33)
$\bar{\eta}$ = average fin efficiency, equation (35)
θ = time
τ = Fourier constant = $\alpha\theta/L^2$
ω = frequency

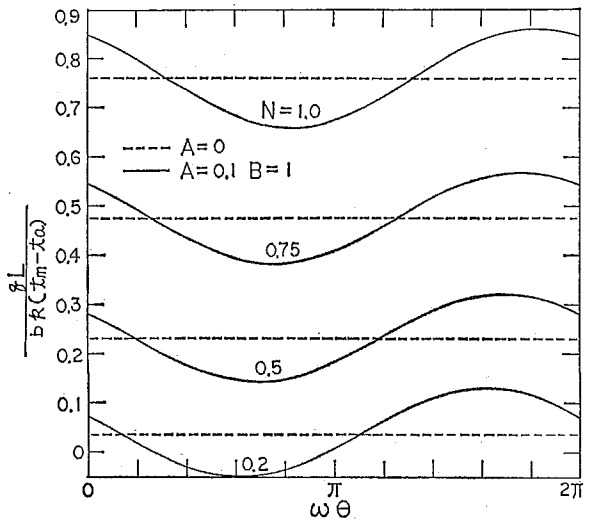

Fig. 2 Effect of parameter N on heat flow rate

$$\frac{qL}{bk(t_m - t_a)} = N \tanh N + \frac{A}{2C}\{\sinh(2u)[u\cos(\omega\theta) - v\sin(\omega\theta)] - \sin(2v)[v\cos(\omega\theta) + u\sin(\omega\theta)]\} \quad (29)$$

Thus, the heat-transfer rate is also composed of two components. The steady component is characterized only by the conventional fin parameter N. The oscillatory component is affected by all three parameters N, B, and A.

Some representative graphs of the heat flow rate are shown in Figs. 2 to 4. The effect of the parameter N is indicated in Fig. 2, in comparison with the steady-state case, for $A = 0.1$ and $B = 1$. The instantaneous heat flux follows a periodic variation as it oscillates around a mean value which is the heat-transfer rate at steady state. The variation of the parameter N has no effect on the amplitude of the oscillation. The phase difference changes, however, with the change of N. The minimum heat flow occurs at $0.6\pi/\omega$ for $N = 0.2$ and at $0.8\pi/\omega$ for $N = 1$, while the minimum base temperature occurs at π/ω. A shift of phase implies a time difference. Thus the heat flow rate leads the temperature variation by $0.4\pi/\omega$ at $N = 0.2$ and by $0.2\pi/\omega$ at $N = 1$.

Figs. 3 and 4 show the effect of the parameter B on the heat flow rate at $N = 0.5$ and $N = 0.1$ respectively. In both cases, the amplitude of the oscillation is greatly affected by the parameter B. The effect is less when the fin is operated at low frequency or the fin material is of high thermal diffusivity. It is interesting to note that negative heat flow results at larger values of B, i.e., high frequency or low thermal diffusivity. This phenomenon is enhanced when the parameter N is small as shown in Fig. 4. The negative heat flow implies a back heat flow from the fin to its base due to the thermal inertia of the fin. However, the oscillation of the heat flow has no effect on the average heat flow over a period of $2\pi/\omega$. From equation (29), it yields

$$\bar{q} = \frac{\omega}{2\pi}\int_0^{\frac{2\omega}{\pi}} q\,d\theta = \frac{bk(t_m - t_a)}{L} N \tanh N \quad (30)$$

The average heat flow equals that of the steady-state case. This fact is indicated by the symmetrical curves shown in Figs. 2 to 4. The cumulative heat flow over a complete cycle is determined from equation (29)

$$Q_c = \int_0^{\frac{2\pi}{\omega}} q\,d\theta \quad (31)$$

or

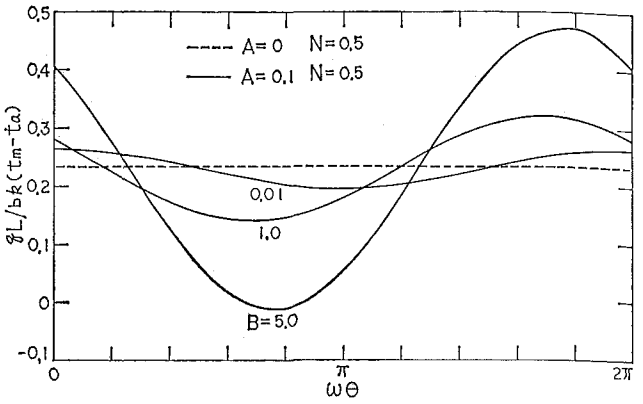

Fig. 3 Effect of parameter B on heat flow rate at $N = 0.5$

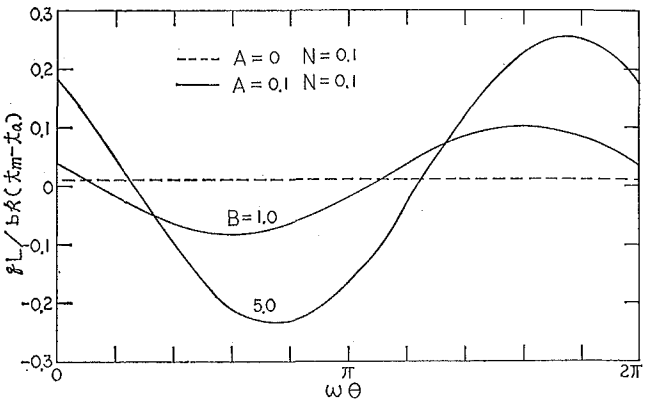

Fig. 4 Effect of parameter B on heat flow rate at $N = 0.1$

$$\frac{Q_c}{\rho LbC_p(t_m - t_a)} = \frac{2\pi N \tanh N}{B} \quad (32)$$

The fact that the cumulative heat flow of a complete cycle decreases with the increase of the frequency parameter B is apparent. The actual time $2\pi/\omega$ over which Q_c is calculated is proportional to $1/B$.

Temperature Distribution. The temperature distributions are interesting since they describe the detailed manner in which the heat transfer is affected by the oscillation of fin temperature. An inspection of equations (25)–(27) reveals that the oscillatory temperature component is directly proportional to the amplitude parameter A and is related in a complicated way to the parameters B and N. Some representative graphs are shown in Figs. 5 to 7 to demonstrate the effect of B and N on temperature distribution. Fig. 5 shows the axial temperature distribution at $A = 0.1$ and $B = 1$, corresponding to the heat flow graphs in Fig. 2. Again, the axial temperature varies with time around a mean value which is the steady-state temperature. It is interesting to note that the sign of the temperature gradient at the fin base changes with time at smaller values of N, Fig. 5(a). The negative gradient explains the back heat flow as indicated in Fig. 2. At larger values of N, the gradient remains positive which results in no back heat flow.

The effect of the parameter B on axial temperature distribution is shown in Fig. 6 at $N = 0.1$ and $A = 0.1$, corresponding to the heat flow graphs in Fig. 4. It is clear that the parameter B causes a larger axial temperature variation and produces negative heat flow. Further calculation shows that this effect is reduced when the parameter N is increased. Some time-wise temperature variations are shown in Fig. 7. Comparison with the imposed variation at fin base ($X = 1$) shows that at a given axial position, both the amplitude and phase of the temperature oscillation are affected by the variations of B and N. The ampli-

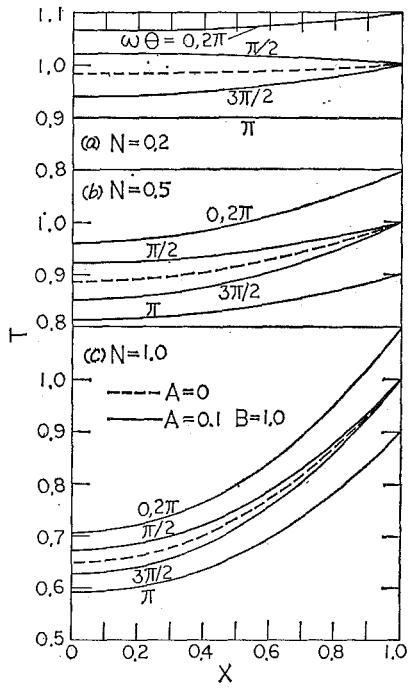

Fig. 5 Effect of parameter N on axial temperature distribution

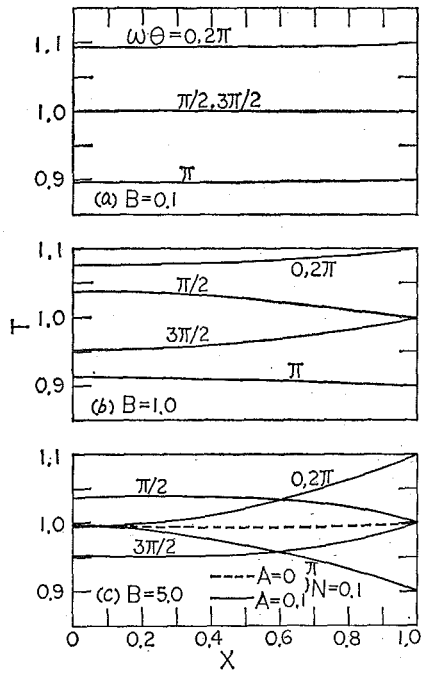

Fig. 6 Effect of parameter B on axial temperature distribution

tude decreases and the phase difference increases with the increase of B. It appears that the parameter N has no significant effect on the oscillation of temperature. Only a large change of temperature level in the axial direction is produced by the variation of N.

Fin Efficiency. The heat-transfer performance of the fin can be expressed in terms of the fin efficiency, which is defined as the ratio of the actual heat transfer to heat transfer from fin surface at base temperature

$$\eta = \frac{q}{2(t_b - t_a)Lh} \tag{33}$$

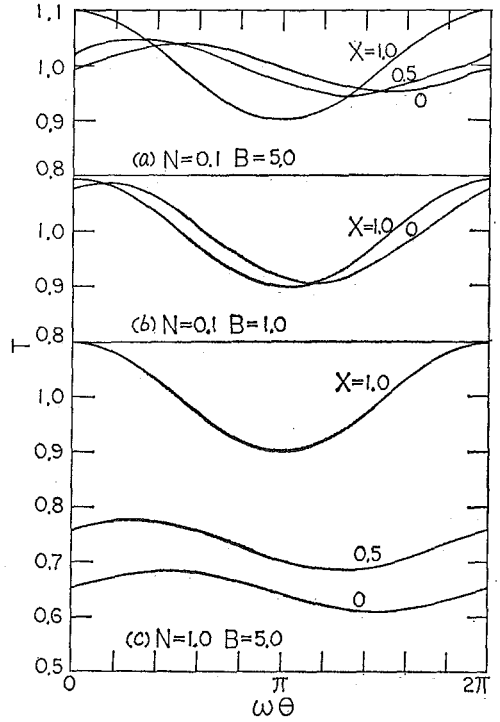

Fig. 7 Representative curves of time-wise temperature variation

Substituting equations (1) and (29) into the above equation gives the instantaneous fin efficiency

$$\eta = \frac{\tanh N}{N(1 + A\cos\omega\theta)} + \frac{A}{N^2C}\left[(u\sinh u\cosh u - v\cos v\sin v)\frac{\cos(\omega\theta)}{1 + A\cos(\omega\theta)} - (v\sinh u\cosh u + u\cos v\sin v)\frac{\sin(\omega\theta)}{1 + A\cos(\omega\theta)}\right] \tag{34}$$

It has been noted that both the temperature and heat flow are composed of a steady component and an oscillatory component. Contrary to this fact, all components of the fin efficiency in equation (34) are time-dependent. A larger oscillation of η is thus expected. On the other hand, the efficiency is time-independent if the denominator and the numerator in equation (33) are in phase. These facts are demonstrated in Figs. 8 and 9. It is seen in Fig. 8 that the efficiency is practically time-independent at larger values of N. The amplitude of the oscillation increases significantly as the parameter N is reduced. The effect of parameter B is shown in Fig. 9. The oscillation of the efficiency increases with the increase of B. This effect is enhanced at small N. An examination of Figs. 2 to 4 reveals that the phase difference between the base temperature and the heat flow is smaller at large N and small B; the phase difference becomes larger when N is reduced and B is increased.

Finally, in the evaluation of fin performance, it is more meaningful to determine the average fin efficiency over a complete cycle. The average fin efficiency is defined as

$$\bar{\eta} = \frac{\omega}{2\pi}\int_0^{\frac{2\pi}{\omega}} \eta d\theta \tag{35}$$

Substituting equation (34) into the above equation gives

$$\bar{\eta} = \frac{\tanh N}{N(1 - A^2)^{1/2}} + \frac{A}{2\pi CN^2}(u\sinh u\cosh u - v\cos v\sin v)I \tag{36}$$

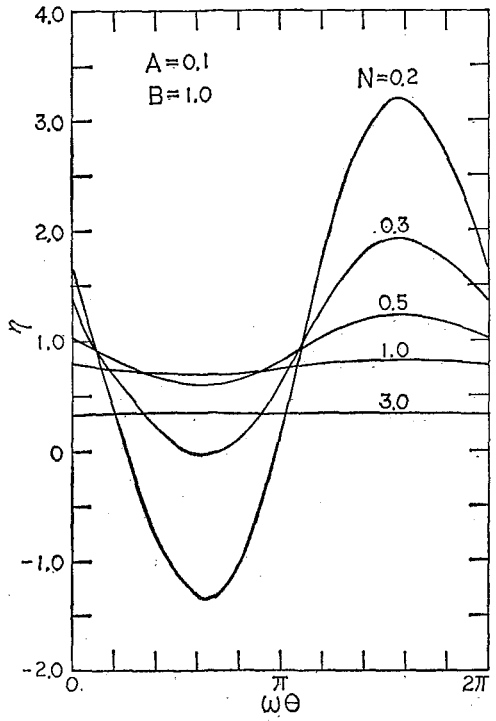

Fig. 8 Effect of parameter N on instantaneous fin efficiency

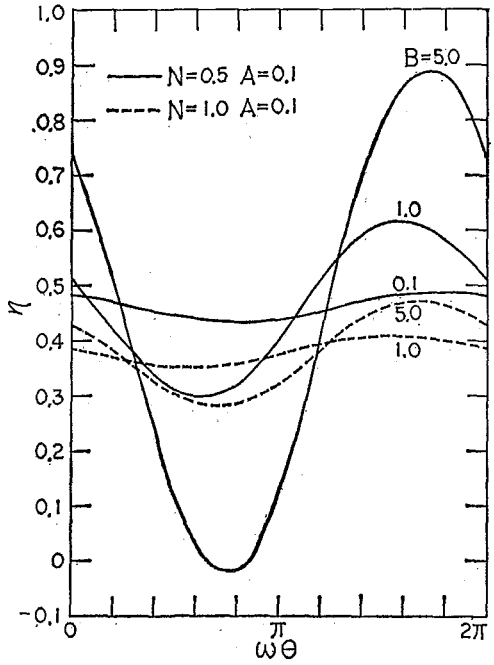

Fig. 9 Effect of parameter B on instantaneous fin efficiency

where

$$I(A) = \int_0^{2\pi} \frac{\cos(\omega\theta)}{1 + A\cos(\omega\theta)}\, d(\omega\theta) \tag{37}$$

Some representative graphs of the average efficiency are shown in Fig. 10 for $A = 0.1$ and $A = 0.05$. It is noted that the oscillation of base temperature affects the average efficiency only when the parameter N is sufficiently small. For small values of N, the parameters B and A reduce the average efficiency significantly. The behavior can be explained by considering the limiting cases of equation (36). It can be shown that

$$\begin{aligned} \bar{\eta} &\to -\infty \quad \text{as} \quad N \to 0 \quad \text{for} \quad B \neq 0, A \neq 1 \\ &\to \frac{1}{(1 - A^2)^{1/2}} \quad \text{as} \quad N \to 0 \quad \text{for} \quad B = 0 \\ &\to 0 \quad \text{as} \quad N \to \infty \end{aligned} \tag{38}$$

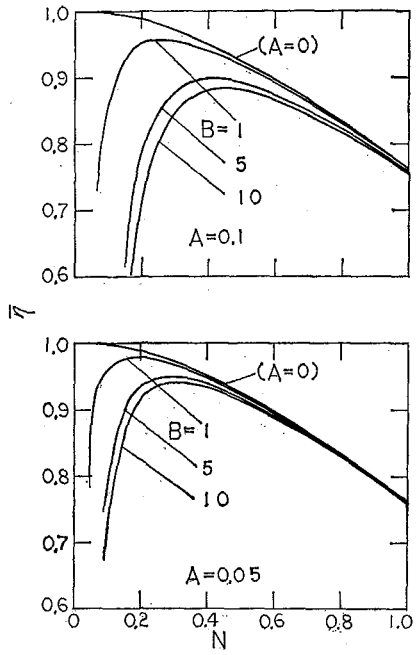

Fig. 10 Average fin efficiency

Conclusions

An analytical method has been developed to determine the heat-transfer process in straight fins with periodic variation of base temperature. The process is governed by three parameters: N, B, and A.

The heat flow rate, temperature, and fin efficiency exhibit a periodic oscillation with the imposed base temperature. The amplitude and phase of the oscillation depend on the three parameters. The oscillation is enhanced when the parameter N is reduced or the parameter B is increased.

Back heat flow occurs when N is small. The oscillation of heat flow has no effect on the time-average heat flow rate.

The time-average efficiency is practically not affected by the oscillation of base temperature when $N > 1$. When $N < 1$, the time-average efficiency is reduced by the increase of parameters B and A.

AVRAM MARKOWITZ
Senior Engineer,
Raytheon Co.,
Bedford, Mass.
Assoc. Mem. ASME

B. B. MIKIC
Associate Professor,
Department of Mechanical Engineering,
Massachusetts Institute of Technology,
Cambridge, Mass.
Mem. ASME

A. E. BERGLES
Professor,
School of Mechanical Engineering,
Georgia Institute of Technology,
Atlanta, Ga.
Mem. ASME

Condensation on a Downward-facing Horizontal Rippled Surface

An analytical investigation is presented for film condensation on a downward-facing horizontal doubly rippled surface. Small undulations having constant radius of curvature are combined with larger cylindrical grooves designed to aid condensate runoff. A direct expression for the condensate film thickness at the top of an undulation crest, as well as on a small-diameter horizontal cylinder, is derived. An upper-bound expression for the condensation rate on the rippled surface is then obtained which predicts that the condensation rate will be five times the rate attainable on a flat horizontal surface of the same projected area. This analytical expression is compared with experimental data.

Introduction

The rapidly increasing use of high-speed high-power electronic components has necessitated the development of electronic cooling systems which employ boiling heat transfer to dielectric fluids. For systems requiring a high degree of reliability and long operating life, the vapor generated must be condensed and recirculated. In the design of pool boilers for electronic components, space limitations and packaging constraints dictate the use of horizontal condensing surfaces of minimum area. It is, therefore, important to examine techniques for augmenting heat transfer in condensation of dielectric fluids on horizontal surfaces.

Condensation occurs when a subcooled surface is exposed to saturated or supersaturated vapor. The liquid condensate formed at the surface normally spreads out and establishes a stable film. Condensation then occurs on the vapor–liquid interface and the heat released is conducted through the liquid film to the condenser surface. However, when the liquid does not wet the surface, individual droplets form, condensation occurs on the drop surface, and the released heat is conducted through the liquid drops to the condenser surface. Most of the heat transfer in dropwise condensation occurs through drops in early stages of growth; as a result heat-transfer coefficients in dropwise condensation are typically one or two orders of magnitude higher than in film condensation [1].[1] Dropwise condensation thus appears to be the obvious technique for increasing the rate of condensation. However, in order to maintain this mode of condensation on a condensing surface, the surface must be treated with a promoter which repels the liquid molecules while being strongly attracted to the surface itself.

A substantial amount of work has been done in identifying successful promoters for dropwise condensation of water vapor and some organic vapors [2]. However, due to the extreme wetting characteristics of fluids generally used in electronic cooling, no promoters have been found for these fluids. As a consequence other augmentation techniques must be considered.

In film condensation the rate of heat transfer is governed by thermal conduction through the liquid film adhering to the surface. Consequently, if augmentation of film condensation is to be achieved, some way must be found to thin the liquid film. In 1953, Gregorig [3], while studying condensation on wavy surfaces, noted that surface tension could give rise to large pressure gradients in the liquid film due to the varying curvature of the condensate surface. Large pressure gradients necessarily lead to thin films, and coefficients of heat transfer several times greater than those observed in normal film condensation can be achieved. Gregorig thus proposed that improved vertical condenser tubes could be made by placing grooves of the proper geometric form parallel to the tube axis. The profile suggested by Gregorig utilized a gradually decreasing solid-surface curvature to produce a very thin, but nearly uniform, condensate film. The same general concept is also valid for a solid surface of constant curvature, which is easier to form in practical applications. This general technique has since been extended to horizontal condenser tubes [4] and vertical-tube preheaters and evaporators [12–14], but cannot be directly applied to flat horizontal surfaces.

On downward-facing plane horizontal surfaces, condensate removal is normally accomplished by drop formation resulting from the growth of disturbances on the liquid–vapor interface [5]. Consequently, it is not sufficient to provide undulations on the

[1] Numbers in brackets designate References at end of paper.

Contributed by the Heat Transfer Division of The American Society of Mechanical Engineers and presented at the AIChE-ASME Heat Transfer Conference, Denver, Colo., August 6–9, 1972. Manuscript received by the Heat Transfer Division March 29, 1971. Paper No. 72-HT-33.

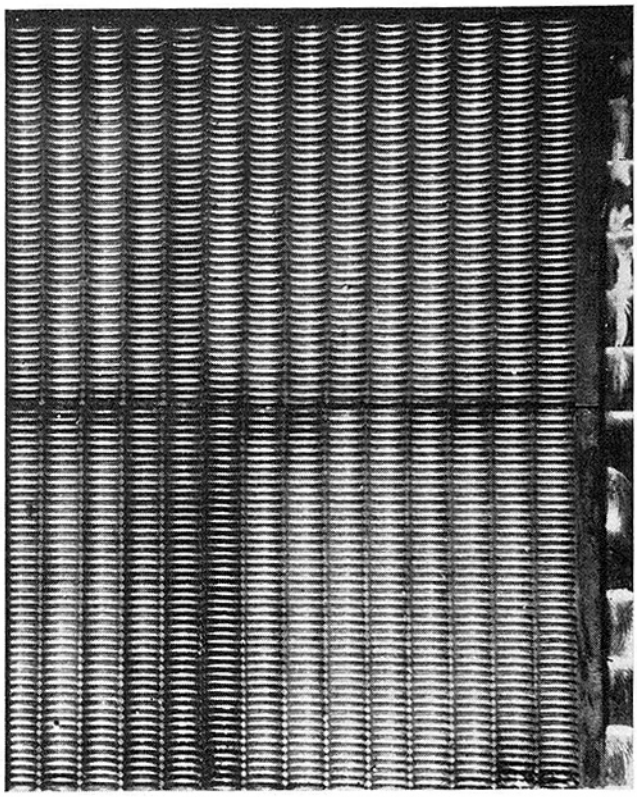

Fig. 1 Photograph of doubly rippled surface

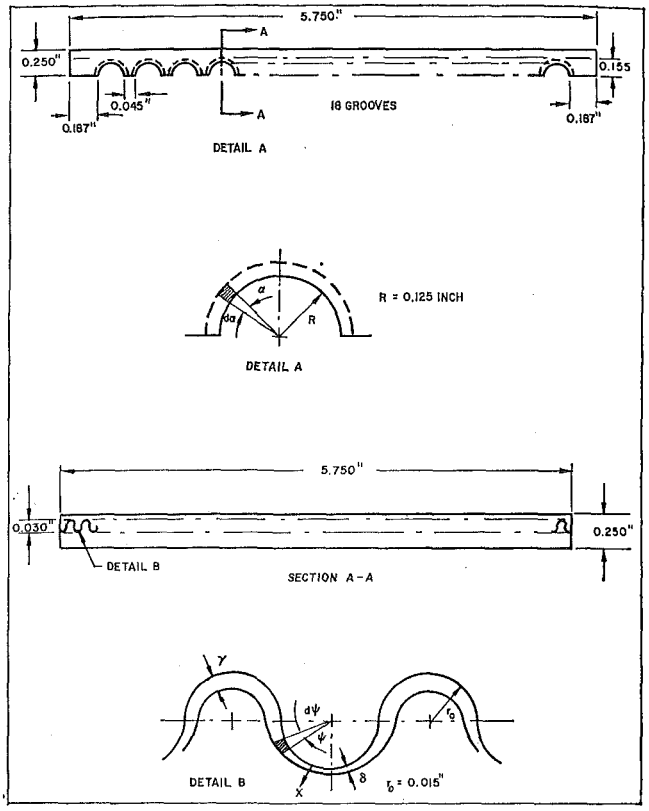

Fig. 2 Schematic and coordinate system for doubly rippled surface

condenser surface; instead a two-dimensional profile as shown in Figs. 1 and 2 is required to facilitate proper draining of the condensate. The doubly rippled surface developed for this study consisted of 18 parallel semicircular grooves of 0.125-in. radius on a 5.75-in. square plate. The internal surface of the grooves contained sinusoidal-like undulations with constant 0.015-in. radius of curvature.[2] The total surface area of the doubly rippled surface was 2.38 times its projected area.

On such a surface, the vapor condensed on the crest of an undulation is pumped by surface-tension forces into the undulation trough. Along the crest, the film thickness, and hence the radius of curvature of the liquid–vapor interface, increases with increasing angle Ψ. The static pressure in the thin liquid film decreases with increasing Ψ, thus yielding the pressure gradient required to pump the condensed liquid into the trough. For small radii of curvature, this pumping can be achieved against the force of gravity.

From the trough the condensate flows by gravity along the arch of the grooves provided in the surface. At the base of the arch, the condensate drips off the surface.

[2] This dimension was suggested by the characteristics of the surface developed by Gregorig [3].

Analysis

At the Undulation Crest. The condensate on a surface undulation shown in Fig. 2 forms a laminar film which flows along the surface. Considering a small-volume element $r_0 d\Psi(\delta - x)$, assuming that the film is thin, $\delta \ll r_0$, and neglecting Ψ-direction momentum changes, a force balance may be written in the Ψ direction as

$$-\mu \frac{dv}{dx} r_0 d\Psi = -g \cos \alpha \sin \Psi(\rho - \rho_v)(\delta - x) r_0 d\Psi + \frac{\partial p_\sigma}{\partial \Psi}(\delta - x) d\Psi \quad (1)$$

Nomenclature

A = surface area
A_p = projected area of rippled surface
c = nondimensional parameter defined in equation (15)
g = gravitational acceleration
g = gravitational constant, 32.17 lb_f-ft/lb_m-sec
h = heat-transfer coefficient
h_{fg} = latent heat of condensation or evaporation
h_{fg}' = $h_{fg} + 0.68 c_p(T_s - T_c)$
k = thermal conductivity
p = pressure
p_σ = refers to pressure gradient due to surface tension
r_0 = radius of curvature of undulation
R = groove radius
S = distance along curved surface
T = temperature
v = velocity
w = ratio of crest to trough diameters
x, y = coordinate axes
α = angle along groove, measured from the vertical
Γ = mass rate of condensate flow per unit width
γ = condensate film thickness in undulation trough
δ = condensate film thickness on undulation crest
$\hat{\lambda}$ = nondimensional condensate film thickness
μ = dynamic viscosity
ρ = mass density
σ = surface tension
Ψ = angle along crest, measured from the vertical
$\hat{\Psi}$ = nondimensional crest angle defined in equation (15)

Subscripts

c = condenser surface
cr = refers to undulation crest
m = average value
0 = at $\Psi = 0$, top of crest
s = saturation
tr = refers to undulation trough
v = vapor

Superscript

$\bar{}$ = average value

Fluid properties pertain to the liquid phase unless otherwise noted.

where the pressure gradient $\partial p_\sigma/\partial\Psi$ is due to surface-tension forces. Rearranging terms

$$-\mu \frac{dv}{dx} r_0 d\Psi = \frac{\partial p_\sigma}{d\Psi}\left[1 - \frac{g \cos\alpha \sin\Psi(\rho - \rho_v)r_0}{\partial p_\sigma/\partial\Psi}\right](\delta - x)d\Psi \tag{2}$$

For values of $g \cos\alpha \sin\psi(\rho - \rho_v)r_0/(\partial p_\sigma/\partial\Psi) < \sim 0.1$, the gravitational term may be neglected relative to the surface-tension term. This relationship is strictly valid at $\Psi \simeq 0$ and $\alpha \simeq \pi/2$ and is approximately valid throughout the range $0 \leq \Psi \leq \pi/2$ and $0 \leq \alpha \leq \pi/2$ along the undulation crests of the surface considered. The elimination of the gravitational term reduces the complexity of equation (2) and can be expected to yield an upper-bound solution for the rate of condensation on a downward-facing undulation.

As a consequence of the thin-film assumption and the constant curvature of the solid surface for $0 < \Psi < \pi/2$, and in the interest of maintaining an upper-bound solution, changes in the center of curvature of the interface can be neglected. As a result, the pressure difference across the curvature of the liquid–vapor interface for $0 < \Psi < \pi/2$ is given by

$$p - p_v = \frac{\sigma}{r_0 + \delta} \tag{3}$$

But p_v is constant, and consequently

$$\frac{\partial p_\sigma}{\partial\Psi} = -\frac{\sigma}{(r_0 + \delta)^2}\frac{d\delta}{d\Psi} \tag{4}$$

or, for $\delta \ll r_0$,

$$\frac{\partial p_\sigma}{\partial\Psi} \cong -\frac{\sigma}{r_0^2}\frac{d\delta}{d\Psi} \tag{5}$$

Substituting for $\partial p_\sigma/\partial\Psi$ in equation (2) and neglecting the gravitational term,

$$\mu \frac{dv}{dx} = \frac{\sigma}{r_0^3}\frac{d\delta}{d\Psi}(\delta - x) \tag{6}$$

Integrating over x to find v

$$v = \frac{\sigma}{r_0^3\mu}\frac{d\delta}{d\Psi}\left(\delta x - \frac{x^2}{2}\right) \tag{7}$$

The mean velocity

$$\bar{v} = \frac{1}{\delta}\int_0^\delta v dx \tag{8}$$

is found to equal

$$\bar{v} = \frac{\sigma}{r_0^3\mu}\frac{d\delta}{d\Psi}\frac{\delta^2}{3} \tag{9}$$

By continuity

$$\Gamma = \rho\bar{v}\delta \tag{10}$$

Then by differentiation

$$d\Gamma = \rho d[\bar{v}\delta] = \frac{\rho\sigma}{r_0^3\mu} d\left[\frac{d\delta}{d\Psi}\frac{\delta^3}{3}\right] \tag{11}$$

and

$$d\Gamma = \frac{\rho\sigma}{r_0^3\mu}\frac{1}{12} d\left[\frac{d\delta^4}{d\Psi}\right] \tag{12}$$

Applying the energy equation by equating the heat released at the interface with the heat conducted through the film and assuming a linear temperature profile in the film,

$$d\Gamma = \frac{k(T_s - T_c)r_0 d\Psi}{\delta h_{fg}'} \tag{13}$$

Equating equations (12) and (13)

$$\delta\left[\frac{d^2\delta^4}{d\Psi^2}\right] = \frac{12\mu r_0^4 k(T_s - T_c)}{\rho\sigma h_{fg}'} \tag{14}$$

This second-order differential equation for δ can be nondimensionalized with $\hat{\lambda} = \left(\frac{\delta}{r_0}\right)^4$, $\hat{\Psi} = \sqrt{c}\Psi$ where

$$c = \left[\frac{12\mu k(T_s - T_c)}{\rho\sigma h_{fg}' r_0}\right] \tag{15}$$

to yield

$$(\hat{\lambda})^{1/4}\frac{d^2\hat{\lambda}}{d\hat{\Psi}^2} = 1 \tag{16}$$

Equation (16) can be solved numerically by finite-difference techniques when two boundary conditions are specified. At the top of the crest where $\hat{\Psi} = 0$, the nondimensional film thickness $\hat{\lambda}$ is finite and equal to $\hat{\lambda}_0$. The slope of the liquid–vapor interface $d\hat{\lambda}/d\Psi$ at $\hat{\Psi} = 0$ is by symmetry equal to zero. Utilizing these boundary conditions, the solution for $(\hat{\lambda})^{1/4}$ as a function of $(\hat{\lambda}_0)^{1/4}$ and $\hat{\Psi}$ in the range $0 < \hat{\Psi} < \frac{\sqrt{c}\pi}{2}$ can be obtained.

To determine the rate of condensive heat transfer on the crest of the undulation, it is now necessary to evaluate the heat-transfer coefficient h_{cr} on the crest. In laminar film condensation h_{cr} can be approximated as

$$h_{cr} = \frac{k}{\delta} \tag{17}$$

Relating back to the nondimensional film thickness $\hat{\lambda}$,

$$h_{cr} = \frac{k}{(\hat{\lambda})^{1/4} r_0} \tag{18}$$

Therefore, the average heat-transfer coefficient on a segment of the surface $0 < \hat{\Psi} < \hat{\Psi}_1$ equals

$$\bar{h}_{cr} = \frac{k}{[\hat{\lambda}_m(\hat{\Psi}_1)]^{1/4} r_0} = \frac{k/r_0}{\left[\frac{1}{\hat{\Psi}_1}\int_0^{\hat{\Psi}_1}(\hat{\lambda})^{1/4} d\hat{\Psi}\right]} \tag{19}$$

As can be seen from equation (19), to fully evaluate $\bar{h}_{cr}$ it is necessary to determine the value of $(\hat{\lambda}_0)^{1/4}$. Alternatively, since r_0 is usually specified it is δ_0 that must in fact be determined. Returning to equation (14) and modifying it slightly

$$\delta\frac{d}{d\Psi}\left[\delta^3\frac{d\delta}{d\Psi}\right] = \frac{3\mu r_0^4 k(T_s - T_c)}{\sigma\rho h_{fg}'} \tag{20}$$

But at $\Psi = 0$, $\delta = \delta_0$ and $d\delta/d\Psi = 0$; therefore,

$$\delta_0^4\left.\frac{d^2\delta}{d\Psi^2}\right|_0 = \frac{3\mu r_0^4 k(T_s - T_c)}{\sigma\rho h_{fg}'} \tag{21}$$

or

$$\delta_0 = \left[\frac{3\mu r_0^4 k(T_s - T_c)}{\sigma\rho h_{fg}'\left.\frac{d^2\delta}{d\Psi^2}\right|_0}\right]^{1/4} \tag{22}$$

To evaluate δ_0 it is therefore necessary to determine $d^2\delta/d\Psi^2$ at $\Psi = 0$. Assuming the liquid–vapor interface at $\Psi = 0$ to follow the contour of the constant-curvature undulation yields, from the definition of surface curvature, $\left.\frac{d^2\delta}{d\Psi^2}\right|_0 = 0$. Alternatively, assum-

ing the interface to lie tangent to the undulation at only $\Psi = 0$ yields $\left.\frac{d^2\delta}{d\Psi^2}\right|_0 = r_0$. Clearly, in the present case $\left.\frac{d^2\delta}{d\Psi^2}\right|_0$ lies somewhere between these two values. However, to maintain the upper-bound nature of the analysis $\left.\frac{d^2\delta}{d\Psi^2}\right|_0$ was chosen equal to r_0. While this choice is somewhat arbitrary, δ_0 is inversely proportional to $\left[\frac{d^2\delta}{d\Psi^2}\right]^{1/4}$, and is, hence, not highly sensitive to the choice of $\left.\frac{d^2\delta}{d\Psi^2}\right|_0$.

Substituting $\left.\frac{d^2\delta}{d\Psi^2}\right|_0 = r_0$ into equation (22) results in

$$\delta_0 = \left[\frac{3\mu r_0{}^3 k(T_s - T_c)}{\sigma\rho h_{fg}{}'}\right]^{1/4} \tag{23}$$

It is interesting to note that a similar expression for δ_0 can be obtained by analogy to gravity-dominated condensation on a cylinder [6] where

$$\delta_0 = \left[\frac{3\mu r_0 k(T_s - T_c)}{g(\rho - \rho_v)\rho h_{fg}{}'}\right]^{1/4} \tag{24}$$

In the present case the gravity term in the denominator of equation (24) is replaced by a surface-tension term with r_0 as the characteristic length. Equation (23) can also be used to evaluate the film thickness for surface-tension-dominated condensation on top of a small-diameter horizontal cylinder.

For Freon-113, at atmospheric pressure and 20 deg F surface subcooling, on an undulation or horizontal cylinder with a 1.5×10^{-2} in. radius of curvature, equation (23) yields $\delta_0 = 4.55 \times 10^{-4}$ in.

On the upper part of the undulation, shown in Fig. 2, the pressure gradient resulting from surface-tension forces leads to an extremely thin condensate film. However, for $\Psi > \pi/2$ the solid-surface curvature reverses and the film thickness is substantially increased. In this region the film thickness δ can no longer be considered very small in relation to r_0, and consequently the above analysis is restricted to $0 \leq \Psi \leq \pi/2$.

At the Undulation Trough. The vapor condensed on the crest of the undulation is pumped by surface tension into the undulation trough. From the trough the condensate flows primarily under the action of gravity along the specified arch and then drips off the doubly rippled surface at the base of the arch. The height of the liquid layer in the trough, γ, increases along the arch and reaches its maximum value at the base of the arch. For values of $\gamma \cong r$ the condensate flowing in the trough may wash or "flood" the undulation crest and substantially increase the thickness on the crest. However, the relatively short path length along the arch suggests that the condensate film remains thin and that flooding is not achieved at commonly employed values of condenser surface subcooling. The condensate film thickness in the trough can be determined approximately in the following manner.

Referring to the differential element in Fig. 2 and assuming that the film is thin and that the liquid–vapor interface is at a uniform height above the surface, a force balance in the α direction yields

$$\mu\frac{dv}{dx} = g(\rho - \rho_v)\sin\alpha(\gamma - x) \tag{25}$$

Integrating across x to find the fluid velocity in the α direction

$$v = \int_0^x \frac{dv}{dx}\,dx = \frac{g}{\mu}(\rho - \rho_v)\sin\alpha\left(x - \frac{x^2}{2}\right) \tag{26}$$

The mean fluid velocity can now be found as

$$\bar{v} = \int_0^\gamma v dx = \frac{g}{\mu}(\rho - \rho_v)\sin\alpha\cdot\frac{\gamma^2}{3} \tag{27}$$

By continuity

$$\Gamma = \rho\bar{v}\gamma = \frac{\rho g(\rho - \rho_v)\sin\alpha\cdot\gamma^3}{3\mu} \tag{28}$$

Equating the condensate flowing in the trough with the sum of the condensate draining off the adjacent crests and the vapor condensing on the liquid film in the trough yields

$$\frac{\rho(\rho - \rho_v)g\sin\alpha\cdot\gamma^3}{3\mu} = \frac{R\alpha(T_s - T_c)k}{h_{fg}{}'}\left[\frac{w}{\bar{\delta}} + \frac{1}{\gamma}\right] \tag{29}$$

where $\bar{\delta}$ is the average film thickness on the crest and w is the ratio of crest to trough diameters ($w = 1$ for a sinusoidal profile). Defining $\beta \equiv \alpha/\bar{\delta}$ and rearranging terms

$$\frac{\rho(\rho - \rho_v)g\sin\alpha}{3\mu}\bar{\delta}^4\beta^4 = \frac{R\alpha(T_s - T_c)k}{h_{fg}{}'}[w\beta + 1] \tag{30}$$

or

$$\frac{\beta^4}{w\beta + 1} = \left[\frac{3\mu Rk(T_s - T_c)\alpha}{\rho(\rho - \rho_v)gh_{fg}{}'\sin\alpha}\right]\left[\frac{1}{r_0{}^4\hat{\lambda}_m}\right] \tag{31}$$

The value of β can be found directly by solving equation (16) for $\hat{\lambda}_m$(at $\Psi = \pi/2$) on the crest surface and inserting the appropriate value in equation (31). The desired value of γ is then, from the definition of β, simply

$$\gamma = \beta\bar{\delta} = r_0\beta\hat{\lambda}_m{}^{1/4} \tag{32}$$

and the condensive heat-transfer coefficient in the undulation trough h_{tr} is

$$h_{tr} = \frac{k}{r_0\beta\hat{\lambda}_m{}^{1/4}} \tag{33}$$

As is clear from equation (31), β and therefore γ are functions of α along the arch.

The insertion of numerical values in equation (31) reveals that for commonly encountered values of subcooling, γ at the base of the arch is as anticipated still small when compared to r_0. However, along the inflection curve where the crest and the trough meet, γ is somewhat greater than δ, evaluated from equation (16), and an analytically induced artificial discontinuity thus exists. For the range of r_0 likely to be chosen in practical application, γ is approximately 30 percent greater than the calculated δ at that point. However, at and near the inflection point the gravitational force neglected in the derivation of equation (16) will act to increase δ and reduce this discontinuity, which will, in any event, be smoothed by surface-tension forces without substantially affecting δ on the crest of the undulation.

To facilitate the evaluation of the rate of condensive heat transfer in the undulation trough, it is appropriate to define an average trough heat-transfer coefficient h_{tr} based on an average value of β along the arch. The desired heat-transfer coefficient can be expressed as

$$\bar{h}_{tr} = \frac{k}{r_0\hat{\lambda}_m{}^{1/4}\bar{\beta}} \tag{34}$$

where $\bar{\beta}$ is evaluated from equation (31) for $0 < \alpha < \pi/2$.

Heat Transfer on Doubly Rippled Surface. The analysis presented in the preceding sections has provided expressions for the condensive heat-transfer coefficients on the undulation crest and in the undulation trough on a doubly rippled surface. Assumptions have been made throughout to minimize the film thickness and, hence, generate an upper-bound solution for the rate of vapor condensation and heat transfer on the surface.

The overall rate of heat transfer on the doubly rippled surface, neglecting temperature variations on the surface, can be expressed as

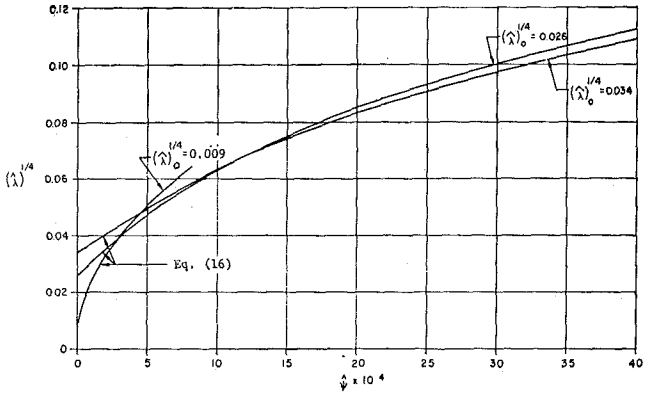

Fig. 3 Nondimensional film thickness along crest of sinusoidal undulation

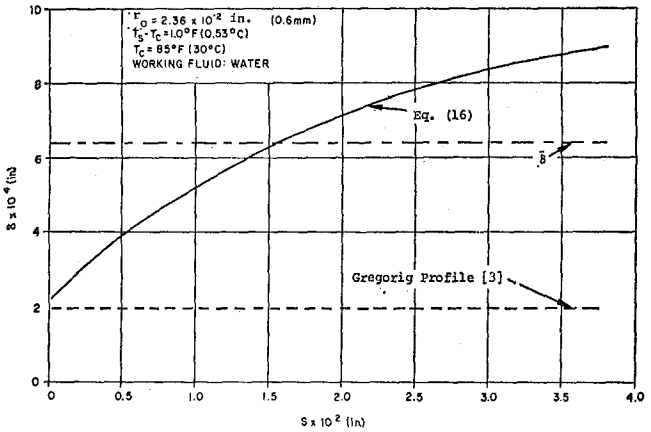

Fig. 4 Condensate film thickness on crest of sinusoidal and Gregorig-type profiles

$$q = (\bar{h}_{cr}A_{cr} + \bar{h}_{tr}A_{tr})(T_s - T_c) \tag{35}$$

where A_{cr} and A_{tr} are the crest and trough surface areas respectively.

For the experimental surface studied

$$A_{cr} = A_{tr} = 1.17A_p$$

where A_p is the projected area of the doubly rippled surface. Therefore, the upper bound on the total rate of heat transfer, q_{max}, on the experimental surface is equal to

$$q_{max} = 1.17A_p(\bar{h}_{cr} + \bar{h}_{tr})(T_s - T_c) \tag{36}$$

and can be evaluated from expressions presented in equations (19) and (34).

Analytical Results and Discussion

Numerical Solution for $\hat{\Lambda}$. The differential equation for $\hat{\Lambda}$, the nondimensional film thickness on the undulation crest, was solved numerically for several values of $\hat{\Lambda}_0$ in the range $0 < \Psi < \pi/2$. The resulting profiles are shown graphically in Fig. 3 and are seen to increase with increasing $\hat{\Psi}$. The slope of the profile, $d(\hat{\Lambda})^{1/4}/d\hat{\Psi}$, is seen to decrease with increasing $\hat{\Psi}$. Both results are in agreement with expectation. As is clear from equations (3) and (4), maintaining the surface curvature r_0 constant requires that the film thickness δ increase with Ψ to produce the desired pressure gradient in the film. As the film thickness increases, the local rate of condensation decreases and the growth rate of the film $d(\hat{\Lambda})^{1/4}/d\hat{\Psi}$ decreases accordingly.

Evaluation of δ_0. The evaluation of the film thickness at the top of the crest, δ_0, is central to the determination of the condensate film profile and the rate of heat transfer on the undulation crest. In his development of this method for a vertical-tube condenser

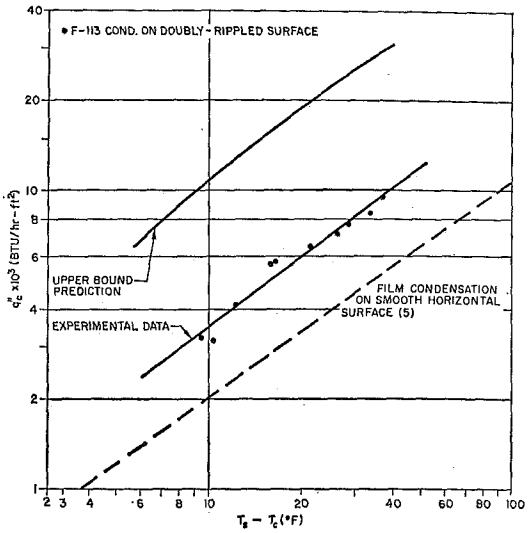

Fig. 5 Condensive limit for doubly rippled horizontal condenser surface

Gregorig [3, 7] specified no direct method for calculating δ_0. In practice he utilized a laborious trial-and-error method based on integral constraints and symmetry conditions [8]. The value of δ_0 determined by equation (23) is compared in Fig. 4 with the value suggested by Gregorig for an undulation with an initial radius of curvature equal to 2.36×10^{-2} in. For steam saturated at 85 deg F and a surface subcooling of 1.0 deg F, equation (23) yields $\delta_0 = 2.24 \times 10^{-4}$ in., while Gregorig determined a value of 1.97×10^{-4} in. Further comparison would be desirable, but the literature contains only this one calculated value.

Variation of δ. Early attempts to exploit surface-tension forces to produce thin condensate films have utilized surfaces of varying radii of curvature. The surfaces were shaped to produce uniform-thickness condensate films along the entire crest surface [3, 4] with δ equal to the value attained at the top of the crest. Due to the difficulties associated with accurately manufacturing such a surface, the use of sinusoidal undulations appeared attractive. However, the use of a sinusoidal undulation rather than a profile with a variable radius of curvature can be expected to result in a larger mean film thickness.

The condensate film thicknesses on the crests of sinusoidal and variable-radius-of-curvature undulations with initial radius of 2.36×10 in. are compared in Fig. 4. For the conditions stated above and in the absence of gravitational effects, the sinusoidal profile yields a film thickness which increases to four times the minimum value at the inflection point of the undulation. The mean film thickness for the sinusoidal profile is thus approximately three times greater than the comparable film thickness on the Gregorig-type profile [3], but still nearly a factor of three less than the average film thickness for the same conditions on a smooth horizontal surface. It is apparent, then, that the use of a sinusoidal rather than a variable-radius-of-curvature profile results in rates of heat transfer which are lower than the maximum obtainable. However, the results of the analysis are in qualitative agreement with expectation and indicate that sinusoidal undulations of sufficiently small radius can be used to substantially reduce the film thickness, and hence significantly increase thermal transport in film condensation on horizontal surfaces.

Heat-Transfer Rate. Utilizing the analytical results and equation (36) it is now possible to calculate the upper limit on the rate of condensive heat transfer on the downward-facing doubly rippled surface of Figs. 1 and 2. The results of these calculations for F-113 and surface subcooling of 7 to 40 deg F at 1 atm are presented in terms of

$$q_c'' = \frac{q}{A_p} = 1.17(\bar{h}_{cr} + \bar{h}_{tr})(T_s - T_c) \tag{37}$$

in Fig. 5. Included is the analytical condensation rate on a flat

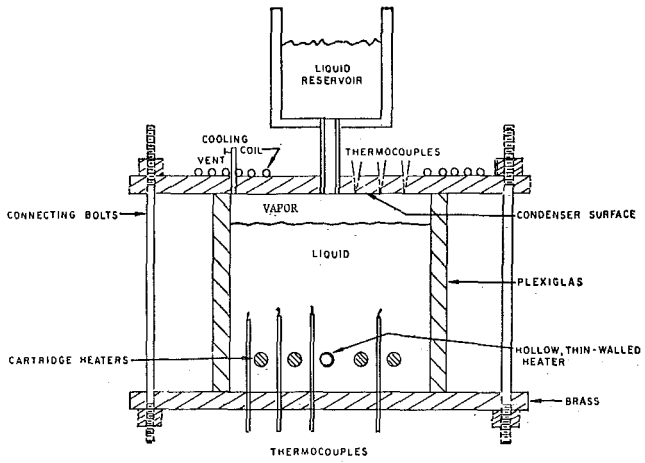

Fig. 6 Schematic of experimental submerged condenser apparatus

downward-facing horizontal surface of the same projected area. The results indicate that a factor of five improvement represents the upper limit for condensive augmentation on a downward-facing doubly rippled surface of this type.

Comparison with Experimental Results

The experimental results for the condensation of F-113 on the doubly rippled surface are shown in Fig. 5 and were obtained with the apparatus shown in Fig. 6. The apparatus and procedure are described in detail in [9].

The attained condenser heat flux, based on the projected area of the undulated surface, is seen to correspond to nearly twice the heat flux associated with film condensation on a smooth horizontal surface of the same projected area. However, the augmented performance is substantially lower than predicted by the upper-bound solution derived above. Due to the complex nature of the governing relations, the precise impact of neglecting the gravity term in equation (2) and the effect of the upper-bound boundary condition in equation (23) on the calculated rate of heat transfer cannot be easily determined. Nevertheless, order-of-magnitude comparison suggests that the upper-bound solution for the surface of interest should not exceed the actual rate of heat transfer by more than about 40 percent. Other factors must therefore be found to account for the wide discrepancy between the analytical prediction and the data.

It appears most likely at this time that, despite a regular degassing procedure [9], the numerous undulations present on the doubly rippled surface may have been partially blanketed by noncondensables. The presence of small amounts of noncondensables has long been known to cause dramatic degradation in condenser performance [10]; however, noncondensables are especially troublesome in condensers with nonuniform heat fluxes. As a result of spatial variations in heat flux the noncondensables collect near the regions of initially high heat flux and thus prevent high rates of condensation in those regions [11]. The implications for the doubly rippled surface which is strongly dependent on nonuniform heat flux are clear. It is noted that fluorocarbons are particularly prone to problems with dissolved gases due to their high gas solubilities. Further testing of the doubly rippled surface in an experimental apparatus equipped with a more sophisticated degassing system would be required to establish the attainable performance level of condensers of this type.

Concluding Remarks

A fundamental analysis of film condensation on a downward-facing horizontal surface with small constant-radius-of-curvature undulations was performed for the region in which surface-tension forces determine the film thickness on the crests.

A direct expression for the condensate film thickness at the top of an undulation crest, or a small-diameter horizontal cylinder, was derived. A numerical solution of the film equations has shown that the film thickness increases along the crest at a decreasing rate.

An upper-bound expression for the heat-transfer rate on a doubly rippled surface was derived. The upper-bound rate for a special surface developed for this study was found to be five times the rate attainable on a flat horizontal surface of the same projected area. Experimental results are well below the predictions, apparently due to the presence of noncondensables.

The general conclusion is that small undulations can be used to augment the rate of condensive heat transfer on flat horizontal surfaces. It is anticipated that such augmentation would be especially significant in modular electronic cooling systems employing inert dielectric fluids and in steam-condensation applications in which greater reliability is desired than generally provided by applied dropwise promoters.

Acknowledgments

This investigation was supported by the Raytheon Company, MSD, of Bedford, Mass., and performed in the M.I.T. Heat Transfer Laboratory. The authors are indebted to Prof. Peter Griffith for his valuable aid throughout this investigation.

References

1 Rose, J. W., "On the Mechanism of Dropwise Condensation," *International Journal of Heat and Mass Transfer*, Vol. 10, 1967, pp. 755–762.

2 Peterson, A. C., and Westwater, J. W., "Dropwise Condensation of Ethylene Glycol," *Chemical Eng. Prog. Symposium Series*, Vol. 62, No. 64, 1966.

3 Gregorig, R., "Hautkondensation an Feingewellten Oberflächen bei Berücksichtigung der Oberflächenspannungen," *Z. Angew. Math. Phys.*, Vol. 5, 1954, p. 36.

4 Nabavian, K., and Bromley, L. A., "Condensation Coefficient of Water," *Chem. Eng. Sci.*, Vol. 18, 1963, pp. 651–660.

5 Gerstmann, J., and Griffith, P., "Laminar Film Condensation on the Underside of Horizontal and Inclined Surfaces," *International Journal of Heat and Mass Transfer*, Vol. 10, 1967, pp. 567–580.

6 Nusselt, W., "Die Oberflächenkondensation des Wasserdampfes," *Z. Ver. Deutsch. Ing.*, Vol. 60, 1910, pp. 541–569.

7 Gregorig, R., *Exchanger De Chaleur*, Librairie Polytechnic Beranger, Paris, France, 1965.

8 Gregorig, R., personal communication to A. E. Bergles, 1970.

9 Markowitz, A., and Bergles, A. E., "Boiling and Condensation in a Liquid-Filled Enclosure," M.I.T. Engineering Projects Laboratory Report 29077-73, 1971.

10 Rohsenow, W. M., and Choi, H. Y., *Heat, Mass and Momentum Transfer*, Prentice-Hall, Englewood Cliffs, N. J., 1961.

11 Gerstmann, J., "Film Condensation on the Underside of a Horizontal Surface," SM thesis, Department of Mechanical Engineering, M.I.T., Cambridge, Mass., 1964.

12 Thomas, D. G., "Enhancement of Film Condensation Heat Transfer Rates on Vertical Wires," *I & EC Fundamentals*, Vol. 6, No. 1, 1967, pp. 97–103.

13 Thomas, D. G., "Enhancement of Film Condensation Rate on Vertical Tubes by Longitudinal Fins," *AIChE Journal*, Vol. 14, 1968, pp. 644–649.

14 Alexander, L. G., and Hoffman, H. W., "Performance Characteristics of Corrugated Tubes for Vertical Tube Evaporators," ASME Paper No. 71-HT-30.

journal of heat transfer

technical briefs

This section consists of contributions of 1500 words or less (about 5 double-spaced typewritten pages, including figures). Technical briefs will be reviewed and approved by the specific division's reviewing committee prior to publication. After approval such contributions will be published as soon as possible, normally in the next issue of the journal.

Finite-Difference Methods for Inhomogeneous Regions

G. J. TREZEK[1] **and J. G. WITWER**[2]

Introduction

THE PURPOSE of this note is to compare three finite-difference formulations of the energy equation with an exact solution. The motivation for considering these calculations stems from mathematical modeling of certain biological systems which requires a steady-state field in a region where the conductivity has a spatial variation. Usually these systems also have complex boundary shapes, so that numerical solutions are inevitable. In order to demonstrate the relative accuracy between the numerical formulations, a simple system of a square having prescribed boundary values was selected. This square is divided into two equal rectangles of different conductivity, joined by a common interface, to model an inhomogeneous region.

Numerical Formulations

When a steady-state temperature field is desired for a region in which the thermal conductivity is dependent upon the spatial location, a solution must be obtained for

$$\nabla(k\nabla T) = 0 \tag{1}$$

The finite-difference representation of equation (1) depends on the manner in which the conductivity variation is treated. A general representation in subscript notation in two dimensions can be given as

$$\beta_1 T(i+1,j) + \beta_2 T(i-1,j) + \beta_3 T(i,j+1) + \beta_4 T(i,j-1) - \beta_0 T(i,j) = 0 \tag{2}$$

where it is readily seen that for a homogeneous medium $\beta_1 = \beta_2 = \beta_3 = \beta_4 = 1$ and $\beta_0 = 4$.

For convenience the following quantities are introduced in the formulations for inhomogeneous regions

$$K_1 = k(i+1,j) \quad K_3 = k(i,j+1) \quad K_0 = k(i,j)$$
$$K_2 = k(i-1,j) \quad K_4 = k(i,j-1) \tag{3}$$

Formulation A is deduced by expanding equation (1) into groups of (a) second-order derivatives of temperature, the homogeneous contribution, and (b) the product of first-order spatial derivatives of temperature and conductivity. This expansion yields

$$\beta_1 = K_0 + (K_1 - K_2)/4 \quad \beta_3 = K_0 + (K_3 - K_4)/4 \quad \beta_0 = 4K_0$$
$$\beta_2 = K_0 - (K_1 - K_2)/4 \quad \beta_4 = K_0 - (K_3 - K_4)/4 \tag{4}$$

Formulation B is based on the application of Kirchhoff's law at an imaginary node placed at the interface between nodes. This allows for the evaluation of a representative conductivity $\bar{k}$ between adjacent nodes, for example, between nodes (i,j) and $(i+1,j)$

$$\bar{k} = 2/[1/k(i,j) + 1/k(i+1,j)] \tag{5}$$

and the values of the β parameters in equation (2) become

$$\beta_l = 2(1/K_l + 1/K_0)^{-1} \tag{6}$$

and

$$\beta_0 = \sum_{l=1}^{4} \beta_l$$

Formulation C is a simplified form of Formulation B in that the values of $\bar{k}$ are obtained by a simple average of the conductivity values of adjacent nodes. Thus, in terms of the previous i,j and $i+1,j$ nodes, equation (5) becomes

$$\bar{k} = [k(i,j) + k(i+1,j)]/2$$

and the expressions for the β parameters in equation (2) are

$$\beta_l = (K_l + K_0)/2 \tag{7}$$

and

$$\beta_0 = \sum_{l=1}^{4} \beta_l$$

Examination of the β terms illustrates the basic difference between the formulations. Formulation A represents the first-order spatial-conductivity derivatives with a central difference so that three adjacent conductivity values are incorporated into the conductivity approximation β. Formulation B treats the conductivity regions as parallel resistors while Formulation C treats them as series resistors.

Based on the evidence of Forsythe and Wasow [1][3] for homogeneous problems, the iterative technique of successive overrelaxation (SOR) was applied to the solution of the system of equations resulting from equation (2). The resulting algorithm has the form

$$T(i,j)_p = (1-\Omega)T(i,j)_{p-1} + \frac{\Omega}{\beta_0}[\beta_1 T(i+1,j)_{p-1} + \beta_2 T(i-1,j)_p + \beta_3 T(i,j+1)_{p-1} + \beta_4 T(i,j-1)_p] \tag{8}$$

[1] Associate Professor, Department of Mechanical Engineering, University of California, Berkeley, Calif. Mem. ASME.

[2] National Institutes of Health Bioengineering Trainee, Department of Mechanical Engineering, University of California, Berkeley, Calif.

Contributed by the Heat Transfer Division of THE AMERICAN SOCIETY OF MECHANICAL ENGINEERS. Manuscript received by the Heat Transfer Division January 19, 1972.

[3] Numbers in brackets designate References at end of technical brief.

where p refers to the current iteration, $p - 1$ to the previously performed iteration, and Ω is the over-relaxation parameter which can have values between one and two. When the term $\Omega = 1$, the SOR method reduces to the scheme of Gauss–Seidel. Basically, as soon as a new $T(i, j)$ value is obtained, it is stored in that particular nodal location and used in subsequent calculations.

Results and Discussion

An analytical solution was obtained for the two-conductivity square by use of the Fourier sine transform. The flux matching condition can be applied in the transform domain allowing the determination of the interface temperature distribution, and subsequently, after transformation, the temperature field in each region.

First an analytical solution and the simple finite-difference formulation were applied to a homogeneous plane with two opposite boundaries at 100 and the other two boundaries at 0 and 200.

In order to assess the effect of truncation error on the accuracy of the numerical solution, a comparison was made between the standard finite-difference solution for 12×12 and 23×23 homogeneous nodal networks and an analytical solution evaluated at equivalent locations. At a typical point, reducing the mesh size by a factor of two reduces the truncation error by about a factor of four. In each case the truncation error was at least an order of magnitude greater than the convergence error, thus the solution was sufficiently converged.

Table 1 Comparison of analytical solution with the four finite-difference formulations for the 2:1 conductivity-ratio square with a 12×12 nodal network

DISPLAY ORDER:
1 Analytic
2 Formulation A
3 Formulation B
4 Formulation C

T = 200

12						
11	147.58 147.43 147.56 147.52	165.50 164.73 164.98 164.90	178.44 171.72 172.06 171.95	175.34 174.67 175.08 174.95	176.43 175.78 176.23 176.08	176.43 — 1 175.78 — 2 176.23 — 3 176.08 — 4
10	124.83 125.01 125.28 125.19	140.35 139.76 140.28 140.11	148.44 147.46 148.18 147.94	152.32 151.19 152.04 151.76	153.87 152.68 153.60 153.30	153.87 152.68 153.60 153.30
9	113.01 112.83 113.28 113.13	122.63 121.86 122.70 122.42	128.45 127.18 128.33 127.96	131.50 129.93 131.30 130.85	132.77 131.06 132.54 132.06	132.77 131.06 132.54 132.06
8	105.03 104.46 105.12 104.91	108.86 107.66 108.90 108.49	111.21 109.47 111.16 110.60	112.40 110.29 112.28 111.63	112.86 110.58 112.72 112.02	112.86 110.58 112.72 112.02
7	98.40 97.35 98.31 98.00	96.69 94.86 96.63 96.04	95.13 92.73 95.11 94.33	94.01 91.20 93.96 93.05	93.39 90.39 93.34 92.37	93.39 90.39 93.34 92.37
6	93.37 92.97 93.20 83.35	87.42 86.88 87.30 87.59	82.82 82.22 82.79 83.18	79.81 79.15 79.81 80.26	78.31 77.63 78.34 78.82	78.31 77.63 78.34 78.82
5	89.07 88.72 88.88 88.99	70.82 79.39 79.68 79.89	73.07 72.64 73.05 73.32	68.81 68.39 68.87 69.20	66.78 66.36 66.87 67.22	66.78 66.36 66.87 67.22
4	82.96 82.54 82.64 82.72	69.64 69.31 69.51 69.65	60.79 60.57 60.84 61.03	55.60 55.42 55.75 55.97	53.23 53.05 53.41 53.65	53.23 53.05 53.41 53.65
3	72.66 62.12 72.18 72.23	54.83 54.74 54.86 54.95	44.85 44.90 45.07 45.18	39.62 39.66 39.86 40.00	37.38 37.28 37.60 37.76	37.38 37.38 37.60 37.76
2	51.21 51.19 51.22 51.24	32.19 32.64 32.70 32.74	24.34 24.62 24.70 24.75	20.79 20.93 21.03 21.09	19.36 19.44 19.54 19.62	19.36 19.44 19.54 19.62
1						
	1	2	3	4	5	6	7

T = 100 (left)
T = 0
REGION II $k_2 = 0.5$
REGION I $k_1 = 1.0$
Center Line of Square

The temperature field generated by each of the finite-difference formulations is compared with the analytical solution at equivalent locations in Tables 1 and 2 for the 2:1 and 50:1 conductivity-ratio planes, respectively. Formulation A cannot be used for a conductivity ratio of 50:1 because β_3 and β_4, equation (4), become negative, thus violating Young's [2] criterion for using the SOR technique. The values in Tables 1 and 2 have a maximum convergence error (evaluated by the method of Carré [3]) of 0.01, which is, for the most part, less than the error due to truncation. Further, it was observed that each formulation converged at the same rate independently of the conductivity ratio.

Comparisons of values obtained with the analytical solution and the three finite-difference formulations on each side of the interface indicate that Formulation B is the most accurate for each conductivity ratio.

Recalling that the absolute error is composed of two errors, the truncation error and the convergence error, a further comparison with corresponding points for a homogeneous field indicates that B does produce some additional truncation error due to the inhomogeneity approximation. That is, the absolute error observed with B is somewhat greater than the observed absolute error at the same point in the associated homogeneous problem. It is observed that along the interface the errors generally increase as the conductivity increases from 1:1 to 2:1 to 50:1, but even this general rule does not always hold at each point. For Formulation B, the maximum error observed along the interface in the 50:1 case is about four times the maximum error observed in the homogeneous case, while in the 2:1 case this factor is about three. For Formulation B, the largest errors occur in the high-conductivity ($k = 1$) half, while for Formulations A and C the largest errors consistently occur in the low-conductivity half.

Formulation B can also be used to advantage when insulated boundaries are considered. By assigning nodal locations ex-

Table 2 Comparison of analytical solution with the four finite-difference formulations for the 50:1 conductivity-ratio square with a 12×12 nodal network

T = 200

12						
11	146.45 146.42 145.81	163.32 162.78 161.63	169.41 169.00 167.41	171.69 171.42 169.52	172.47 172.25 170.20	172.47 — 1 172.25 — 3 170.20 — 4
10	122.46 122.89 121.62	135.81 135.71 133.31	142.12 141.82 138.50	144.73 144.41 140.48	145.63 145.32 141.07	145.63 145.32 141.07
9	109.19 109.43 107.37	115.34 115.36 111.47	118.31 118.14 112.81	119.35 119.10 112.81	119.58 119.31 112.54	119.58 119.31 112.54
8	99.42 99.47 96.38	98.19 98.15 92.37	96.41 96.28 88.48	94.72 94.53 85.41	93.70 93.51 83.74	93.70 93.50 83.74
7	90.41 80.31 85.77	81.64 81.48 73.18	74.44 74.29 63.30	69.36 69.25 56.62	66.75 66.67 53.27	66.75 66.67 53.27
6	85.38 85.20 85.29	72.37 62.15 72.32	62.12 61.97 62.19	55.16 55.11 55.36	51.67 51.67 51.94	51.67 51.67 51.94
5	83.45 83.23 83.29	69.14 68.93 69.05	58.27 58.17 58.32	51.12 51.12 51.30	47.61 47.66 47.85	47.61 47.65 47.85
4	79.14 78.80 78.84	62.35 62.17 62.24	50.65 50.65 50.75	43.45 43.54 43.67	40.05 40.17 40.31	40.05 40.17 40.31
3	70.28 69.79 69.82	50.29 50.29 50.34	38.52 38.70 38.77	32.03 32.23 32.31	29.13 29.32 29.41	29.13 29.32 29.41
2	50.07 50.07 50.09	30.01 30.50 30.52	21.30 21.64 21.67	17.14 17.36 17.40	15.40 15.56 15.60	15.40 15.56 15.60
1						
	1	2	3	4	5	6	7

T = 100 (left)
T = 0
REGION II $k_2 = 0.02$
REGION I $k_1 = 1.0$
Center Line of Square

DISPLAY ORDER:
1 Analytic
3 Formulation B
4 Formulation C

terior to the boundary a low conductivity (usually several orders of magnitude lower than the adjacent interior point), additional nodes or internal computational checks to determine the boundary nature are not required. This results in a considerable savings in computation time. The accuracy of this technique was verified by comparison with an analytic solution for a simple rectangle having an insulated boundary.

It would be fortunate if these studies could be repeated with more complex boundaries and/or more complex inhomogeneity distributions. However, since analytical solutions could not be obtained for such geometries, error estimates must be made from simple geometries such as studied here. These results suggest that the error produced by an inhomogeneous formulation (i.e., Formulation B) is of the same order as the truncation error of the more simple homogeneous problem.

References

1 Forsythe, G. E., and Wasow, W. R., *Finite Difference Methods for Partial Differential Equations*, John Wiley & Sons, New York, N. Y. 1960.

2 Young, D. M., "Iterative Methods for Solving Partial Differential Equations of Elliptic Type," *Trans. American Math. Society*, Vol. 76, 1954, p. 92.

3 Carré, B. A., "The Determination of the Optimum Accelerating Factor for Successive Over-Relaxation," *Computer Journal*, Vol. 4, No. 1, 1961, p. 73.

Spectral Emittance of Apollo-12 Lunar Fines

RICHARD C. BIRKEBAK[1]

Introduction

THE Apollo-12 landing site, as well as the Apollo-11 site, was found to be covered by a thick layer of soil or fines (powder). Calculation of lunar heat flow and heat balance on equipment and astronauts placed on the moon depends on the thermophysical properties of this material [1].[2]

The thermophysical properties reported to date include the directional spectral reflectance [2–4], the thermal conductivity [2, 5, 6] and the specific heat [7]. The results of the spectral-emittance studies that we are reporting here add to the growing list of thermophysical properties of lunar material. In this paper we describe the experimental results obtained for Apollo-12 sample no. 12070, 125.

The sample studied, no. 12070, is from the contingency sample collected on a rim of a small crater 15 m northwest of the lunar module (LM) on the Ocean of Storms. The fines consisted of particles in sizes from a diameter of 100 μm down to less than 1 μm with most of the particles being at the lower end of the range [8]. Because of the nature of lunar fines one must consider the effects of density or compaction on the results. In a recent paper [4] we have shown that the reflectance is affected in the wavelength range from 0.55 to 2.2 μm by the bulk density of the sample.

When an Apollo-12 fines sample is prepared by simply pouring it into a container and carefully leveling the surface, a bulk density of approximately 1300 kg/m^3 is obtained. During the Apollo-12 mission, core-tube samples were obtained. Our bulk densities were selected according to the bulk densities of the core-tube samples reported in the Apollo-12 "Preliminary Science Report" [9]. This reports an average in-situ bulk density of 1800 $\pm$ 200 kg/m^3. In our study we used bulk densities from 1400 kg/m^3 to 1900 kg/m^3.

The nature of the sample dictated that we use a horizontal sample in the measurement technique. The sample was mounted in a sample heating cup and positioned in a known radiation environment. Besides the sample holder, a heated reference blackbody was placed in the environmental chamber. Transfer optics was used to view either the sample or blackbody and to direct the energy into a Perkin-Elmer 112U spectrometer.

The environmental chamber surrounding the sample and heated blackbody was a water-cooled blackened-interior 0.20-m-dia stainless-steel sphere. The chamber has ports for the sample, blackbody holders, and viewing optics. Thermocouples were used to measure the interior temperature of the sphere, the surface temperature and temperature gradient in the fines, and the blackbody temperature.

We designed the viewing optics so that by rotating an optical bench either the sample or blackbody could be viewed. The image of either the sample or blackbody was focused to over-illuminate the entrance slit of the 112U spectrometer.

When we have the spectrometer slit focused, in turn, on the sample, heated blackbody, and blackened surrounds of the chamber, the spectrometer output along with the temperature measurements can be analyzed to give the following result for the spectral emittance [10]:

$$\epsilon(\theta, \lambda, T) = \frac{\Delta(S) - \Delta(R)}{\Delta(B) - \Delta(R)} \frac{\exp [c_2/\lambda T_R] - \exp [c_2/\lambda T_B]}{\exp [c_2/\lambda T_R] - \exp [c_2/\lambda T_S]} \times \frac{\exp [c_2/\lambda T_S] - 1}{\exp [c_2/\lambda T_B] - 1} \quad (1)$$

which is our working equation. This equation was derived for a solid surface. For a powder surface such as lunar fines the generalized Kirchhoff's law was assumed to apply [11] in order to satisfy the conditions for this equation.

The spectrometer was interfaced with a Hewlett-Packard 2114B minicomputer. This system allowed us to automatically scan the wavelength range and to perform the necessary operations required to obtain data for use in equation (1) and to obtain the spectral emittance as a function of wavelength directly.

Results and Discussion

Prior to measuring the emittance of the lunar fines we ran several checks on the apparatus to establish the reproducibility of the measurements and the stability of the system. Several runs were made using the heated blackbody both as the sample and reference surfaces. For the wavelength range from 2 to 14 μm we measured an emittance of 1.0 $\pm$ 0.01. This we felt was acceptable for the method. As a second check we ran a stainless-steel surface coated with 3M Black Velvet paint. For wavelengths from 6 to 12 μm an emittance of 0.955 $\pm$ 0.005 was obtained. These results established that the system worked and that we could use it to measure the spectral emittance of a sample to within $\pm$1 percent.

We have obtained results on Apollo-12 fines for bulk densities of approximately 1400, 1600, 1710, and 1900 kg/m^3. The angle of viewing, θ, used in our experiment was 10 deg. Each curve in Fig. 1 represents an average of 3 or more runs that we made at the specified density.

The sample temperature used in equation (1) was calculated from the measured temperature gradient and the temperature measured near the surface, and from the known sample thickness and thermocouple location. If we use the calculated surface temperature rather than the temperature measured at 0.46 mm below the surface in equation (1), the difference in emittances obtained from the two temperatures ranges from essentially zero at 2.5 μm to 1 percent higher at 14 μm. The surface tem-

[1] Professor, Department of Mechanical Engineering, University of Kentucky, Lexington, Ky. Mem. ASME.

[2] Numbers in brackets designate References at end of technical brief.

Contributed by the Heat Transfer Division of THE AMERICAN SOCIETY OF MECHANICAL ENGINEERS. Manuscript received by the Heat Transfer Division September 3, 1971.

terior to the boundary a low conductivity (usually several orders of magnitude lower than the adjacent interior point), additional nodes or internal computational checks to determine the boundary nature are not required. This results in a considerable savings in computation time. The accuracy of this technique was verified by comparison with an analytic solution for a simple rectangle having an insulated boundary.

It would be fortunate if these studies could be repeated with more complex boundaries and/or more complex inhomogeneity distributions. However, since analytical solutions could not be obtained for such geometries, error estimates must be made from simple geometries such as studied here. These results suggest that the error produced by an inhomogeneous formulation (i.e., Formulation B) is of the same order as the truncation error of the more simple homogeneous problem.

References

1 Forsythe, G. E., and Wasow, W. R., *Finite Difference Methods for Partial Differential Equations*, John Wiley & Sons, New York, N. Y. 1960.

2 Young, D. M., "Iterative Methods for Solving Partial Differential Equations of Elliptic Type," *Trans. American Math. Society*, Vol. 76, 1954, p. 92.

3 Carré, B. A., "The Determination of the Optimum Accelerating Factor for Successive Over-Relaxation," *Computer Journal*, Vol. 4, No. 1, 1961, p. 73.

Spectral Emittance of Apollo-12 Lunar Fines

RICHARD C. BIRKEBAK[1]

Introduction

THE Apollo-12 landing site, as well as the Apollo-11 site, was found to be covered by a thick layer of soil or fines (powder). Calculation of lunar heat flow and heat balance on equipment and astronauts placed on the moon depends on the thermophysical properties of this material [1].[2]

The thermophysical properties reported to date include the directional spectral reflectance [2–4], the thermal conductivity [2, 5, 6] and the specific heat [7]. The results of the spectral-emittance studies that we are reporting here add to the growing list of thermophysical properties of lunar material. In this paper we describe the experimental results obtained for Apollo-12 sample no. 12070, 125.

The sample studied, no. 12070, is from the contingency sample collected on a rim of a small crater 15 m northwest of the lunar module (LM) on the Ocean of Storms. The fines consisted of particles in sizes from a diameter of 100 μm down to less than 1 μm with most of the particles being at the lower end of the range [8]. Because of the nature of lunar fines one must consider the effects of density or compaction on the results. In a recent paper [4] we have shown that the reflectance is affected in the wavelength range from 0.55 to 2.2 μm by the bulk density of the sample.

When an Apollo-12 fines sample is prepared by simply pouring it into a container and carefully leveling the surface, a bulk density of approximately 1300 kg/m^3 is obtained. During the Apollo-12 mission, core-tube samples were obtained. Our bulk densities were selected according to the bulk densities of the core-tube samples reported in the Apollo-12 "Preliminary Science Report" [9]. This reports an average in-situ bulk density of 1800 $\pm$ 200 kg/m^3. In our study we used bulk densities from 1400 kg/m^3 to 1900 kg/m^3.

The nature of the sample dictated that we use a horizontal sample in the measurement technique. The sample was mounted in a sample heating cup and positioned in a known radiation environment. Besides the sample holder, a heated reference blackbody was placed in the environmental chamber. Transfer optics was used to view either the sample or blackbody and to direct the energy into a Perkin-Elmer 112U spectrometer.

The environmental chamber surrounding the sample and heated blackbody was a water-cooled blackened-interior 0.20-m-dia stainless-steel sphere. The chamber has ports for the sample, blackbody holders, and viewing optics. Thermocouples were used to measure the interior temperature of the sphere, the surface temperature and temperature gradient in the fines, and the blackbody temperature.

We designed the viewing optics so that by rotating an optical bench either the sample or blackbody could be viewed. The image of either the sample or blackbody was focused to over-illuminate the entrance slit of the 112U spectrometer.

When we have the spectrometer slit focused, in turn, on the sample, heated blackbody, and blackened surrounds of the chamber, the spectrometer output along with the temperature measurements can be analyzed to give the following result for the spectral emittance [10]:

$$\epsilon(\theta, \lambda, T) = \frac{\Delta(S) - \Delta(R)}{\Delta(B) - \Delta(R)} \frac{\exp [c_2/\lambda T_R] - \exp [c_2/\lambda T_B]}{\exp [c_2/\lambda T_R] - \exp [c_2/\lambda T_S]} \times \frac{\exp [c_2/\lambda T_S] - 1}{\exp [c_2/\lambda T_B] - 1} \quad (1)$$

which is our working equation. This equation was derived for a solid surface. For a powder surface such as lunar fines the generalized Kirchhoff's law was assumed to apply [11] in order to satisfy the conditions for this equation.

The spectrometer was interfaced with a Hewlett-Packard 2114B minicomputer. This system allowed us to automatically scan the wavelength range and to perform the necessary operations required to obtain data for use in equation (1) and to obtain the spectral emittance as a function of wavelength directly.

Results and Discussion

Prior to measuring the emittance of the lunar fines we ran several checks on the apparatus to establish the reproducibility of the measurements and the stability of the system. Several runs were made using the heated blackbody both as the sample and reference surfaces. For the wavelength range from 2 to 14 μm we measured an emittance of 1.0 $\pm$ 0.01. This we felt was acceptable for the method. As a second check we ran a stainless-steel surface coated with 3M Black Velvet paint. For wavelengths from 6 to 12 μm an emittance of 0.955 $\pm$ 0.005 was obtained. These results established that the system worked and that we could use it to measure the spectral emittance of a sample to within $\pm$1 percent.

We have obtained results on Apollo-12 fines for bulk densities of approximately 1400, 1600, 1710, and 1900 kg/m^3. The angle of viewing, θ, used in our experiment was 10 deg. Each curve in Fig. 1 represents an average of 3 or more runs that we made at the specified density.

The sample temperature used in equation (1) was calculated from the measured temperature gradient and the temperature measured near the surface, and from the known sample thickness and thermocouple location. If we use the calculated surface temperature rather than the temperature measured at 0.46 mm below the surface in equation (1), the difference in emittances obtained from the two temperatures ranges from essentially zero at 2.5 μm to 1 percent higher at 14 μm. The surface tem-

[1] Professor, Department of Mechanical Engineering, University of Kentucky, Lexington, Ky. Mem. ASME.

[2] Numbers in brackets designate References at end of technical brief.

Contributed by the Heat Transfer Division of THE AMERICAN SOCIETY OF MECHANICAL ENGINEERS. Manuscript received by the Heat Transfer Division September 3, 1971.

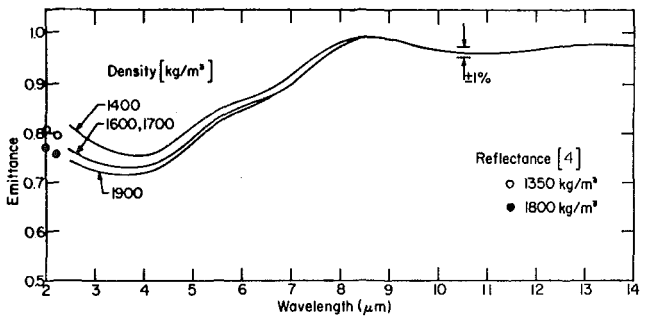

Fig. 1 Spectral emittance of Apollo-12 lunar fines

perature for all measurements was approximately 380 deg K, a temperature very near the maximum temperature experienced by the sample on the moon [1].

Clearly evident in Fig. 1 is the effect of bulk density. Because the results for densities of 1600 and 1710 kg/m³ were so close together, we have drawn a single curve through them. The emittance decreases with increasing density for the shorter wavelengths, with a change of approximately 7 percent at 3 μm between the smallest and largest densities, and as the wavelengths become larger the difference becomes negligible. The greatest uncertainties in our measurements are for wavelengths from 2 to 2.5 μm, and in this region the maximum effect of density [4] on reflectance was shown to occur. As the surface becomes more compacted, that is, a greater number of particles per unit volume, the void fraction decreases; therefore, the size of the cavities in the surface which absorb and emit energy are reduced and the emittance decreases. From our results we see that we are approaching or have reached the limit where the porosity of the sample does not affect the emittance value, that is, the material behaves as if it were a solid material. This conclusion was also reached for visible reflectance measurement [4].

The emittance is compared to the directional-reflectance result [4] for the wavelength range where they overlap near 2 μm, and our present results are good for the higher densities, that is, there is a reasonable match of the measured values of emittance and one minus the reflectance, but poor agreement for the density of 1400 kg/m³.

The total emittance as a function of temperature has been calculated for a bulk density of 1900 kg/m³. The lunar emittance varies from 0.972 to 0.927 for a temperature range from 90 to 400 deg K, the expected temperature range on the lunar surface. The equation representing the results is

$$\epsilon = 0.9843 - 0.2037 \times 10^{-3}T + 0.1863 \times 10^{-5}T^{-2} - 0.6765 \times 10^{-8}T^{-3} + 0.6436 \times 10^{-11}T^{-4} \quad (2)$$

where T is the absolute temperature in degrees Kelvin.

References

1 Cremers, C. J., Birkebak, R. C., and White, J. E., "Lunar Surface Temperatures at Tranquillity Base," *AIAA Journal*, Vol. 9, No. 10, 1971, pp. 1899–1903.

2 Birkebak, R. C., Cremers, C. J., and Dawson, J. P., "Thermal Radiation Properties and Thermal Conductivity of Lunar Material," *Apollo 11 Lunar Science Conference*, 1970, pp. 724–725.

3 Birkebak, R. C., Cremers, C. J., and Dawson, J. P., "Directional Spectral and Total Reflectance of Lunar Material," *Pro. Apollo 11 Lunar Sci. Conf. Geochim. Cosmochim. Acta Suppl. 1*, Vol. 3, 1970, pp. 1993–2000.

4 Birkebak, R. C., Cremers, C. J., and Dawson, J. P., "Spectral Directional Reflectance of Lunar Fines as a Function of Bulk Density," *Pro. of the 2nd Lunar Sci. Conf.*, Vol. 3, 1971, pp. 2197–2202.

5 Cremers, C. J., Birkebak, R. C., and Dawson, J. P., "Thermal Conductivity of Fines from Apollo 11," *Pro. Apollo 11 Lunar Sci. Conf. Geochim. Cosmochim. Acta Suppl. 1*, Vol. 3, 1970, pp. 2045–2050.

6 Cremers, C. J., and Birkebak, R. C., "Thermal Conductivity of Fines from Apollo 12," *Pro. of the 2nd Lunar Sci. Conf.*, Vol. 3, 1971, pp. 2311–2315.

7 Robie, R. A., Hemingway, B. S., and Wilson, W. H., "Specific Heats of Lunar Surface Material from 90° to 350°K," *Pro. Apollo 11 Lunar Sci. Conf. Geochim. Cosmochim. Acta Suppl. 1*, Vol. 3, 1970, pp. 2361–2367.

8 Gold, T., O'Leary, B. T., and Campbell, M. J., "Physical Properties of the Apollo 12 Lunar Fines," *Apollo 12 Lunar Science Conference* (unpublished proceedings), Jan. 1971.

9 Scott, R. F., Carrier, W. D., Costes, N. C., and Mitchell, J. K., "Mechanical Properties of the Lunar Regolith," Apollo 12 Preliminary Science Report, NASA SP-235, 1970, pp. 61–182.

10 Birkebak, R. C., "A Technique for Measuring Spectral Emittance," *Rev. Sci. Inst.*, July 1972.

11 Aronson, J. R., Emslie, A. G., Rooney, T. P., Coleman, I., and Horlick, G., "Spectral Emittance and Reflectance of Powders," *Appl. Opt.*, Vol. 8, 1969, p. 1639.

Generalized Correlation for Film Boiling

L. DAVIS CLEMENTS[1] and C. PHILLIP COLVER[1]

Nomenclature

g = gravitational acceleration, ft/sec²

g_c = gravitational constant, lb_m-ft/lb_f-sec²

h_{fg} = latent heat of vaporization, Btu/lb_m

k = thermal conductivity, Btu/ft-hr-deg R

q = heat flux, Btu/ft²-hr

B = Laplace reference length $= \left(\frac{g_c\sigma}{g(\rho_l - \rho_v)}\right)^{1/2}$, ft

C_p = heat capacity, Btu/lb_m-deg R

L = characteristic length, ft

Nu_B = Nusselt number based on Laplace reference length $= \frac{qB}{k\Delta T}$

Nu_L = Nusselt number based on characteristic heater dimension $= \frac{qL}{k\Delta T}$

Nu_λ = Nusselt number based on critical wavelength $= \frac{q\lambda}{k\Delta T}$

Pr = Prandtl number $= \frac{C_p\mu}{k}$

Ra = Rayleigh number $= \frac{L^3 g\rho_f(\rho_l - \rho_f)\mathrm{Pr}_f}{\mu_f{}^2}$

T_c = critical temperature, deg R

T_r = reduced temperature $= \frac{T_{\mathrm{sat}}}{T_c}$

T_{sat} = saturation temperature, deg R

T_{wall} = heater surface temperature, deg R

ΔT = temperature driving force $= T_{\mathrm{wall}} - T_{\mathrm{sat}}$, deg R

λ = critical wavelength $= 2\pi\left(\frac{g_c\sigma}{g(\rho_l - \rho_v)}\right)^{1/2}$, ft

μ_f = vapor-film viscosity, lb_m/ft-hr

ρ_f = average vapor-film density, lb_m/ft³

ρ_l = saturated liquid density, lb_m/ft³

ρ_v = saturated vapor density, lb_m/ft³

σ = surface tension, lb_f/ft

θ = heat parameter $= \frac{h_{fg}}{C_p\Delta T}$

θ' = modified heat parameter $= \frac{h_{fg}}{C_p\Delta T}\left(1 + 0.5\frac{C_p\Delta T}{h_{fg}}\right)$

θ'' = modified heat parameter $= \frac{h_{fg}}{C_p\Delta T}\left(1 + 0.34\frac{C_p\Delta T}{h_{fg}}\right)^2$

[1] School of Chemical Engineering and Materials Science, University of Oklahoma, Norman, Okla.

Contributed by the Heat Transfer Division of THE AMERICAN SOCIETY OF MECHANICAL ENGINEERS. Manuscript received by the Heat Transfer Division February 26, 1971.

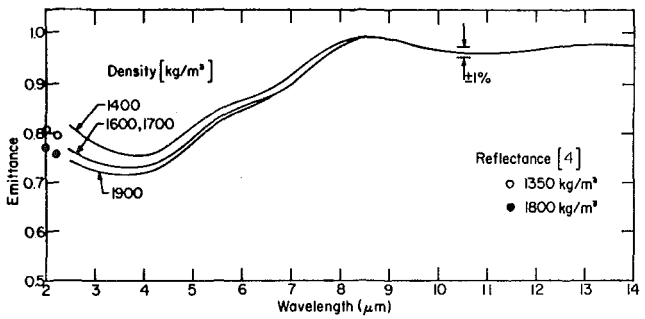

Fig. 1 Spectral emittance of Apollo-12 lunar fines

perature for all measurements was approximately 380 deg K, a temperature very near the maximum temperature experienced by the sample on the moon [1].

Clearly evident in Fig. 1 is the effect of bulk density. Because the results for densities of 1600 and 1710 kg/m³ were so close together, we have drawn a single curve through them. The emittance decreases with increasing density for the shorter wavelengths, with a change of approximately 7 percent at 3 μm between the smallest and largest densities, and as the wavelengths become larger the difference becomes negligible. The greatest uncertainties in our measurements are for wavelengths from 2 to 2.5 μm, and in this region the maximum effect of density [4] on reflectance was shown to occur. As the surface becomes more compacted, that is, a greater number of particles per unit volume, the void fraction decreases; therefore, the size of the cavities in the surface which absorb and emit energy are reduced and the emittance decreases. From our results we see that we are approaching or have reached the limit where the porosity of the sample does not affect the emittance value, that is, the material behaves as if it were a solid material. This conclusion was also reached for visible reflectance measurement [4].

The emittance is compared to the directional-reflectance result [4] for the wavelength range where they overlap near 2 μm, and our present results are good for the higher densities, that is, there is a reasonable match of the measured values of emittance and one minus the reflectance, but poor agreement for the density of 1400 kg/m³.

The total emittance as a function of temperature has been calculated for a bulk density of 1900 kg/m³. The lunar emittance varies from 0.972 to 0.927 for a temperature range from 90 to 400 deg K, the expected temperature range on the lunar surface. The equation representing the results is

$$\epsilon = 0.9843 - 0.2037 \times 10^{-3}T + 0.1863 \times 10^{-5}T^{-2} - 0.6765 \times 10^{-8}T^{-3} + 0.6436 \times 10^{-11}T^{-4} \quad (2)$$

where T is the absolute temperature in degrees Kelvin.

References

1 Cremers, C. J., Birkebak, R. C., and White, J. E., "Lunar Surface Temperatures at Tranquillity Base," *AIAA Journal*, Vol. 9, No. 10, 1971, pp. 1899–1903.

2 Birkebak, R. C., Cremers, C. J., and Dawson, J. P., "Thermal Radiation Properties and Thermal Conductivity of Lunar Material," *Apollo 11 Lunar Science Conference*, 1970, pp. 724–725.

3 Birkebak, R. C., Cremers, C. J., and Dawson, J. P., "Directional Spectral and Total Reflectance of Lunar Material," *Pro. Apollo 11 Lunar Sci. Conf. Geochim. Cosmochim. Acta Suppl. 1*, Vol. 3, 1970, pp. 1993–2000.

4 Birkebak, R. C., Cremers, C. J., and Dawson, J. P., "Spectral Directional Reflectance of Lunar Fines as a Function of Bulk Density," *Pro. of the 2nd Lunar Sci. Conf.*, Vol. 3, 1971, pp. 2197–2202.

5 Cremers, C. J., Birkebak, R. C., and Dawson, J. P., "Thermal Conductivity of Fines from Apollo 11," *Pro. Apollo 11 Lunar Sci. Conf. Geochim. Cosmochim. Acta Suppl. 1*, Vol. 3, 1970, pp. 2045–2050.

6 Cremers, C. J., and Birkebak, R. C., "Thermal Conductivity of Fines from Apollo 12," *Pro. of the 2nd Lunar Sci. Conf.*, Vol. 3, 1971, pp. 2311–2315.

7 Robie, R. A., Hemingway, B. S., and Wilson, W. H., "Specific Heats of Lunar Surface Material from 90° to 350°K," *Pro. Apollo 11 Lunar Sci. Conf. Geochim. Cosmochim. Acta Suppl. 1*, Vol. 3, 1970, pp. 2361–2367.

8 Gold, T., O'Leary, B. T., and Campbell, M. J., "Physical Properties of the Apollo 12 Lunar Fines," *Apollo 12 Lunar Science Conference* (unpublished proceedings), Jan. 1971.

9 Scott, R. F., Carrier, W. D., Costes, N. C., and Mitchell, J. K., "Mechanical Properties of the Lunar Regolith," Apollo 12 Preliminary Science Report, NASA SP-235, 1970, pp. 61–182.

10 Birkebak, R. C., "A Technique for Measuring Spectral Emittance," *Rev. Sci. Inst.*, July 1972.

11 Aronson, J. R., Emslie, A. G., Rooney, T. P., Coleman, I., and Horlick, G., "Spectral Emittance and Reflectance of Powders," *Appl. Opt.*, Vol. 8, 1969, p. 1639.

Generalized Correlation for Film Boiling

L. DAVIS CLEMENTS[1] and C. PHILLIP COLVER[1]

Nomenclature

g = gravitational acceleration, ft/sec²
g_c = gravitational constant, lb_m-ft/lb_f-sec²
h_{fg} = latent heat of vaporization, Btu/lb_m
k = thermal conductivity, Btu/ft-hr-deg R
q = heat flux, Btu/ft²-hr
B = Laplace reference length $= \left(\frac{g_c\sigma}{g(\rho_l - \rho_v)}\right)^{1/2}$, ft
C_p = heat capacity, Btu/lb_m-deg R
L = characteristic length, ft
Nu_B = Nusselt number based on Laplace reference length $= \frac{qB}{k\Delta T}$
Nu_L = Nusselt number based on characteristic heater dimension $= \frac{qL}{k\Delta T}$
Nu_λ = Nusselt number based on critical wavelength $= \frac{q\lambda}{k\Delta T}$
Pr = Prandtl number $= \frac{C_p\mu}{k}$
Ra = Rayleigh number $= \frac{L^3 g\rho_f(\rho_l - \rho_f)Pr_f}{\mu_f{}^2}$
T_c = critical temperature, deg R
T_r = reduced temperature $= \frac{T_{sat}}{T_c}$
T_{sat} = saturation temperature, deg R
T_{wall} = heater surface temperature, deg R
ΔT = temperature driving force $= T_{wall} - T_{sat}$, deg R
λ = critical wavelength $= 2\pi\left(\frac{g_c\sigma}{g(\rho_l - \rho_v)}\right)^{1/2}$, ft
μ_f = vapor-film viscosity, lb_m/ft-hr
ρ_f = average vapor-film density, lb_m/ft³
ρ_l = saturated liquid density, lb_m/ft³
ρ_v = saturated vapor density, lb_m/ft³
σ = surface tension, lb_f/ft
θ = heat parameter $= \frac{h_{fg}}{C_p\Delta T}$
θ' = modified heat parameter $= \frac{h_{fg}}{C_p\Delta T}\left(1 + 0.5\frac{C_p\Delta T}{h_{fg}}\right)$
θ'' = modified heat parameter $= \frac{h_{fg}}{C_p\Delta T}\left(1 + 0.34\frac{C_p\Delta T}{h_{fg}}\right)^2$

[1] School of Chemical Engineering and Materials Science, University of Oklahoma, Norman, Okla.

Contributed by the Heat Transfer Division of THE AMERICAN SOCIETY OF MECHANICAL ENGINEERS. Manuscript received by the Heat Transfer Division February 26, 1971.

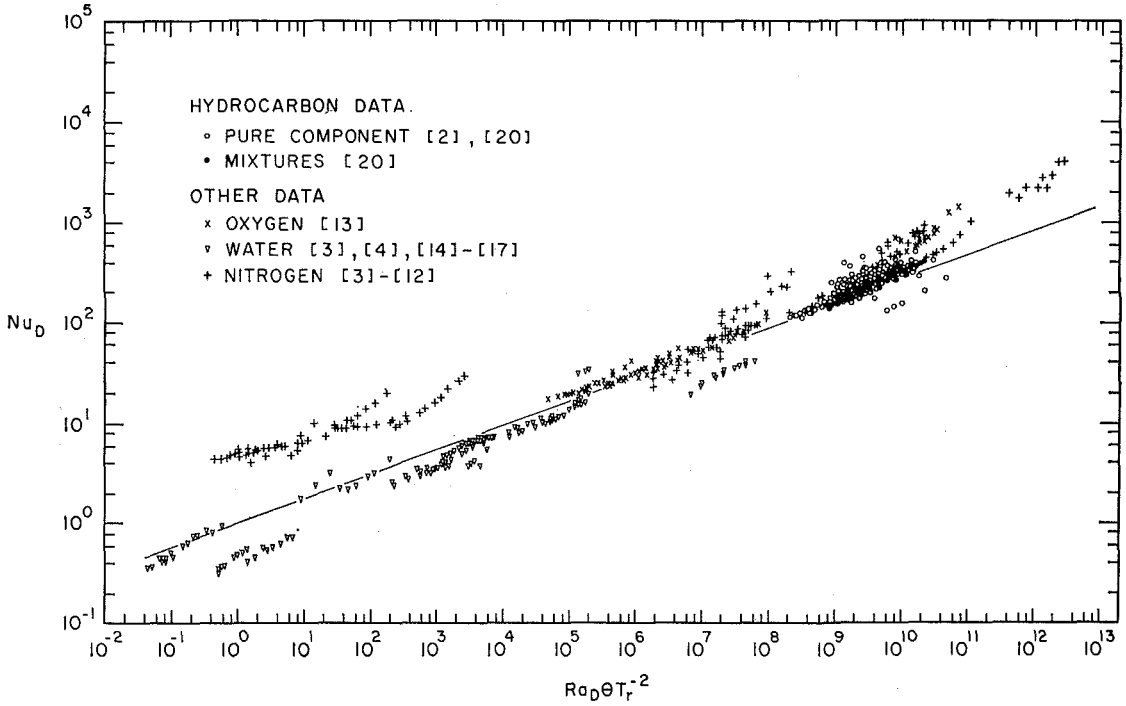

Fig. 1 Comparison of equation (3) with experimental data

THIS brief note presents a generalized correlation for stable natural-convection film-boiling heat transfer. It will be seen that the proposed correlation, which results from an extension of previous theoretical and correlational work, compares more favorably than any existing correlation with data for a variety of substances on several heater types, and over a wide range of system pressures.

Previous Correlations

A comprehensive presentation of the theoretical and semi-empirical correlations which have been mentioned in the literature was presented by the authors in an earlier paper [1].[2] Those correlations to be presented here relate most directly to the development of the newly proposed correlation.

Bromley [3, 4], after making several simplifying assumptions, analytically described stable film boiling from a horizontal tube heater. Principally, he assumed that heat transfer took place solely by conduction and radiation through a thin vapor film surrounding the heater. Correlating the results with his experimental data gave the relationship

$$Nu_D = 0.62(Ra\ \theta')_f^{1/4} \tag{1}$$

where the Nusselt number Nu_D uses the heater diameter as the characteristic dimension. Modifications of Bromley's equation by Pomerantz [24] and Breen and Westwater [21] are shown in Table 1.

Analyses based wholly on Taylor's instability theory have provided several physical models for stable film boiling. Considering the four possible models as discussed by Frederking [25], Sciance et al. [2] found a statistical preference for that which assumed regular vapor release and laminar vapor flow. To improve on the accuracy of the correlation for their hydrocarbon data over a wide pressure range, Sciance, et al. [2] incorporated the factor T_r^{-2} and determined the best-fit relation

$$Nu_B = 0.369[Ra\ \theta' T_r^{-2}]_f^{0.267} \tag{2}$$

where the Nusselt number Nu_B is based on the Laplace reference length. A similar relationship proposed by Frederking [23] is given in Table 1.

Proposed Correlation

The primary goal in developing a new film-boiling correlation was to simultaneously account for the dependence of stable film-boiling behavior upon the characteristic heater dimension and system pressure. To accomplish this end, most of the film-boiling correlations presently available [1] were tested with a considerable body of data [1]. Data were selected for substances in which properties were available or could be reliably determined. It was determined that equation (1) proposed by Bromley statistically compares best with data at a constant pressure but with varied heater diameter, and that equation (2) proposed by Sciance et al. [2] best represents data over a wide pressure range. Then a complete analysis was carried out on the models and dimensionless parameters commonly associated with film boiling. It was found on correlating over 750 experimental data values for water [3, 4, 14–19], nitrogen [3–12], oxygen [13], and a number of pure-

[2] Numbers in brackets designate References at end of technical brief.

Table 1 Comparison of film-boiling correlations

Author	Correlation	Average percent deviation (754 data values)
This work	$Nu_L = 0.94(Ra_D\theta' T_r^{-2})_f^{1/4}$	21.8
Sciance et al. [2]	$Nu_B = 0.369(Ra_B\theta' T_r^{-2})_f^{0.267}$	32.0
Bromley [3, 4]	$Nu_D = 0.62(Ra_D\theta')_f^{1/4}$	30.2
Breen and Westwater [21]	$Nu_\lambda = \left[0.59 - \frac{0.069\lambda}{D}\right]^{1/4} [Ra_\lambda\theta'']_f^{1/4}$	58.5
Berenson [22]	$Nu_B = 0.425[Ra_B\theta']_f^{1/4}$	38.3
Frederking [23]	$Nu_B = 0.2[Ra_B\theta']_f^{1/4}$	47.8
Pomerantz [24]	$Nu_D = 0.62\left[\frac{D}{\lambda}\right]^{0.172} [Ra\ \theta'']_f^{1/4}$	36.3

component [2, 20] and mixture [20] hydrogen systems on a wide variety of heaters and a large range of pressures that the following relationship was better than all correlations tested:

$$\mathrm{Nu}_L = 0.94(\mathrm{Ra}\ \theta' T_r^{-2})^{1/4} \tag{3}$$

Here the Nusselt number Nu_L is to be based upon the characteristic heater dimension L. For example, for a cylindrical heater L is the heater diameter, and for a flat-plate heater L may be the plate diameter or its width. Fig. 1 shows the comparison of equation (3) to the data, while Table 1 indicates the average absolute deviations for equation (3) and a number of commonly used correlations. It is immediately evident from Table 1 that equation (3) compares with the data decidedly better than any of the other expressions available.

References

1 Clements, L. D., and Colver, C. P., "Natural Convection Film Boiling Heat Transfer," *Industrial and Engineering Chemistry*, Vol. 62, No. 9, 1970, pp. 26–46.

2 Sciance, C. T., Colver, C. P., and Sliepcevich, C. M., "Film Boiling Measurements and Correlation for Liquified Hydrocarbon Gases," *Chemical Engineering Progress Symposium Series*, Vol. 63, No. 77, 1967, pp. 115–119.

3 Bromley, L. A., "Heat Transfer in Stable Film Boiling," *Chemical Engineering Progress*, Vol. 46, No. 5, 1950, pp. 221–227.

4 Bromley, L. A., "Heat Transfer in Stable Film Boiling," AECD2295, 1948.

5 Wayner, P. C., and Bankoff, S. G., "Film Boiling with Suction on an Electrically Heated Porous Plate," *AIChE Journal*, Vol. 11, No. 1, 1965, pp. 59–64.

6 Ruzicka, J., "Heat Transfer to Boiling Nitrogen," in: *Problems of Low Temperature Physics*, Vol. 1, Pergamon Press, New York, N. Y., 1959, pp. 323–329.

7 Weil, L., "Coefficients d'echange dans les gaz liquifies bouillants," *Proceedings of Eighth International Congress of Refrigeration*, 1951, pp. 181–185.

8 Weil, L., and Lacaze, A., "Coefficients d'echange thermique dans l'azote bouillants," *Comp. Rend.*, Vol. 230, No. 1, 1950, pp. 186–188.

9 Cowley, C. W., Timson, W. J., and Sawdye, J. A., "A Method for Improving Heat Transfer at a Boiling Fluid," *Industrial and Engineering Chemistry, Process Design Developments*, Vol. 1, No. 2, 1962, pp. 81–84.

10 Flynn, T. M., Draper, J. W., and Roos, J. J., "The Nucleate and Film Boiling Curve of Liquid Nitrogen at One Atmosphere," *Advances in Cryogenic Engineering*, Vol. 7, 1962, pp. 539–545.

11 Frederking, T. H. K., "Film Boiling of Helium I and Other Liquified Gases on Single Wires," *AIChE Journal*, No. 3, 1959, pp. 403–406.

12 Frederking, T. H. K., and Clark, J. A., "Natural Convection Film Boiling on a Sphere," *Advances in Cryogenic Engineering*, Vol. 8, 1963, pp. 501–506.

13 Banchero, J. T., Barker, G. E., and Boll, R. H., "Stable Film Boiling of Liquid Oxygen Outside Single Horizontal Tubes and Wires," *Chemical Engineering Progress Symposium Series*, Vol. 51, 1955, pp. 21–31.

14 Grassman, P., and Hauser, J. J., "Heat Transfer from Wires to Subcooled and Boiling Water," *International Journal of Heat and Mass Transfer*, Vol. 7, 1964, p. 211.

15 Di Cicco, D. A., and Schoenhals, R. J., "Heat Transfer in Film Boiling With Pulsating Pressures," JOURNAL OF HEAT TRANSFER, TRANS. ASME, Series C, Vol. 86, No. 3, Aug. 1964, pp. 457–461.

16 McAdams, W. H., Addoms, J. N., Rinaldo, P. M., and Day, R. S., "Heat Transfer from Single Horizontal Wires to Boiling Water," *Chemical Engineering Progress*, Vol. 44, No. 8, 1948, pp. 639–646.

17 Tachibana, F., and Fukui, S., "Heat Transfer in Film Boiling to Subcooled Liquids," *International Developments in Heat Transfer*, 1961, pp. 219–223.

18 Nishikawa, K., and Shimomura, R., "Boiling Heat Transfer at the Coexistence of Nucleate and Film Regions," *Bulletin of the Japan Society of Mechanical Engineers*, Vol. 7, No. 26, 1964, p. 399.

19 Nishikawa, K., Shimomura, R., Hatano, M., and Nagatomo, H., "Investigation of Surface Film Boiling under Free Convection," *Bulletin of the Japan Society of Mechanical Engineers*, Vol. 10, No. 37, 1967, pp. 123–131.

20 Wright, R. D., Clements, L. D., and Colver, C. P., "Nucleate and Film Boiling of Ethane–Ethylene Mixtures," *AIChE Journal*, Vol. 17, No. 3, 1971, pp. 626–630.

21 Breen, B. P., and Westwater, J. W., "Effect of Diameter of Horizontal Tubes on Film Boiling Heat Transfer," *Chemical Engineering Progress*, Vol. 58, No. 7, 1962, pp. 67–72.

22 Berenson, P. J., "Film-Boiling Heat Transfer From a Horizontal Surface," JOURNAL OF HEAT TRANSFER, TRANS. ASME, Series C, Vol. 83, No. 3, Aug. 1961, pp. 351–358.

23 Frederking, T. H. K., "Film Boiling of Helium I and Other Liquefied Gases on Single Wires," *AIChE Journal*, Vol. 5, No. 3, 1959, pp. 403–406.

24 Pomerantz, M. L., "Film Boiling on a Horizontal Tube in Increased Gravity Fields," JOURNAL OF HEAT TRANSFER, TRANS. ASME, Series C, Vol. 86, No. 2, May 1964, pp. 213–219.

25 Frederking, T. H. K., Wu, Y. C., and Clement, B. W., "Effects of Interfacial Instability of Film Boiling of Saturated Liquid Helium I above a Horizontal Surface," *AIChE Journal*, Vol. 12, No. 2, 1966, pp. 238–244.

Efficient Computation of Radiant-Interchange Configuration Factors within the Enclosure

E. F. SOWELL[1] **and P. F. O'BRIEN**[2]

IT IS well known that due to the laws of reciprocity and flux conservation, not all of the n^2 radiant-interchange configuration factors for an n-surface enclosure are independent [1].[3] Thus, theoretically, the analyst of the radiative exchange problem within the general enclosure comprised of plane, convex, and concave surfaces need only refer to the fundamental definition of the configuration factor (or a computational procedure based upon this definition) $n(n-1)/2$ times in order to assemble the entire matrix of these factors, F. However, in practice it is often found that the $n(n-1)/2$ factors most easily determined by the definition fill in the F-matrix in such a way that the determination of the remaining factors by reciprocity and conservation is not a sequential process and is generally quite confusing. This is evidenced by the fact that computer programs requiring the F-matrix generally apply only reciprocity, either allowing conservation to be violated $\left(\sum_j F_{ij} \neq 1\right)$, or enforcing it by normalization of each row. Neither of these methods is strictly correct, and moreover the analyst is required to calculate n factors from the definition which could and should be calculated from conservation. In this note, a straightforward method is presented whereby the entire F-matrix is calculated given only the minimum number of factors by enforcing reciprocity and conservation.

The method presented here is based upon the fact that one factor in each row of the F-matrix must be determined by the conservation equation for that row. That is

$$F_{iJ(i)} = 1 - \sum_{\substack{j=1 \\ j \neq J(i)}}^{n} F_{ij} \qquad i = 1, 2, \ldots, n \tag{1}$$

where the column index of the factor to be determined by the ith conservation equation is designated $J(i)$. With certain restrictions discussed below, the $J(i)$ can be selected freely within each row.

Equation (1) is not a suitable computational algorithm, however, since there may be yet-undetermined factors in the summation on the right-hand side. This difficulty is eliminated by a matrix formulation of the conservation relationship in which the n $F_{iJ(i)}$ defined by equation (1) are solved for simultaneously.

The law of flux conservation in vector-matrix notation is

---

[1] Litton Ship Systems, Culver City, Calif. Mem. ASME.

[2] University of California at Los Angeles, Los Angeles, Calif.

[3] Numbers in brackets designate References at end of technical brief.

Contributed by the Heat Transfer Division of THE AMERICAN SOCIETY OF MECHANICAL ENGINEERS. Manuscript received by the Heat Transfer Division November 10, 1971.

component [2, 20] and mixture [20] hydrogen systems on a wide variety of heaters and a large range of pressures that the following relationship was better than all correlations tested:

$$\mathrm{Nu}_L = 0.94(\mathrm{Ra}\ \theta' T_r^{-2})^{1/4} \tag{3}$$

Here the Nusselt number Nu_L is to be based upon the characteristic heater dimension L. For example, for a cylindrical heater L is the heater diameter, and for a flat-plate heater L may be the plate diameter or its width. Fig. 1 shows the comparison of equation (3) to the data, while Table 1 indicates the average absolute deviations for equation (3) and a number of commonly used correlations. It is immediately evident from Table 1 that equation (3) compares with the data decidedly better than any of the other expressions available.

References

1 Clements, L. D., and Colver, C. P., "Natural Convection Film Boiling Heat Transfer," *Industrial and Engineering Chemistry*, Vol. 62, No. 9, 1970, pp. 26–46.

2 Sciance, C. T., Colver, C. P., and Sliepcevich, C. M., "Film Boiling Measurements and Correlation for Liquified Hydrocarbon Gases," *Chemical Engineering Progress Symposium Series*, Vol. 63, No. 77, 1967, pp. 115–119.

3 Bromley, L. A., "Heat Transfer in Stable Film Boiling," *Chemical Engineering Progress*, Vol. 46, No. 5, 1950, pp. 221–227.

4 Bromley, L. A., "Heat Transfer in Stable Film Boiling," AECD2295, 1948.

5 Wayner, P. C., and Bankoff, S. G., "Film Boiling with Suction on an Electrically Heated Porous Plate," *AIChE Journal*, Vol. 11, No. 1, 1965, pp. 59–64.

6 Ruzicka, J., "Heat Transfer to Boiling Nitrogen," in: *Problems of Low Temperature Physics*, Vol. 1, Pergamon Press, New York, N. Y., 1959, pp. 323–329.

7 Weil, L., "Coefficients d'echange dans les gaz liquifies bouillants," *Proceedings of Eighth International Congress of Refrigeration*, 1951, pp. 181–185.

8 Weil, L., and Lacaze, A., "Coefficients d'echange thermique dans l'azote bouillants," *Comp. Rend.*, Vol. 230, No. 1, 1950, pp. 186–188.

9 Cowley, C. W., Timson, W. J., and Sawdye, J. A., "A Method for Improving Heat Transfer at a Boiling Fluid," *Industrial and Engineering Chemistry, Process Design Developments*, Vol. 1, No. 2, 1962, pp. 81–84.

10 Flynn, T. M., Draper, J. W., and Roos, J. J., "The Nucleate and Film Boiling Curve of Liquid Nitrogen at One Atmosphere," *Advances in Cryogenic Engineering*, Vol. 7, 1962, pp. 539–545.

11 Frederking, T. H. K., "Film Boiling of Helium I and Other Liquified Gases on Single Wires," *AIChE Journal*, No. 3, 1959, pp. 403–406.

12 Frederking, T. H. K., and Clark, J. A., "Natural Convection Film Boiling on a Sphere," *Advances in Cryogenic Engineering*, Vol. 8, 1963, pp. 501–506.

13 Banchero, J. T., Barker, G. E., and Boll, R. H., "Stable Film Boiling of Liquid Oxygen Outside Single Horizontal Tubes and Wires," *Chemical Engineering Progress Symposium Series*, Vol. 51, 1955, pp. 21–31.

14 Grassman, P., and Hauser, J. J., "Heat Transfer from Wires to Subcooled and Boiling Water," *International Journal of Heat and Mass Transfer*, Vol. 7, 1964, p. 211.

15 Di Cicco, D. A., and Schoenhals, R. J., "Heat Transfer in Film Boiling With Pulsating Pressures," JOURNAL OF HEAT TRANSFER, TRANS. ASME, Series C, Vol. 86, No. 3, Aug. 1964, pp. 457–461.

16 McAdams, W. H., Addoms, J. N., Rinaldo, P. M., and Day, R. S., "Heat Transfer from Single Horizontal Wires to Boiling Water," *Chemical Engineering Progress*, Vol. 44, No. 8, 1948, pp. 639–646.

17 Tachibana, F., and Fukui, S., "Heat Transfer in Film Boiling to Subcooled Liquids," *International Developments in Heat Transfer*, 1961, pp. 219–223.

18 Nishikawa, K., and Shimomura, R., "Boiling Heat Transfer at the Coexistence of Nucleate and Film Regions," *Bulletin of the Japan Society of Mechanical Engineers*, Vol. 7, No. 26, 1964, p. 399.

19 Nishikawa, K., Shimomura, R., Hatano, M., and Nagatomo, H., "Investigation of Surface Film Boiling under Free Convection," *Bulletin of the Japan Society of Mechanical Engineers*, Vol. 10, No. 37, 1967, pp. 123–131.

20 Wright, R. D., Clements, L. D., and Colver, C. P., "Nucleate and Film Boiling of Ethane–Ethylene Mixtures," *AIChE Journal*, Vol. 17, No. 3, 1971, pp. 626–630.

21 Breen, B. P., and Westwater, J. W., "Effect of Diameter of Horizontal Tubes on Film Boiling Heat Transfer," *Chemical Engineering Progress*, Vol. 58, No. 7, 1962, pp. 67–72.

22 Berenson, P. J., "Film-Boiling Heat Transfer From a Horizontal Surface," JOURNAL OF HEAT TRANSFER, TRANS. ASME, Series C, Vol. 83, No. 3, Aug. 1961, pp. 351–358.

23 Frederking, T. H. K., "Film Boiling of Helium I and Other Liquefied Gases on Single Wires," *AIChE Journal*, Vol. 5, No. 3, 1959, pp. 403–406.

24 Pomerantz, M. L., "Film Boiling on a Horizontal Tube in Increased Gravity Fields," JOURNAL OF HEAT TRANSFER, TRANS. ASME, Series C, Vol. 86, No. 2, May 1964, pp. 213–219.

25 Frederking, T. H. K., Wu, Y. C., and Clement, B. W., "Effects of Interfacial Instability of Film Boiling of Saturated Liquid Helium I above a Horizontal Surface," *AIChE Journal*, Vol. 12, No. 2, 1966, pp. 238–244.

Efficient Computation of Radiant-Interchange Configuration Factors within the Enclosure

E. F. SOWELL[1] **and P. F. O'BRIEN**[2]

IT IS well known that due to the laws of reciprocity and flux conservation, not all of the n^2 radiant-interchange configuration factors for an n-surface enclosure are independent [1].[3] Thus, theoretically, the analyst of the radiative exchange problem within the general enclosure comprised of plane, convex, and concave surfaces need only refer to the fundamental definition of the configuration factor (or a computational procedure based upon this definition) $n(n-1)/2$ times in order to assemble the entire matrix of these factors, F. However, in practice it is often found that the $n(n-1)/2$ factors most easily determined by the definition fill in the F-matrix in such a way that the determination of the remaining factors by reciprocity and conservation is not a sequential process and is generally quite confusing. This is evidenced by the fact that computer programs requiring the F-matrix generally apply only reciprocity, either allowing conservation to be violated $\left(\sum_j F_{ij} \neq 1\right)$, or enforcing it by normalization of each row. Neither of these methods is strictly correct, and moreover the analyst is required to calculate n factors from the definition which could and should be calculated from conservation. In this note, a straightforward method is presented whereby the entire F-matrix is calculated given only the minimum number of factors by enforcing reciprocity and conservation.

The method presented here is based upon the fact that one factor in each row of the F-matrix must be determined by the conservation equation for that row. That is

$$F_{iJ(i)} = 1 - \sum_{\substack{j=1 \\ j \neq J(i)}}^{n} F_{ij} \qquad i = 1, 2, \ldots, n \tag{1}$$

where the column index of the factor to be determined by the ith conservation equation is designated $J(i)$. With certain restrictions discussed below, the $J(i)$ can be selected freely within each row.

Equation (1) is not a suitable computational algorithm, however, since there may be yet-undetermined factors in the summation on the right-hand side. This difficulty is eliminated by a matrix formulation of the conservation relationship in which the n $F_{iJ(i)}$ defined by equation (1) are solved for simultaneously.

The law of flux conservation in vector-matrix notation is

---

[1] Litton Ship Systems, Culver City, Calif. Mem. ASME.

[2] University of California at Los Angeles, Los Angeles, Calif.

[3] Numbers in brackets designate References at end of technical brief.

Contributed by the Heat Transfer Division of THE AMERICAN SOCIETY OF MECHANICAL ENGINEERS. Manuscript received by the Heat Transfer Division November 10, 1971.

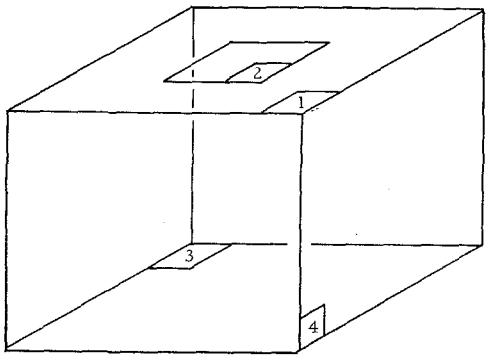

Fig. 1 Example enclosure defined by 4 surfaces

$$AFU = AU \tag{2}$$

where U is the unit n-vector and A is a diagonal matrix of the enclosure surface areas. Now consider F to be the sum of two $n \times n$ matrices F' and F'' such that F' contains only the known or given F_{ij} and their symmetric counterparts determined by reciprocity, with zeros elsewhere. Then F'' has only the $F_{iJ(i)}$ entries and their symmetric counterparts, and equation (2) becomes

$$AF'U + AF''U = AU \tag{3}$$

in which the second term contains all the unknown factors. This term can be represented also as

$$AF''U = BX \tag{4}$$

where X is a vector of unknown "exchange areas"

$$X_i = A_i F_{iJ(i)} \qquad i = 1, 2, \ldots, n \tag{5}$$

The matrix B which makes equation (4) true is found to be composed of ones and zeros such that

$$\left.\begin{aligned} b_{ij} &= 1 \quad \text{for} \quad i = j \text{ or } i = J(j) \\ &= 0 \text{ otherwise} \end{aligned}\right\} \tag{6}$$

Substituting equation (4) into equation (3) and solving for X gives

$$X = B^{-1}A(I - F')U \tag{7}$$

where I is the identity matrix. This is the solution to the problem, since the unknown factors are related to X by equation (5).

It is important to note that B^{-1} must exist in order to determine a unique X. In systems with $n > 4$, it is possible to select a J such that this condition is not met, indicating that equations (1) are not linearly independent in the unknown factors. In this case a different J must be selected. The only other restriction which must be placed on the selection of J is that reciprocity cannot be violated among the members of J, i.e., $J(i) = k$ precludes $J(k) = i$.

An example will clarify the method. Consider the enclosure shown in Fig. 1 in which the upper surface is divided into two regions, 1 and 2, the lower surface is designated by 3, and all vertical surfaces are designated by 4. The F-matrix describing this enclosure has only $n(n-1)/2 = 6$ independent factors, but 4 of these are obviously zero since surfaces 1, 2, and 3 are each planar and 1 and 2 are coplanar. Therefore, only two factors need be determined by the definition or by a program [2]. The two most easily determined in this manner are F_{31} and F_{32}, which we will now assume to be available and designated by a and b respectively. The partially filled F-matrix F' is then

$$F' = \begin{bmatrix} 0 & 0 & (A_3/A_1)a & 0 \\ 0 & 0 & (A_3/A_2)b & 0 \\ a & b & 0 & 0 \\ 0 & 0 & 0 & 0 \end{bmatrix}$$

in which use has been made of reciprocity.

Now, the above selection of known factors leaves the last element in each row to be determined by conservation, so that $J = (4, 4, 4, 4)$. This gives the B-matrix from equation (6)

$$B = \begin{bmatrix} 1 & 0 & 0 & 0 \\ 0 & 1 & 0 & 0 \\ 0 & 0 & 1 & 0 \\ 1 & 1 & 1 & 1 \end{bmatrix}$$

from which the inverse is found by elementary row operations [3]

$$B^{-1} = \begin{bmatrix} 1 & 0 & 0 & 0 \\ 0 & 1 & 0 & 0 \\ 0 & 0 & 1 & 0 \\ -1 & -1 & -1 & 1 \end{bmatrix}$$

By equation (7) the unknown exchange areas are

$$X = \begin{bmatrix} 1 & 0 & 0 & 0 \\ 0 & 1 & 0 & 0 \\ 0 & 0 & 1 & 0 \\ -1 & -1 & -1 & 1 \end{bmatrix} \begin{bmatrix} A_1 & 0 & 0 & 0 \\ 0 & A_2 & 0 & 0 \\ 0 & 0 & A_3 & 0 \\ 0 & 0 & 0 & A_4 \end{bmatrix}$$

$$\times \begin{bmatrix} 1 & 0 & -(A_3/A_1)a & 0 \\ 0 & 1 & -(A_3/A_2)b & 0 \\ -a & -b & 1 & 0 \\ 0 & 0 & 0 & 1 \end{bmatrix} \begin{bmatrix} 1 \\ 1 \\ 1 \\ 1 \end{bmatrix}$$

$$= \begin{bmatrix} A_1[1 - (A_3/A_1)a] \\ A_2[1 - (A_3/A_2)b] \\ A_3(1 - a - b) \\ A_4 - A_1[1 - (A_3/A_1)a] - A_2[1 - (A_3/A_2)b] \\ \qquad - A_3(1 - a - b) \end{bmatrix}$$

By equation (5), the unknown factors and their symmetric counterparts are then determined, completing the example.

The foregoing example was chosen to be of small dimension in order to facilitate a hand calculation. The method is also well suited to computer calculations, and should find application in

Table 1 Computer procedure

1	Read non-zero values of n(n-1)/2 or fewer known factors and their indices, and J(i), i = 1 to n. Also, A(i), i = 1 to n.
2	Compute symmetric counterparts of input factors by reciprocity.
3	Compute C = A(I-F')U, i.e., $C_i = A_i(1 - \sum_j F'_{ij})$, i = 1 to n.
4	Set up B according to Equation (6).
5	Invert B; give error report and exit if determinant is zero.
6	Calculate $X = B^{-1}C$.
7	Calculate $F_{iJ(i)}$ and $F_{J(i)i}$ from Equation (5) and insert into F' matrix, thus creating the final F.
NOTE:	Checks should be made on the input data to ensure that input F_{ij} values are not redundant and do not conflict with those to be calculated, and that J is self-consistent as discussed above.

programs which require the F-matrix. It has been programmed in the APL and PL/1 programming languages at UCLA and in Fortran at Jet Propulsion Laboratories [4]. A suitable procedure is shown in Table 1.

References

1 Howell, J. R., and Siegel, R., "Thermal Radiation Heat Transfer," NASA SP-164, 1969, p. 39.

2 Toups, K. A., "A General Computer Program for the Determination of Radiant-Interchange Configuration and Form Factors—CONFAC II," North American Aviation SID 65-1043-2, 1965.

3 Carnahan, B., Luther, H. A., and Wilkes, J. O., *Applied Numerical Methods*, John Wiley & Sons, New York, N. Y., 1969, p. 269.

4 Sowell, E. F., "Environmental Radiation from Fluorescent Ceiling Systems," PhD dissertation, University of California at Los Angeles, March 1972.

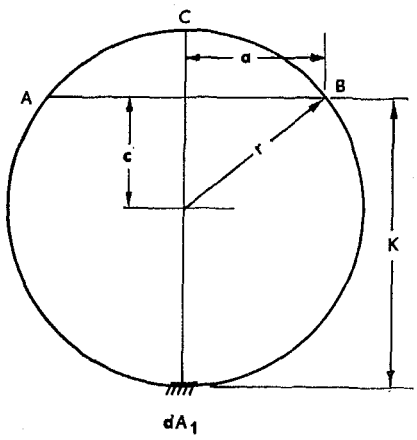

Fig. 1 Radiation from a plane point source to a coaxial disk

Radiation Shape Factors from Plane Point Sources

B. T. F. CHUNG[1] and P. S. SUMITRA[2]

IN THEIR recent paper, Feingold and Gupta [1][3] have developed a useful technique to calculate the radiation shape factors from spheres and long cylinders without involving multiple integrals. This technique will now be extended to determine the shape factors from planar point sources to a certain class of surfaces. In the previous reference, the configuration factors are derived regardless of the validity of Lambert's cosine law, whereas in this work Lambert's law is the basic assumption of the analysis. Analytical and graphical representations of shape factor for certain elementary configurations, some heretofore unavailable, are obtained.

Evaluation of Shape Factors

The view factors from a planar point source to the following configurations are to be presented: (1) coaxial circular disk, (2) very thin coaxial ring, (3) segment of a coaxial disk, (4) coaxial regular polygon, (5) coaxial isosceles triangle, (6) coaxial right circular cylinder, (7) coaxial sphere, and (8) orthogonal sphere.[4]

Referring to Fig. 1 and employing the basic mechanism in [1], we may state that the view factor from the element dA_1 to a coaxial disk AB is the same as that from dA_1 to the hollow spherical segment ACB. Since both dA_1 and the segment ACB lie on the same spherical enclosure, with the aid of Lambert's law the shape factor from dA_1 to ACB may be obtained as the area ratio of spherical segment ACB to the total area of the sphere [2], i.e.,

$$F_{dA_1-\text{disk}} = \frac{1}{2}\left(1 - \frac{c}{r}\right)$$

where c and r (see Fig. 1) may be solved from the following simple algebra equations:

$$r^2 - c^2 = a^2$$

$$r + c = K$$

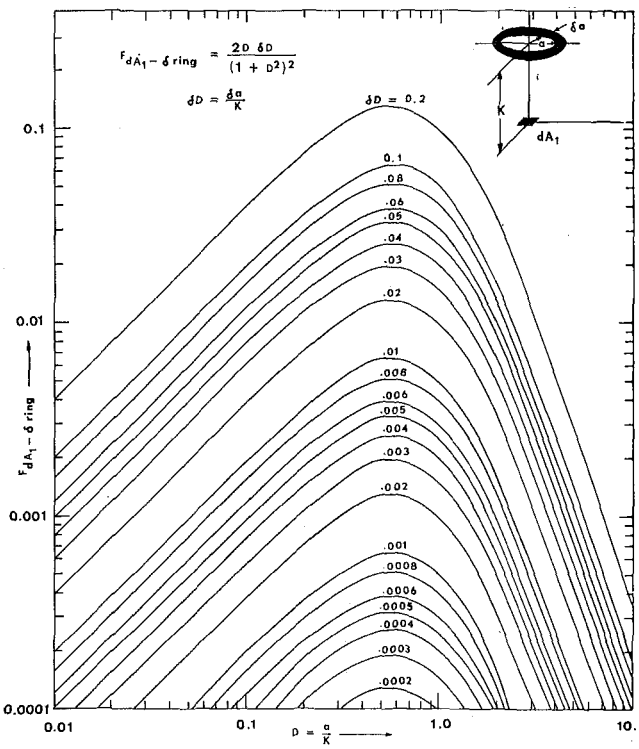

Fig. 2 Shape factors from a plane point source to a very thin coaxial ring

Hence it follows immediately

$$F_{dA_1-\text{disk}} = \frac{a^2}{K^2 + a^2} \tag{1}$$

Certainly, equation (1) can be arrived at by the methods of multiple integration [3], contour integration [4], and unit sphere [2]. However, the present approach appears to be much simpler.

Case 2 may be readily obtained by differentiating $F_{dA_1-\text{disk}}$ in equation (1). Case 3 follows from a single integration of $F_{dA_1-\delta\ \text{seg. ring}}$, the shape factor from element dA_1 to a segment of coaxial thin ring. Once the shape factors from an element to the coaxial disk and the coaxial segment of disk are known, Cases 4 to 6 can be solved by flux algebra. Referring to Fig. 5-A, it can be easily proved that the shape factor from a planar point source dA_1 to a coaxial sphere is equivalent to that from dA_1 to the coaxial circular disk AB. This leads to the same problem as Case 1 of which the solution is available. Similarly, the view factor between the plane point source dA_1 (see Fig. 5-B) and an orthogonal sphere is the same as that between dA_1

---

[1] Assistant Professor, Mechanical Engineering Department, University of Akron, Akron, Ohio. Assoc. Mem. ASME.

[2] Graduate Assistant, Mechanical Engineering Department, University of Akron, Akron, Ohio.

[3] Numbers in brackets designate References at end of technical brief.

[4] For brevity, we define that a sphere is "orthogonal" with respect to an element if the normal of the element is perpendicular to the line joining the element to the center of the sphere.

Contributed by the Heat Transfer Division of THE AMERICAN SOCIETY OF MECHANICAL ENGINEERS. Manuscript received by the Heat Transfer Division November 10, 1971.

programs which require the F-matrix. It has been programmed in the APL and PL/1 programming languages at UCLA and in Fortran at Jet Propulsion Laboratories [4]. A suitable procedure is shown in Table 1.

References

1 Howell, J. R., and Siegel, R., "Thermal Radiation Heat Transfer," NASA SP-164, 1969, p. 39.

2 Toups, K. A., "A General Computer Program for the Determination of Radiant-Interchange Configuration and Form Factors—CONFAC II," North American Aviation SID 65-1043-2, 1965.

3 Carnahan, B., Luther, H. A., and Wilkes, J. O., *Applied Numerical Methods*, John Wiley & Sons, New York, N. Y., 1969, p. 269.

4 Sowell, E. F., "Environmental Radiation from Fluorescent Ceiling Systems," PhD dissertation, University of California at Los Angeles, March 1972.

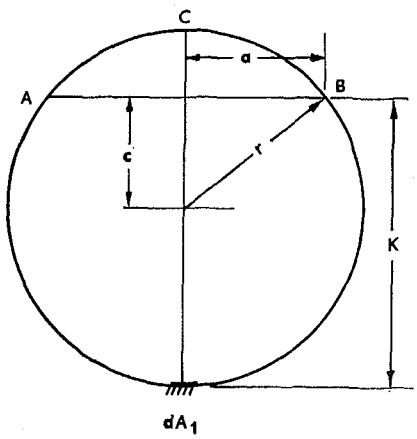

Fig. 1 Radiation from a plane point source to a coaxial disk

Radiation Shape Factors from Plane Point Sources

B. T. F. CHUNG[1] and P. S. SUMITRA[2]

IN THEIR recent paper, Feingold and Gupta [1][3] have developed a useful technique to calculate the radiation shape factors from spheres and long cylinders without involving multiple integrals. This technique will now be extended to determine the shape factors from planar point sources to a certain class of surfaces. In the previous reference, the configuration factors are derived regardless of the validity of Lambert's cosine law, whereas in this work Lambert's law is the basic assumption of the analysis. Analytical and graphical representations of shape factor for certain elementary configurations, some heretofore unavailable, are obtained.

Evaluation of Shape Factors

The view factors from a planar point source to the following configurations are to be presented: (1) coaxial circular disk, (2) very thin coaxial ring, (3) segment of a coaxial disk, (4) coaxial regular polygon, (5) coaxial isosceles triangle, (6) coaxial right circular cylinder, (7) coaxial sphere, and (8) orthogonal sphere.[4]

Referring to Fig. 1 and employing the basic mechanism in [1], we may state that the view factor from the element dA_1 to a coaxial disk AB is the same as that from dA_1 to the hollow spherical segment ACB. Since both dA_1 and the segment ACB lie on the same spherical enclosure, with the aid of Lambert's law the shape factor from dA_1 to ACB may be obtained as the area ratio of spherical segment ACB to the total area of the sphere [2], i.e.,

$$F_{dA_1-\text{disk}} = \frac{1}{2}\left(1 - \frac{c}{r}\right)$$

where c and r (see Fig. 1) may be solved from the following simple algebra equations:

$$r^2 - c^2 = a^2$$

$$r + c = K$$

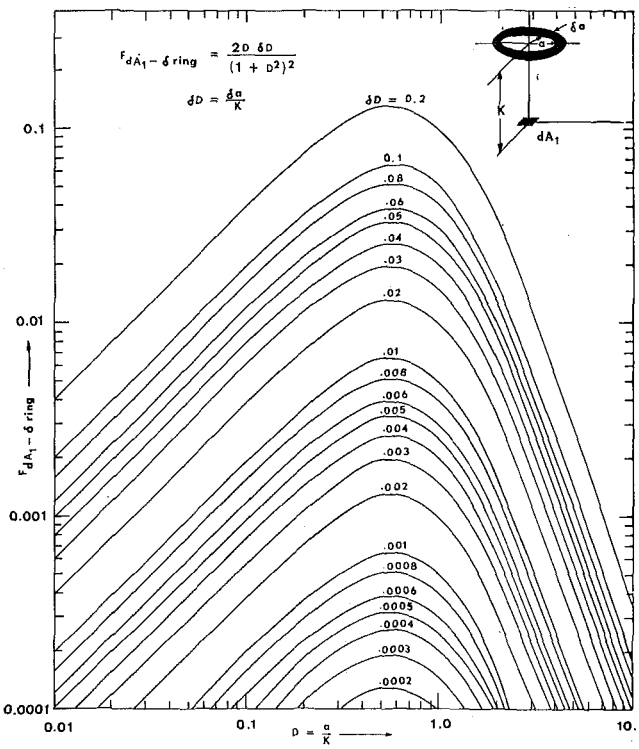

Fig. 2 Shape factors from a plane point source to a very thin coaxial ring

Hence it follows immediately

$$F_{dA_1-\text{disk}} = \frac{a^2}{K^2 + a^2} \tag{1}$$

Certainly, equation (1) can be arrived at by the methods of multiple integration [3], contour integration [4], and unit sphere [2]. However, the present approach appears to be much simpler.

Case 2 may be readily obtained by differentiating $F_{dA_1-\text{disk}}$ in equation (1). Case 3 follows from a single integration of $F_{dA_1-\delta\ \text{seg. ring}}$, the shape factor from element dA_1 to a segment of coaxial thin ring. Once the shape factors from an element to the coaxial disk and the coaxial segment of disk are known, Cases 4 to 6 can be solved by flux algebra. Referring to Fig. 5-A, it can be easily proved that the shape factor from a planar point source dA_1 to a coaxial sphere is equivalent to that from dA_1 to the coaxial circular disk AB. This leads to the same problem as Case 1 of which the solution is available. Similarly, the view factor between the plane point source dA_1 (see Fig. 5-B) and an orthogonal sphere is the same as that between dA_1

---

[1] Assistant Professor, Mechanical Engineering Department, University of Akron, Akron, Ohio. Assoc. Mem. ASME.

[2] Graduate Assistant, Mechanical Engineering Department, University of Akron, Akron, Ohio.

[3] Numbers in brackets designate References at end of technical brief.

[4] For brevity, we define that a sphere is "orthogonal" with respect to an element if the normal of the element is perpendicular to the line joining the element to the center of the sphere.

Contributed by the Heat Transfer Division of THE AMERICAN SOCIETY OF MECHANICAL ENGINEERS. Manuscript received by the Heat Transfer Division November 10, 1971.

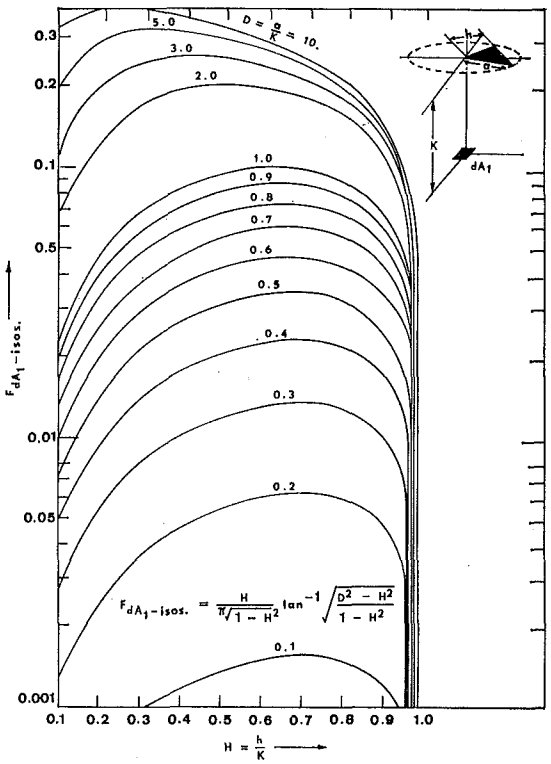

Fig. 3 Shape factors from a plane point source to an isosceles triangle

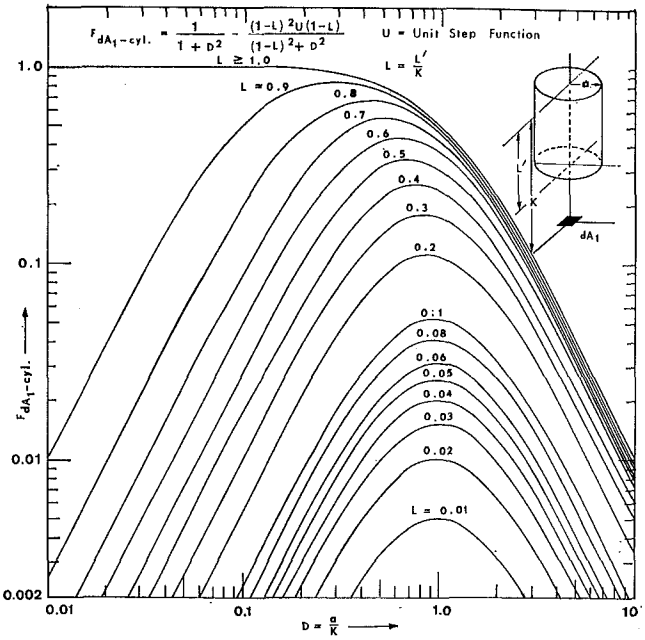

Fig. 4 Shape factors from a plane point source to a coaxial right circular cylinder

and the semicircular disk DB, and therefore the solution for Case 8 is obtainable. Results for Cases 7 and 8 from the present analysis are in good agreement with those computed by Clark and Anderson [5] based on an approximate analysis. The shape factors for Cases 7 and 8 have significant applications in the radiant exchange between a spacecraft and celestial bodies. In this connection it is worthy to mention another case, namely, the radiation view factor between a planet and a spherical satellite. Employing the same principle presented in [1], we can state that the shape factor from the spherical point source ds_1 (see Fig. 5-C) to the sphere s_2 is equivalent to the area ratio of spherical segment ADB to the total spherical surface $4\pi r^2$. This ratio yields the identical expression derived by Watt [6] using a multiple-integral technique.

To facilitate engineering applications, the view factor graphs, the analytical solutions,[5] and the associated geometric sketches are presented in Figs. 2 to 5.

References

1 Feingold, A., and Gupta, K. G., "New Analytical Approach to the Evaluation of Configuration Factors in Radiation From Spheres and Infinitely Long Cylinders," JOURNAL OF HEAT TRANSFER, TRANS. ASME, Series C, Vol. 92, No. 1, Feb. 1970, pp. 69–76.

[5] The graphical representations for Cases 3 and 4 are omitted. Their analytical solutions are given respectively by

$$F_{dA_1-\text{poly.}} = \frac{nH}{\pi\sqrt{1+H^2}} \tan^{-1}\sqrt{\frac{D^2-H^2}{1+H^2}}$$

(n = no. of edges of polygon)

and

$$F_{dA_1-\text{seg.}} = \frac{1}{\pi}\left[\frac{D^2}{1+D^2}\cos^{-1}\left(\frac{H}{D}\right) - \frac{H}{\sqrt{1+H^2}}\tan^{-1}\sqrt{\frac{D^2-H^2}{1+H^2}}\right].$$

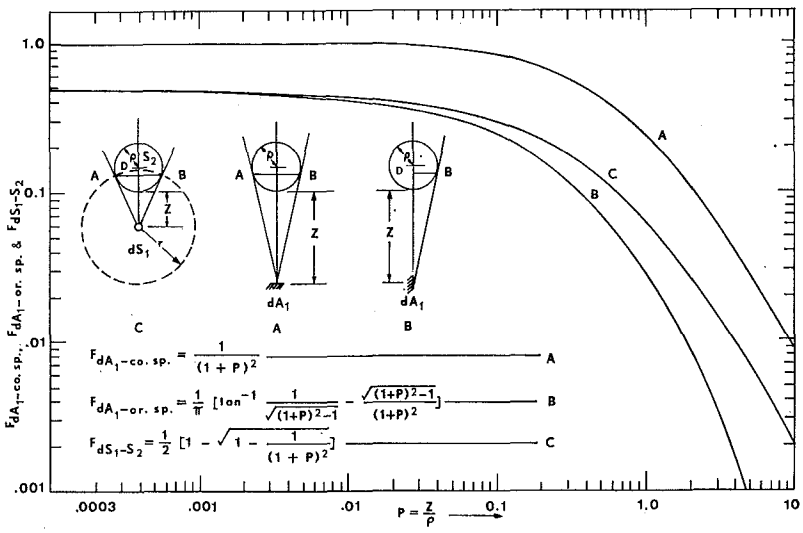

Fig. 5 Shape factors from planar and spherical point sources to a sphere

2 Hottel, H. C., and Sarofim, A. F., *Radiative Transfer*, McGraw-Hill, New York, N. Y., 1967.
3 Hamilton, D. C., and Morgan, W. R., "Radiant Interchange Configuration Factors," NACA Tech. Note No. 2836, 1952.
4 Sparrow, E. M., "A New and Simpler Formulation for Radiative Angle Factors," JOURNAL OF HEAT TRANSFER, TRANS. ASME, Series C, Vol. 85, No. 2, May 1963, pp. 81–88.
5 Clark, L. W., and Anderson, E. C., "Geometric Shape Factors for Planetary-Thermal and Planetary-Reflected Radiation Incident upon Spinning and Non-spinning Spacecraft," NASA Technical Note No. D-2835, 1965.
6 Watts, R. G., "Radiant Heat Transfer to Earth Satellites," JOURNAL OF HEAT TRANSFER, TRANS. ASME, Series C, Vol. 87, No. 3, Aug. 1965, pp. 369–373.

Free Convective Heat Transfer from Vertical Cones

P. H. OOSTHUIZEN[1] and E. DONALDSON[2]

Introduction

SEVERAL analytical studies of free convective heat transfer rates from right circular cones are available. Hering and Grosh [1],[3] by ignoring certain terms in the boundary-layer equations, obtained a similarity solution. This solution applies when curvature effects are small. Kuiken [2] considered the full boundary-layer equations and obtained a series-type solution. A numerical solution of the boundary-layer equations is given in [3], and this predicts a local heat transfer rate distribution that agrees closely with that predicted by Kuiken's analysis.

The measurement of free convective heat transfer rates from cones appears to have received little attention. In the present study some measurements of mean heat transfer rates are described.

Apparatus and Method

Mean heat transfer rates from seven cones have been measured. The dimensions of the seven cones used are given in Table 1. D is the diameter of the upper end of the cone, l is its vertical height, and ϕ is its included angle. The diameter of the tip of the cone varied from cone to cone from about 0.03 in. to about 0.04 in. Since this was small compared to the other dimensions of the cones, it was felt that the effect of the finite tip size and its variation was negligible.

The cones were made of solid aluminum with caps made from an insulating material attached to their upper ends. The mean heat transfer rates from the cones were determined by heating them to a temperature of about 320 deg F and then measuring the rate at which they cooled when suspended vertically in still air with the points of the cones being, of course, downward. Temperatures were measured by means of thermocouples inserted into holes drilled at various points in the cones. These thermocouples showed that, as expected, the cone temperatures remained effectively uniform during the cooling. In deducing the heat transfer rate it was therefore assumed that the cone temperature remained uniform. Measurements were taken while the cones cooled from about 300 deg F to about 120 deg F. With the smallest cone this took about 15 min. Unsteady effects on the heat transfer rate were therefore assumed to be negligible.

The mean convective heat transfer rate was determined from the total heat transfer rate by subtracting the radiant heat transfer rate. This radiant heat transfer rate was small in all tests, amounting to less than 5 percent of the total heat transfer.

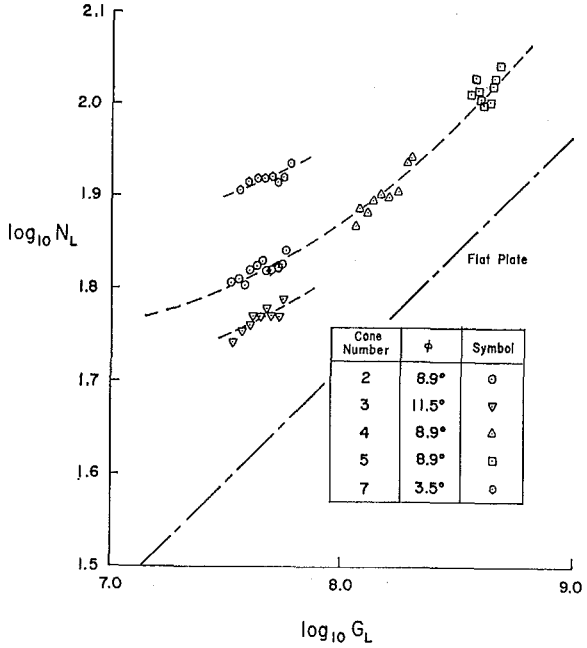

Fig. 1 Variation of Nusselt number with Grashof number

Results

The heat transfer rate from right circular cones can, of course, be correlated in the following way:

$$N_L = \text{function } (G_L, \text{Pr}, \phi) \quad (1)$$

where N_L is the mean Nusselt number based on the slant height L of the cone, i.e., hL/k; G_L is the Grashof number based on the slant height and multiplied by cos ϕ, i.e., $\beta g(T_w - T_\infty)L^3 \cos \phi/\nu^2$ where $(T_w - T_\infty)$ is the temperature difference and β, g, and ν are as conventionally used; Pr is the Prandtl number; and ϕ is the included angle.

The Prandtl number remained effectively constant during the present tests and N_L was, therefore, a function of G_L and ϕ alone.

The variation of N_L with G_L for five of the cones is shown in Fig. 1. The results for the remaining two cones are omitted for clarity. In obtaining these results, the fluid properties have been evaluated at the mean film temperature.

Three of the cones for which results are given in Fig. 1 have the same included angle ϕ of 8.9 deg, and a curve through these three results is shown. Also shown, for comparison, is the experimentally determined variation of N_L with G_L for flat plates (L in this case being the vertical height of the plate) as given in [4], for example. It will be seen that, as expected from Kuiken's [2] analysis, the values of N_L for the cones are considerably higher than those for a flat plate, and that as the angle ϕ decreases the value of N_L increases at a given value of G_L.

Table 1

Cone number	D, in.	l, in.	ϕ, deg
1	0.58	8	3.8
2	1.22	8	8.9
3	1.67	8	11.5
4	1.87	12	8.9
5	2.50	16	8.9
6	0.89	8	6.3
7	0.50	8	3.5

[1] Associate Professor, Department of Mechanical Engineering, Queen's University, Kingston, Ontario, Canada.
[2] Department of Mechanical Engineering, Queen's University, Kingston, Ontario, Canada.
[3] Numbers in brackets designate References at end of technical brief.
Contributed by the Heat Transfer Division of THE AMERICAN SOCIETY OF MECHANICAL ENGINEERS. Manuscript received by the Heat Transfer Division April 4, 1972.

2 Hottel, H. C., and Sarofim, A. F., *Radiative Transfer*, McGraw-Hill, New York, N. Y., 1967.
3 Hamilton, D. C., and Morgan, W. R., "Radiant Interchange Configuration Factors," NACA Tech. Note No. 2836, 1952.
4 Sparrow, E. M., "A New and Simpler Formulation for Radiative Angle Factors," JOURNAL OF HEAT TRANSFER, TRANS. ASME, Series C, Vol. 85, No. 2, May 1963, pp. 81–88.
5 Clark, L. W., and Anderson, E. C., "Geometric Shape Factors for Planetary-Thermal and Planetary-Reflected Radiation Incident upon Spinning and Non-spinning Spacecraft," NASA Technical Note No. D-2835, 1965.
6 Watts, R. G., "Radiant Heat Transfer to Earth Satellites," JOURNAL OF HEAT TRANSFER, TRANS. ASME, Series C, Vol. 87, No. 3, Aug. 1965, pp. 369–373.

Free Convective Heat Transfer from Vertical Cones

P. H. OOSTHUIZEN[1] and E. DONALDSON[2]

Introduction

SEVERAL analytical studies of free convective heat transfer rates from right circular cones are available. Hering and Grosh [1],[3] by ignoring certain terms in the boundary-layer equations, obtained a similarity solution. This solution applies when curvature effects are small. Kuiken [2] considered the full boundary-layer equations and obtained a series-type solution. A numerical solution of the boundary-layer equations is given in [3], and this predicts a local heat transfer rate distribution that agrees closely with that predicted by Kuiken's analysis.

The measurement of free convective heat transfer rates from cones appears to have received little attention. In the present study some measurements of mean heat transfer rates are described.

Apparatus and Method

Mean heat transfer rates from seven cones have been measured. The dimensions of the seven cones used are given in Table 1. D is the diameter of the upper end of the cone, l is its vertical height, and ϕ is its included angle. The diameter of the tip of the cone varied from cone to cone from about 0.03 in. to about 0.04 in. Since this was small compared to the other dimensions of the cones, it was felt that the effect of the finite tip size and its variation was negligible.

The cones were made of solid aluminum with caps made from an insulating material attached to their upper ends. The mean heat transfer rates from the cones were determined by heating them to a temperature of about 320 deg F and then measuring the rate at which they cooled when suspended vertically in still air with the points of the cones being, of course, downward. Temperatures were measured by means of thermocouples inserted into holes drilled at various points in the cones. These thermocouples showed that, as expected, the cone temperatures remained effectively uniform during the cooling. In deducing the heat transfer rate it was therefore assumed that the cone temperature remained uniform. Measurements were taken while the cones cooled from about 300 deg F to about 120 deg F. With the smallest cone this took about 15 min. Unsteady effects on the heat transfer rate were therefore assumed to be negligible.

The mean convective heat transfer rate was determined from the total heat transfer rate by subtracting the radiant heat transfer rate. This radiant heat transfer rate was small in all tests, amounting to less than 5 percent of the total heat transfer.

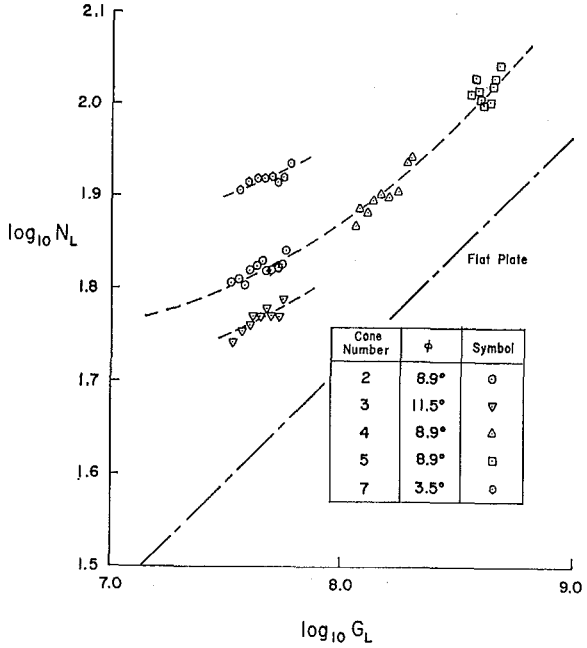

Fig. 1 Variation of Nusselt number with Grashof number

Results

The heat transfer rate from right circular cones can, of course, be correlated in the following way:

$$N_L = \text{function } (G_L, \text{Pr}, \phi) \quad (1)$$

where N_L is the mean Nusselt number based on the slant height L of the cone, i.e., hL/k; G_L is the Grashof number based on the slant height and multiplied by cos ϕ, i.e., $\beta g(T_w - T_\infty)L^3 \cos \phi/\nu^2$ where $(T_w - T_\infty)$ is the temperature difference and β, g, and ν are as conventionally used; Pr is the Prandtl number; and ϕ is the included angle.

The Prandtl number remained effectively constant during the present tests and N_L was, therefore, a function of G_L and ϕ alone.

The variation of N_L with G_L for five of the cones is shown in Fig. 1. The results for the remaining two cones are omitted for clarity. In obtaining these results, the fluid properties have been evaluated at the mean film temperature.

Three of the cones for which results are given in Fig. 1 have the same included angle ϕ of 8.9 deg, and a curve through these three results is shown. Also shown, for comparison, is the experimentally determined variation of N_L with G_L for flat plates (L in this case being the vertical height of the plate) as given in [4], for example. It will be seen that, as expected from Kuiken's [2] analysis, the values of N_L for the cones are considerably higher than those for a flat plate, and that as the angle ϕ decreases the value of N_L increases at a given value of G_L.

Table 1

Cone number	D, in.	l, in.	ϕ, deg
1	0.58	8	3.8
2	1.22	8	8.9
3	1.67	8	11.5
4	1.87	12	8.9
5	2.50	16	8.9
6	0.89	8	6.3
7	0.50	8	3.5

[1] Associate Professor, Department of Mechanical Engineering, Queen's University, Kingston, Ontario, Canada.
[2] Department of Mechanical Engineering, Queen's University, Kingston, Ontario, Canada.
[3] Numbers in brackets designate References at end of technical brief.
Contributed by the Heat Transfer Division of THE AMERICAN SOCIETY OF MECHANICAL ENGINEERS. Manuscript received by the Heat Transfer Division April 4, 1972.

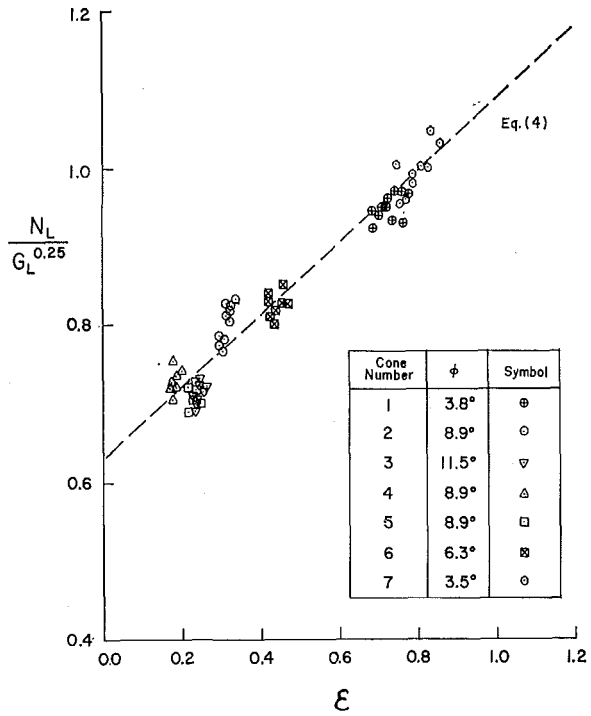

Fig. 2 Correlation of results for all cones

Now it can be deduced from Kuiken's [2] work that for a given Prandtl number the heat transfer rate from a cone will be given by an equation of the form

$$N_L/G_L^{0.25} = K[1 + f(\epsilon)] \quad (2)$$

where K is a constant and, for cones having a uniform surface temperature, ϵ is given by

$$\epsilon = \frac{2}{G_L^{0.25} \tan(\phi/2)} \quad (3)$$

The results for all the cones have therefore been replotted in the form $N_L/G_L^{0.25}$ against ϵ in Fig. 2. It will be seen that the results are well correlated in this form and can be approximately represented by the following equation:

$$N_L/G_L^{0.25} = 0.63(1 + 0.72\epsilon) \quad (4)$$

Conclusions

Mean free convective heat transfer rates from a series of comparatively slender cones have been measured. It has been shown that these results can be correlated in terms of a variable of the type that was introduced by Kuiken, and an empirical equation in terms of this variable has been derived.

Acknowledgments

This work was supported by the National Research Council of Canada under grant number A5573.

References

1 Hering, R. G., and Grosh, R. J., "Laminar Free Convection from a Non-Isothermal Cone," *International Journal of Heat and Mass Transfer*, Vol. 5, 1962, pp. 1059–1068.

2 Kuiken, H. K., "Axisymmetric Free Convection Boundary-Layer Flow Past Slender Bodies," *International Journal of Heat and Mass Transfer*, Vol. 11, 1968, pp. 1141–1153.

3 Oosthuizen, P. H., and Wu, E., "A Numerical Study of Some Laminar Free Convection Problems," Report 2-71, Thermal and Fluid Sciences Group, Queen's University, Kingston, Ontario, Canada, 1971.

4 Kreith, F., *Principles of Heat Transfer*, 2nd ed., International Textbook Co., Scranton, Pa., 1967, pp. 335.

Transient versus Steady-State Nucleate Boiling

F. L. OWENS, JR.[1] and L. W. FLORSCHUETZ[2]

A COMPARISON of transient and steady-state pool-boiling data using the same heating surface was recently reported by Veres and Florschuetz [1].[3] They cited a number of investigations in which the transient calorimeter technique was used to construct characteristic boiling curves or portions of such curves. Their results provided direct experimental evidence that heat-transfer characteristics for transient film boiling, including the minimum film boiling point, for systems of sufficient thermal capacity can be considered quasi-steady. Thus, film-boiling curves constructed from transient test data for such systems can be expected to represent the correct steady-state boiling characteristics for the same or an identical system. However, their results for the nucleate-boiling region were not conclusive. The heating element for their tests was a 1-in-dia solid copper sphere. The sphere was inductively heated for the steady-state tests, but the induction field was not present during the transient cooling tests. It seemed likely that the presence of the induction field was augmenting the steady-state nucleate-boiling heat rates, so that with respect to nucleate boiling the system could not be considered as being the same as for the transient tests. The purpose of this note is to report subsequent results comparing steady-state and transient nucleate pool-boiling data for the same heating surface using direct electric-resistance heating for the steady-state tests.

The heating surface was the top of a solid cylindrical copper block, 2 in. in diameter by $^1/_2$ in. thick, press-fitted into a Teflon base. The heating element consisted of a coiled resistance wire impregnated in a silicone-rubber dielectric film bonded to the base of the copper block by the manufacturer of the element. The boiling vessel was a 12-in. length of 2-in-ID standard glass pipe clamped to the Teflon base. Two 30-gage copper–constantan thermocouples, denoted TC1 and TC2, were located along the disk centerline at points $^1/_{16}$ in. from the top and bottom surfaces of the copper block. They were inserted in 0.055-in. holes drilled from the circumferential surface of the copper block with good thermal contact insured by aluminum powder tamped into the holes. The test fluid was Freon-113 at saturation conditions. All tests were conducted at atmospheric pressure levels.

Transient and steady-state data for the heating surface as originally machined (surface 2A) are compared in Fig. 1. Subsequently, the surface was polished and another series of test runs was performed. The comparison for this surface, denoted as 2H, is presented in Fig. 2. Prior to each series of test runs, the vessel and heating surface were thoroughly rinsed with distilled water and acetone. The fluid level was maintained at 6 in. above the heating surface. The system was degassed by prolonged boiling.

The steady-state heat fluxes were calculated from the measured power input to the heating element. Losses were determined to range from about 4–6 percent. Heat losses were estimated by measuring the steady-state power input to the element with the heating surface insulated. The losses were neglected in computing the steady-state heat fluxes plotted in Figs. 1 and

[1] Captain, United States Air Force, Vandenberg AFB, Calif.; formerly Graduate Student, Department of Mechanical Engineering, Arizona State University, Tempe, Ariz. Assoc. Mem. ASME.

[2] Associate Professor, Department of Mechanical Engineering, Arizona State University, Tempe, Ariz. Mem. ASME.

[3] Numbers in brackets designate References at end of technical brief.

Contributed by the Heat Transfer Division of THE AMERICAN SOCIETY OF MECHANICAL ENGINEERS. Manuscript received by the Heat Transfer Division August 12, 1971.

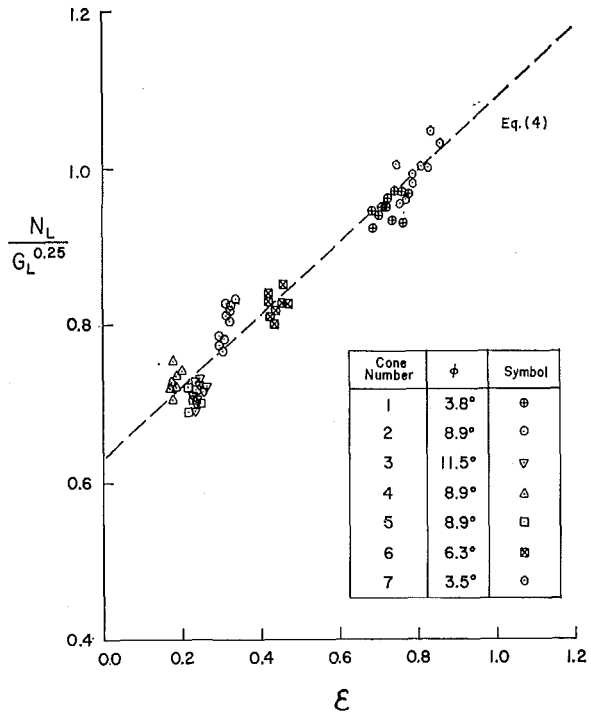

Fig. 2 Correlation of results for all cones

Now it can be deduced from Kuiken's [2] work that for a given Prandtl number the heat transfer rate from a cone will be given by an equation of the form

$$N_L/G_L^{0.25} = K[1 + f(\epsilon)] \tag{2}$$

where K is a constant and, for cones having a uniform surface temperature, ϵ is given by

$$\epsilon = \frac{2}{G_L^{0.25} \tan(\phi/2)} \tag{3}$$

The results for all the cones have therefore been replotted in the form $N_L/G_L^{0.25}$ against ϵ in Fig. 2. It will be seen that the results are well correlated in this form and can be approximately represented by the following equation:

$$N_L/G_L^{0.25} = 0.63(1 + 0.72\epsilon) \tag{4}$$

Conclusions

Mean free convective heat transfer rates from a series of comparatively slender cones have been measured. It has been shown that these results can be correlated in terms of a variable of the type that was introduced by Kuiken, and an empirical equation in terms of this variable has been derived.

Acknowledgments

This work was supported by the National Research Council of Canada under grant number A5573.

References

1 Hering, R. G., and Grosh, R. J., "Laminar Free Convection from a Non-Isothermal Cone," *International Journal of Heat and Mass Transfer*, Vol. 5, 1962, pp. 1059–1068.

2 Kuiken, H. K., "Axisymmetric Free Convection Boundary-Layer Flow Past Slender Bodies," *International Journal of Heat and Mass Transfer*, Vol. 11, 1968, pp. 1141–1153.

3 Oosthuizen, P. H., and Wu, E., "A Numerical Study of Some Laminar Free Convection Problems," Report 2-71, Thermal and Fluid Sciences Group, Queen's University, Kingston, Ontario, Canada, 1971.

4 Kreith, F., *Principles of Heat Transfer*, 2nd ed., International Textbook Co., Scranton, Pa., 1967, pp. 335.

Transient versus Steady-State Nucleate Boiling

F. L. OWENS, JR.[1] and L. W. FLORSCHUETZ[2]

A COMPARISON of transient and steady-state pool-boiling data using the same heating surface was recently reported by Veres and Florschuetz [1].[3] They cited a number of investigations in which the transient calorimeter technique was used to construct characteristic boiling curves or portions of such curves. Their results provided direct experimental evidence that heat-transfer characteristics for transient film boiling, including the minimum film boiling point, for systems of sufficient thermal capacity can be considered quasi-steady. Thus, film-boiling curves constructed from transient test data for such systems can be expected to represent the correct steady-state boiling characteristics for the same or an identical system. However, their results for the nucleate-boiling region were not conclusive. The heating element for their tests was a 1-in-dia solid copper sphere. The sphere was inductively heated for the steady-state tests, but the induction field was not present during the transient cooling tests. It seemed likely that the presence of the induction field was augmenting the steady-state nucleate-boiling heat rates, so that with respect to nucleate boiling the system could not be considered as being the same as for the transient tests. The purpose of this note is to report subsequent results comparing steady-state and transient nucleate pool-boiling data for the same heating surface using direct electric-resistance heating for the steady-state tests.

The heating surface was the top of a solid cylindrical copper block, 2 in. in diameter by $^1/_2$ in. thick, press-fitted into a Teflon base. The heating element consisted of a coiled resistance wire impregnated in a silicone-rubber dielectric film bonded to the base of the copper block by the manufacturer of the element. The boiling vessel was a 12-in. length of 2-in-ID standard glass pipe clamped to the Teflon base. Two 30-gage copper–constantan thermocouples, denoted TC1 and TC2, were located along the disk centerline at points $^1/_{16}$ in. from the top and bottom surfaces of the copper block. They were inserted in 0.055-in. holes drilled from the circumferential surface of the copper block with good thermal contact insured by aluminum powder tamped into the holes. The test fluid was Freon-113 at saturation conditions. All tests were conducted at atmospheric pressure levels.

Transient and steady-state data for the heating surface as originally machined (surface 2A) are compared in Fig. 1. Subsequently, the surface was polished and another series of test runs was performed. The comparison for this surface, denoted as 2H, is presented in Fig. 2. Prior to each series of test runs, the vessel and heating surface were thoroughly rinsed with distilled water and acetone. The fluid level was maintained at 6 in. above the heating surface. The system was degassed by prolonged boiling.

The steady-state heat fluxes were calculated from the measured power input to the heating element. Losses were determined to range from about 4–6 percent. Heat losses were estimated by measuring the steady-state power input to the element with the heating surface insulated. The losses were neglected in computing the steady-state heat fluxes plotted in Figs. 1 and

[1] Captain, United States Air Force, Vandenberg AFB, Calif.; formerly Graduate Student, Department of Mechanical Engineering, Arizona State University, Tempe, Ariz. Assoc. Mem. ASME.

[2] Associate Professor, Department of Mechanical Engineering, Arizona State University, Tempe, Ariz. Mem. ASME.

[3] Numbers in brackets designate References at end of technical brief.

Contributed by the Heat Transfer Division of THE AMERICAN SOCIETY OF MECHANICAL ENGINEERS. Manuscript received by the Heat Transfer Division August 12, 1971.

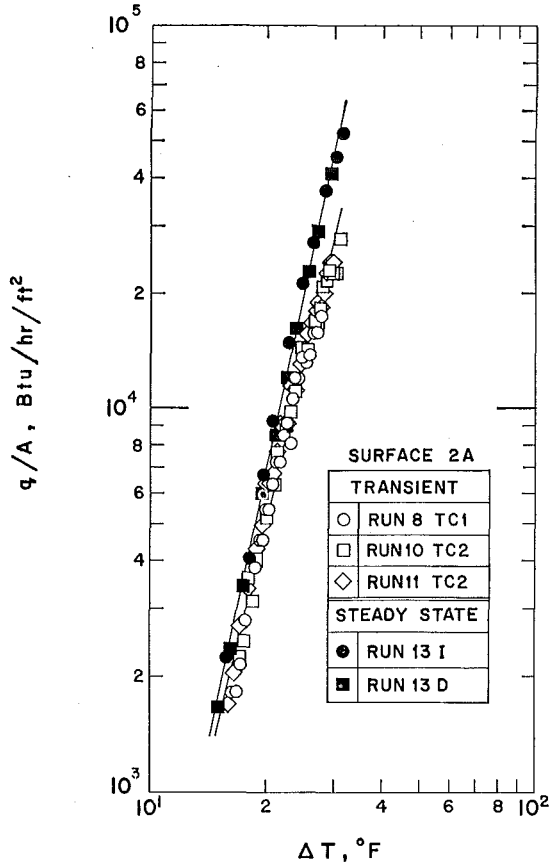

Fig. 1 Experimental data for surface 2A; transient runs 9 and 12, omitted for clarity, were similar to runs 8, 10, and 11; straight lines are least-squares fits

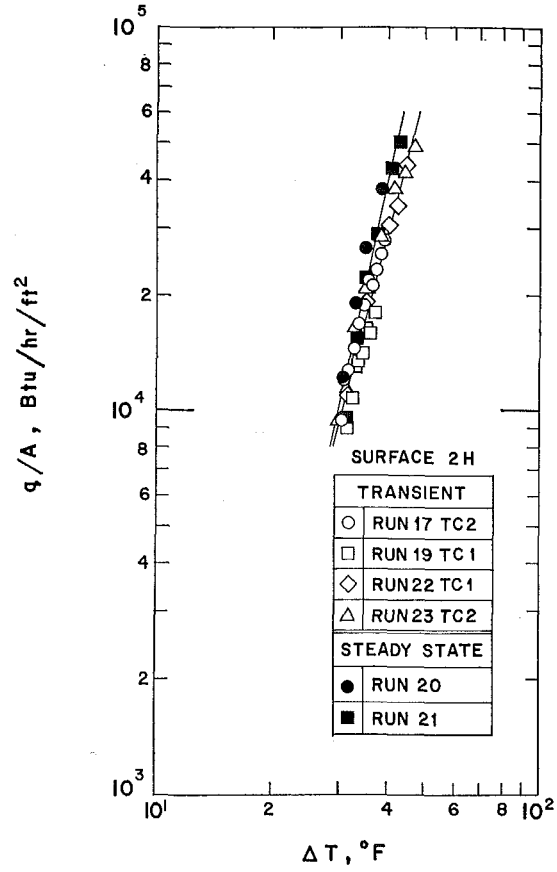

Fig. 2 Experimental data for surface 2H; transient runs 16 and 18, omitted for clarity, were similar to runs 17, 22, and 23; straight lines are least-squares fits

2. Surface temperatures were determined by a linear extrapolation of the measured temperatures. Runs 13I and 20 were made using an increasing power-level sequence, followed by runs 13D and 21, respectively, using a decreasing power-level sequence. The reproducibility is satisfactory, although close examination of the data reveals a very slight hysteresis.

All transient runs, except 22 and 23, were made by cutting power to the heating element after a relatively high nucleate-boiling flux had been established and recording the transient temperature response of the copper block. Reduction of the data was based on the assumption that the copper block could be thermally lumped. Thus, the plotted data points actually represent q/A versus $(T - T_{sat})$, where q/A was computed from

$$q/A = -\frac{Mc_p(T)}{A}\frac{dT}{dt} \tag{1}$$

Here q/A is heat flux, M is the mass of the copper block, c_p is its specific heat, A is the heat-transfer surface area, T_{sat} is saturation temperature, and t is time. T was represented by either TC1 or TC2 for a given test run as indicated in Figs. 1 and 2. The reduced data indicated that which of the two thermocouple responses was used to represent T was not of significance. This does not necessarily mean, however, that the lumped-system assumption, even in this case, is completely justified, as will be pointed out shortly. To check for the significance of heat interactions with the insulating material during the transient cooling runs, the time interval during which the initial rate of nucleate boiling was maintained just prior to cutting power was substantially reduced in some of the runs for each surface condition. Thus, less energy was stored in the insulation and a different initial temperature distribution existed in the insulation. This did not cause a significant effect, indicating that heat gain from the hot insulation during transient cooling of the copper block was negligible. Runs 22 and 23 were made with the system initially operating in the stable film-boiling region. The results agree well with the data from the runs initiated in the nucleate-boiling region. The data for several transient runs have been omitted from Figs. 1 and 2 to prevent overcrowding of data points. For surface 2A omitted data from runs 9 and 12 overlap the transient data that are presented. For surface 2H, omitted runs 16 and 18 overlap runs 17, 22, and 23. Run 19, for an unexplained reason, deviates somewhat more from the other transient runs for surface 2H than they deviate from each other, but has still been included in the analysis of the data.

The straight lines in Figs. 1 and 2 represent least-squares fits to the data points.[4] The heat fluxes for the transient tests fall somewhat below the steady-state fluxes for both surface conditions, particularly at the higher flux levels. Only part of the discrepancy can be attributed to the neglect of the losses for the steady-state tests. Since the characteristic time for the transient cooling process was clearly much larger than that associated with the bubble-growth-and-departure phenomena, better agreement might be expected. To assess in detail the importance of the lumped-system assumption used in reducing the transient test data, the following procedure was adopted.

The nonsteady-heat-conduction equation applied to the copper block modeled as an infinite plane slab was solved numerically, using as a nonlinear boundary condition for the heating surface the least-squares fit to the steady-state data. The bottom surface was assumed perfectly insulated. The initial condition was a linear temperature distribution corresponding to the nucleate-boiling flux which existed at the initiation of a transient cooling run. Nine nodal points spaced $^1/_{16}$ in. apart were used for the

[4] The data, originally presented and analyzed in [2], have been re-analyzed to insure that all points used are well within the nucleate-boiling region and that transient and steady-state data points used for comparison for a given surface fall in the same range of heat fluxes. The main conclusions, however, remain unchanged.

finite-difference calculation. Thus, two of the nodes corresponded with the thermocouple locations. The numerical solution for $T_1(t)$, which corresponded with TC1, was then used in equation (1) to compute the heat flux. This heat flux was then plotted versus $(T_1 - T_{sat})$. The same procedure was repeated using the numerical solution for $T_2(t)$, which corresponded with TC2. Except for an initial transient the two plots coincided, corroborating the experimental result that data reduction based on either TC1 or TC2 gave essentially the same results. However, these curves did not coincide with the imposed boundary condition at the heating surface as they would if the lumped-system assumption were exact, but rather showed a discrepancy like that existing between the steady-state and transient data as compared in Figs. 1 and 2. Thus, the apparent discrepancy between steady-state and transient results in these figures is primarily due to the lumped-system assumption. Additionally allowing for the minor steady-state losses, the correct heat fluxes for the transient runs were within 8 percent of the steady-state fluxes for surface 2A and within 5 percent for surface 2H. For a given heat flux the ΔT's differed by less than 2 percent. This is acceptable agreement for nucleate-boiling conditions.

It is reasonable to expect that transient nucleate-boiling phenomena occurring during the cooling of systems of sufficient thermal capacity can be assumed to be quasi-steady. The results reported here provide experimental verification of this expectation.

References

1 Veres, D. R., and Florschuetz, L. W., "A Comparison of Transient and Steady-State Pool-Boiling Data Obtained Using the Same Heating Surface," JOURNAL OF HEAT TRANSFER, TRANS. ASME, Series C, Vol. 93, No. 2, May 1971, pp. 229–232.

2 Owens, F. L., Jr., "Measurements of Nucleate Pool Boiling from a Horizontal Surface Comparing Transient and Steady State Techniques," MS thesis, Arizona State University, Tempe, Ariz., 1969.

The Effect of Thermal Conductivity and Base-Temperature Depression on Fin Effectiveness

D. E. KLETT[1] and J. W. McCULLOCH[2]

Introduction

EQUATIONS commonly presented in heat-transfer texts [1–3][3] governing temperature distributions and heat fluxes for extended surfaces (fins) are generally based upon the assumption of constant temperature at the base of the fin. The base temperature is taken to be that of the body to which the fin is attached. A study by Sparrow and Hennecke [4], however, indicates that the temperature at the base of a fin may be substantially reduced by the presence of the fin. In addition, little attention has been paid to the effects of employing fin materials differing from that of the parent body. This note examines the effect of fin conductivity on the base-temperature depression and fin effectiveness for two-dimensional rectangular fins.

Analysis

The investigation deals with two-dimensional rectangular fins of length L and width t as shown in Fig. 1. Properties pertaining to the body are denoted by the subscript I and those pertaining to the fin are denoted by the subscript II.

The steady-state temperature distribution in the body and fin is governed by Laplace's equation subject to convective boundary conditions on all exposed surfaces and a closure condition within the body far from the fin given by

$$-k_I \frac{T - T_s}{x} = h(T_s - T_\infty)$$

where x is the coordinate distance normal to the surface ($x < 0$ for points in the body), h is the convective film coefficient, T_∞ is the ambient temperature, and T_s is the surface temperature in the absence of the fin.

The condition to be satisfied at the interface between body and fin is

$$k_I \left.\frac{\partial T}{\partial x}\right|_I = k_{II} \left.\frac{\partial T}{\partial x}\right|_{II}$$

Introducing the Biot number

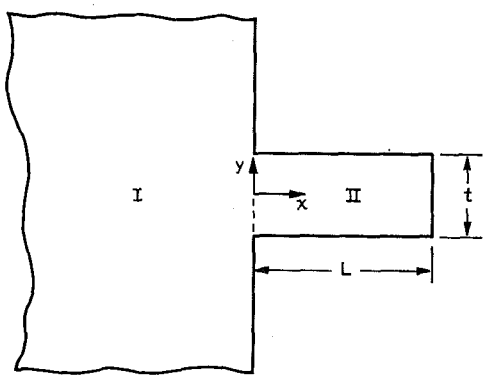

Fig. 1 Geometry and nomenclature

$$\mathrm{Bi} = \frac{ht}{k}$$

and nondimensionalized temperature, coordinates, and conductivity

$$\theta = \frac{T - T_\infty}{T_s - T_\infty}$$

$$\xi = \frac{x}{t} \qquad \eta = \frac{y}{t} \qquad K_{II} = \frac{k_{II}}{k_I}$$

results in the following set of dimensionless equations:

$$\frac{\partial^2\theta}{\partial\xi^2} + \frac{\partial^2\theta}{\partial\eta^2} = 0 \qquad \text{throughout the solid}$$

$$\frac{\partial\theta}{\partial\xi} + \mathrm{Bi}\,\theta = 0 \qquad \text{on surfaces normal to the } x \text{ direction}$$

$$\frac{\partial\theta}{\partial\eta} + \mathrm{Bi}\,\theta = 0 \qquad \text{on surfaces normal to the } y \text{ direction}$$

$$\theta = 1 - \mathrm{Bi}_I\xi \qquad \text{in the body far from the fin}$$

$$\left.\frac{\partial\theta}{\partial\xi}\right|_I = K_{II} \left.\frac{\partial\theta}{\partial\xi}\right|_{II} \qquad \text{at the interface}$$

These equations were solved numerically for fin length-to-width ratios of 2, 4, and 8 and fin-to-body thermal-conductivity ratios of 1, 4, 10, and 20.

Calculations were continued into the body and above the fin for a distance of 22 fin widths. Results were also obtained extending calculations 8 and 12 fin widths into the body. No significant differences were noted in the results for 12 and 22 fin widths.

[1] Bell Telephone Laboratories, Greensboro, N. C.

[2] Bell Telephone Laboratories, Greensboro, N. C. Assoc. Mem. ASME.

[3] Numbers in brackets designate References at end of technical brief.

Contributed by the Heat Transfer Division of THE AMERICAN SOCIETY OF MECHANICAL ENGINEERS. Manuscript received by the Heat Transfer Division December 17, 1971.

finite-difference calculation. Thus, two of the nodes corresponded with the thermocouple locations. The numerical solution for $T_1(t)$, which corresponded with TC1, was then used in equation (1) to compute the heat flux. This heat flux was then plotted versus $(T_1 - T_{sat})$. The same procedure was repeated using the numerical solution for $T_2(t)$, which corresponded with TC2. Except for an initial transient the two plots coincided, corroborating the experimental result that data reduction based on either TC1 or TC2 gave essentially the same results. However, these curves did not coincide with the imposed boundary condition at the heating surface as they would if the lumped-system assumption were exact, but rather showed a discrepancy like that existing between the steady-state and transient data as compared in Figs. 1 and 2. Thus, the apparent discrepancy between steady-state and transient results in these figures is primarily due to the lumped-system assumption. Additionally allowing for the minor steady-state losses, the correct heat fluxes for the transient runs were within 8 percent of the steady-state fluxes for surface 2A and within 5 percent for surface 2H. For a given heat flux the ΔT's differed by less than 2 percent. This is acceptable agreement for nucleate-boiling conditions.

It is reasonable to expect that transient nucleate-boiling phenomena occurring during the cooling of systems of sufficient thermal capacity can be assumed to be quasi-steady. The results reported here provide experimental verification of this expectation.

References

1 Veres, D. R., and Florschuetz, L. W., "A Comparison of Transient and Steady-State Pool-Boiling Data Obtained Using the Same Heating Surface," JOURNAL OF HEAT TRANSFER, TRANS. ASME, Series C, Vol. 93, No. 2, May 1971, pp. 229–232.

2 Owens, F. L., Jr., "Measurements of Nucleate Pool Boiling from a Horizontal Surface Comparing Transient and Steady State Techniques," MS thesis, Arizona State University, Tempe, Ariz., 1969.

The Effect of Thermal Conductivity and Base-Temperature Depression on Fin Effectiveness

D. E. KLETT[1] and J. W. McCULLOCH[2]

Introduction

EQUATIONS commonly presented in heat-transfer texts [1–3][3] governing temperature distributions and heat fluxes for extended surfaces (fins) are generally based upon the assumption of constant temperature at the base of the fin. The base temperature is taken to be that of the body to which the fin is attached. A study by Sparrow and Hennecke [4], however, indicates that the temperature at the base of a fin may be substantially reduced by the presence of the fin. In addition, little attention has been paid to the effects of employing fin materials differing from that of the parent body. This note examines the effect of fin conductivity on the base-temperature depression and fin effectiveness for two-dimensional rectangular fins.

Analysis

The investigation deals with two-dimensional rectangular fins of length L and width t as shown in Fig. 1. Properties pertaining to the body are denoted by the subscript I and those pertaining to the fin are denoted by the subscript II.

The steady-state temperature distribution in the body and fin is governed by Laplace's equation subject to convective boundary conditions on all exposed surfaces and a closure condition within the body far from the fin given by

$$-k_I \frac{T - T_s}{x} = h(T_s - T_\infty)$$

where x is the coordinate distance normal to the surface ($x < 0$ for points in the body), h is the convective film coefficient, T_∞ is the ambient temperature, and T_s is the surface temperature in the absence of the fin.

The condition to be satisfied at the interface between body and fin is

$$k_I \left.\frac{\partial T}{\partial x}\right|_I = k_{II} \left.\frac{\partial T}{\partial x}\right|_{II}$$

Introducing the Biot number

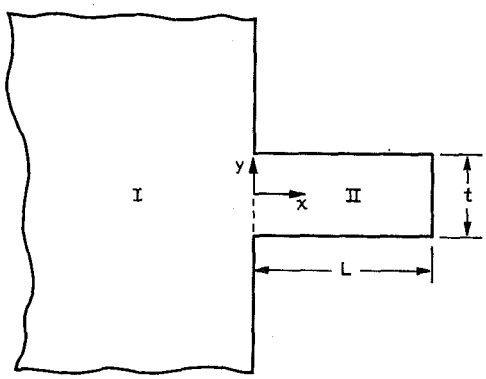

Fig. 1 Geometry and nomenclature

$$\mathrm{Bi} = \frac{ht}{k}$$

and nondimensionalized temperature, coordinates, and conductivity

$$\theta = \frac{T - T_\infty}{T_s - T_\infty}$$

$$\xi = \frac{x}{t} \qquad \eta = \frac{y}{t} \qquad K_{II} = \frac{k_{II}}{k_I}$$

results in the following set of dimensionless equations:

$$\frac{\partial^2\theta}{\partial\xi^2} + \frac{\partial^2\theta}{\partial\eta^2} = 0 \qquad \text{throughout the solid}$$

$$\frac{\partial\theta}{\partial\xi} + \mathrm{Bi}\,\theta = 0 \qquad \text{on surfaces normal to the } x \text{ direction}$$

$$\frac{\partial\theta}{\partial\eta} + \mathrm{Bi}\,\theta = 0 \qquad \text{on surfaces normal to the } y \text{ direction}$$

$$\theta = 1 - \mathrm{Bi}_I\xi \qquad \text{in the body far from the fin}$$

$$\left.\frac{\partial\theta}{\partial\xi}\right|_I = K_{II} \left.\frac{\partial\theta}{\partial\xi}\right|_{II} \qquad \text{at the interface}$$

These equations were solved numerically for fin length-to-width ratios of 2, 4, and 8 and fin-to-body thermal-conductivity ratios of 1, 4, 10, and 20.

Calculations were continued into the body and above the fin for a distance of 22 fin widths. Results were also obtained extending calculations 8 and 12 fin widths into the body. No significant differences were noted in the results for 12 and 22 fin widths.

[1] Bell Telephone Laboratories, Greensboro, N. C.

[2] Bell Telephone Laboratories, Greensboro, N. C. Assoc. Mem. ASME.

[3] Numbers in brackets designate References at end of technical brief.

Contributed by the Heat Transfer Division of THE AMERICAN SOCIETY OF MECHANICAL ENGINEERS. Manuscript received by the Heat Transfer Division December 17, 1971.

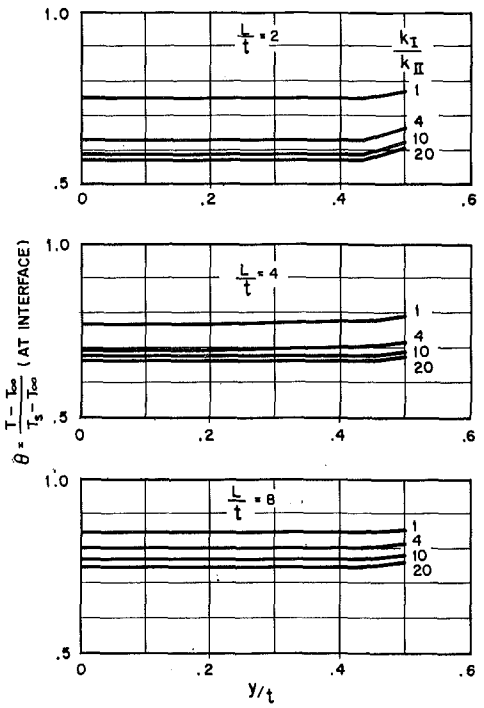

Fig. 2 Base-temperature depression versus conductivity

During calculations the Biot number was held constant for the body at the optimum value based on minimum weight for maximum heat transfer for a given aspect ratio [3]

$$\mathrm{Bi}_{\mathrm{I}} = \left(\frac{t}{L}\right)^2$$

The Biot number for the fin is then given by

$$\mathrm{Bi}_{\mathrm{II}} = \frac{\mathrm{Bi}_{\mathrm{I}}}{K_{\mathrm{II}}}$$

Results and Conclusions

Figure 2 presents fin base temperatures for various aspect and thermal-conductivity ratios. Dimensionless temperature at the fin base is plotted versus transverse location for various conductivity ratios. It is evident that increasing the thermal conductivity of the fin decreases the temperature at the base, as one would expect. It is also evident from Fig. 2 that increasing the length-to-width ratio lessens the effect of thermal conductivity. The effect of a twentyfold increase in the thermal conductivity is reduced from 24 percent for $L/t = 2$ to 12 percent for $L/t = 8$ based on the centerline temperature at the base. As L/t increases the base temperature approaches the wall temperature in the absence of the fin due to the manner in which the Biot numbers are chosen.

The effect of thermal conductivity on fin effectiveness is shown in Fig. 3.[4] It is seen here that fin effectiveness increases rapidly as conductivity increases up to a conductivity ratio of about 10. Thereafter, using higher conductivity fins produces little advantage, either in fin effectiveness or in the lowering of surface temperatures.

The results indicate that the temperature depression at the base of fins may be substantial for small L/t ratios and should be given consideration in fin design. Employing fin materials of thermal conductivity greater than the parent body can be an effective method for improving fin effectiveness while at the same time increasing the importance of giving proper consideration to base-temperature depression.

[4] Fin effectiveness is defined as the ratio of the heat transferred by the fin to the heat that would be transferred from the fin base area of the body in the absence of the fin.

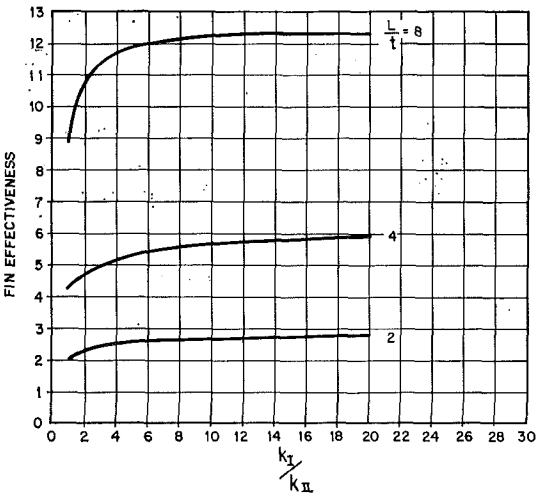

Fig. 3 Fin effectiveness versus conductivity

References

1 Kreith, F., *Principles of Heat Transfer*, International Textbook Co., Scranton, Pa., 1965.

2 Holman, J. P., *Heat Transfer*, McGraw-Hill, New York, N. Y., 1968.

3 Eckert, E. R. G., and Drake, R. M., Jr., *Heat and Mass Transfer*, McGraw-Hill, New York, N. Y., 1959.

4 Sparrow, E. M., and Hennecke, D. K., "Temperature Depression at the Base of a Fin," JOURNAL OF HEAT TRANSFER, TRANS. ASME, Series C, Vol. 92, No. 1, Feb. 1970, pp. 204–206.

A Simple Analysis of Laminar Film Condensation with Suction[1]

JOHN LIENHARD[2] and VIJAY DHIR[3]

Nomenclature

$a = \mu k \Delta T / g \rho_f (\rho_f - \rho_v) h_{fg}'$

$b = \dfrac{\rho_f h_{fg}' v_w}{k \Delta T}\left[1 + 0.32\dfrac{c_p \Delta T}{h_{fg}'}\right]$, suction parameter

c_p = specific heat of condensate

g = gravitational acceleration

h = heat-transfer coefficient

h_{fg} = latent heat of vaporization

h_{fg}' = h_{fg} corrected to account for sensible heat of subcooling

k = thermal conductivity of condensate

Nu = local Nusselt number, hx/k

Nu_0 = local Nusselt number without suction

Pr = Prandtl number

R = radius of curvature of an axisymmetric body

v_w = suction velocity at the wall

x = distance along plate from leading edge

α = thermal diffusivity

Γ_c = rate of mass flow of condensate per unit breadth

[1] This work received support under NASA grant NGR/18-001-035.

[2] Professor of Mechanical Engineering, University of Kentucky, Lexington, Ky. Mem. ASME.

[3] Research Assistant, Mechanical Engineering Department, University of Kentucky, Lexington, Ky. Student Mem. ASME.

Contributed by the Heat Transfer Division of THE AMERICAN SOCIETY OF MECHANICAL ENGINEERS. Manuscript received by the Heat Transfer Division June 25, 1971.

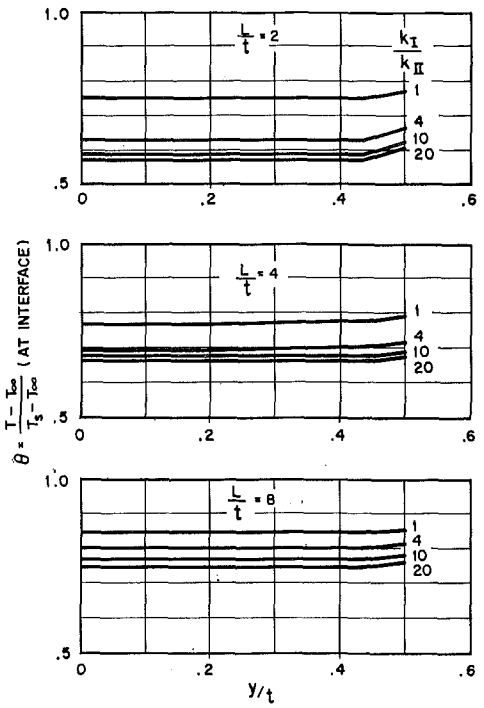

Fig. 2 Base-temperature depression versus conductivity

During calculations the Biot number was held constant for the body at the optimum value based on minimum weight for maximum heat transfer for a given aspect ratio [3]

$$\mathrm{Bi_I} = \left(\frac{t}{L}\right)^2$$

The Biot number for the fin is then given by

$$\mathrm{Bi_{II}} = \frac{\mathrm{Bi_I}}{K_{II}}$$

Results and Conclusions

Figure 2 presents fin base temperatures for various aspect and thermal-conductivity ratios. Dimensionless temperature at the fin base is plotted versus transverse location for various conductivity ratios. It is evident that increasing the thermal conductivity of the fin decreases the temperature at the base, as one would expect. It is also evident from Fig. 2 that increasing the length-to-width ratio lessens the effect of thermal conductivity. The effect of a twentyfold increase in the thermal conductivity is reduced from 24 percent for $L/t = 2$ to 12 percent for $L/t = 8$ based on the centerline temperature at the base. As L/t increases the base temperature approaches the wall temperature in the absence of the fin due to the manner in which the Biot numbers are chosen.

The effect of thermal conductivity on fin effectiveness is shown in Fig. 3.[4] It is seen here that fin effectiveness increases rapidly as conductivity increases up to a conductivity ratio of about 10. Thereafter, using higher conductivity fins produces little advantage, either in fin effectiveness or in the lowering of surface temperatures.

The results indicate that the temperature depression at the base of fins may be substantial for small L/t ratios and should be given consideration in fin design. Employing fin materials of thermal conductivity greater than the parent body can be an effective method for improving fin effectiveness while at the same time increasing the importance of giving proper consideration to base-temperature depression.

[4] Fin effectiveness is defined as the ratio of the heat transferred by the fin to the heat that would be transferred from the fin base area of the body in the absence of the fin.

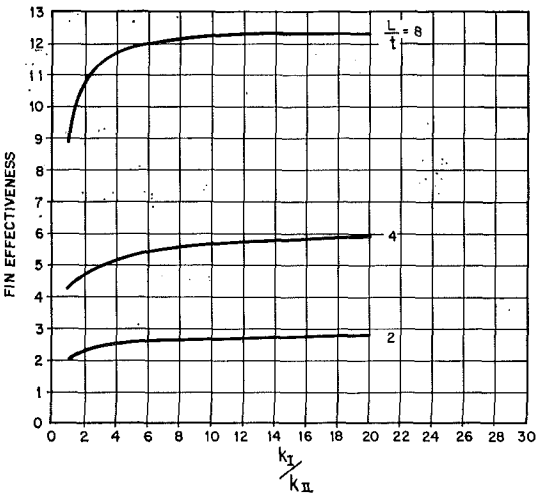

Fig. 3 Fin effectiveness versus conductivity

References

1 Kreith, F., *Principles of Heat Transfer*, International Textbook Co., Scranton, Pa., 1965.

2 Holman, J. P., *Heat Transfer*, McGraw-Hill, New York, N. Y., 1968.

3 Eckert, E. R. G., and Drake, R. M., Jr., *Heat and Mass Transfer*, McGraw-Hill, New York, N. Y., 1959.

4 Sparrow, E. M., and Hennecke, D. K., "Temperature Depression at the Base of a Fin," JOURNAL OF HEAT TRANSFER, TRANS. ASME, Series C, Vol. 92, No. 1, Feb. 1970, pp. 204–206.

A Simple Analysis of Laminar Film Condensation with Suction[1]

JOHN LIENHARD[2] and VIJAY DHIR[3]

Nomenclature

$a = \mu k \Delta T / g \rho_f (\rho_f - \rho_v) h_{fg}'$

$b = \dfrac{\rho_f h_{fg}' v_w}{k \Delta T}\left[1 + 0.32\dfrac{c_p \Delta T}{h_{fg}'}\right]$, suction parameter

c_p = specific heat of condensate

g = gravitational acceleration

h = heat-transfer coefficient

h_{fg} = latent heat of vaporization

h_{fg}' = h_{fg} corrected to account for sensible heat of subcooling

k = thermal conductivity of condensate

Nu = local Nusselt number, hx/k

$\mathrm{Nu_0}$ = local Nusselt number without suction

Pr = Prandtl number

R = radius of curvature of an axisymmetric body

v_w = suction velocity at the wall

x = distance along plate from leading edge

α = thermal diffusivity

Γ_c = rate of mass flow of condensate per unit breadth

[1] This work received support under NASA grant NGR/18-001-035.

[2] Professor of Mechanical Engineering, University of Kentucky, Lexington, Ky. Mem. ASME.

[3] Research Assistant, Mechanical Engineering Department, University of Kentucky, Lexington, Ky. Student Mem. ASME.

Contributed by the Heat Transfer Division of THE AMERICAN SOCIETY OF MECHANICAL ENGINEERS. Manuscript received by the Heat Transfer Division June 25, 1971.

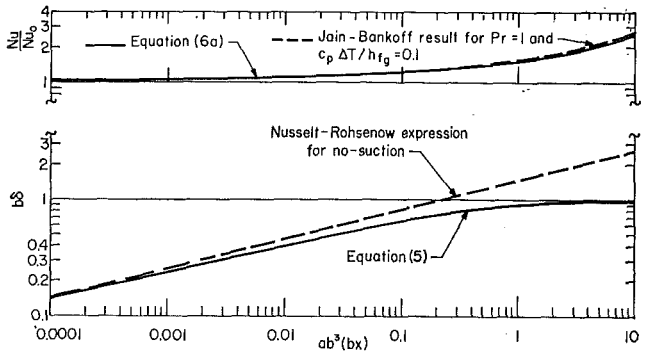

Fig. 1 Variation of normalized Nusselt number and dimensionless film thickness with dimensionless position

ΔT = difference between saturation temperature and wall temperature
δ = condensate film thickness
μ = viscosity of condensate
ρ_f, ρ_g = densities of liquid and saturated vapor, respectively

Laminar film condensation on a vertical plate with a uniform suction velocity v_w at the wall has been analyzed as a boundary-layer problem both by Jain and Bankoff [1][4] and by Yang [2]. Using their very complete numerical solutions to fix the limitations on our results, we shall obtain a simple closed solution for the problem using Nusselt's method [3] as adapted by Rohsenow [4]. We shall also show how it might be adapted to a large class of additional problems of condensation with suction.

Neglecting inertia in the condensate flow leads to Nusselt's parabolic velocity profile regardless of whether any suction occurs. The condensate flow rate Γ_c based on this profile is

$$\Gamma_c = g(\rho_f - \rho_g)\rho_f\delta^3/3\mu \tag{1}$$

Since the temperature distribution can be assumed approximately linear, the energy balance is

$$h\Delta T = \frac{k\Delta T}{\delta} = \rho_f v_w(h_{fg} + c_p\Delta T) + h_{fg}'\frac{d\Gamma_c}{dx}$$

or

$$\frac{k\Delta T}{\delta} = \rho_f v_w(h_{fg}' + 0.32c_p\Delta T) + h_{fg}'\frac{d\Gamma_c}{dx} \tag{2}$$

where $h_{fg}' \equiv h_{fg} + 0.68\ c_p\Delta T$, the latent heat as corrected by Rohsenow for nonlinearity of the temperature profile. This correction should still be valid with suction as long as the velocity profile is not distorted.

Substitution of equation (1) in equation (2) and rearrangement of the result gives

$$\frac{(b\delta)^3 d(b\delta)}{1 - b\delta} = (ab^3)d(bx) \tag{3}$$

The two scale factors in this expression are

$$a \equiv \frac{\mu k\Delta T}{g\rho_f(\rho_f - \rho_g)h_{fg}'} \quad \text{ft}^3,$$

$$b \equiv \frac{\rho_f h_{fg}' v_w}{k\Delta T}\left[1 + 0.32\frac{c_p\Delta T}{h_{fg}'}\right] \quad \text{ft}^{-1} \tag{4}$$

Integration of equation (3) with the boundary condition $\delta(x = 0) = 0$ gives

$$(ab^4x) + \ln(1 - b\delta) + b\delta + (b\delta)^2/2 + (b\delta)^3/3 = 0 \tag{5}$$

The limit of equation (5) as the suction parameter b approaches zero is $ax = \delta^4/4$, which is exactly the Nusselt–Rohsenow result for the no-suction case.

Finally, the Nusselt number is given by

$$\mathrm{Nu} = \frac{(k/\delta)x}{k} = \frac{1}{ab^3}\frac{(ab^4x)}{(b\delta)} \tag{6}$$

For the no-suction limit this becomes the Nusselt–Rohsenow expression

$$\mathrm{Nu}_0 = x^{3/4}/(4a)^{1/4} \tag{7}$$

Using Nu_0 to normalize the Nusselt number for the suction case, we obtain

$$\mathrm{Nu}/\mathrm{Nu}_0 = \frac{[4ab^3(bx)]^{1/4}}{b\delta} \tag{6a}$$

Equations (5) and (6a) are plotted in Fig. 1, and the $ax = \delta^4/4$ asymptote is included for comparison with equation (5).

Equation (5) shows that for $x > 2/ab^4$, suction will cause the film to approach a terminal thickness. Thus

$$\lim_{x\to\infty}\delta = \frac{1}{b} \qquad \lim_{x\to\infty}\mathrm{Nu} = bx \qquad \text{and} \qquad \lim_{x\to\infty}h = kb \tag{8}$$

Equations (5)–(8) are based on the assumption of a nearly linear temperature profile as well as the neglect of inertia. The range of validity of these assumptions is set by comparing our results with [1] and [2]. If Pr is on the order of unity, our solution is almost exact for $c_p\Delta T/\mathrm{Pr}h_{fg} < 0.1$. Since higher values of $c_p\Delta T/\mathrm{Pr}h_{fg}$ lead to ripply films or turbulent flows at increasingly small x, neither the boundary-layer solution nor ours has much value beyond 0.1. Fig. 1 includes Jain and Bankoff's result for Pr = 1 and $c_p\Delta T/\mathrm{Pr}h_{fg} = 0.1$. It is everywhere within 4 percent of ours.

For Pr $\ll$ 1 our prediction is inaccurate, but the existing boundary-layer treatments are also unrealistic in this range owing to the dominant effects of interfacial resistance and unknown accomodation coefficients. For Pr > 1 the limiting value of $c_p\Delta T/\mathrm{Pr}h_{fg}$ is smaller but the limiting value of $c_p\Delta T/h_{fg}$ is largely compensated by the increased Pr. The leading edge is also excluded from the present analysis, but under the same general conditions that exclude it from the boundary-layer analysis. Thus the present simple analysis can replace the more complex boundary-layer treatments in almost all situations of practical importance.

Finally, [1] provides an exact prediction of the limiting solutions for large x. For δ, Jain and Bankoff show

$$\exp(\delta v_w/\alpha) - 1 = c_p\Delta T/h_{fg}(1 + c_p\Delta T/h_{fg}) \tag{9}$$

This reduces to within 4 percent of equation (8) for $c_p\Delta T/h_{fg} \leq 0.1$.

The real potential advantage of combining suction with condensation is to be found in the region of constant δ. Not only can turbulence and ripples be suppressed to improve heat transfer but the efficient laminar process can itself be vastly improved. In this range

$$\frac{\mathrm{Nu}}{\mathrm{Nu}_0} \simeq \sqrt{2}(ab^4x)^{1/4} \qquad ab^4x > 2 \tag{10}$$

If, for example, steam at 1 atm is condensed under ΔT = 20 deg F, then v_w need only be 4×10^{-5} ft/sec to stabilize the film 0.1 ft from the leading edge. Four feet from the leading edge the heat-transfer coefficient would be increased more than fourfold over the no-suction value.

Recently we showed [5] how to adapt the Nusselt–Rohsenow solution to the general problem of condensation in an x-dependent gravity field $g(x)$ on axisymmetric bodies of radius $R = R(x)$. That can also be done in the present situation; however, a closed solution is not obtainable. If we consider such variation and

[4] Numbers in brackets designate References at end of technical brief.

allow v_w to be an independently specifiable function of x as well, equation (2) then takes the form

$$\frac{k\Delta T}{\delta} = \rho_f v_w(x)(h_{fg}' + 0.32c_p\Delta T) + \frac{h_{fg}'}{2\pi R(x)}\frac{d[2\pi R(x)\Gamma_c]}{dx} \quad (2a)$$

which reduces to

$$\frac{\delta}{3a(x)gR}\frac{d(gR\delta^3)}{dx} = (1 - b(x)\delta) \quad (11)$$

The numerical solution of equation (11) subject to the condition $\delta(x = 0) = 0$ will give $\delta(x)$ for any arbitrary specification of $g(x)$, $R(x)$, and $v_w(x)$. Substitution of the result into Nu $= x/\delta$ will give Nu subject to roughly the same limitations that apply to equations (5)–(8).

Conclusions

1 Prior boundary-layer solutions for condensation with suction can be replaced with a simple Nusselt–Rohsenow calculation in almost all cases of practical importance. The results of this calculation are given for the flat plate in Fig. 1.

2 Cases of suction with arbitrarily specified $v_w(x)$, $g(x)$, and/or axisymmetry can readily be calculated using equation (11).

3 Suction shows great promise for condensation on flat plates with $ab^4x > 2$. In this case $h \simeq kb$.

References

1 Jain, K. C., and Bankoff, S. G., "Laminar Film Condensation on a Porous Vertical Wall With Uniform Suction Velocity," JOURNAL OF HEAT TRANSFER, TRANS. ASME, Series C, Vol. 86, No. 4, Nov. 1964, pp. 481–489.

2 Yang, J. W., "Effect of Uniform Suction on Laminar Film Condensation on a Porous Vertical Wall," JOURNAL OF HEAT TRANSFER, TRANS. ASME, Series C, Vol. 92, No. 2, May 1970, pp. 252–256.

3 Nusselt, W., "Die Oberflächenkondensation des Wasserdampfes," *Z. Ver. Deutsch. Ing.*, Vol. 60, 1916, pp. 541–546, 569–575.

4 Rohsenow, W. M., "Heat Transfer and Temperature Distribution in Laminar-Film Condensation," TRANS. ASME, Vol. 78, 1956, pp. 1645–1648.

5 Dhir, V. K., and Lienhard, J. H., "Laminar Film Condensation on Plane and Axisymmetric Bodies in Nonuniform Gravity," JOURNAL OF HEAT TRANSFER, TRANS. ASME, Series C, Vol. 93, No. 1, Feb. 1971, pp. 97–100.